Charles University in Prague
Faculty of Mathematics and Physics

Physical Modelling of Flow and Diffusion in Urban Canopy

Klára Bezpalcová

Doctoral Thesis

November 2006

Physical Modelling of Flow and Diffusion in Urban Canopy

Klára Bezpalcová

Department of Meteorology and Environment Protection
Faculty of Mathematics and Physics
Charles University in Prague

Supervisor: Doc. RNDr. Zbyněk Jaňour, DrSc.
Institute of Thermomechanics
Academy of Sciences of the Czech Republic, Prague

Abstract

Dispersion of pollutants in urban areas is still one of the most challenging tasks in environmental sciences. Complex processes like the dispersion of car exhaust in street canyons or the dispersion of accidental releases of harmful substances in built-up areas are not yet fully understood. For a better understanding of the driving phenomena it is helpful to study flow and dispersion of pollutants within an idealised urban setting first.

An example of a simplified roughness setup at full scale is the Mock Urban Setting Test - MUST, carried out at US Army's Dugway Proving Ground. In order to extend the field data set as well as to enhance the representativeness of the MUST field data it was decided to carry out a complementing study in a boundary layer wind tunnel. At a scale of 1:75 the mean flow and turbulence structure within regular obstacle array was simulated.

During an extensive measurement campaign in the wind tunnel firstly flow field, including mean and turbulent characteristics, within the container array for different wind directions was studied. The second step was replication of specific set of field dispersion experiments. After the validation of the model set-up, by comparison with field results, detailed dispersion measurements were carried out for different wind directions and source conditions (for continuous as well as sudden tracer releases).

Travelling time of the pollutant through the container array was estimated by three different methods: (i) spatial concentration correlations function; (ii) the time delay of a sudden released tracer at a detector position; (iii) the time based on the measured wind speed along the tracer trajectory. Comparable results for all three methods and different travelling time behaviour for points situated along and perpendicular to street canyons have been detected.

Although a reasonable good agreement between the MUST field and wind tunnel data has been found, the wind tunnel data showed smaller uncertainties mainly due to the stationary experiment conditions and longer averaging time. Therefore the wind tunnel results were essential for understanding of physical processes and employment of the MUST field data.

Acknowledgement

Foremost, I would like to thank my supervisor Zbyněk Jaňour. He was patiently guiding me throughout the course of boundary layer meteorology as well as fluid dynamics and I learned a lot through many discussions on various themes with him.

I am very thankful to the staff (present-day as well as former) of Environmental Wind Tunnel Laboratory of Meteorological Institute of University of Hamburg, Germany. Namely I want to thank Bernd Leitl who was my advisor and provided experimental method support as well as many very fruitful discussions during my 13-month stay in the Meteorological Institute of University of Hamburg, which I greatly appreciate. I would like to thank Frank Harms for the assistance during the long measurement campaign, the workshop for the technical support, Frauke Pascheke for providing the spectra analysis software, and Merike Schultz for encouragement of any kind.

Finally, I would like to thank Kate Richards for her advices regarding English language.

This work was supported by the research project AV0Z20760514 of the Institute of Thermomechanics AS CR and Czech-German bilateral project D29-CZ 14/04-05 in the frame of PPP program of DAAD and AS CR.

Contents

List of Symbols and Abbreviations

c	Concentration of passive pollutant
c^*	Dimensionless concentration
c_p	Specific heat at constant pressure
c_V	Specific heat at constant volume
d_0	Displacement height
D_m	Molecular diffusivity coefficient for passive pollutant
Ec	Eckert number
f	Frequency
$\mathbf{f}_{\text{drag}}$	Drag force per mass unit
Fr	Froude number
ft	Filling time
$\mathbf{g} = (0, 0, -g)$	Acceleration due to gravity
H	Characteristic obstacle height
H_S	Turbulent heat flux
I_c	Intensity of concentration fluctuation
I_u, I_v, I_w	Intensity of turbulence for u, v, w velocity components
k	von Kármán constant, $k = 0.4$ in this work
Kurt	Kurtosis, the fourth order statistical moment
L	Monin-Obukhov lenght
L_c	Integral length scale based on the r_c function
lt	Flushing time
L_{ux}, L_{uy}, L_{uz}	Integral length scale at x, y, z directions based on the r_u, r_v, r_w functions
m	Mass
n	Normalised frequency
p	Pressure
Pr	Prandtl number
Q_{source}	Tracer flux from a source
r_u, r_v, r_w	Temporal velocity autocorrelation functions
r_c	Temporal concentration autocorrelation function
r_{SC}	Temporal concentration spatial correlation function
R	Gas constant
Re	Reynolds number
Re_B	Building Reynolds number
Re_*	Roughness Reynolds number

Ri	Richardson number
S_{uu}, S_{vv}, S_{ww}	Spectral function
Sc	Schmidt number
Skew	Skewness, the third order statistical moment
st	Stationary time
St	Strouhal number
t	Time
T	Temperature
T_c	Integral time scale based on r_c
t_{SC}	Time lag corresponding to the maximum of the r_{SC} function
T_u, T_v, T_w	Integral time scale based on the r_u, r_v, r_w functions
tt	Travelling time
U	Mean wind speed at x direction
u_e	Effective transport speed
U_{ref}	Reference wind speed at 8 m at the South tower
u_*	Friction velocity
u_δ	Mean wind speed at the top of the ABL
$\overline{u'w'}$	Vertical momentum transport
$\mathbf{v} = (u, v, w)$	Velocity vector
V	Mean wind speed at y direction
$v_{\text{pollutant}}$	Advective velocity of the pollutant
v_{source}	Tracer discharge from the source
W	Mean wind speed at z direction
$\mathbf{x} = (x, y, z)$	Spatial coordinates
z_0	Roughness lenght
z_d	Detector's height
α	Power law exponent
γ_0	Zero intermittency factor
γ_{tm}	Twice mean intermittency factor
δ	Boundary layer depth
Δ	Separation distance
$\triangle x$	Projection of the separation distance to the x-axis
$\triangle y$	Projection of the separation distance to the y-axis
θ	Potential temperature
κ	Heat conductivity of air
μ	Dynamic viscosity coefficient
ν	Kinematic viscosity coefficient
ϱ	Density
σ	Standard deviation, the second order statistical moment
τ	Time lag
$\boldsymbol{\tau} = \tau_{ij}$	Reynolds stress tensor; $i, j = u, v, w$
Φ_c	Net body source
Φ_θ	Net source of heat
ω	Angular frequency
$\boldsymbol{\Omega}$	Vector of the angular velocity of the earth's rotation

Operators:

$(\ )_0$	Characteristic value
$(\ )_{\mathrm{amax}}$	Maximum of the absolute value
$(\ )_{\mathrm{field}}$	Measured in the MUST field
$(\ )_{\mathrm{FS}}$	Values scaled to the full (field) scale
$(\ )_{\mathrm{MS}}$	Values scaled to the model (reduce or wind-tunnel) scale
$(\ )_{\mathrm{rms}}$	Standard deviation
$(\ )_{u,v,w}$	Values corresponding to u, v, w velocity component
$(\ )_{\mathrm{WT}}$	Measured in the wind tunnel
$(\ )^*$	Dimensionless form
$\overline{(\ )}$	Time average
$\langle\ \rangle$	Ensemble average
$(\ )'$	Turbulent part

Abbreviations:

2-D	Two-dimensional
3-D	Three-dimensional
ABL	Atmospheric Boundary Layer
AGL	Above Ground Level
CFD	Computational Fluid Dynamic
dPID	Digital Photo-Ionisation Detector
ETWL	Environmental Wind Tunnel Laboratory
FFID	Fast Flame Ionisation Detector
IS	Inertial Sublayer
LDA	Laser Doppler Anemometry
LES	Large Eddy Simulation
LNG	Liquefied Natural Gas
MUST	Mock Urban Setting Trial
RANS	Reynolds Average Navier-Stokes equations
RS	Roughness Sublayer
SFID	Slow Flame Ionisation Detector
UABL	Urban Atmospheric Boundary Layer
UCL	Urban Canopy Layer
UV	LDA set-up for u and v velocity components measurement
UVIC	Ultra Violet Ion Collector Detector
UW	LDA set-up for u and w velocity components measurement

Chapter 1

Introduction

The turbulent dispersion of pollutant in the atmosphere is a subject of interest in a range of diverse applications and has been studied for a wide variety of terrain characteristics and environments. Since earliest systematic field investigation of air pollution (in late 1940s) the sophistication of measurement equipment and modelling approaches has steadily increased. Nevertheless, the physical complexity of the phenomena is still not completely understood. The dispersion of pollutants is fairly well understood in open, unobstructed, relatively flat and homogeneous terrain (see e.g. Pasquill, 1974), but this same level of understanding for dispersion in a much more complicated urban environment is lacking at present. In the urban regime, many new effects come into play as the turbulent flow interacts with isolated or groups of obstacles, possessing a large range of shapes, sizes and configurations. The differences between traditional open terrain applications of atmospheric dispersion and that in an urban environment are greatest at the smaller scales of single buildings or small group of buildings, where the explicit details of geometry and arrangement of buildings greatly influences the approach statistically well described flow.

Concentration of air pollutants in urban areas is determined by complex dispersion processes of emissions from a wide variety of sources. Primary sources of pollutants results from production and utilisation of energy - coal- and oil-fired power plants, transportation vehicles and systems, industrial plants, and domestic use. Non-persistent sources, but very significant occurrences with regard to life and economics losses, are accidental (and possibly deliberate) releases of toxic, flammable or radioactive materials.

Dispersion modelling is widely used tool to assess the environmental impacts to human activities on air quality by decision making bodies. Environmental assessments during planning are required by the EU directive 85/337/EEC (European Commision, 1985). However, it was proposed also by the COST action 732 (Quality Assurance and Improvement of Micro-scale Meteorological Models, Schatzmann and Britter, 2005) that these applied models are not capable to sufficiently predict all spatial and temporal pollutant concentration variation and hence it is important to increase their reliability using experimentally verified scientific basis. Urban dispersion model parameterisations to date have generally relied on data obtained from wind tunnels or water channels, as well

as some field trials.

The study of dispersion through large idealised arrays of obstacles is an important method of obtaining a better understanding of dispersion through a real urban environment. Field and laboratory studies of idealised obstacle arrays are necessarily simplifications of the real, complex, urban environment. These types of geometries, however, should display some of the characteristics of the more complex, real-world configurations, and show some generally valid rules.

Conducting outdoor dispersion field trials in large-scale idealised arrays, and even more in real urban areas, is very costly, and a great challenge in terms of logistics and execution. However, a greater diversity and quality of data-sets is still required to serve as guidance and a validation tool in the development of more complex, physics-based models of urban dispersion. Such considerations have served as strong motivation to conducting a series of field and supporting laboratory experiments involving obstacle arrays.

The field trial known as MUST (Mock Urban Setting Trial - Biltoft, 2001; Yee and Biltoft, 2004) was designed to overcome the scaling and measurement limitations of laboratory experiments and the characterisation difficulties presented by the real urban settings. The MUST field trial was undertaken at U.S. Army Dugway Proving Ground, Utah, and involved a large regular 12 by 10 array of shipping containers set up on a flat desert landscape that produced urban-scale roughness over a 200-m square area. The container spacing was chosen to establish a wake interference flow regime typical for many U.S. and European sub-urban settings.

The behaviour of the real atmosphere is extremely variable and often difficult to measure and characterise. Laboratory conditions, on the other hand, provide strictly controlled experimental environments, where particular configurations of interest can be investigated in detail, thus being able to fill in data gaps unavoidably encountered in an experiment in the real atmosphere. Certain interesting configurations may just not be realised in a particular full-scale experiment (for example, a particular wind direction of interest). Because of the ability to tightly control parameters in the laboratory, i.e. in a wind tunnel, more stationary conditions can be simulated, giving measurements and results based on more certain input conditions. This leads to better convergence of the statistics of time series measurements, or better stochastic stationarity. It also provides better defined boundary conditions when running computational models for validation or other purposes. With the motivation to realise the benefits of synchronised efforts in field observations and modelling studies, the wind tunnel study presented was initiated. An excellent opportunity was opened for a direct comparison of field observations and wind tunnel modelling results.

The simulation of a full-scale trial in smaller laboratory studies has the potential to provide a very detailed and complete physical picture of flow and plume dispersion at a range of scales. Most importantly, features of the dispersion process which transcend the various scales can be studied, and an appreciation of how well the simplified and controlled environment of a wind tunnel can reproduce full scale results can be gained. This will lead to an understanding of the validity and limitations of the field experiments as an aid to construct

algorithms for atmospheric dispersion models.

This wind tunnel study presented here focuses on these main topics:

- Reproducibility of field measurements and dependence of results on an averaging time;
- Detailed flow field pattern: horizontal planes and vertical profiles of turbulent flow properties;
- Spatial and temporal variability of a tracer concentration;
- Estimation of the travelling time of a tracer inside an idealised urban canopy using two different methods.

The first chapter introduces the theory of atmospheric boundary layer physical modelling and previous works with similar topic are mentioned here. The next part briefly describes the field experiment MUST and the important features with respect to the reduced scale experiments are highlighted. The third chapter shows the MUST field experiment, its set-up, the strength and weakness of the experimental data. The wind-tunnel experimental background and the methodology are described in chapter 4. Chapter 5 gives the overview of the approach boundary layer characteristics in the wind tunnel. The results are divided into two chapters: the sixth chapter presents the turbulent flow properties measured within and above the container array and the seventh chapter contains the tracer concentration measurement, which consists of a concentration measurement validation, single concentration statistics, spatial concentration correlations, and the puff experiments. Some comparison of the field and wind tunnel measurements can be found in chapters five to seven, if it was possible.

Chapter 2

Urban Boundary Layer

The main topic of this work is the study of flow and dispersion within an idealised urban canopy. This topic is essentially connected with the aerodynamics of the atmospheric boundary layer (ABL). Therefore the first chapter will introduce some of the main features of ABL, especially those important for reduced scale modelling and modifications caused by urban canopies. The theory chapter is not intended to be either complete nor systematic, but to introduce this topic to readers who are not familiar with this topic.

The atmospheric boundary layer, sometimes also called planetary boundary layer, is defined as that part of the atmosphere that is directly influenced by the presence of the earth's surface, and responds to surface forcing with a timescale of about an hour or less (Stull, 1988). This forcing includes frictional drag, evaporation and transpiration, heat transfer, pollutant emission, and terrain induced flow modification. The ABL thickness is quite variable in time and space, ranging from hundreds of metres to a few kilometres. There are much more detailed books about ABL (e.g. Stull, 1988; Kaimal and Finnigan, 1994), and only parts essential for this work will be summarised here and all sections will be focused on processes characteristic for the urban boundary layer (UABL).

2.1 Atmospheric Boundary Layer Structure

Typical ABL has a well defined structure that evolves with the diurnal cycle as shown Fig. 2.1 (Stull, 1988). Three major components of this structure are:

The mixed layer, sometimes called mixing layer, is a layer with well mixed properties. The turbulence in the mixed layer is usually convective driven, although a nearly well-mixed layer can form in regions of strong winds. Even when convection is the dominant mechanism, there is usually wind shear across the top of a mixed layer that contributes to the turbulence generation. The resulting turbulence tends to mix heat, moisture and momentum uniformly in the vertical axis. The temperature stratification produced this way is the adiabatic lapse rate and is characterised by the

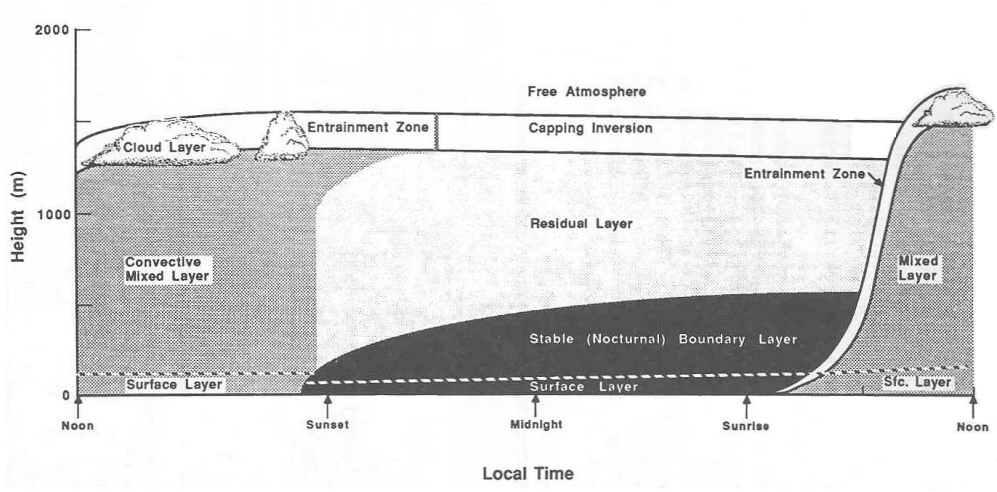

Figure 2.1: The boundary layer in an ideal case consists of three major parts: a very turbulent mixed layer; a less-turbulent residual layer containing former mixed-layer air; and a nocturnal stable boundary layer of sporadic turbulence. Adapted from Stull (1988).

constant potential temperature, θ, vertical profile. The height of the mixed layer, z_i, is typically 1–2 km by mid-afternoon.

The stable boundary layer is characteristic for the night-time. The buoyant plumes lose their energy source near the surface where the ground is cooling quickly from a radiative heat loss to space and this causes a rapid collapse of turbulent motion in ABL. The air immediately above the surface cools and mixes progressively upward through the action of turbulence generated by a wind shear. The inversion that begins to form at the surface grows steadily to a depth of 100–200 m by midnight (Kaimal and Finnigan, 1994).

The residual layer is a less-turbulent layer containing former mixed-layer air created above the stable boundary layer. The residual layer does not have a direct contact with the ground. During the night, the nocturnal stable boundary layer gradually increases in thickness by modifying the bottom of the residual layer.

The lowest part of ABL is called the **surface layer**. There is no precise definition of the surface layer. Qualitatively, it is the region at the bottom of the boundary layer where all turbulent fluxes (e.g. fluxes of momentum, heat, scalar fluxes) vary by less than 10% of their magnitude. That's why the surface layer is sometimes called the constant-shear layer. The flow is relatively insensitive to the earth's rotation and the wind structure is determined primarily by the surface friction and the vertical temperature gradient. This work will predominantly focus on processes within the surface layer.

The lowest part of ABL is the **microlayer** or **interfacial layer** and it was identified in the lowest few centimetres of air, where molecular transport dom-

inates over turbulent transport. This layer is observed mainly above aerodynamically smooth surfaces as a flat grassland. This layer becomes very shallow in urban areas, however, similar layers can be also found on the building walls.

2.2 Equations for Turbulent Flow

Turbulence is an essential part of the atmospheric boundary layer that must be quantified in order to study processes within it. The randomness of turbulence makes a deterministic description difficult. Instead, we are forced to use statistics, where we are limited to average or expected measures of turbulence.

Turbulent flows like those in the ABL can be thought of as superposition of eddies spread over a wide range of sizes. These eddies interact continuously with the mean flow, from which they derive their energy, and also with each other. The large energy-containing eddies, which contain most of the kinetic energy and which are responsible for most of the turbulent transport, arise through instabilities in the background flow. The random forcing that provokes these instabilities is provided by the existing turbulence. The energy-containing eddies themselves are also subject to instabilities, which in their case are provoked by other eddies. This imposes upon them a finite lifetime before they break up into smaller eddies. This process is repeated in all scales until the eddies become sufficiently small that viscosity can affect them directly and convert their kinetic energy to internal energy, i.e. heat.

To understand the conversion of mean kinetic energy into turbulent kinetic energy in the large eddies, the handing down of this energy to eddies of smaller and smaller scale in an 'eddy cascade' process, and its ultimate conversion to heat by viscosity, we must isolate the different scales of turbulent motion and separately observe their behaviour. Taking Fourier spectra of the turbulence offers a convenient way of doing this.

Figure 2.2 shows an example of the spectrum of a wind speed measured near the ground. The ordinate is a measure of relative turbulent energy that is associated with a particular eddy size. The abscissa gives the eddy size. Peaks in the spectrum show which eddies contribute the most to the turbulence kinetic energy. The peak on the far left with period of near 100 hours corresponds to wind speed variation associated with the passage of weather systems. The next peak, at 24 hours, shows diurnal increase of wind during the day and decrease during the night. The peak on the far right is the turbulent one having duration of 10 seconds to 10 minutes. The separate study of the turbulent part is possible thanks to the wide spectral gap between the synoptic and the turbulent part of the spectra. The contribution of synoptic scale motion to the whole energy budget of the flow in a time scale 1 hour or less can be neglected (except very strong and fast weather systems, which can dramatically influence spectral characteristics even in this time scale).

2.2.1 Governing Equations of Motion

To quantitatively describe and forecast processes in ABL, we use the equations of classical fluid mechanics (Tritton, 1988). These equations, known as equa-

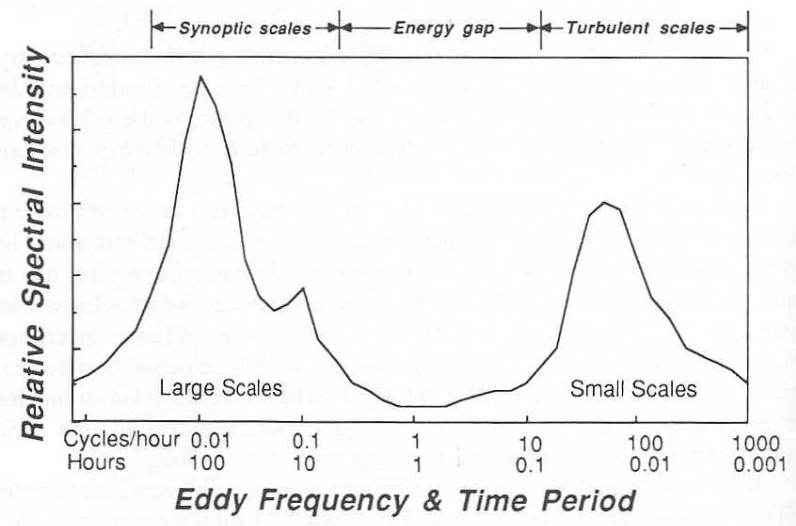

Figure 2.2: Schematic energy spectrum of wind speed near the ground. Adapted from Stull (1988).

tions of motion, contain space and time derivatives, hence initial and boundary conditions are required for solution.

Five equations form the theoretical foundation of boundary layer meteorology. The theory is given in every introductory book (e.g. Monin and Yaglom, 1971; Stull, 1988; Tritton, 1988), thus only a brief overview will be given here:

Equation of state - Ideal gas law describes the state of gases.

$$p = \varrho R T \tag{2.1}$$

where p is the pressure, ϱ is the density, T is the temperature, and R is the gas constant. We assume atmospheric air to be an ideal gas.

Conservation of mass - Continuity equation

$$\frac{d\varrho}{dt} + \varrho\,(\nabla \cdot \mathbf{v}) = 0 \tag{2.2}$$

where ϱ is the density, $\frac{d}{dt}$ is the total derivative, $\mathbf{v} = (v_1, v_2, v_3) = (u, v, w)$ is the air velocity in standard meteorological right-handed coordinate system (u is in the direction of the mean flow in the horizontal plane, v is in the direction perpendicular to the mean flow in the horizontal plane, and w is the vertical component), $\nabla = (\frac{\partial}{\partial x}, \frac{\partial}{\partial y}, \frac{\partial}{\partial z})$ is the differential vector operator, and x, y, z are the spatial coordinates also in the standard meteorological right-handed coordinate system.

Conservation of momentum for fluid flow on the Earth, which comes out from Newton's second law. This vector equation is sometimes called Navier-Stokes equation.

$$\frac{d\mathbf{v}}{dt} = -\frac{1}{\varrho}\nabla p + \mathbf{g} - 2\,\mathbf{\Omega} \times \mathbf{v} - \mathbf{\Omega} \times (\mathbf{\Omega} \times \mathbf{r}) + \mathbf{f}_{\mathbf{drag}} \tag{2.3}$$

where $\mathbf{g}$ is the acceleration due to gravity, $\mathbf{\Omega}$ is the vector of the angular velocity of the earth's rotation, $\mathbf{r}$ is the position vector (the origin of the coordinate system is the Earth's centre in this case), $\times$ is the vector product, and $\mathbf{f_{drag}}$ is the drag force.

Conservation of heat - First law of thermodynamics

$$\frac{\delta q}{dt} = c_v \frac{dT}{dt} + \frac{p}{\varrho} \nabla \cdot \mathbf{v} \tag{2.4}$$

where q is the heat and c_v is the specific heat at the constant volume.

Conservation of a scalar quantity

$$\varrho \frac{dc}{dt} = \nabla \cdot (\varrho D_m \nabla c) + \Phi_c, \tag{2.5}$$

where c is a scalar quantity, D_m is the coefficient of the molecular diffusion and Φ_c is the net body source (sources minus sinks).

2.2.2 Boundary Layer Approximations

The complete set of equations 2.1 - 2.5 is so complex that no analytical solution is known. We have two possibilities how to treat this problem: either find the exact analytical solution of a very simplified set of equations, or find an approximate numerical solution of less simplified set of equations.

The equations 2.1 - 2.5 are the governing equations for fluid motion in general. Under certain conditions, in the surface layer in our case, the magnitudes of some terms in the governing equations become smaller than the other and can be neglected. Following simplifications are valid when considering the surface layer processes:

- The processes are stationary, i.e. the statistical properties of variables do not change with time, in the time scale, which is characteristic for a given system (time scale is approximately half an hour in the case of the surface layer).
- The effects of the Earth's rotation, i.e. Coriolis and centrifugal forces, are very small in comparison to the other processes. Its turning effect on wind within the surface layer is negligible (Panofsky and Dutton, 1984; Plate, 1981).
- The hydrostatic equilibrium: $\frac{\partial p}{\partial z} = -\varrho g$ (Stull, 1988).
- The mass conservation equation 2.2 is replaced by the condition that the flow is nondivergent and incompressible: $\nabla \cdot \mathbf{v} = 0$ (Stull, 1988).
- The Boussinesq approximation: The basis of this approximation is that the temperature varies little in the surface layer flows, and therefore the density varies little except of the buoyancy driven motion. Thus the variation in the density is neglected everywhere except in the buoyancy term (Panofsky and Dutton, 1984; Stull, 1988).

- Observations in ABL indicate that the molecular diffusion terms are several order of magnitude smaller than the other terms and can be neglected (Stull, 1988).
- The drag force will be considered only as viscous stress on the mean motion, mathematically: $\mathbf{f_t} = \nu \nabla \cdot \nabla \mathbf{v} = \nu \Delta \mathbf{v}$, where ν is the kinematic viscosity of air and it is supposed to be constant in the surface layer (Stull, 1988).

Another very useful tool for turbulence description is a statistical approach. The statistical treatment of turbulent flows distinguishes the time mean (marked with a line over it) and the turbulent (marked with a prime) part of all instantaneous values, labelled ψ.

$$\psi = \overline{\psi} + \psi'. \tag{2.6}$$

Let us introduce the Reynolds averaging (Monin and Yaglom, 1971) in time

$$\overline{(\psi)} = \overline{(\overline{\psi} + \psi')} = \overline{\overline{\psi}} + \overline{\psi'} = \overline{\psi} + \overline{\psi'} \tag{2.7}$$

and the only way to fulfill this equation is

$$\overline{\psi'} = 0. \tag{2.8}$$

Considering the above mentioned simplifications and using the statistical approach for turbulent flow (dividing all quantities to mean and turbulent part) the set of equations 2.1 - 2.5 for time averaged values (marked with a line over them) transforms into (Panofsky and Dutton, 1984; Stull, 1988)

$$\overline{p} = \overline{\varrho} R \overline{T} \tag{2.9}$$

$$\nabla \cdot \overline{\mathbf{v}} = 0 \tag{2.10}$$

$$\frac{\partial \overline{\mathbf{v}}}{\partial t} + \overline{\mathbf{v}} \cdot \nabla \overline{\mathbf{v}} + \overline{\mathbf{v}' \cdot \nabla \mathbf{v}'} = -\frac{1}{\overline{\varrho}} \nabla p' + \frac{\theta'}{\overline{\theta}} \mathbf{g} + \nu \Delta \mathbf{v} \tag{2.11}$$

$$\frac{\partial \overline{\theta}}{\partial t} + \overline{\mathbf{v}} \cdot \nabla \overline{\theta} + \overline{\mathbf{v}' \cdot \nabla \theta'} = \frac{\Phi_\theta}{\overline{\varrho}\, c_p} \tag{2.12}$$

$$\frac{\partial \overline{c}}{\partial t} + \overline{\mathbf{v}} \cdot \nabla \overline{c} + \overline{\mathbf{v}' \cdot \nabla c'} = \Phi_c \tag{2.13}$$

where Φ_θ is the net source of heat, c_p is the specific heat at a constant pressure. θ is the potential temperature defined as

$$\theta = T \left(\frac{p_0}{p} \right)^{\frac{R}{c_p}} \tag{2.14}$$

where $p_0 = 10^5$ Pa is a reference pressure value.

Because of the nonlinear transport terms in some equations, small-scale terms, i.e. the turbulent parts, appear in the averaged mean equations. In a physical sense it means, that large-scale quantities can be changed by small-scale

mixing. The vector equation 2.11 is called Reynolds-averaged Navier-Stokes (RANS) equation.

Let us now define the Reynolds stress tensor $\boldsymbol{\tau}$ (second order symmetric tensor) representing the momentum transport, or flux, (for more details about a relation between fluxes and stresses see e.g. Stull, 1988), as

$$\tau_{ij} = -\varrho\, \overline{v_i' v_j'} \tag{2.15}$$

where v_i' and v_j' are turbulent components of the velocity vector. Assuming the constant air density the third term in equation 2.11 can be rewritten as

$$\overline{\mathbf{v}' \cdot \nabla \mathbf{v}'} = \frac{1}{\overline{\varrho}} \nabla \cdot \boldsymbol{\tau} \tag{2.16}$$

The Reynolds stress tensor components, also known as the Reynolds stresses or shear stresses, provide the turbulent mechanism for the momentum transport. Consequently, the term $\overline{v_i' v_j'}$ is called momentum flux and since the air density ϱ is considered to be constant, the momentum fluxes, which are directly measurable, will be often shown in this work instead of the Reynolds stresses. Dimension analysis (Stull, 1988; Panofsky and Dutton, 1984) shows that only the components $\tau_{xz} = -\varrho\, \overline{u'w'}$ and $\tau_{yz} = -\varrho\, \overline{v'w'}$ are significant for surface layer processes.

Similar expressions for the turbulent fluxes of the potential temperature, $\overline{v_i'\theta'}$, and scalar quantity, $\overline{v_i'c'}$, can be derived from the third terms of equations 2.12 and 2.13, respectively (for more details see Tritton, 1988; Panofsky and Dutton, 1984).

No general solution of the equation system 2.1 - 2.5 exists in turbulent fluid dynamics. The most problematic terms are just these terms with the product of two 'primed' variables and the number of unknown variables is larger than the number of equations. When prognostic or diagnostic equations for 'primed' terms are included even more unknown variables appear. Thus, the description of turbulent motion in these equations is not closed. The approximations and parameterisations of some term are necessary to ensure solvability of this equation system. These approaches are called **closure assumptions** and more about them can be found e.g. in Stull (1988).

2.2.3 Taylor's Hypothesis

Two quite different ways of looking at a flow are considered in fluid mechanics. In the first we choose a fixed location and take measurements of the temporal variation observed as the fluid moves past. This method of observation is called the Eulerian approach. In the second way, known as the Lagrangian method, we imagine we are attached to a fluid parcel and follow it.

If we want information on the size of eddies and on the scales of motion, we need a snapshot picture of the boundary layer. Unfortunately, instead of observing a large region of space at an instant time (the Lagrangian approach), we usually make measurements at one point in space over a long time period (the Eulerian approach).

To convert these temporal measurements into spatially distributed data, we commonly adopt Taylor's frozen turbulence hypothesis, which assumes that eddies are frozen as they are convected by the mean wind past a sensor. Thus, the wind speed could be used to translate turbulence measurements as a function of time to their corresponding measurements in space, so the means and variances measured in time must equal those measured in space. We know, however, that atmospheric turbulence is neither frozen nor transported precisely at local mean wind speed. However, these conditions are valid in the atmosphere when the measurement location and period are chosen carefully (for more details see Stull, 1988; Panofsky and Dutton, 1984).

Since all the measurements in the field and the wind tunnel experiment were performed by sensors fixed in space, the Taylor's hypothesis will be used in this work to obtained spectral characteristics and to transform time spectral characteristics to spatial ones.

2.3 Similarity theory

To accurately reflect real urban settings, scale modelling requires both dynamical and geometrical similarity to the real world. Providing geometrical similarity is not fundamentally difficult. It requires manufacturing a model of the investigated area at scale and the preparation of the wind tunnel to model an appropriate boundary layer flow in the same scale. Dynamical similarity requirements include the similarity of radiation, flow, and of thermal inertia.

Dynamic similarity between two systems relates to forces and requires that the forces involved also appear as constant ratios. If this occurs, then the contributions to the accelerations will be the same in both model and prototype. Ensuring the dynamical similarity of flow requires considerable analysis of dimensionless governing equations.

There are two ways in which to obtain the similarity criteria. The first approach is the Buckingham π-theorem of dimensional analysis. This says that the functional dependence between a certain number of variables can be reduced by the number of independent dimensions occurring in those variables to give a set of independent, dimensionless numbers. Therefore for the purposes of the experimenter, different systems which share the same description by dimensionless numbers are equivalent (for derivation see e.g. Stull, 1988).

The second approach (Panofsky and Dutton, 1984) is based on governing equation conversion. By setting each variable equal to the product of a dimensionless form and a factor involving scales that carry the dimensions. We can divide out of the equations a suitable collection of scales and thus the relative magnitudes of the forces are revealed by dimensionless numbers.

2.3.1 Monin-Obukhov Similarity Theory

This theory (Monin and Yaglom, 1971), which is part of the Buckingham π-theory for the lowest part of ABL, is summarised in every atmospheric boundary layer textbook (e.g. Stull, 1988), states that the mean wind and temperature profiles, and turbulent velocities in the ideal surface layer, which is created

above an infinite homogeneous rough surface, are completely determined by three scaling lengths z_0, d_0, L, and a scaling velocity u_*, as defined below. Afterwards all others variables within the surface layer can be expressed using only these four scales (will be discussed in section 2.4).

The surface roughness length, z_0**,** is a measure of the amount of mechanical mixing introduced by the surface roughness elements and, as a rough rule of thumb, is equal to about 0.1 to 0.2 times the average height of the roughness elements. For more reliable estimation of the surface roughness length see section 2.4.

The displacement length, d_0**,** is a scaling length that becomes important for describing the wind profile at elevations close to the average roughness obstacle height, and for densely packed roughness elements. It describes the vertical displacement (from the ground surface) of the effective ground level and is approximately equal to 0.5 times the roughness obstacle height for densely packed sharp-edges obstacles as urban centres. The displacement length, d_0, equals about 0.1 to 0.2 times the average height of the roughness obstacles for more loosely packed obstacles such a residential developments.

The Monin-Obukhov length, L**,** accounts for the effect of stability and is proportional to u_*^3 divided by the turbulent heat flux, H_S, to and from the ground surface:

$$L = -\frac{u_*^3 \, \varrho \, c_p \, \overline{\theta}}{k \, g \, H_S}. \tag{2.17}$$

where c_p is the specific heat of air at a constant pressure, $\overline{\theta}$ is the mean potential temperature of atmospheric air, k is von Kármán constant, and g is the acceleration due to the gravity.

According to Monin-Obukhov similarity theory, L completely determines effects of atmospheric thermal stratification on the wind speed vertical profile (Hanna et al., 1982) and can be estimated from a simultaneous fluctuation measurement of wind velocity and temperature, by sonic anemometry for example.

Although boundary layers are rarely perfectly neutral, there are situations such as strong winds and overcast skies where the boundary layer is approximately neutrally stratified. In a neutral boundary layer the only turbulent kinetic energy generation mechanism is mechanical, associated with wind shear and surface stress. The Monin-Obukhov length is infinite in these conditions and u_* becomes an important scaling quantity.

The friction velocity, u_***,** is the fundamental scaling velocity and equals the square root of the surface Reynolds stress, τ_0, divided by the air density ϱ. The surface Reynolds stress can be observed by special instruments that directly measure the drag at the surface, or by fast response turbulence instruments using the definition

$$\tau_0 = -\varrho \overline{u'w'} = \varrho u_*^2 \tag{2.18}$$

where u' is the longitudinal wind speed fluctuation, w' is the vertical wind speed wind fluctuation, and the average is over a sufficient long time period (about 1 hour in full scale). The friction velocity can also be estimated from wind observations by using the equation of the logarithmic wind profile, see below.

The Reynolds stress, $\tau = \tau_{xz} + \tau_{yz}$, by definition decreases by only about 10% in the ideal surface layer, which is created above an infinite homogeneous rough surface, (the lowest 50 to 100 m), leading to the assumption of a constant stress layer or constant u_* layer near the ground. Turbulent velocities are proportional to u_* in this layer.

The estimation of particular values of these scales for a given situation can be crucial for the relevance of this concept. Two classes of approaches are available: geometric methods that use algorithms that relate aerodynamic parameters (z_0, d_0, and u_*) to measures of a surface morphometry (e.g. plan area aspect ratio, frontal area aspect ratio); and anemometric methods that use field observations of wind or turbulence to solve for aerodynamic parameters included in theoretical relations derived from the logarithmic wind profile. Both methods have advantages and disadvantages. The geometric methods are often used in full-scale studies because of lack of instrumentation to properly describe vertical profiles of flow properties; wind tunnel modelling is usually equipped with sufficient experimental apparatus and the more accurate anemometric methods can be used. The comprehensive study of aerodynamic characteristics of urban areas is given e.g. in Grimmond and Oke (1999).

2.3.2 Similarity Numbers

Let us introduce the dimensionless variables as:

$$
\begin{aligned}
\mathbf{v}^* &= \frac{\mathbf{v}}{U_0} \\
\mathbf{x}^* &= \frac{\mathbf{x}}{L_0} \\
t^* &= \frac{t}{t_0} \\
T^* &= \frac{T}{T_0} \\
\overline{\theta}^* &= \frac{\overline{\theta}}{T_0} \\
\theta'^* &= \frac{\theta'}{\triangle T_0} \\
\varrho^* &= \frac{\varrho}{\varrho_0} \\
p^* &= \frac{p}{\varrho_0\, U_0^2} \\
\Phi_T^* &= \frac{\Phi_T}{\frac{T_0}{\triangle T_0}\frac{U_0^2\,\varrho_0\,\nu}{L_0^2}}
\end{aligned}
\tag{2.19}
$$

where subscript 0 denotes the characteristic scales, and $\triangle T_0$ is characteristic temperature difference. The characteristic scales are typical measures of the problem, e.g. the dimension of the obstacle for the length scale L_0, or mean wind speed in a certain height within the surface layer for the velocity scale U_0. However, the choice is arbitrary and the conclusion does not depend on the details of them.

The dimensionless concentration of a tracer emitted from a point source is defined as

$$c^* = \frac{c\, U_0\, L_0^2}{Q_{\text{source}}} \tag{2.20}$$

where Q_{source} is source strength (a mass or volume per unit time, according to measured concentration - a mass or volume ratio).

Applying definitions 2.19 on the simplified equations 2.2 - 2.5 we obtain

$$\begin{aligned}
\left[\frac{L_0}{U_0\, t_0}\right] \frac{d\varrho^*}{dt^*} &= -\varrho^* \left(\nabla^* \cdot \mathbf{v}^*\right) \\
\left[\frac{L_0}{U_0\, t_0}\right] \frac{d\mathbf{v}^*}{dt^*} &= \nabla^* p'^* + \left[\frac{\triangle T_0}{T_0} \frac{L_0}{U_0^2} g_0\right] \frac{\theta'^*}{\overline{\theta}^*}\, \mathbf{g}^* + \left[\frac{\nu}{L_0\, U_0}\right] \Delta^* \mathbf{v}^* \\
\left[\frac{L_0}{U_0\, t_0}\right] \frac{dT^*}{dt^*} &= \left[\frac{\kappa}{\varrho_0\, c_p\, \nu}\right] \left[\frac{\nu}{L_0\, U_0}\right] \Delta^* T^* + \left[\frac{\nu}{L_0\, U_0}\right] \left[\frac{U_0^2}{c_p\, \triangle T_0}\right] \Phi_\theta^* \\
\left[\frac{L_0}{U_0\, t_0}\right] \frac{dc}{dt^*} &= \left[\frac{\nu}{L_0\, U_0}\right] \left[\frac{D_m}{\nu}\right] \Delta^* c
\end{aligned} \tag{2.21}$$

where κ is heat conductivity.

Six dimensionless ratios (in square brackets) multiplying dimensionless dependent variables have appeared in these equations. Any solution of the system of equations 2.21 depends on the boundary conditions, the initial conditions, the forcing, and the values of the six dimensionless parameters. Ensuring geometrical (boundary) and dynamical (forcing described by the dimensionless number) similarity the prototype and the model can be described by the same set of equations, and thus the phenomena detected on the model is also present on prototype.

All these similarity numbers cannot be matched for prototype and model together in principal. Let us discuss each of them:

Strouhal number is defined as

$$St = \frac{U_0\, t_0}{L_0} \tag{2.22}$$

and is an important parameter for non-stationary and oscillating processes (for more details see Tritton, 1988). We will focus on stationary processes and St will serve us to define characteristic time t_0 and dimensionless time t^*

$$t_0 = \frac{L_0}{U_0} \Rightarrow t^* = \frac{t\, U_0}{L_0} \tag{2.23}$$

Prandtl number is the ratio of two fluid properties, and approximates to the ratio of the momentum diffusivity, i.e. the kinematical diffusivity, and the thermal diffusivity. Thus it is itself determined by the choice of fluid.

$$Pr = \frac{\varrho_0 \, c_p \, \nu}{\kappa} \tag{2.24}$$

The similarity according to Prandtl number is by-itself fulfilled using air as a medium in a wind tunnel.

Schmidt number is the mass transfer analogy of the Prandtl number.

$$Sc = \frac{\nu}{D_m} \tag{2.25}$$

It is the ratio of the kinematical viscosity and the molecular diffusivity of a passive tracer. The similarity according Sc is again ensured by-itself in the wind tunnel modelling.

Eckert number expresses the relationship between the flow's kinetic energy and enthalpy, and is used to characterise dissipation.

$$Ec = \frac{U_0^2}{c_p \, \triangle T_0} \tag{2.26}$$

The Eckert number is interconnected with **Mach number** and it is only important in high speed compressible flow (Cermak, 1984).

Richardson number is the ratio of the potential to kinetic energy of a turbulent flow.

$$Ri = \frac{\triangle T_0}{T_0} \frac{L_0}{U_0^2} g_0 \tag{2.27}$$

If the Richardson number is much less than unity, buoyancy is unimportant in the flow. If it is much greater than unity, buoyancy is dominant (in the sense that there is an insufficient kinetic energy to homogenise the fluid). If the Richardson number is of order unity, then the flow is likely to be buoyancy-driven: the energy of the flow derives from the potential energy in the system originally. Our experiments (field and wind tunnel) were conducted under neutrally or almost neutrally stratified ABL where $Ri \doteq 1$. For detailed discussion and linkage relations of Richardson number Ri and **Froude number** Fr (the reciprocal of the square root of the Richardson number) see e.g. Tritton (1988).

Reynolds number is the ratio of the inertial to viscous forces and is used for determining whether a flow will be laminar or turbulent.

$$Re = \frac{L_0 \, U_0}{\nu} \tag{2.28}$$

Reynolds number for ABL is usually calculated with the characteristic length defined as the ABL depth, $L_0 = \delta$, and with characteristic wind speed at the top of ABL, $U_0 = U_\delta$. For urban surface layer processes

it is more appropriate to define characteristic values which are directly involved. The most frequently used values are average building height, H, for L_0 and wind speed of the undisturbed impinging flow on this height, U_H, for U_0. This newly defined similarity number is called **Building Reynolds number**, Re_B.

Taking the typical values for the flow in the field during MUST experiment (Biltoft, 2001): $H = 2.54$ m, $U_H = 4$ m/s; and in the wind tunnel (model scale was 1:75) $H = 0.034$ m, $U_H = 3.5$ m/s; ones gets

$$\begin{aligned} Re_{B\,\text{field}} &\approx 680{,}000 \\ Re_{B\,\text{wind tunnel}} &\approx 8{,}000 \end{aligned}$$

It is obvious that the Reynolds number in the field is of the order 2 greater than in the wind tunnel. The Reynolds number equality can be fulfilled only using extremely high wind speeds in the wind tunnel (several hundreds m s^{-1}). The facilities which are commonly used for physical modelling can not operate with such wind speeds. Nevertheless, the magnitude of both Re_B is so large that the viscous term in the second equation of the equation system 2.21 $Re_B^{-1}\Delta^*\mathbf{v}^*$ will be strongly suppressed by the factor Re_B^{-1} in both cases. This suppressing and consequently neglecting of the viscous terms in RANS is the basis of the widely used 'Reynolds number similarity' theory.

To explain the Reynolds number similarity, it is supposed that turbulent eddies of different sizes affect one another only if their sizes are comparable. Then interaction between the large, energy-containing eddies and much smaller viscous eddies take place between a considerable number of intermediary stages, and they are completely independent except that the viscous eddies dissipate the energy loss of the large eddies to the heat. It follows that the motion on the large scale is essentially inviscid and thus independent on the Re, or Re_B respectively (for more detail see e.g. Tennekes and Lumley, 1972; Townsend, 1976; Tritton, 1988).

The structure of the motion is independent of the fluid viscosity once the Reynolds number is high enough. The critical value of Re_B is in order of several thousands and is unique for every case.

2.4 Urban Surface Layer

There is a fundamental difference between flows in an urban canopy and those above a homogeneous canopy, i.e. typical vegetative canopy (Oke, 1987; Finnigan, 2000). Raupach et al. (1980) and Rotach (1993a,b) have highlighted and described the existence of finer structures within the urban surface layer. An urban surface consists of low and high buildings, trees, and other roughness elements, which are arrayed in blocks or standing by themselves, intersected by streets, crossings or open surfaces. This complex morphology results in a modified flow and turbulence structure in the lowest few tens of metres of UABL. The problem of the fine structures of the flow in the urban surface layer was

also study by Cheng and Castro (2002a); Kastner-Klein and Rotach (2004). According to their works the lowest part of the ABL over cities, the urban surface layer, has to be considered in three parts (see Figure 2.3):

Urban Canopy Layer (UCL) has a depth approximately equal to the mean building height H, or the zero-plane displacement d_0 (defined in the section 2.3.1). The structure of the flow field is very complex and only a few studies have focused on this region (e.g. Kastner-Klein and Rotach, 2004; Hanna et al., 2002; Schultz et al., 2005).

Roughness Sublayer (RS) is the layer just above UCL and turbulence structure here is fully three-dimensional and depends explicitly on the properties of the underlying roughness. In the vertical, RS extends from roof level up to a level at which the horizonal homogeneity of the flow is achieved. The estimations of the RS height vary in the literature, for example: 2 to 5 times average building height H (Kastner-Klein and Rotach, 2004), or 2.5 to 3 H (Roth, 2000). It can occupy a significant part of the urban surface layer in the areas with high-rise buildings.

Inertial Sublayer (IS) is the upmost part of the surface layer and the previously (in section 2.1) defined properties of the surface layer are fully valid there. The turbulent fluxes are approximately constant in all directions and the vertical profile of the mean wind speed can be described by the well-known logarithmic law (see below).

The urban environment is composed of individual buildings, therefore the flow pattern in the urban surface layer depends upon the geometry of the build-

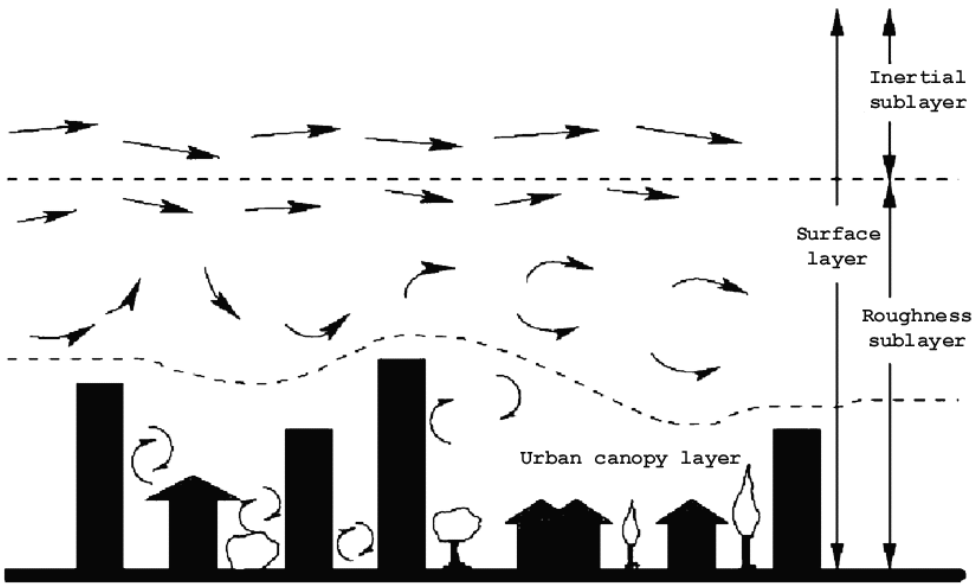

Figure 2.3: Scheme of the flow within surface layer through and over an urban area. Adapted from Britter and Hanna (2003).

ing array, especially the relative obstacle spacing (L/H, where L is the along wind spacing of the buildings), sometimes called **aspect ratio** (Oke, 1987). One can also define relative obstacle width as W/H, where W is the obstacle width. The dependence of the flow pattern on these two numbers is shown in Figure 2.4.

If the buildings are widely spaced ($L/H > 3$) the flow pattern appears almost the same as if they were isolated (Figure 2.5a). At a closer spacing (L/H is approximately between 1.5 and 3) the wakes of the individual buildings interfere and leading to more complicated, so-called the wake interference flow (Figure 2.5b). For an aspect ratio close to unity the main flow starts to skim over the building tops and derives a vortex in the cavity, which is often represented by a street (Figure 2.5c).

Isolated roughness, wake interference, and skimming flow are used as descriptive terms for situations where the wind is normal to the long axis of a street. If the wind is oriented at some oblique angle the vortexes are usually transform to form a 'cork-screw' motion along the street. The approach flow, which is parallel to the street, can be channelled and it can cause an increase in the wind speed. The situation also differs if the height of the buildings vary considerably.

The shipping containers were used during the MUST experiment to simulate an ideal urban setting (for detailed description of the site see chapter 3). The array set-up gave the aspect ratio $L/H = 3.1$ and the relative obstacle width $W/H = 4.8$. The expected flow pattern according to the diagram in Fig. 2.4, where the appropriate position of the MUST set-up is marked with the red cross, is somewhere between the isolated roughness and wake interference flow.

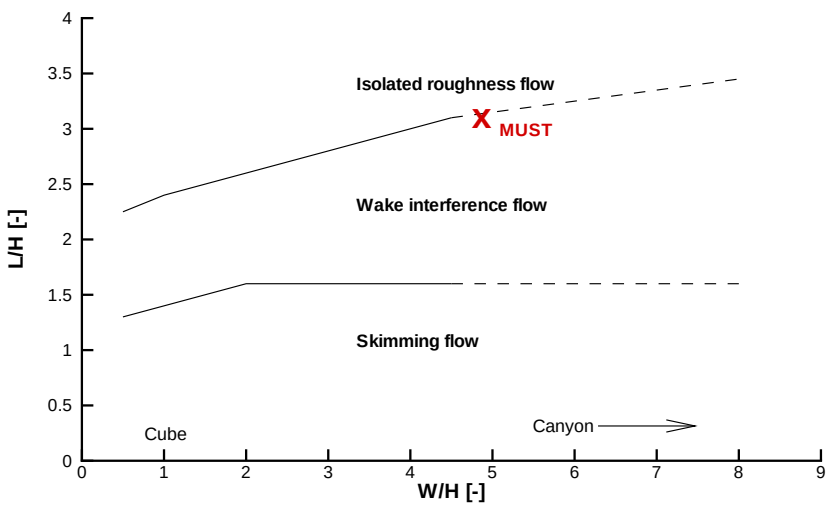

Figure 2.4: Schematic diagram showing the ranges of the relative obstacle spacing and relative obstacle width to which each flow regime applies. The position of the MUST experiment is depicted by red cross. Modified after Hanna and Britter (2002).

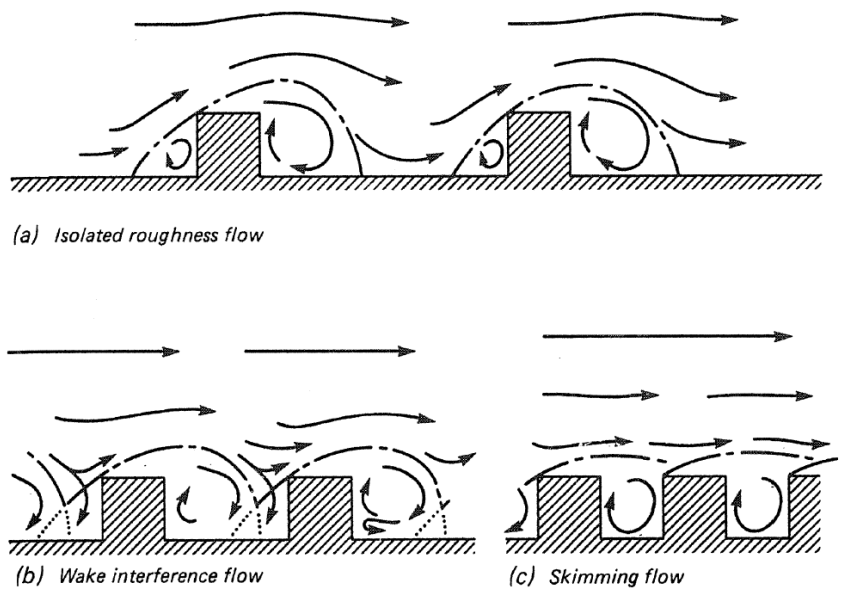

Figure 2.5: Flow regimes associated with the different urban geometries. Adapted from Oke (1987).

The flow measurements presented in chapter 6 are showing that the obstacle array of the MUST experiment produced the wake interference flow.

2.4.1 Vertical Profiles

Whereas in the Urban Canopy Layer and Roughness Sublayer the mean velocity profile strongly depends on exact position, in Inertial Sublayer the flow is fully adapted to the integrated effects of underlying urban surface, and the vertical profiles of time averaged wind properties can be expressed by simple rules. The rules used in wind tunnel modelling are most often empirical ones and are based on field observations. The authorities, e.g. national wind engineering associations, have summarised these rules for wind tunnel modelling of atmospheric flow and dispersion in several guidelines and monographs, for example: ASCE (1995); Counihan (1972); ESDU (1985); Snyder (1981); VDI Guideline 3783/12 (2000).

The profile parameters and profiles themselves strongly depend on the type of the surface. We can distinguish these four main types of surface roughness:

Slightly rough terrain is represented by surfaces covered by ice, snow, or water surfaces without waves. The roughness length z_0 lies in range from 10^{-5} to 10^{-2} m.

Moderately rough terrain is designation for grasslands and farmlands. The roughness length z_0 varies in range from 10^{-2} to 10^{-1} m.

Rough terrain is represented by parks, bushes, or suburban areas. The typical values of z_0 range from 0.1 to 0.5 m for this terrain type.

Very rough terrain is designation for forrest or inner-city areas. The roughness length z_0 is higher than 0.5 m, up to several metres.

For a detailed overview of the roughness class see e.g. Snyder (1981), for different terrain type profile parameters see e.g. ESDU (1985); VDI Guideline 3783/12 (2000).

Mean wind velocity

The mean velocity profile is sketched in Fig. 2.6. It can be treated by the **logarithmic law** in IS in contrast to lower layers where individual obstacles influence the flow. The formula for the logarithmic law can be derive (see e.g. Stull, 1988) from dimension analysis using the scales introduced in section 2.3.1 for neutral stratification (Monin-Obhukov length $L \to \infty$).

$$\overline{u}(z) = \frac{u_*}{k} \ln \frac{z - d_0}{z_0}, \; z \geq z_0 + d_0. \tag{2.29}$$

where u_* is friction velocity, k is von Kármán constant, set to 0.4 in this work, z_0 is roughness length, and d_0 is zero plane displacement and everything is in standard right-handed meteorological coordinate system (x-axis is in the direction of the mean wind direction).

Another widely used profile is the **exponential profile**, also called power

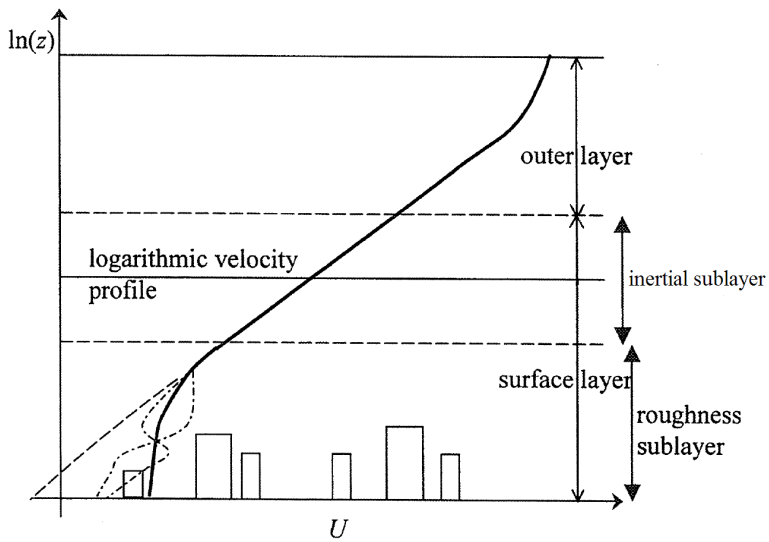

Figure 2.6: Schematic diagram of the urban surface layer structure. Adapted from Hanna and Britter (2002).

law, which is valid in the upper part of the surface layer:

$$\overline{u}(z) = \overline{u}_{\text{ref}} \left(\frac{z - d_0}{z_{\text{ref}} - d_0} \right)^{\alpha} \tag{2.30}$$

where z_{ref} is the reference height (it should be in the middle of the IS), $\overline{u}_{\text{ref}}$ is the average wind velocity at the reference height, and α is the profile exponent.

Turbulence intensity

Turbulence intensity is defined as

$$I_i(z) = \frac{\sigma_i(z)}{\overline{u}(z)};\ i = u, v, w \tag{2.31}$$

where σ_i is the standard deviation of the respective velocity component and $\overline{u}(z)$ is the mean wind speed. All values are local properties, i.e. the intensity of turbulence can vary in the space (for ideal ABL, where horizontal homogeneity is expected, I_i varies only with the vertical coordinate z). The variation of the longitudinal turbulence intensity I_u in the IS is given by (Snyder, 1981)

$$I_u(z) = \alpha \frac{\ln \frac{30}{z_0}}{\ln \frac{z}{z_0}}, \tag{2.32}$$

where α is the power law exponent from equation 2.30; or stated by the recommended ranges for different roughness class proposed by ESDU (1985). Intensities for different components are connected in every height via relationship:

$$\sigma_u : \sigma_v : \sigma_w = 1 : 0.75 : 0.5 \tag{2.33}$$

Reynolds stress

The Inertial Sublayer is defined as a region with a constant shear. However, it was the scope of several works (e.g. Kastner-Klein and Rotach, 2004; Cheng and Castro, 2002a; Schultz et al., 2005) to investigate shear stress, i.e. transport of momentum, inside the urban surface layer and they have come to different conclusions. It was shown, that profiles at positions away from a roughness change and for constant obstacles height the maximum shear stress occurs at approximately the height of the obstacles (Kastner-Klein and Rotach, 2004; Cheng and Castro, 2002a) or slightly higher at $z/H = 1.5$ (Oikawa and Meng, 1995). Below this height the shear stress carried by the fluid decreases to zero as the buildings take up part of the stress through the drag forces on them. Above the obstacle height the shear stress decreases with height with some limited evidence of a constant shear stress region. Finite fetch experiments make conclusions concerning a constant shear-stress region difficult (Schultz et al., 2005). Since the maximum shear stress should equate to the surface shear stress and determine the surface friction velocity, which is important scaling parameter, the good knowledge of shear stress profiles in different situations is highly important.

Integral scales

If we want to describe the evolution of a fluctuation function $u(t)$, we need to know how the values at different times are related. Let us define the temporal autocorrelation function for $u(t)$ wind component as (Kaimal and Finnigan, 1994)

$$r_u(\tau) = \frac{\overline{u'(t)\,u'(t+\tau)}}{\sigma_u^2} \tag{2.34}$$

and analogically for the $v(t)$ and $w(t)$ components. The autocorrelation function is symmetric in time lag τ and independent on t due to statistical stationary turbulence. The temporal integral time scales T_u is defined as

$$T_u \equiv \int_0^\infty r_u(\tau)\,d\tau \tag{2.35}$$

According to Taylor's hypothesis of frozen turbulence the temporal integral time scale T_u can be transform to the spatial integral time scale L_u by simple relationship

$$L_u = T_u\,U \tag{2.36}$$

Instead of L_u, L_v and L_w the notation L_{ux}, L_{uy} and L_{uz} will be used to emphasise that the values are derived from one-point time series with the mean wind direction corresponding to x-axis.

The parameterisation of L_{ux} vertical profile was proposed by Counihan (1972). His concept is based on experimental data and can be described as a gentle increase with the elevation to the top of the surface layer (larger and larger vortexes can contribute to the energy cascade with the increasing distance from the ground).

Spectral characteristics

The Fourier transform of the covariance function $r_u(\tau)\,\sigma_u^2$ converts the covariance to the energy spectrum (Kaimal and Finnigan, 1994), which is helpful to distinguish energy in essential and nonessential regions. The spectral function is defined as

$$S_u(f) = 2\int_{-\infty}^{\infty} r_u(\tau)\,e^{-2\pi\tau f}\,d\tau \tag{2.37}$$

where f is the frequency, connected with the angular frequency ω via $\omega = 2\,\pi\,f$, to give

$$\sigma_u^2 = \int_0^\infty S_u(f)\,df \tag{2.38}$$

The most commonly used parameterisation of the free velocity spectra above a flat homogeneous surface within ABL surface layer for neutral conditions was given by Kaimal et al. (1972) and it is based on the Kansas experiment from

year 1968:

$$
\begin{aligned}
S^*_{uu} &= \frac{n\,S_u(n)}{u_*^2} = \frac{102\,n}{(1+33\,n)^{5/3}} \\
S^*_{vv} &= \frac{n\,S_v(n)}{u_*^2} = \frac{17\,n}{(1+9.5\,n)^{5/3}} \\
S^*_{ww} &= \frac{n\,S_w(n)}{u_*^2} = \frac{2.1\,n}{(1+5.3\,n)^{5/3}}
\end{aligned}
\tag{2.39}
$$

where n is non-dimensional frequency $n = f(z - d_0)/U$ and U is the mean wind speed at the observational height z. However, this parameterisation arosed from open terrain measurements, it is also used for more rough terrains as urban areas. Another concepts of the spectra parameterisation (also based on experimental data) are listed e.g. in VDI Guideline 3783/12 (2000) or in Simiu and Scanlan (1986).

2.4.2 Pollutant Dispersion

Urban air pollution was originally considered as a local problem mainly associated with domestic heating and industrial emissions, which are now very well controllable. Despite significant improvements in fuel and engine technology, urban environments are mostly dominated by traffic emissions in present days.

The main traffic-related pollutants are CO, NO_X, hydrocarbons, and particles. CO is an imperfect fuel combustion product. Combustion also produces a mixture of NO_2 and NO (together labelled NO_X), of which more than 90% is in the form of NO. A wide range of unburned and chemically transformed hydrocarbons (benzene, toluene, ethane, ethylene, pentane, etc.) is emitted by motor vehicles through a number of different processes (evaporation, fuel tank displacement, oil seep, etc.). Finally, particles of condensed carbonaceous materials are emitted mainly by diesel and poorly maintained petrol vehicles.

The dispersion of gaseous pollutants in UCL depends generally on the rate at which the streets exchange air vertically with the above roof-level atmosphere and laterally with connecting streets (Barlow and Belcher, 2002). Due to the very short distances between sources and receptors within UCL, only very fast chemical reactions have a significant influence on the measured concentrations (Berkowicz, 1997). For this reason, most traffic-related pollutants (e.g. CO and hydrocarbons) can be considered as practically an inert species within these distances. This is not the case either for NO_2; which dissociates extremely fast in the presence of light, or for NO, which also reacts very fast with O_3 (Palmgren et al., 1996). The time scales of these chemical reactions are of the order of tens of seconds, thus comparable with residence times of the pollutants in street canyons. Thus the NO_X concentration is a quantity, which is as a bulk characteristic modelled in the wind tunnels.

Turbulent dispersion is very complicated phenomenon, nevertheless it can be treated statistically and the results of such a statistical approach are simple descriptive tools. An operational urban dispersion models (e.g. SYMOS'97, the operational dispersion model used in Czech Republic, Bubník et al., 1998)

often uses a simple dispersion scheme as Gaussian plume model, where effective transport speed and spread sigma parameters, which depend on the ABL thermal stability, are main arguments. This approach is much more well-founded for open terrain than for the urban areas.

The effective transport speed (or the cloud advection speed) u_e, of a pollutant cloud can be defined as the (vertical) integral of the concentration-weighted wind speed.

$$u_e = \frac{\int u(x,y,z)c(x,y,z)dz}{\int c(x,y,z)dz} \tag{2.40}$$

where z is the height above ground, $c(x,y,z)$ is the spatial-variable concentration of a pollutant, and $u(x,y,z)$ is the spatial-variable wind speed.

The dispersion situation within UCL is shown in Fig. 2.7. As the cloud disperses upward from a ground-based release, it encounters stronger wind speeds and the cloud accelerates as it moves downwind. However, the wind profile in complex in urban areas is not well defined and varying with time and space. The integration in the equation 2.40 should be performed on a limited space and during a sufficient long time period to smooth instantaneous behaviour. Experiments by Davidson et al. (1995, 1996); Theurer et al. (1996) indicated that Gaussian plume model can be used for a distance from a source much greater than integral length scale L_{ux}. Another experiment by Feddersen (2005) showed difficulties with an estimation of an effective transport speed, which seems to not be constant but dependent on distance from a source, as illustrated in Fig. 2.7.

For puffs or for strongly time-varying releases, the wind speed determines the time lag between the release of the pollutant and its arrival at any downwind location, which is approximately equal to the distance divided by the wind speed, or better divided by the effective transport speed. The question of puff releases is not very well described in literature. Most of the studies are related to the heavy gas dispersion (or liquefied natural gas - LNG), which was the

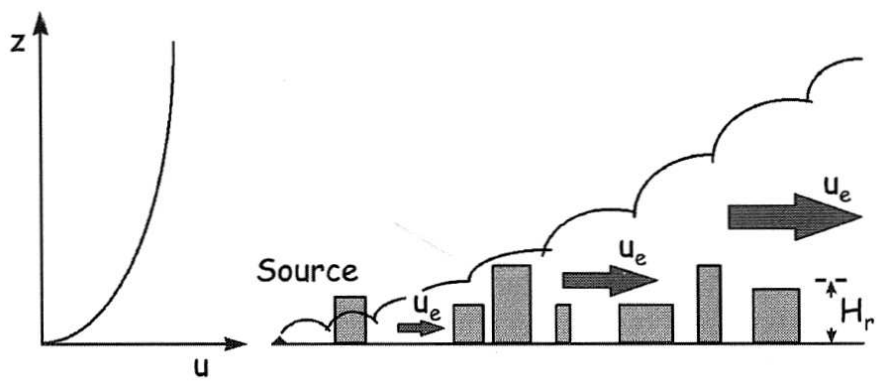

Figure 2.7: Schematic diagram of a cloud released at the ground illustrating how u_e increases with downwind distance. Adapted from Hanna and Britter (2002).

main topic of works done in the eighties and early nineties in consequence of environmental risks (e.g. Meroney and Lohmeyer, 1984; Zimmerman and Chatwin, 1995; McQuaid, 1985).

2.5 Aspects of Different Scales

As was said before, it is a characteristic feature of the atmosphere that its motion takes place at a wide range of scales: from large weather systems down to eddies on a scale of millimetres responsible for the ultimate dissipation into heat. Despite the fact that the motion of the atmosphere has been described by the Navier-Stokes equations for more than 100 years, the numerical models of the atmosphere cannot yet represent all the scales. This is a reason to divide the atmosphere motions into ranges of scales, suggesting parameterisations for the processes that are dominant for the specific scale and defining the limits in time and space. The urban boundary layer is no exception from this, but it is even more complicated because of its spatial and time variability.

The different splitting of the scales can be found in nearly every UABL textbook or review. In contrast to older ones (e.g. Oke, 1987), where the smallest micro-scale included everything up to 1 km, the newer studies have finer structure in the smallest scales. The following discussion will be broken down into four ranges of the length scales according to Britter and Hanna (2003): regional (up to 100 or 200 km), city scale (up to 10 or 20 km), neighbourhood scale (up to 1 or 2 km), and street scale (less than $\sim$ 100 to 200 m).

2.5.1 The Regional Scale

The regional scale is affected by the urban area or areas. For example, the urban heat island circulations, some enhanced precipitation, and an urban pollutant plume can extend to these distances. At this scale the mean synoptic meteorological patterns are given and an urban area represents a perturbation, causing deceleration and deflection of the flow, as well as changes to the surface-energy budget and the thermal structure (Oke, 1987).

2.5.2 The City Scale

The city scale represents the diameter of an average urban area. At these scales the variations in flow and dispersion around individual buildings or groups of similar buildings have been mostly averaged out. Wind flow models developed for this range pay little attention to the details of the flow within the urban canopy layer. Most of the mass of a pollutant cloud travelling over this distance will be above the height of the buildings. The local effects like a sea breeze or a valley wind are important factors (Batchvarova and Gryning, 2006).

2.5.3 The Neighbourhood Scale

On the neighbourhood scale buildings still may be treated in a statistical way, some statistical homogeneity may be anticipated. However, the approach may

be different to that on the city scale. The city then is seen as being composed of these neighbourhoods. At the neighbourhood scale we want to know more about the flow within the urban canopy layer. The wind flow, particularly within UCL, may also be changing as it moves from one neighbourhood to the next. The pollutant cloud travelling over this distance remain within UCL because of building wakes existence. This is of particular relevance when considering the consequences and risks associated with an accidental or deliberate release of hazardous materials within cities.

An increase in surface roughness and variations in building heights produces a significant increase of turbulence levels. This causes a reduction in ground-level concentrations that arise from ground-level releases for situations where the pollutant cloud depth is much larger than the height of the surface obstacles (Britter and Hanna, 2003). The increased turbulence within UCL (in comparison with open terrain) produces greater dispersion coefficients that tend to reduce concentrations. However, the accompanying reduction of the advection velocity within the canopy and the presence of wake regions tends to increase concentrations. The relative magnitudes of these opposing effects determine whether the obstacles lead to increased or decreased concentrations as the roughness is increased.

2.5.4 The Street Scale

The street (canyon) scale is particularly studied in the context of urban air quality where the dominant sources of pollution, vehicle emissions, are in close proximity to the pollutant receptors of concern. In cities both the sources and the receptors are within a very complex geometry and this geometry can support a sheltering effect from the diluting influence of the wind. Flow and dispersion near street intersections are also of interest as it is the acceleration of vehicles away from traffic lights and/or pedestrian crossings that gives rise of pollutant emission rates and consequently poor urban air quality. It can be of particular interest when regulatory pollutant monitoring stations are placed within street canyons. Also the location of building ventilation intakes is sensitive to the anticipated distribution of pollutants on the spatial scale of the buildings or the streets.

The illustrative street-canyon flow is basically a turbulent shear flow above a rectangular cavity with the mean flow direction perpendicular to the axis of the street canyon. For a canyon of near unity aspect ratio a recirculating flow is set up in the canyon driven by momentum transport from the shear layer above (Bezpalcová, 2005; Kastner-Klein et al., 2001). The flow direction at the bottom of the canyon is then towards the lee wall of the canyon and nearly zero in magnitude in the canyon centre. The recirculating flow is neither steady nor symmetric.

The situation starts to be more complicated when we leave the basic set-up. The rectangular street canyons with a large aspect ratio allow for possible reattachment of the separating shear layer off the lee wall to the floor of the street canyon (see section 2.4 and 2.5). For small aspect ratios there can be a counter-rotating vortex below the main recirculation flow. Irregular street

canyons with the lee wall and the downwind wall having different elevations introduce further complications to the flow as well as different roof shapes (Rafailidis, 1997), and a wind direction not perpendicular to the street axis.

Poor urban air quality is often associated with low wind-speed conditions. Other sources of turbulence like the mechanical production from the motion of vehicles, also known as a traffic induced turbulence, as well as the thermal production from the environment or from vehicles, come into play during these conditions. Laboratory and field measurements of the turbulence produced by modelled traffic in street canyons showed that the traffic produced turbulence can be a significant source of turbulence when compared with that arising from the mean wind (Di Sabatino et al., 2003; Kastner-Klein et al., 2003). However, this topic is still very questionable. The same situation is with the thermal effects. The numerical simulations (Uehara et al., 2000; Kim and Baik, 1999) showed that the thermal effects can completely drive the flow inside the street canyon and the circulation is dependent on a position of local heating. In fact, a differential heating can even shift the flow from one-vortex flow to a flow with several contra-rotative vortices. However, nor field neither wind tunnel study has proven this strong influence of the street canyon heating.

The comprehensive review of experiments and modelling approach for street scales is given e.g. in Kanda (2006); Vardoulakis et al. (2003).

2.6 Methods of Investigation

Field data in real cities acquired using towers, aircraft, and satellites give us a range of valuable information but have not yet provided a comprehensive understanding of the complicated physical processes that contribute to the urban climate. Reduced-scale physical models provide an alternative and powerful method to study urban climate. In addition, it is difficult for such scaled-down models to meet all of the similarity requirements. Nevertheless, they are especially useful to investigate systematically relations between surface structures and physical processes within the surface layer, thereby providing the physical parameters needed to construct and evaluate numerical models, which are based on solution of simplified governing equations.

2.6.1 Full Scale Experiments

Among tracer experiments only few are designed to investigate the dispersion in urban areas, and were conducted during two time periods of particular interest. Following the success of the Prairie Grass experiment over flat simple terrain (Barad, 1959), the Saint Louis Dispersion Study (McElroy, 1969), was successfully carried out from 1963 to 1965. The data formed the basis for the curves of σ_y and σ_z that were devised to form Gaussian type atmospheric type models (see below) for the description of an atmospheric dispersion in regulatory modelling. This was done by relating the plume spread to measured meteorological parameters, such as Pasquill stability classes. One significant conclusion was that for urban low level releases it was necessary to assign an initial plume spread.

Increasingly, urban climate research is being conducted in large projects, campaigns made by groups of scientists and agencies. This, in part, reflects trends in science for interdisciplinary, multi-method investigations and the increasing attention being directed to the environmental problems and issues in urban settings. Such studies allow a wide range of boundary and initial conditions to be checked, and it provides benefits given by multiple people and instrumentation that could not otherwise be deployed. One of the earliest large urban campaigns was the METROMEX study, conducted in St. Louis in the summers (from June to August) from 1971 through 1976 (Changnon, 1981).

The demand on urban dispersion insight increased dramatically after the terrorist attack on the 11th September, 2001 in New York City and Washington D.C. This initiated several urban scale tracer experiments in Europe and the U.S. These experiments included extensive meteorological measurements, as appropriate for modern tracer studies. The field study overview is given e.g. by Grimmond (2006).

The latter experiments often rely also on remotely sensed observations (aircraft, satellite, lidar, etc.). For example, a project in Marseille, France, (Mestayer et al., 2005) within the UBL/CLU - ESCOMPTE project allowed observations of surface temperature of individual wall facets to be integrated with remote sensing of the boundary layer and also by remote sensing from satellites. Urban 2000 project integrated observations from the Salt Lake Basin (Allwine et al., 2002) with detailed data collected on dispersion around individual buildings. A very important feature of these large projects is the integration of different types of measurement techniques, tower-based and remote sensing technologies. New insight into the comparability and complementarities of data derived from these different types of observations has resulted.

Increasingly, notably in Europe, international cooperation is also a trait of such projects; see for example the BUBBLE project (Basel Urban Boundary Layer Experiment, within the framework of COST action 715 - Meteorology applied to urban pollution problems, Rotach et al., 2004). More recently, the Joint Urban 2003 campaign, conducted in Oklahoma City, focused on improving our understanding of transient release and dispersion processes in complex urban areas as well as the compilation of reference data sets for the validation of LES numerical models (Allwine, 2004). The United Kingdom project DAPPLE (Dispersion of Air Pollution and Penetration into the Local Environment) is another example of a huge project combining many different approaches. The fieldwork of DAPPLE project is based at and around the Marylebone Road and Gloucester Place intersection in Central London (Arnold et al., 2004).

2.6.2 Reduce Scale Experiments

The history of reduced scale (or physical) experiments probably begins at the Gustave Eiffel laboratory, where building wind loads were investigated at the end of nineteenth century. The next important step was taken by Ludwig Prandtl, who figured out the similarity between atmospheric boundary layer and Prandtl boundary layer on a wall (Tritton, 1988), although the Reynolds numbers have different magnitudes for both cases. The progress of reduce

scale experiments were open after Prandtl's work. The rapid evolution started in fifties mainly in the field of wind loadings, bluff body aerodynamics, and aeroelasticity. Dispersion modelling seriously started at Fort Collins, Colorado, USA laboratory leaded by Prof. Cermak (Cermak, 1971, 1984). Since that time reduce scale modelling has been widely used to solve problems within ABL.

A number of experimental studies of dispersion in large groups of regular obstacles, which should represent simplified urban areas, have appeared in the past decade in the literature. Davidson et al. (1995, 1996) compared some small-scale field investigations with wind-tunnel simulations at a range of scales (1:20 and 1:200), with quantitative measurements only being undertaken in a staggered array of cubical obstacles. A range of mean and concentration fluctuation statistics were compared to control plumes, measured at the same site in the absence of obstacles. In a similar fashion, Macdonald et al. (1997, 1998) compared wind-tunnel simulations of a field experiment involving cubical obstacles, this time for a greater range of plan area densities, and larger obstacle arrays. Attention remained focused on mean concentrations and associated dispersion parameters in these investigations. In contrast to the current investigations, it is also worth noting that these previous studies mainly considered source positions upwind of the first row of obstacles (with the exception of Macdonald et al., 1998), which can influence the initial plume development differently. Work of Theurer et al. (1996) also considered an application of their results through hybrid modelling of semi-empirical near field dispersion using the wind tunnel data, and far-field standard Gaussian plume modelling.

The latter work (e.g. Cheng and Castro, 2002a; Schultz et al., 2005) employed extensive measurements of idealised urban areas to get insight into processes within the lowest part of the surface layer and to find suitable parameterisation of these processes for meso-scale models.

Experiments are ale conducting in reduce scale considering particular city. These experiment are usually part of the 'large experiments', which where mentioned above, for example: Joint Urban 2003 (Leitl et al., 2005), BUBBLE (Feddersen, 2005), DAPPLE (Robins and Cheng, 2005).

2.6.3 Numerical Experiments

Dispersion models are now widely used for assessing air quality by providing prediction of present and future air pollution levels as well as temporal and spatial variations. The models are treated from two different aspects. The first one is an operational one, which is required by decision making bodies. It means that the results must be clear and available immediately. The second aspect is credibility, i.e. the physics inside the model should be as complete as it is possible. The second approach ought to be prefered, however the programming and calculation time of such models is inappropriate for an air quality 'nowcasting'. Reviews of transport and dispersion models are available e.g. in Hanna et al. (1982); Vardoulakis et al. (2003).

Some examples of operational models are:

- The simplest and the most frequently used are Gaussian models, introduced by Sutton (Sutton, 1932) and improved by Pasquill (Pasquill,

1961, 1974); Gifford (Gifford, 1961, 1968) and many others. The three-dimensional concentration field from a point source is described by a Gaussian function, and these models rely on an appropriate selection of the plume spread functions σ_y and σ_z, which are generally expressed in terms of Pasquill atmospheric stability classes.

- A few dispersion models are based on solving the pollutant conservation equation using Gradient models or K-theory. The eddy diffusivity coefficient K is expressed as an empirical function of scaling parameters.

- Some models make use of Lagrangian particle dispersion models, where the individual trajectories of thousands of particles are tracked by the computer.

- For estimating transport and dispersion at distances ranging from a few to 100 kilometres, intermediate-scale or meso-scale puff models are often used. The pollutant release is modelled as a series of puffs, which are allowed to have curved trajectories to account for space and time variation in meteorology.

- Close to buildings or other obstacles, the flow and dispersion can be calculated using building downwash or vent models. These simplified models account for the presence of displacement zones and recirculating cavities.

With advances in a computer power, computational fluid dynamics (CFD) models can predict highly resolved three-dimensional time dependent distribution of wind flow and material concentration. Computational fluid dynamics is a general term used to describe the analysis of systems involving a fluid flow, heat transfer and associated phenomena by means of computer-based numerical methods. They usually include advanced turbulence treatment schemes, which make them more or less suitable for small-scale pollutant dispersion applications. Existing turbulence models can be classified in two broad categories:

- The classical models based on RANS flow equations, e.g. the $k-\varepsilon$ turbulence models, when treating flow around bluff bodies do not perform well.

- Large eddy simulations, (LES), (Kanda et al., 2004) are computationally very demanding and therefore mainly used in research applications. Although the equations of motion together with conservation laws can be applied directly to turbulent flow, rarely have we sufficient initial and boundary condition information to resolve all motion scales down to the smallest eddies. For simplicity, we instead pick some cut-off eddy size below which only statistical effects of a turbulence are included. Large eddy simulation techniques uses cut-off vortex magnitude in the range from several metres to approximately 100 m depending on an area of interest.

Thus some of the well-known traditional methods of dispersion estimation, such as Gaussian plume models, will most likely perform poorly in urban canopy

without significant modification (Feddersen, 2005). It is in such regimes, however, that a lot of interest for the applications of dispersion models lies, as it is at these near-field scales where the most serious threats to human health are posed from toxic releases of materials.

2.6.4 Verification and Validation of Models

The issue of comparing grid-averaged quantities (models output) and quantities defined at a point (full or reduced scale experiments), has never been fully resolved. Numerical models often prove themselves as an adequate representation of reality in terms of the quality of the physical modelling of scalar transport phenomena, as well as, the accuracy and model results. On the other hand, the comparison of model results with field or wind-tunnel data shows significant discrepancies (Schatzmann and Leitl, 2002). The difference can occur for two reasons: because of the simplified physics implemented in numerical models (there is no generally accepted model of turbulence, which can be applied for the complicated urban geometry); and because of a limited domain size and a limited spatial representation of the complex physical urban canopy systems. The geometry is simplified in the models, buildings are missing details like slanted roofs or oriels, the dimensions are adapted to grid that can cause significant changes of the building size. Oblique street canyons are represent with step-like structures which heavily influence flow within these streets.

Many practical models are simple idealisations, which have been tested on a few streets; and lots of full and/or reduce scale experiments were used to verify dispersion models. For example: some laboratory experiments (e.g. Davidson et al., 1995; Macdonald et al., 1997, 1998) showed that a conventional Gaussian plume model provides an appropriate structure for the problem of simple geometries. Field experiments which focus on dispersion from low-level sources in real cities are rare. The extensive laboratory experiments by Hall et al. (1996b) have been used to develop a simple urban dispersion model (Hall et al., 1997) based principally on data correlations.

Some recent studies tried to compare different numerical models with each other and also with full and/or reduced scale experiments. Examples of this are the German project 'Podbi exercise' (Lohmeyer et al., 2002) or an international project TRAPOS (Optimisation of Modelling Methods for Traffic Pollution in Streets, Ketzel, 2002). The outgoing COST action 732: 'Quality Assurance of Microscale Meteorological Models' (Schatzmann and Britter, 2005) supported by the European Science Foundation was designed to bring together experts working in this field, to review currently used approaches, and to recommend how to improve and assure the quality of numerical micro-meteorological models.

Chapter 3

Field Experiment MUST

The Mock Urban Setting Trial (MUST) was designed to provide insight into the instantaneous dispersion of a tracer through a large array of building-like obstacles. The study was motivated, in part, by a need to provide a better understanding of how the structure of a plume is modified as it disperses through a large array of obstacles, and to subsequently identify the physical mechanisms responsible for this modification (Biltoft, 2001). With this in mind, not only mean concentration field characteristics but also higher order statistical moments of the instantaneous plume concentration were measured at a large number of positions downwind of point sources located both upwind of and within an obstacle array for a number of different release heights.

3.1 Site Topography

The measurements were carried out in September 2001 at Horizontal Grid on the U.S. Army Dugway Proving Ground, located in the Great Basin Desert of northwestern Utah. The site elevation was 1310 m above mean sea level and predominantly flat. The terrain slopes gently upwards to the south with a slope of approximately 0.05%. Terrain features that may influence winds over Horizontal Grid include sand dunes 4 to 6 m in height located at about 1 km to the north. At about 12 km south-east of the site, Granite Mountain rises 700 m above the basin floor (visible in Figure 3.1). Approximately 24 km north-east of the site is Cedar Mountain whose ridge rises 600 m above the basin floor. During the experiments, the horizontally homogeneous site was naturally covered with a mixture of sparse greasewood and sagebrush ranging in height from about 0.4 to 0.75 m (Fig. 3.1). The average roughness length, $z_0 = 0.045 \pm 0.005$ m, and the displacement height, $d_0 = 0.37 \pm 0.09$ m, were determined from the mean wind profiles measured under near-neutral stratification (Yee and Biltoft, 2004). Both z_0 and d_0 were not dependent on the wind direction.

3.2 Obstacle Array and Coordinate System

Each obstacle was a standard shipping container, with a width $W_{c\,\mathrm{FS}} = 12.2$ m, length $L_{c\,\mathrm{FS}} = 2.42$ m, and height $H_{\mathrm{FS}} = 2.54$ m. A total of 120 obstacles were

Figure 3.1: The container array of the MUST experiment located in the Great Basin Desert. The highest T tower (32 m) is visible in the middle of the array and Granite Mountain, which is at the picture background, is 12 km far away. Picture was taken from the MUST database.

Figure 3.2: Part of the container array consisting of the regular 40-feet shipping containers and the upwind 16 m mast, labelled S tower. Picture was taken from the MUST database.

placed in an aligned configuration consisting of 12 rows of 10 obstacles each with an average obstacle spacing of $W_{\mathrm{FS}} = 7.9$ m in the spanwise direction and $L_{\mathrm{FS}} = 12.9$ m in the lengthwise direction. Part of the array and surrounding vegetation are shown in Fig. 3.2. Consequently, the overall width and length of the obstacle array were 193 m and 171 m, respectively. This gives a frontal area density (the frontal face area of the containers relative to the plan area of the frontal container row, Grimmond and Oke, 1999) of 0.10 and a plan area density (the plan area of the containers relative to the total surface area of the array) of 0.096 for the MUST set-up. The positioning of the containers was so that it would form a regular array, however, the small offsets were necessary to avoid damages on wires and instrumentations, and several alignment errors were unavoidable due to the uneven nature of the Basis floor (the misalignment is clearly shown in Fig. 3.3). For ease of reference, each row and column of the obstacle array was assigned a letter from A through L and a number from 0 through 9, respectively, Fig. 3.3. Thus, obstacle A0 was located in the north-east corner of the array, and obstacles A0 through A9 define the north-west border of the array. Similarly, obstacle L0 was located in the south east corner of the array, and obstacles L0 through L9 formed the south-east border of the array. The axis, which is normal to the long face of the array obstacles, was oriented 28.25° west of north.

The x (lengthwise) and y (spanwise) coordinates are in this work defined so that $x = 0$ m and $y = 0$ m is at the centre of the obstacle array. The z (vertical) coordinate is defined so that $z = 0$ m is the ground surface beneath the obstacles. Consequently, with this coordinate system, the positive x-axis is directed 28.25° west of north, whereas the positive y-axis is directed 28.25° south of west and z-axis is directed upwards. The wind direction is therefore always relative to the containers array and positive angles are in the counter-clockwise direction, i.e. 0° approach wind is normal to the frontal face, 90° is parallel with the longer container wall and headed south-west. With respect to the original reference system used in the field (Biltoft, 2001), the origin of the coordinate system used in this work is shifted 88 m along the x-axis and 82 m along the y-axis and orientation of both axes is turned.

3.3 Instrumentation

The MUST field experiment was well equipped with meteorological and aerodynamical instrumentations. Details of the set-up are given in Biltoft (2001), thus only a brief summary of the instrumentation used to acquire the data, which will be shown in next chapters, will be presented. Supportive meteorological measurements, which were conducted near (to a distance of 5 km) or within the test site, were made using the following instrumentation:

- a tethered balloon sounding system measuring wind velocity, temperature, humidity and pressure;
- a fiberoptic-quartz thermometer used to measure the temperature differences between the surface and 2-m above ground level (AGL);

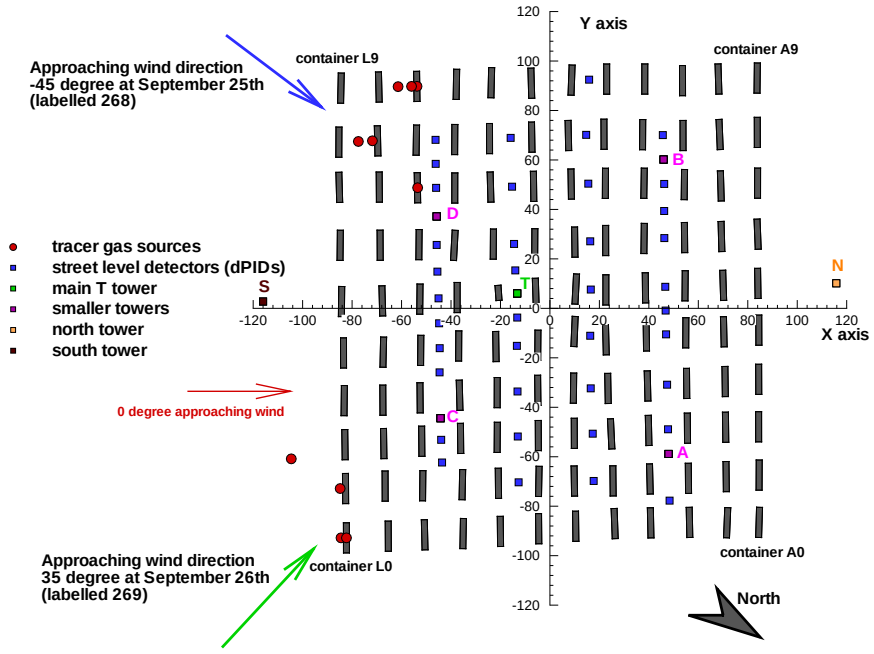

Figure 3.3: Field experiment instrumentation sketch. The coloured arrows imply the wind direction, black arrow showing north. Coloured squares show the instrumentation: purple are the smaller 16 m towers (A–D) equipped with 2-D sonic anemometers and UVIC tracer detectors; brown and orange are the S and N towers, respectively, equipped with 2-D sonic anemometers; green is the main 32 m T tower provided with 3-D sonic anemometers and dPID tracer detectors; and blue squares depict the street level (at height 1.6 m) tracer dPIDs detectors. Red circles show the positions of the tracer sources. All dimensions are in metres.

- a sound direction and ranging (sodar) providing 10-minutes averaged wind profiles between 15 and 200 m AGL;
- a Portable Weather Information and Display System, which had several monitoring stations positioned around Horizontal Grid at distances of several kilometres from grid centre;
- thermocouples for temperature measurement;
- actinometers producing measurements of solar and terrestrial radiation;
- infrared imaging radiometers sensitive to the tracer gas allowing spatial imaging of the dispersion;
- a wind profiler radar.

The layout of the selected instrumentations is depicted in Fig. 3.3.

Mean Velocity and Turbulence Measurements

Measurements of the vertical profiles of the mean horizontal wind velocity and turbulence in the upwind flow were obtained from a 16 m telescoping pneumatic mast (labelled S tower, i.e. south) erected 30.5 m ($12H$) upwind of the centre-line of the front of the obstacle array (Fig. 3.3). This mast was instrumented with three two-dimensional (2-D) sonic anemometer/thermometers measuring in horizontal plane at 4, 8, and 16 m levels. Similar 2-D sonic anemometer/thermometers were mounted 4, 8, and 16 m up the 16 m pneumatic mast (labelled N tower, i.e. north) deployed 30.5 m ($12H$), downwind of the back of the obstacle array. Courtesy of four three-dimensional (3-D) sonic anemometer/thermometers at 4, 8, 16, and 32 m on the 32 m lattice tower (labelled T tower or main) located near the centre of the obstacle array, the complete vertical profiles of the mean wind speed and 3-D turbulence characteristics, as the intensities of turbulence and Reynolds stresses, were obtained. The typical measuring frequency of the anemometers were 10 Hz and the locations of the towers are shown in Fig. 3.3.

Concentration Measurement

In each experiment, propylene (C_3H_6) tracer gas was released at a point from a specially designed gas dissemination system that used a mass flow controller to maintain a constant flow rate. The instantaneous plume concentrations were measured with two types of fast-response photo-ionisation detectors; namely, digital photo-ionisation (dPID) detectors and Ultra Violet Ion Collector (UVIC) detectors. Both types of detectors provide a frequency response of 50 Hz with a sensitivity of about 0.01 ppm by volume of propylene. Horizontal profiles of concentration statistics were measured using 40 dPIDs, which were arranged along four horizontal sampling lines that were parallel to and centred in the street canyons. Sampling lines were centred in the street canyons between obstacle rows I and J ,G and H, E and F, and C and D, respectively. The concentration detectors along the four horizontal sampling lines were placed at a height, $z_d = 1.8$ m ($z_d/H = 0.71$). Vertical profiles of concentration statistics were characterised by 8 dPIDs deployed on the 32 m T tower near the centre of the obstacle array at heights of 1, 2, 4, 6, 8, 10, 12, and 16 m and by 24 UVICs mounted on the four 6 m towers A, B, C, and D. On each of these 6 m towers, 6 UVICs were deployed at the following levels: 1, 2, 3, 4, 5, and 5.9 m. In each experiment, the propylene gas was released and sampled continuously over a period of approximately 15 minutes. At the flow rates for the gas release (between 150 and 225 liter per minute), the negative buoyancy effects of the gas were insignificant, i.e. the release was passive. Time series of instantaneous concentrations were measured at various points in both horizontal and vertical cross-sections through the dispersing plume at various downwind distances from the source. Measurements were made for various source positions with respect to containers. The locations of the instruments are also shown in Fig. 3.3.

Data Reduction

The data set, used in this instance, were already pre-processed and a detailed description of the experiments and the data pre-processing can be found in Biltoft (2001). The majority of the MUST field campaigns were carried out during the late evening and night, and that, together with the desert surrounding, ensures slightly stable to very stably ABL stratification at the test site. Some others, e.g. the numerical study by Nelson et al. (2004) or wind tunnel study by Gailis and Hill (2006), were able to model different stratifications and therefore they could use data obtained during measurement in a stably stratified ABL. Our intention was to model the test site in the wind tunnel with a neutrally stratified ABL. Hence we have chosen only two days (the 25th and the 26th September, 2001, according to Julian calendar labelled 268 and 269, respectively) with relatively strong wind (between 7 and 11 m s^{-1} measured at the 32 m elevation on the T tower). This strong wind produced a sufficiently high level of turbulence when interacting with the underlying roughness and this mechanically generated turbulence mixes the surface-layer air and breaks up the stable stratification. On these two chosen days the wind direction varied from -40° to -51° and from 28° to 45°, respectively. The wind directions are always related to the container array and not to the points of the compass. They are shown in Fig. 3.3 for two measurement days.

3.4 Approach Flow Characteristics

Since, we have considered as a suitable only the data obtained during two days with strong wind, only the following instruments were available to deliver the data for an assessment of the approach wind characteristics (a tethered balloon was not operated because of the strong wind): sodar and 2-D sonic anemometers placed at 3 elevations on the S tower. The comparison of the approach flow vertical profiles obtained from different measurement methods is shown in Fig. 3.4, which was enclosed to the complete field data-set. It is clearly visible that the measurements of the velocity magnitude vary quite a lot (the left part of the Fig. 3.4). In contrast, the measurement of the wind direction is consistent and even no significant change of wind direction with elevation has been observed (the scale in the right part of Fig. 3.4 is rather fine and therefore the pronounced changes are not so significant as they seem to be). Another problem is the impossible estimation of the Reynolds stress, since the anemometers on the S tower were only 2-D, i.e. they were measuring only the horizontal components of an approach wind and not w wind component, which is crucial for a Reynolds stress estimation. Finally, the vertical profiles obtained from sodar measurements were too coarse to adequately fit the logarithmic vertical profile (equation 2.29), from which characteristics like the roughness length, z_0, displacement height, d_0, and friction velocity ,u_*, are usually derived. Although the other authors (e.g. Yee and Biltoft, 2004) did so, we are not confident to do so, because of the unknown data uncertainties.

Since the field data show uncertainties (different outcomes from different instruments) and some important quantities have been missed (rather coarse

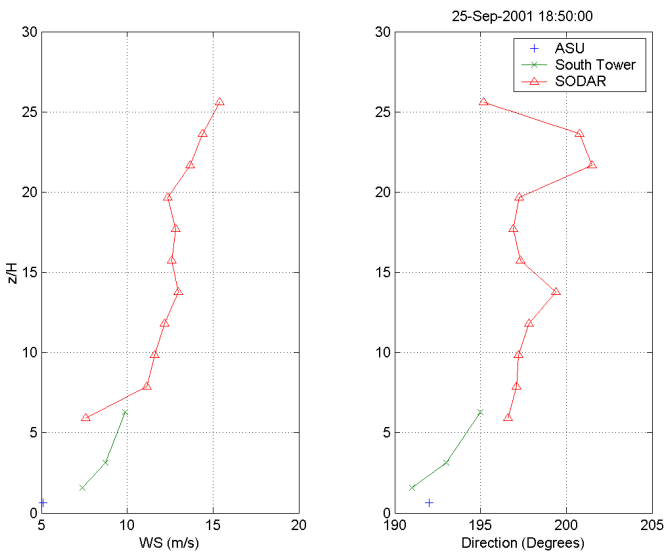

Figure 3.4: An example of approach wind vertical profiles in the MUST field experiment measured at 25th September 2001 at 18:50 of the local time. The left chart shows the vertical profile of the mean wind speed, and the right shows the wind direction of approaching flow at different elevations. The red line and triangles depicted the sodar measurement, green line and crosses belong to S tower measurement, and blue cross shows values measured by one of the street level anemometers. Adapted from Biltoft (2001).

measurement grid and missing vertical wind speed component measurements and consequently also Reynolds stress measurements), we decided to model the atmospheric boundary layer not according to what was measured in the field, but to model a boundary layer according to what is recommended for a slightly rough terrain type by tables (ESDU, 1985; Snyder, 1981; VDI Guideline 3783/12, 2000). For more details of modelled ABL see chapter 5.

The Monin-Obukhov length L will serve as an atmosphere stability class indicator. The direct measurement (or more precisely determination) of L comes from the definition of the turbulent heat flux (analogically to the definition of the turbulent momentum fluxes - the Reynolds stresses)

$$H_S = \varrho\, c_p\, \overline{w'\theta'}, \tag{3.1}$$

which transforms the definition of L (equation 2.17) to

$$L = -\frac{u_*^3\, \overline{\theta}}{k\, g\, \overline{w'\theta'}}, \tag{3.2}$$

where all the quantities are measurable. The only available 3-D velocity and temperature measurements (necessary for $\overline{w'\theta'}$ determination) were from the T tower (see Fig. 3.3). The modified Monin-Obukhov length definition (equation

3.2) will be use to verify or to confute the assumption that a strong wind can break down the surface layer stratification.

The dependency of the Pasquill's stability classes on the Monin-Obukhov length and the roughness length is shown in Fig. 3.5. Taking the MUST field roughness length value $z_0 = 0.045$ m (Yee and Biltoft, 2004), ranges for neutral to stable Pasquill's turbulence types for the MUST field experiment were obtained:

Pasquill's stability class		lower limit for $1/L$	upper limit for $1/L$
D	neutral	-0.02	0.02
E	slightly stable	0.02	0.06
F	moderately stable	0.06	0.14
G	extremely stable	0.14	

Transforming the table values and values obtained from T tower measurement (usually statistics of 900-s time series) into a graphic form (Fig. 3.6) we can see the Monin-Obukhov length development during the two chosen days. On 25th September (left picture) ABL was neutral in the evening (approximately until 8 PM), gradually becoming more stable (after 22 hour of the local time), and finally becoming slightly stable (before midnight). Also the difference between measurements at different elevations is clearly pronounced. It indicates disequilibrium of the boundary layer flow and the influence of the container

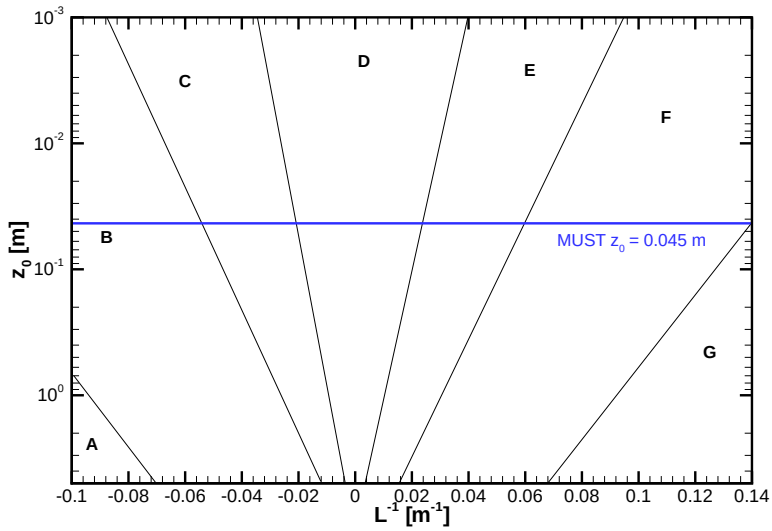

Figure 3.5: The Pasquill's stability classes as a function of the Monin-Obukhov length L and the roughness length z_0. A, extremely unstable conditions; B, moderately unstable conditions; C, slightly unstable conditions; D, neutral conditions; E, slightly stable conditions; F moderately stable conditions; G, extremely stable conditions. The MUST field roughness length (Yee and Biltoft, 2004) is imprinted by blue line. Modified after Hanna et al. (1982) and Golder (1972).

array on the flow (L is larger in the lower elevations, i.e. the air is better mixed near to the obstacles). The duration of the measurement was much shorter on the second day, 26th September (right picture in Fig. 3.6), however, the overlapped intervals seems to show a similar behaviour of the Monin-Obukhov length during the late evenings for both days.

Figure 3.6 evidently breaks up our assumption of neutral surface-layer stratification. On the other hand, the scatter of L measurements were large and without being present in the field during the experiment is hard to determine the measurement representativeness and reliability. Therefore the comparison of the wind-tunnel data will be done with respect to these findings.

3.5 Other Studies Connected to the MUST Experiment

The MUST field data are widely used for a validation of numerical models, for example the FLACS CFD air quality model (Hanna et al., 2004) and the Feflo-Urban CFD model (Camelli et al., 2004). Due to a presence of a nearly ideal artificial built-up area and various ABL stratifications it was used also for a radiative scheme validation (Milliez et al., 2006).

The same topic as this work (wind tunnel modelling of the MUST experiment) was focus of another study by Gailis and Hill (2006). This study was conducted on a model in the scale 1:50 and also the stability of ABL was modelled. However, this study just repeated the measurement conducted in the field, did not extent the measurement area or number of points, or carried on any verification experiments, which are one of the most important parts of this work.

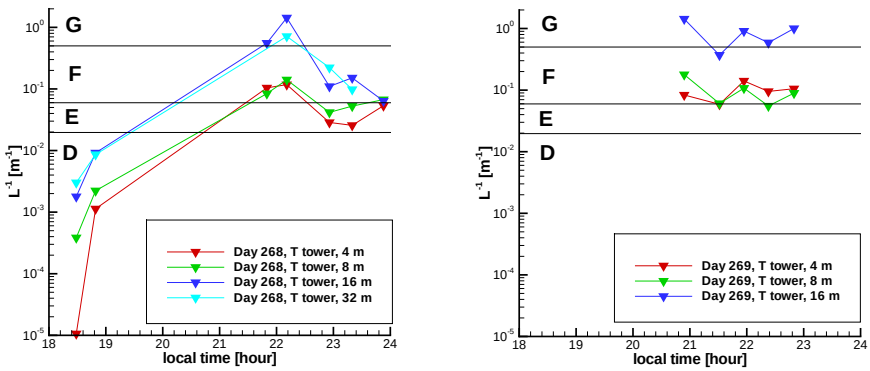

Figure 3.6: The Monin-Obukhov length L measured on the T tower at different elevations as a function of local time. Horizontal lines and letters indicate borders between each of the Pasquill's stability classes. The left part shows measurement from the 25th September (day 268) and the right part the 26th September (day 269), respectively.

Chapter 4

Experimental set-up

The experimental set-up used during the wind tunnel modelling of the MUST field experiment will be described below. The measurements were realised during a 6 months extensive campaign, from March to August 2005.

4.1 Wind Tunnel 'WOTAN'

The experiments were carried out in the large boundary layer wind tunnel facility 'WOTAN' of the Environmental Wind Tunnel Laboratory (EWTL) of the Meteorological Institute at the University of Hamburg. A schematic drawing of the 26 m long wind tunnel with a 18 m long interior test section is shown in Fig. 4.1. Its rectangular cross section is 4 m wide and 2.75 to 3.25 m high. The tunnel consists of an intake nozzle with 300 mm deep honeycomb flow straightener, up to 12 m long flow development zone for boundary layer development and a test section with two turn tables. The flow is driven by an axial blower 3.2 m in diameter and the whole facility is operated in suction mode, so that, the flow disturbance by the wind tunnel drive does not effect the flow in the test section. The mean free stream wind speed in the wind tunnel can be adjusted approximately from 0.5 to 20 m s^{-1}. An adjustable ceiling allows the longitudinal pressure gradient across the test section to be minimised. Twenty-two pressure probes are installed pairwise at opposing side walls, i.e. pressure measurements can be done at 11 locations along the wind tunnel axis. Inside the wind tunnel a traverse system allows automatic positioning of measurement probes. The system is operated by positioning software installed on a PC outside the wind tunnel. The traverse system was used with a positioning accuracy better than 0.1 mm in each space dimension. The overall accuracy of measuring devices positioning in respect of model coordinates was better than 1 mm.

In order to ensure consistency of experimental results compiled from different test runs, a reference free stream wind speed was monitored during measurement. A Prandtl-type pneumatic probe was placed just at the wind tunnel entrance, Fig. 4.2, at the height 1710 mm above the wind-tunnel floor and 740 mm from the right wind tunnel wall. Pressure differences were measured with a MKS BARATRON® differential pressure transducer. The pressure transducer was repeatedly calibrated and tested against an independent, certificated

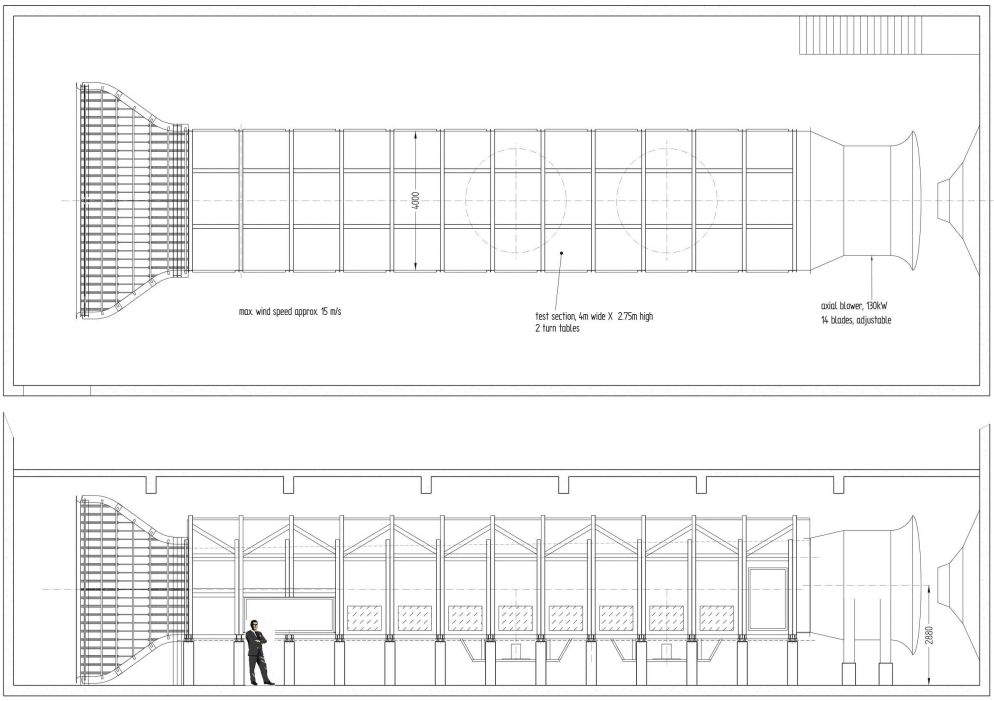

Figure 4.1: The large boundary layer wind tunnel facility 'WOTAN' of the Environmental Wind Tunnel Laboratory of the Meteorological Institute at the University of Hamburg.

pressure standards (fine-pressure-balance, Junkalor®) to ensure high quality reference measurements.

To speed up the unaffected development of the boundary layer above a rough wall so-called 'turbulence generators' or 'spires' were mounted directly behind the intake nozzle of the wind tunnel, and the entire wind-tunnel floor was covered by roughness elements made from L-shaped aluminium profiles and fixed to the floor by magnetic foil. The descriptions of the turbulence generators, roughness elements and their configuration used during the campaigns are given in Appendix A.

Flow velocity measurements were made using a two-dimensional Laser Doppler anemometry (LDA) from DANTEC®. The equipment included a continuous air-cooled laser unit, transmitter-based FiberFlow optical system 60X40, a fiber-optic probe with focal distance 800 mm equipped with mirror (Fig. 4.3), a Flow Processor BSA F70, and BSA Flow Software. The LDA is non-intrusive, component-resolving flow measurement with very high spatial and temporal resolution. Seeding particles were provided by the 'Tour- Hazer' from Smoke Factory® using Tour-Hazer-Fog. The details and principle of LDA can be found in section 4.3 below.

For the dispersion experiments different point sources were operated with ethane (C_2H_6) as a neutrally buoyant tracer gas. The wind tunnel is situated in a large closed hall, thus the wind tunnel can be considered as 'quasi-closed'

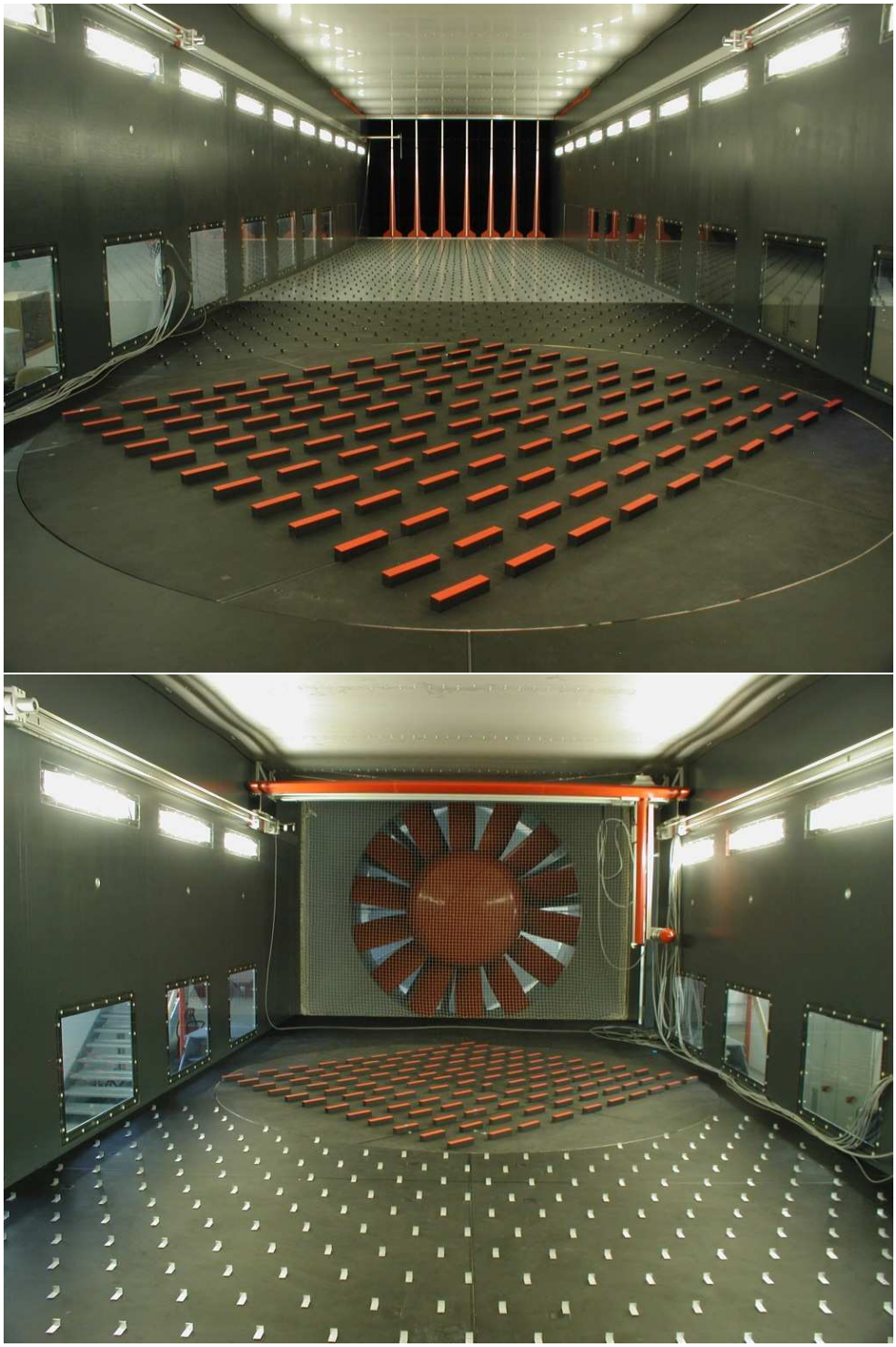

Figure 4.2: The model installed in the 'WOTAN' wind tunnel (looking upstream in the upper picture and downstream in the lower picture). Upper picture shows turbulence generators (spires). Prandtl tube was placed between the first and the second spires on the left-hand side. The lower picture shows the traverse system, the floor roughness in the development section, and the model and wind tunnel drive.

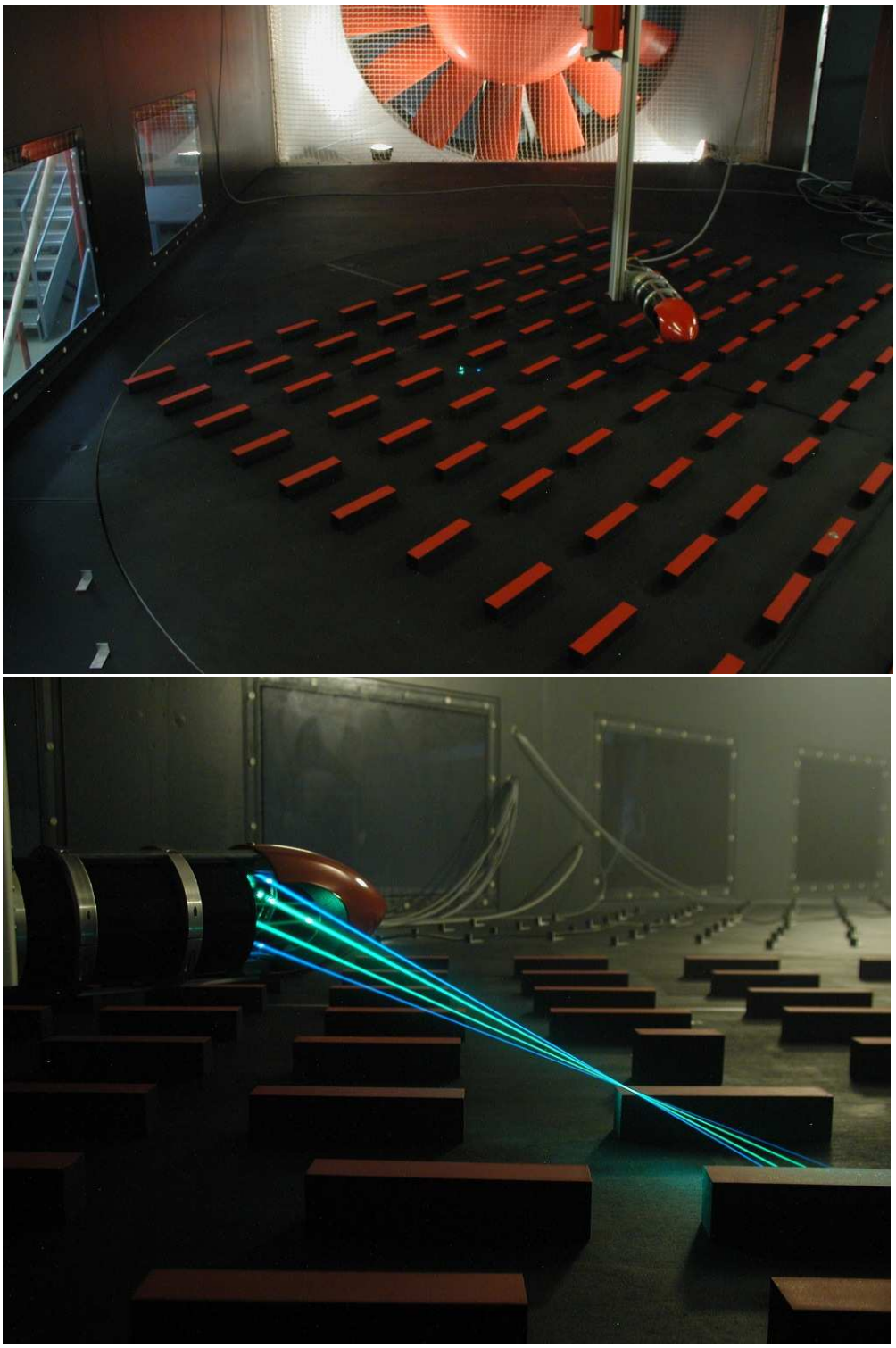

Figure 4.3: The mounting of the LDA probe (upper picture) and details of the front mirror and four beams of 2-D LDA system measuring u and w wind velocity component (lower picture).

facility, since the same air was still circulating in it. During the measurements the tracer was released in the wind tunnel, then it dispersed to the air, and retain in the hall, i.e. in the tunnel, well mixed with the air. The background concentration of hydrocarbons therefore increased steadily and it influenced measured values on the model. This concentration was increasing with the time of the measurement and hence the continual recording of the background concentration was very important and were conducted using the slow Flame Ionisation Detector (SFID) Rosemount® Analytical Model 400A from Emerson (Fig. 4.4). The concentrations within the model were measured using a fast Flame Ionisation Detector (FFID) HFR400 from Cambustion Ltd. (Fig. 4.5). Both measuring devices were calibrated (Fig. 4.6) at least three time a day with certified calibration gases corresponding to four reference ethane concentrations as given by the manufacturer: 0 ppm (synthetic air), 256 ppm, 777 ppm and 1207 ppm. The FFID signal was amplified and filtered using the Kemo VBF44 multi-channel filter/amplifier system from Kemo Inc. (Fig. 4.6). The FFID probe was mounted with a needle of length 300 mm and an inner diameter of 0.3 mm. Given the pressure difference between ambient pressure and the pressure inside the combustion chamber of about 150 mmHg and a combustion chamber temperature of about 210°C, the maximal FFID frequency response to concentration fluctuations as given by the manufacturer was about 160 Hz. The details and principle of Flame Ionisation Detectors can be found in section 4.4 below. For precise trace's dosing, electronic mass flow controller Brooks® 5861S from Emerson (with range 0-10 l hour^{-1} or 2-100 l hour^{-1}, Fig. 4.6) was utilised. Also this device were calibrated against independent standard providing by Brooks Vol-U-Meters.

The tracer dispersion was studied during two different campaigns. The first focused on statistically stationary processes using a continuous constant flow rate of the tracer from the source. The second part investigated a temporal behaviour of the tracer concentration during sudden time-limited releases and was primarily aimed at looking at the statistic parameter dependency on a release time and the Reynolds number. The instantaneous releases were providing by a magnetic valve, which let through a tracer with a constant selectable time step (Fig. 4.5). This valve was placed behind the mass flow controllers and during the closing period of the source the tracer was blown off to an exhaust tube to prevent pressure changes at the mass flow controllers and consequently the inaccuracy of the tracer flow rate estimation.

4.2 Wind Tunnel Model of the Test Site

The model of the MUST field site was built in the scale 1:75. That means: width $W_{c\,\mathrm{MS}} = 163$ mm, length $L_{c\,\mathrm{MS}} = 32$ mm, height $H_{\mathrm{MS}} = 34$ mm, average obstacle spacing of $W_{\mathrm{MS}} = 105$ mm in the spanwise direction and $L_{\mathrm{MS}} = 172$ mm in the lengthwise direction, the overall width and length of the obstacle array of 2573 mm and 2280 mm, respectively, with diagonal of 3438 mm. The scale, in which the model was manufactured, is important, since this scale applies to the approach flow, namely for characteristics length scales such as

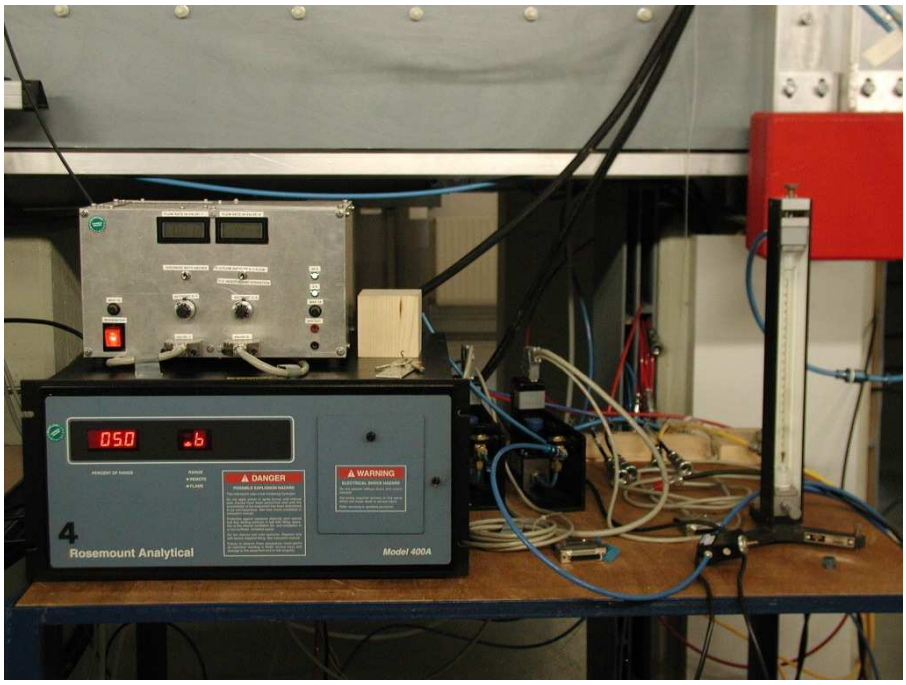

Figure 4.4: The Slow Flame Ionisation Detector (blue box), the mass flow controllers (black, next to SFID) and their control unit (silver box), and a rotameter for rough estimate of the flow rate via calibrating device.

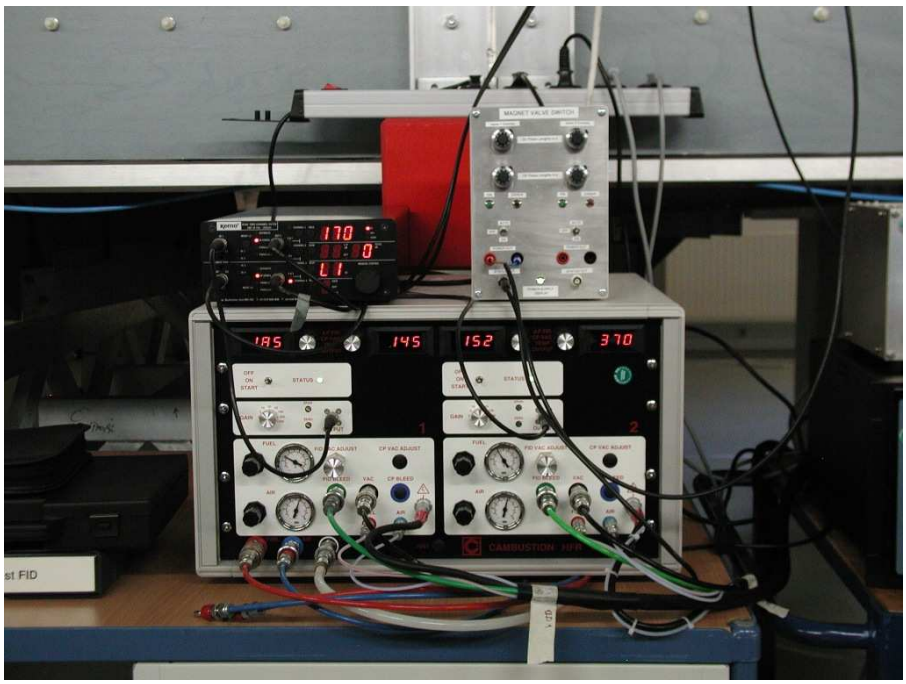

Figure 4.5: The control unit of Fast Flame Ionisation Detector (lower box with tubing), the signal amplifying and filtering device KEMO (black box) and magnetic valve control unit, which allows to regularly switch on and off the source (silver box).

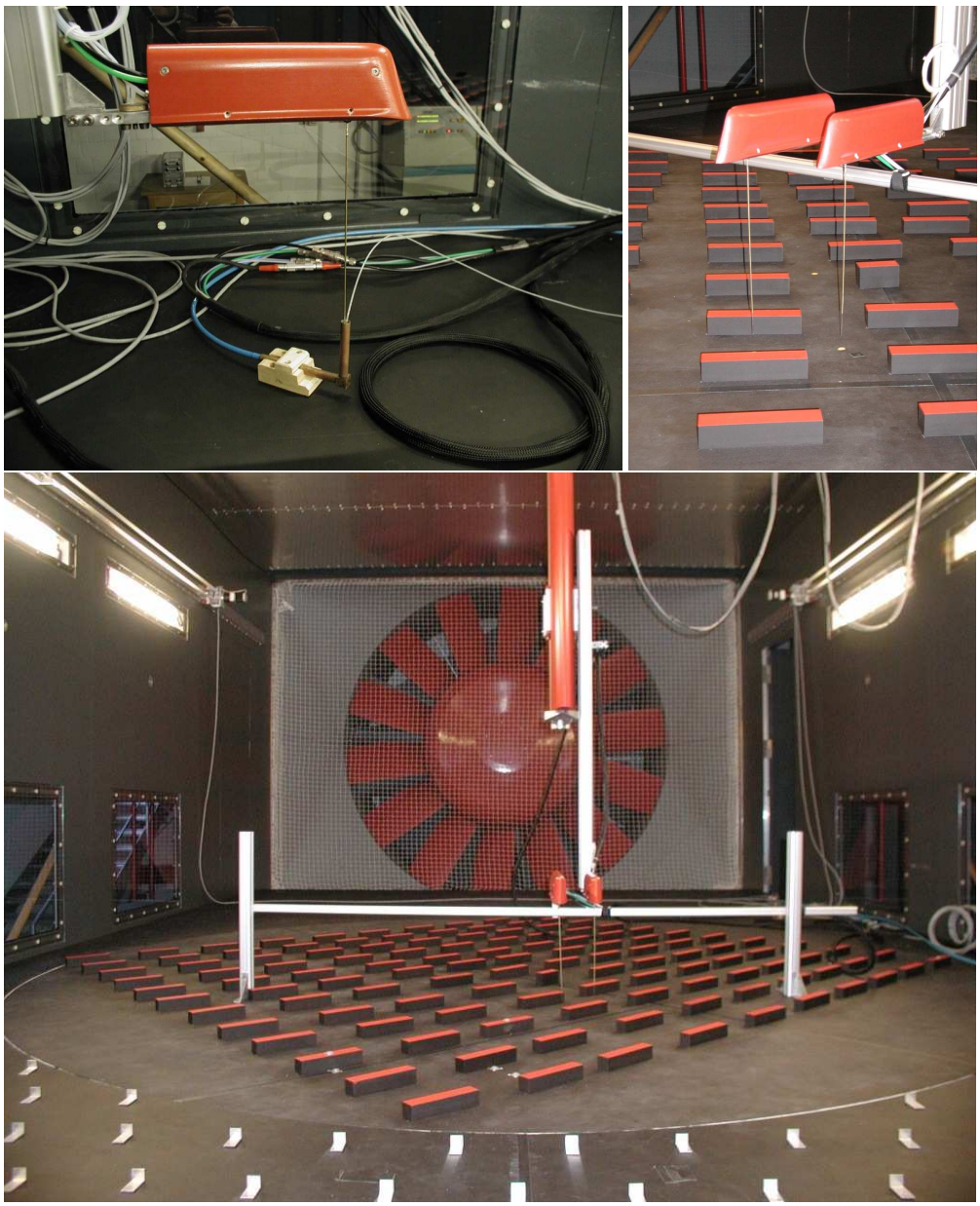

Figure 4.6: The calibration device for FFID (red body and needle) and SFID (with tubing) - on the left; two FFID chambers mounted in the wind tunnel (the first probe on the traverse, the second probe on the tripod) - at the bottom; a detail of two FFID probes - on the right.

the roughness length or integral length scale (see chapter 5 below). This scale was chosen on the basis of three factors: firstly, the experiments had been planed for different wind directions and thus it was demanded that the whole model must fit the wind tunnel turn table (diameter 3.5 m, Fig. 4.1); secondly, the bigger scale offered better spatial and therefore via dimensionless time definition (equation 2.23) temporal resolution; and last, but not least, the feasibility of the

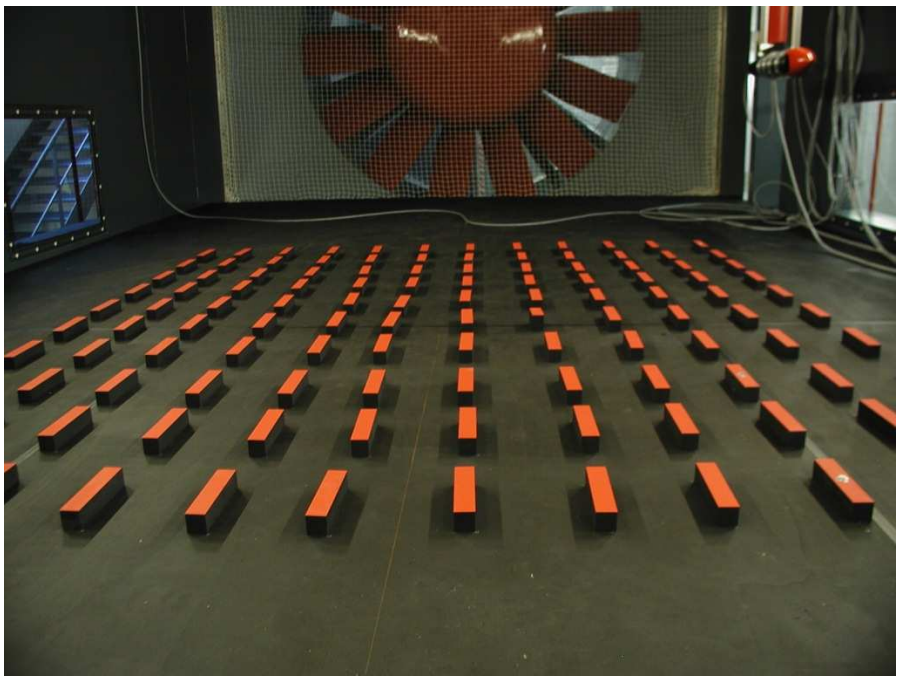

Figure 4.7: Irregularities in the containers arrangement.

'WOTAN' wind tunnel boundary layer modelling. The array was not perfectly regular in the field and these irregularities were kept as well as the replacement of one container by a service car in the wind tunnel model (Fig. 4.7, detailed description can be found in Appendix B).

Six tracer point sources were build within the model. These six sources had positions identical to those used during the field campaigns conducted in the

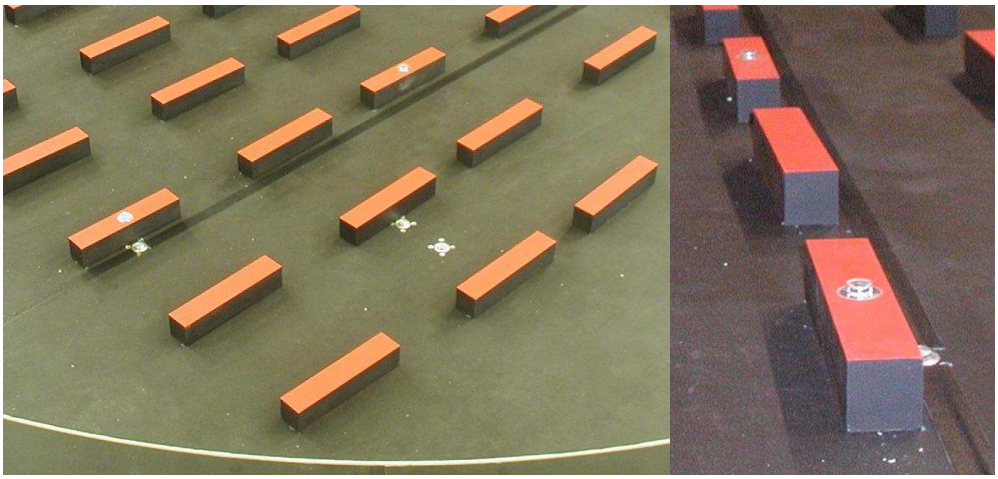

Figure 4.8: Detail of build-in ground-level and roof-top sources.

two chosen days (25th and 26th September) and their coordinates are given in Appendix B. It was clear that the source design used in the field experiment can not be replicated to the scale in the wind tunnel. The field source was a vertically oriented outlet pipe with diameter about 0.05 m, which rested on a weir wheel or tripod 0.15 m above the surface for the ground-level releases (Biltoft, 2001). Downsizing by the geometric scale factor of 75 gives a source dimension of approximately 0.7 mm. If we consider the usual tracer release of gas about 50 l hour^{-1}, the output velocity of the tracer reaches 40 m s^{-1}. This is too large to be desirable and therefore deviations from the field source design were unavoidable. The experience with the EWTL group from the previous projects (e.g. Feddersen, 2005; Leitl et al., 2005) was used to design the point sources used here. The ground level sources had a body under the surface, the output coincided with the ground level and only the cover fixed by three struts rose to the height of 4 mm (0.3 m in the full scale) above the surface. This design obstructs to a vertical jet development and ensured the source area (cylinder jacket) of $5.5 \cdot 10^{-5}$ m^2. Therefore the outlet tracer velocity is approximately 0.25 m s^{-1} for flow rate 50 l hour^{-1}. A different tracer source design in the field and in the wind tunnel is unavoidable and its consequences have to be taken in account. The greatest differences due to the source design would appear very close to the source (up to several source diameters. i.e. about 1 m in the full scale). Since the flow within the roughness canopy (all used sources were ground level sources) is very turbulent, the rapid mixing of a tracer and clear air takes place here. Therefore the initial source conditions are very quickly forgotten and for the far field, e.g. the next street canyon, such a difference in the source design is negligible and will not influence the concentration field, which is of our interest. The influence of the source design and tracer flow rate was tested and results can be found in section 7.1.4.

4.3 Principle of Laser Doppler Anemometry

The fundamental principles of LDA are given in the technical LDA manual (DANTEC Dynamics, 2006) by the manufacturer or in Fingerson and Menon (1999) and can be summarised as follows. Initially, for simplicity, an one-dimensional system will be described. The method overview is schematically shown in Fig. 4.9. Two coherent laser beams of the same wavelength are arranged to intersect in a certain measurement volume thereby producing a fringe pattern (i.e. interference pattern) of high and low intensity strips. If the wavelengths are exactly equal and the beams are coherent the fringe pattern is stationary and the regions of high and low intensities form parallel planes. Knowing the laser beams wavelength and intersect angle, the distance of these planes can derived (DANTEC Dynamics, 2006). Seeding particles, i.e. fog droplets, which can be assumed as non-affecting the flow are introduced into the flow. Any particle of appropriate quality travelling through the measurement volume scatters laser light whenever it passes through one of the high intensity planes thereby producing a flickering scatter signal on its way through the volume. This flickering scatter signal is termed as a 'Doppler burst', the

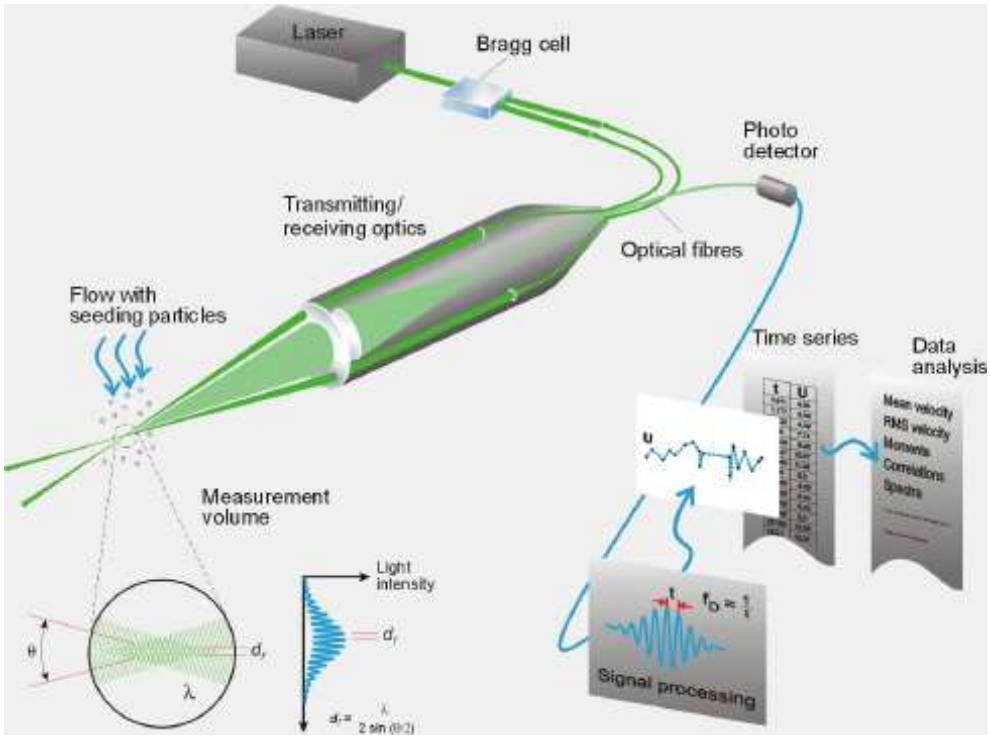

Figure 4.9: Laser Doppler Anemometry principle. Adapted from DANTEC Dynamics (2006).

idealised case, which is shown in the lower part of Fig. 4.9. Each signal maximum in the burst corresponds to the passage of the particle through one plane of high light intensity. The frequency of this flashing signal depends on the particle's velocity component perpendicular to the light planes and thereby allows the determination of this particular velocity component. Two coherent beams are emitted by the optical probe connected with the laser via optical fiber, see Fig. 4.3. The returned scattered signal is received by the same probe and again via fiber optic transfer to the photomultiplier. The signal is amplified here and then processed by the BSA Flow Processor, which is part of the DANTEC® system. The BSA processor filters out noise and the final signal, the ideal one is shown in the lower left corner in Fig. 4.9, is used to derive velocity.

The whole LDA system is except the main principle completed with another upgrading features that sophisticated measurement. More than one component measurement is ensured by using two or three different laser beam colours and their separate processing. The interference pattern, i.e. light planes, must be perpendicular to the velocity component, which should be measured, thus any chosen velocity component can be measured by careful adjustment of the fringe pattern's orientation. The LDA system used here had two components and therefore, two measurement volumes of essentially the same size and at the same location were created. The measurement volume forms approximately an ellipsoid and its measures depend on the intersecting angle of the two beams

and thereby on the focal length of the laser probe, which was 500 mm in our case. The measuring volume was 0.1 x 0.1 x 1 mm and the fringe spacing approximately 3 μm in the used LDA set-up. The precise alignment of the measurement volumes position for both velocity component is essential for synchronised measurements, where not only one component, but cross-component statistics, like Reynolds stresses, are derived. The spatial alignment was adjusted, the time synchronisation is ensures by the BSA processor, when only signals coming at the same time (with variable accuracy) from both channels, i.e. components, are accepted.

The measuring volume corresponds to 7.5 x 7.5 x 75 mm in the full scale. This dimensions are fully comparable with dimensions of ultra-sonic anemometers used in the MUST field campaign. The LDA system tracks particles in whole measuring volume. Therefore the obtained result is na integral value of the measurement volume. This behaviour can caused measurement uncertainties in regions with a steep velocity gradient or a shear, where the dimension of the measuring volume can not be neglected. The vivid example of this situation is a small difference of the mean flow values measured at the same point with a different orientation of the LDA probe shown in Fig. 5.11 (the largest difference can be found in the lowest positions, where the vertical gradient is greatest). The longest dimension of the measuring volume is oriented along the z-axis during the UV measurement (Fig. 4.10, green lines). The oval is showing a projection of an ellipsoid to the xz plane. The range in z-axis (showed by the vertical lines), where LDA is measuring, is much wider than for the UW set-up (Fig. 4.10, blue lines) and therefore also the velocity range is much wider for the UV set-up. This can be reason for poor agreement between these two set-ups results. Fig. 4.10 is not in the scale (measuring volume is much smaller) in order to magnify the above described phenomenon. All boundary layer documentation data presented in chapter 5 are based on UW set-up measurements, which have higher accuracy in the laterally homogeneous approach flow. Measurements in sections 6.1 and 6.2 were conducted with UV set-up and UW set-up, respectively. Since the flow field inside the Roughness Sublayer is highly non-stationary and spatially inhomogeneous, the results presented in the chapter 6 have to interpreted as an integral value of 1 mm area in the vertical and horizontal direction in the case of UV set-up and UW set-up, respectively.

The seeding particles (i.e. fog droplets) must be of appropriate size. The droplets should be of the same magnitude as the fringes to returned strong signal. The smaller ones will have less intense scatter, while the larger ones could interfere more fringes at one moment and the scatter light will have not processable shape. The large particles are also heavier and therefore can influence the flow, which is undesirable. The smoke generator used during the measurement operates dependently on the ambient conditions. For example humidity, which were not fully under control in the wind tunnel hall, influenced the size of the smoke droplets and consequently an efficiency of the measurement. However, this phenomenon had not radical significance for the quality of the measurement.

Another improvement of the system is needed to distinguish the two possible velocity directions perpendicular to the parallel planes and to measure zero

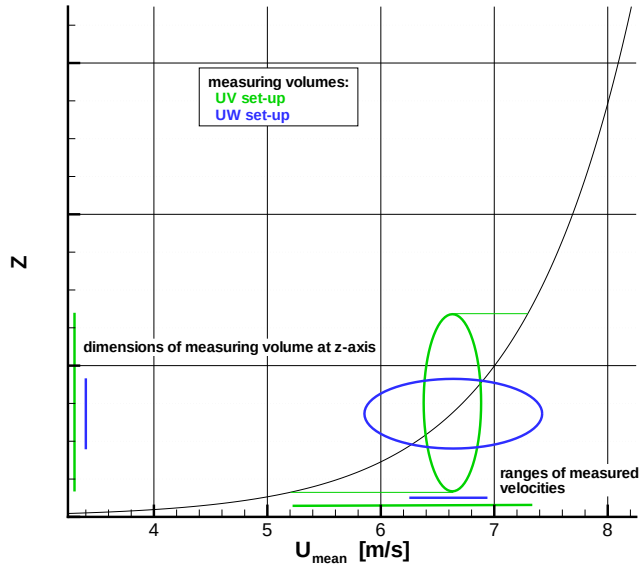

Figure 4.10: The influence of the LDA measuring volume orientation (depicted by ovals) on the measured values. Not in the scale.

velocity with sufficient accuracy. This is ensured by the Brag cell, which shifts the frequency of one laser beam by a small amount (40 MHz in the usual LDA systems). This shift is negligible in comparison with the used light beams, which had wavelengths 514 nm (blue) for longitudinal and 488 nm (green) for lateral components, respectively, and these wavelengths correspond to the frequency of about 10^{14} Hz, which is 7 orders higher than the shift. The fringe pattern due to this shift is not stationary but moves continuously through the measurement volume in a direction perpendicular to the planes with the shifting frequency and therefore even the static particles return the fringe signals. On the other hand, any particle with the respective velocity component exactly equal to the fringe pattern's velocity is invisible to the system and the fringe pattern's velocity constitutes a threshold velocity. Particle velocity directions can be determined uniquely in all those flows where all particle velocities stay strictly on one side of this threshold velocity (either smaller or larger).

4.4 Principle of Flame Ionisation Detectors

The flame ionisation detector (FID) is the industry standard method of measuring hydrocarbon concentration (Cambustion, 2006). The main component of the Slow Flame Ionisation Detector (SFID) and Fast Flame Ionisation Detector (FFID) is the combustion chamber where a flame is constantly maintained by the continuous insertion of fuel (hydrogen) and air. Concentration samples of hydrocarbons (ethane in our case) are sucked into the chamber through a thin needle (FFID) (Fig. 4.6) or tube (SFID) from the sampling location. The

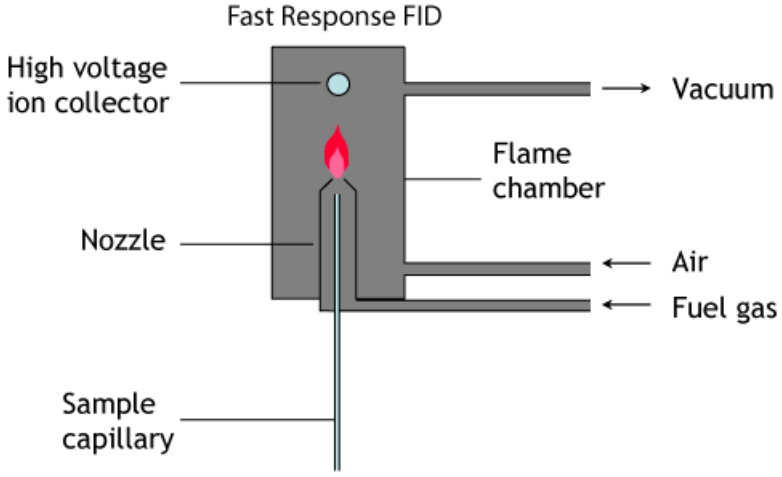

Figure 4.11: Scheme of the burning chamber of Fast Flame Ionisation Detector. Adapted from Cambustion (2006).

sample gas is introduced into a hydrogen flame inside the FID. Any hydrocarbons in the sample will produce ions when they are burnt. Ions are detected using a metal collector and their number, i.e. an electrical current across this collector, is proportional to the rate of ionisation which in turn depends upon the concentration of hydrocarbons in the sample gas. A concentration value can be obtained by the use of an appropriate calibration curve.

The main physical difference between SFID and FFID is the insertion point of the sample into the combustion chamber. Within SFID the sample is mixed with the fuel before it gets into the combustion chamber and the chamber is situated outside the wind tunnel and therefore the passage of the sample is rather long and it is limitary mixed during transport in the tube. This set-up allows fluctuation response times in order of few seconds. Within FFID (Fig. 4.11) the sample and the fuel are brought together only at the location of the flame within the combustion chamber, no mixing occurs before the actual combustion, and the passage of the sample is very short by virtue of chamber construction (chamber can be placed inside the wind tunnel). This modification allows fluctuation response times of about milliseconds. A transformation of a FFID signal output to concentration values depends sensitively on the flow rate through the detector and the temperature within the combustion chamber. Ambient conditions influence all these parameters and they typically change during the day or with increasing time of system operation. Therefore careful and frequently repeated signal calibrations are necessary and they were done during the whole dispersion measurement campaign at least twice a day (typically three times: in the morning, at noon, and at the end of the measurements for that day).

4.5 Measurement Accuracy

The results, which will be presented in the chapters 6 and 7, have some uncertainties. An origin and magnitude of these uncertainties will be described below.

Accuracy of the Positioning

The model was built up in the scale 1:75 according to full scale coordinates given in Biltoft (2001). The maximum error in the model set-up was 1 mm.

The internal coordinates system of the 3-D traverse system and a connected measuring device (LDA or FFID) had to be linked with the model coordinate system. This procedure was successfully done for each instrumentation set-up with accuracy of 1 mm.

The whole model was placed on the turn table for easy change of the wind direction. The overall accuracy of the turn table, i.e. wind direction, setting was better than 0.5°.

Accuracy of the Flow Measurement

The LDA reference book (DANTEC Dynamics, 2006) says that the velocity estimation by LDA has accuracy of 0.05 m s^{-1}. The accuracy is even better (approximately 0.02 m s^{-1}) from our experience.

Accuracy of the Concentration Measurement

The accuracy of the Slow and Fast Flame Ionisation Detector measurements was varying day to day based on an actual devices set-up and adjustment. The first source of inaccuracy was calibration. Calibration was checked several times per day an the accuracy of it was always better than 3% for FFID and 1% for SFID. The detectable concentration minimum was between 1 and 2 ppm for both devices.

Accuracy of the Source Strength Measurement

The accuracy of the electronic mass flow controller Brooks® 5861S used for the source strength measurement is 1% of the full scale range. That means 1 l $hour^{-1}$ in the most cases (for the measurement range 2-100 l $hour^{-1}$) or 0.1 l $hour^{-1}$ (for the measurement range 0-10 l $hour^{-1}$).

Chapter 5

Modelled Boundary Layer Flow

During the three months of testing more than 100 different spires/roughness elements configurations were tested in the wind tunnel in order to properly model the wind flow conditions expected to be present at the full scale. Since the MUST field data were insufficient to completely describe the approach flow (discussed in the section 3.4), it was decided to set up the boundary layer flow primarily based on the information of the surface roughness type around the field site given in the guidelines (e.g. ESDU, 1985; Snyder, 1981; VDI Guideline 3783/12, 2000). For the flat open terrain roughness present at the MUST field experiment, a slightly rough boundary layer flow needed to be modelled. The wind tunnel used enabled only a neutrally stratified flow to be modelled and therefore the reference values were chosen for a neutrally stratified ABL although the MUST field data were obtained under slightly stable conditions - the Pasquill's turbulence types E and F (see section 3.4).

5.1 Generation of the Boundary Layer

Generating a turbulent boundary layer over roughness elements is principle of the atmospheric boundary layer wind-tunnel modelling. Because of the limited length of the approach flow section, additional features like roughness elements and turbulence generators (see appendix A and Fig. 4.2) are required. When generating a turbulent boundary layer, the requirement of a minimum roughness Reynolds number Re_* must be considered.

$$Re_* = \frac{u_* \, z_0}{\nu} = \frac{0.35\,\mathrm{m\,s^{-1}} \cdot 0.22\,\mathrm{mm}}{1.5 \cdot 10^{-5}\,\mathrm{m^2\,s^{-1}}} \doteq 5.9 \tag{5.1}$$

where the friction velocity, u_*, and roughness length, z_0, were determined from the logarithmic vertical profile of the mean wind speed in the wind tunnel (equation 2.29 and section 5.3.1, see below). The roughness Reynolds number Re_* for our set-up is about 5.9 using these values. Sutton (1949) suggested a critical value of 2.5, which is commonly accepted. Another value, $Re_* = 5$, was proposed by Plate (1981), but Snyder and Castro (1998) showed that $Re_* = 1$

is large enough to ensure aerodynamically rough flow. Only minor effects were observed by Snyder (2001) on most variables when $0.5 < Re_* < 1.0$, but below $Re_* = 0.5$, strong effects of laminar flow were evident. The value reached in the wind tunnel satisfied even the strongest criterion given by Plate (1981).

The blockage of the wind-tunnel test section by the model itself and by the instrumentation may affect the flow on the model. A maximum non-affecting value of the blockage coefficient (the ratio of the projected area of the obstacles along the main wind direction to the cross-sectional area of the wind-tunnel test section) of 5% is recommended (VDI Guideline 3783/12, 2000) for the enclosed test sections. Using the cross-sectional area of the WOTAN wind-tunnel test section 12 m^2 and the dimensions of the containers (section 4.2), the blockage coefficient for the MUST wind-tunnel experiment was 0.46% for the 0° and 180° approach wind direction (see Fig. 3.3), 0.11% for the 90° and −90° approach wind direction, and the maximum blockage coefficient approaches 0.97% for the diagonal (around −45° and 45°) wind orientations, where the container array acts like a solid wall with the container height and the array diagonal width. The traverse system (Fig. 4.2) with all its components has a blockage coefficient of about 2%. The sum of the blockages caused by the model and the traverse system is much smaller than the given threshold of 5% and therefore the flow on the model should not be influenced by the finite dimensions of the test section.

The influence of the blockage effect of the model and the traverse system can be also checked by measuring the static pressure gradient along the wind-tunnel test section. The pressure gradient can be controlled by varying the wind-tunnel ceiling with both the model and the traverse system inside. The criterion for a negligible axial static pressure gradient is given in VDI Guideline 3783/12 (2000):

$$|p^*| = \left| \frac{\frac{\partial p}{\partial x} \cdot \delta}{\frac{\varrho}{2} \cdot u_\delta^2} \right| \leq 0.05 \tag{5.2}$$

where p^* is the dimensionless static pressure gradient, $\delta = 0.5$ m is the height of the simulated boundary layer and $u_\delta = 6$ m s^{-1} is the flow velocity at the top of the simulated boundary layer, i.e. the free stream velocity, and $\varrho = 1.28$ kg m^3 is the air density. Values measured on the walls of the wind tunnel are shown in Fig. 5.1. All measured values lie within an area enclosed by the red lines, where p^* can be assume to be sufficiently small according to criterion 5.2. The last point ($x_{\mathrm{MS}} = 1.5$ m) does not fit with the rest of the measurement due to presence of the traverse in this position. The measurements were always taken approximately 0.5 m in front of the traverse at which point no interference of the flow by the traverse has been observed.

The zero static pressure gradient along the wind-tunnel test section is required for the boundary layer equilibrium. This equilibrium is pronounced by the constant Reynolds shear stress layer (Raupach et al., 1991). If the boundary layer is not in an equilibrium stage, a constant Reynolds stress profile in the Inertial Sublayer is impossible to achieve.

Another boundary layer quality indicator is the lateral homogeneity of measured quantities. The reason for a nonhomogeneous lateral flow inside the wind

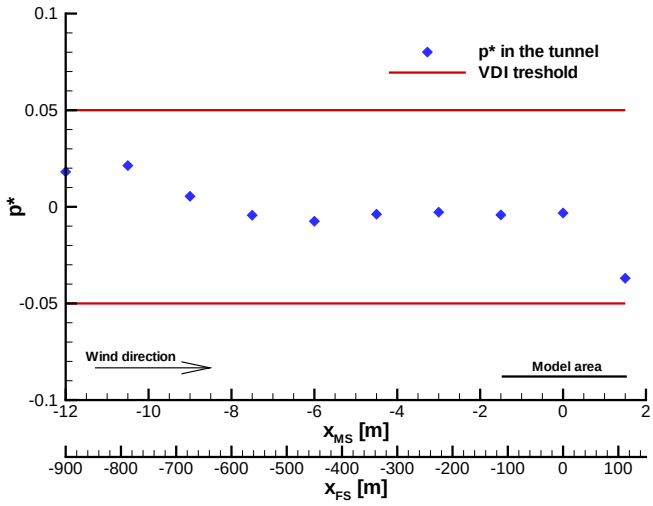

Figure 5.1: Layout of the dimensionless pressure gradients $p*$ (blue dots) along the wind tunnel. The red lines show the recommended maximum (equation 5.2, VDI Guideline 3783/12, 2000), coordinate $x = 0$ shows centre of the model.

tunnel is its placement inside an asymmetric and a relatively small (in comparison with the wind tunnel) hall. Consequently, there are pressure and flow velocity distribution inhomogeneities at the intake section, which can infiltrate through the wind tunnel itself. The position of each of the spires were therefore adjusted very carefully and the final irregular set-up (see appendix A) eliminated the asymmetry of the hall thus achieves ac laterally homogeneous flow within the wind-tunnel test section.

Lateral homogeneity was checked for properties such as mean wind speed, intensity of turbulence, spectral characteristics, etc. at all three wind-vector components. A sufficient lateral homogeneity was found in all cases and therefore only some examples of measured lateral profiles are shown in Fig. 5.2 and 5.3.

The lateral profiles were measured at three different horizontal levels: at 50, 100 and 200 mm in model scale, which translates to 3.75, 7.5 and 15 m in the full scale, or at $1.5H$, $3H$ and $6H$ in the dimensionless coordinates, respectively. The profiles were situated at the beginning of the test section (in front of the turn-table with the model, where x_{MS} = -1920 mm, or x_{FS} = -144 m). A perfect lateral homogeneity was not observed in any case, however, the relative variations across the model area were $\pm 5\%$ for the mean wind speed components, Fig. 5.2, and $\pm 8\%$ for the higher-order statistics, like the intensity of turbulence and the momentum flux $\overline{u'w'}$, Fig. 5.3. The values obtained at the same point by two different LDA set-ups were in very good agreement, which shows a precise adjustment of the system (see discussion in section 4.3). The variation in magnitudes are comparable with the total measurement uncertainties (see section 5.4).

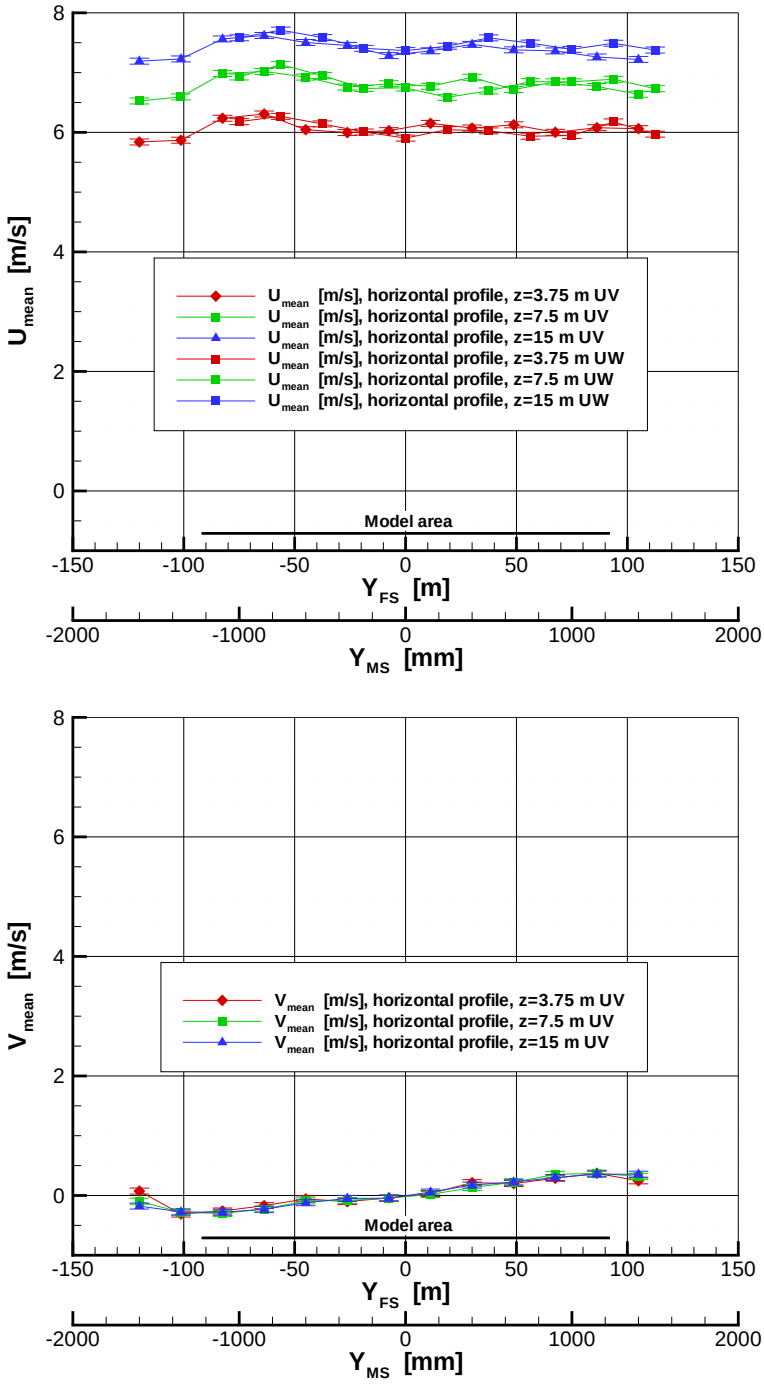

Figure 5.2: The mean wind speed components $\overline{u}$ (upper chart) and $\overline{v}$ (lower chart) measured at three different levels (indicated by the different colours) and with two different LDA set-ups (data obtained during the UV and UW measurements are indicated by the deltas and squares, respectively). The x-axis shows the whole width of the wind tunnel and the position of the model is highlighted.

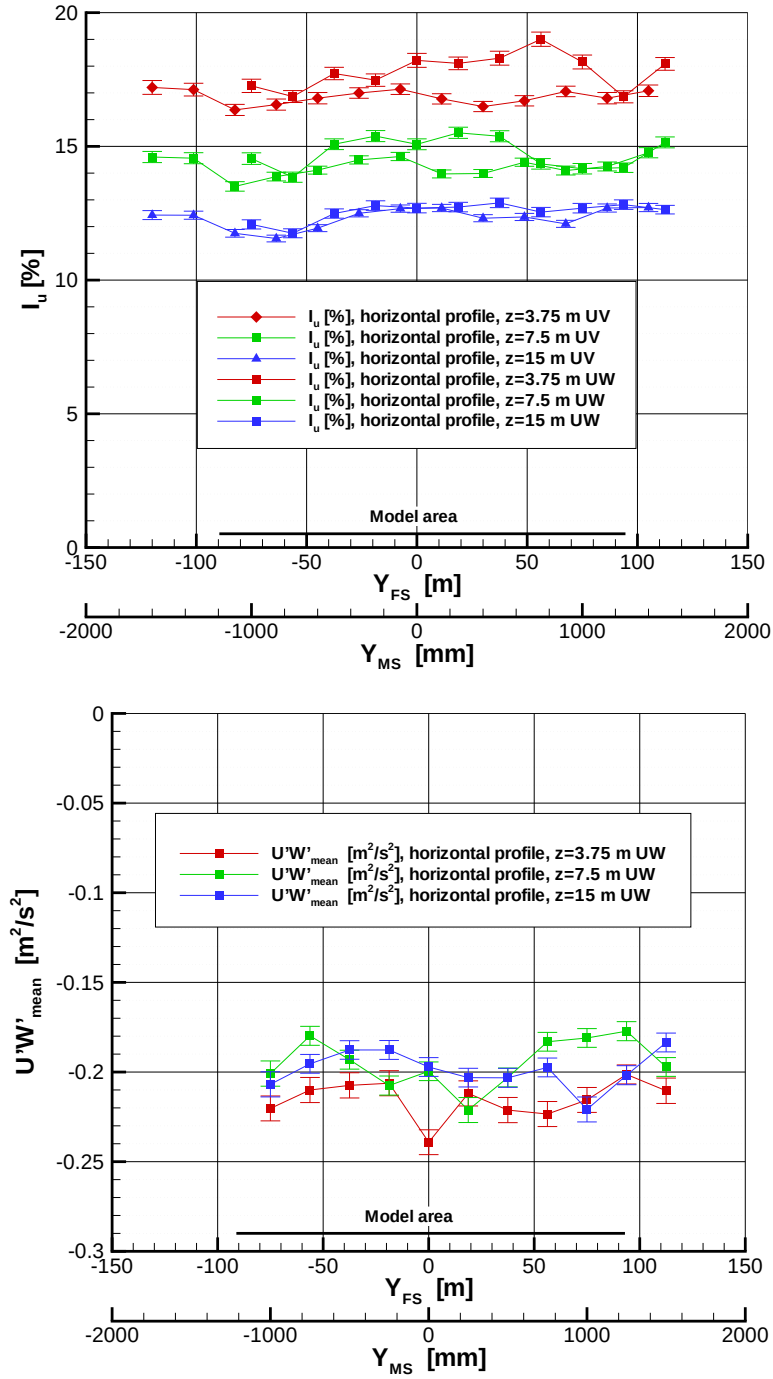

Figure 5.3: The intensity of turbulence for u-wind component (left) and the momentum flux $\overline{u'w'}$ measured at three different levels (indicated by different colours) and with two different LDA set-ups (data obtained during UV and UW measurements are indicated by deltas and squares, respectively). The x-axis shows the whole width of the wind tunnel and the position of the model is highlighted.

5.2 Reference Wind Speed and Reynolds Number Independence

The importance of the reference wind speed measurement was mentioned in section 4.1. The optimal configuration is a measurement of the reference wind speed at the same point as in the field campaign. The wind speed time series from the S tower (see the MUST field set-up description in chapter 4) were the most complete approach flow measurements of the MUST field campaign. Hence this measurement was chosen to be the reference wind speed U_{ref} used in the dimensionless values. Unfortunately, the Prandtl tube could not be place directly at the position of the S tower for two reasons: firstly, the position of the S tower was too close to the array, that the presence of the Prandtl tube and its mounting would heavily disturb the flow; secondly, if the probe would have been mounted at this place, it would turn with the model when changing the wind direction, which could cause measurement errors, since the Prandtl tube should be parallel to the flow at all times. If the approach flow direction has an oblique angle to the Prandtl tube axis the velocity magnitude is not measured correctly. Therefore the Prandtl tube was mounted at the mouth of the wind tunnel (Fig. 4.2, described in section 4.1), and the measurement of the MUST field reference wind speed directly at the position of the S tower were conducted by LDA. The relationship between the values measured by the Prandtl tube at the wind-tunnel entrance and by LDA are shown in Fig. 5.4.

The LDA measurements were conducted at all three levels (at 4, 8, and 16 m AGL depicted in Fig. 5.4 by green, red, and blue colours, respectively) and also with two different set-ups of the LDA system (UV measurement and UW measurement depicted by the diamonds and triangles, respectively). The values obtained were plotted against each other in order to determine a relation between the wind tunnel and field reference velocity measurements.

When recording an instantaneous wind speed time series the methods of the probability theory and statistics can by used. Fig. 5.4 shows various central moments of the instantaneous wind speed measured by LDA as a function of the reference mean wind speed measured by the Prandtl tube at the wind-tunnel entrance (denoted $U_{\text{Prandtl tube}}$).

The zero central moment is the mean value and is shown in upper left graph in Fig. 5.4. It is evident that all corresponding points lie in one line for the whole range of measured values and the conversion factors can be estimated by the least square method as follow:

$$U_{\text{S Tower 16 m}} = 0.697 \cdot U_{\text{Prandtl tube}} \tag{5.3}$$

$$U_{\text{S Tower 8 m}} = 0.634 \cdot U_{\text{Prandtl tube}} \tag{5.4}$$

$$U_{\text{S Tower 4 m}} = 0.552 \cdot U_{\text{Prandtl tube}} \tag{5.5}$$

where $U_{\text{S Tower 16 m}}$ is the reference wind speed measured by LDA at the 16 m level of the S tower and the values measured at 8 and 4 m levels are denoted analogically.

The first central moment is zero by definition.

The second central moment is called the variance, and is usually denoted σ^2, where σ represents the standard deviation. The standard deviation is the most common measure of a statistical dispersion. It is a measure of the average distance of the data values from their mean and in fluid mechanics it is used for the turbulence intensity definition (equation 2.31). The upper right graph in Fig. 5.4 shows the turbulence intensity of the u wind component, again as a function of $U_{\text{Prandtl tube}}$. The intensity of the turbulence should be independent on the approach wind speed, i.e. constant, according to similarity theory (section 2.3). The intensity of the turbulence is dependent on the mean wind speed if $U_{\text{S Tower 8 m}}$ is less than approximately 2.5 m s^{-1}.

Skewness, the third standardised moment, is a measure of the asymmetry of the probability distribution function of a random variable. Roughly speaking, a distribution function has a positive skew (right-skewed) if the higher tail is longer and a negative skew (left-skewed) if the lower tail is longer.

$$\text{Skew} = \frac{\mu_3}{\sigma^3} \tag{5.6}$$

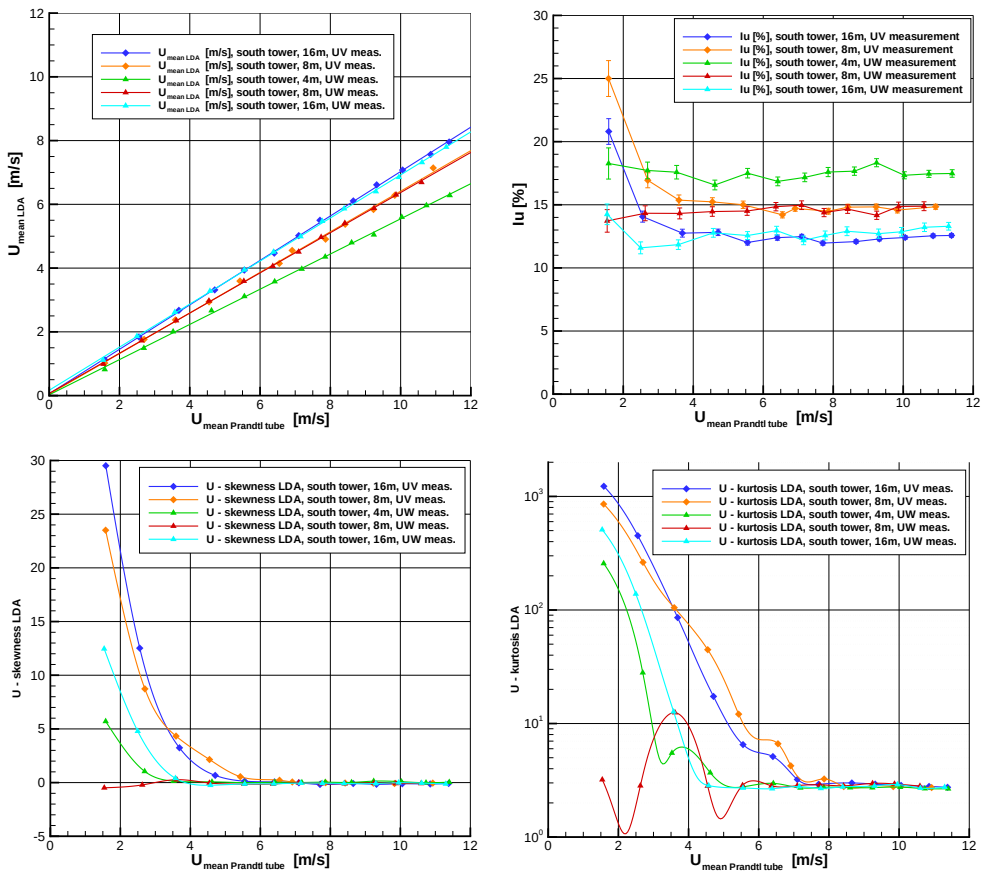

Figure 5.4: The flow properties measured by LDA at the south tower positions (at 4, 8, and 16 m AGL) as a function of the reference mean wind speed measured by Prandtl tube at the wind tunnel entrance.

where μ_3 is the third central moment. The skewness plotted against $U_{\text{Prandtl tube}}$ is shown in bottom left graph in Fig. 5.4. The skewness has a similar behaviour as the intensity of turbulence, but the constant value of Skew was reached with the higher reference wind speeds - about 3.5 m s^{-1}.

Kurtosis, sometimes called flatness, is the fourth standardised moment. A high kurtosis distribution has a sharper 'peak' and fatter 'tails', while a low kurtosis distribution has a more rounded peak with wider 'shoulders'.

$$\text{Kurt} = \frac{\mu_4}{\sigma^4} \tag{5.7}$$

where μ_4 is the fourth central moment. Kurt is shown in bottom right picture in Fig. 5.4 and again the constant value was reached only for the higher wind speeds, approximately from 4.5 m s^{-1}.

The 8 m level measurement at the south tower was chosen as the reference wind speed for the whole campaign, because of the best reliability (the 4 m elevation can be affect by local surface inhomogeneities, at the 16 m level the MUST field time series was not complete). From this point forward the reference speed will be taken as the 8 m south tower measurement obtained as $0.634 \cdot U_{\text{Prandtl tube}}$. Also the Building Reynolds number and dimensionless values will be calculated using this reference wind speed value.

The absolute values of constant Skew = 0 ± 0.1 and Kurt = 2.8 ± 0.1 measured in the approach boundary layer are very close to values which have a Gaussian distribution (Skew = 0, Kurt = 3). Fig. 5.4 proves that the overall set-up of the boundary layer development section shows sensitivity of the higher order central moments on the approach wind speed, i.e. on the Reynolds number. The later convergence of the higher order moments was not caused by the averaging time, i.e. the number of samples (ensured by the data processing tests). Big differences were also observed between the values obtained from the different LDA set-ups (UV and UW orientation of the probe), which can be caused by the different orientation of the measuring volume and thus consequently by the different sampling conditions (discussed in sections 4.3 and 5.4).

It is likely that the higher order central moments are very important for the passive tracer dispersion. Therefore it should be modelled properly. Consequently, all measurements were conducted with the minimum reference wind speed $U_{\text{Prandtl tube}} = 7$ m s^{-1}, i.e. $U_{ref} = 4.5$ m s^{-1}, $Re_B = 10000$, where independence of all four central moments on the wind speed was found.

5.3 Boundary Layer Flow Properties

Boundary layer flow properties as given below precisely describe the approach flow characteristics, which are important for possible repetitions (by the means of physical or mathematical modelling) of the experiments. The spatial coordinates will be given as full scale measures and all quantities have been re-scaled to $U_{ref} = U_{\text{S Tower 8 m}} = 5$ m s^{-1}.

The following section will be of similar structure to that of the section 2.4 and the general description of the Surface Layer properties given there will be

compared with the characteristics obtained on the wind tunnel model of the MUST experiment.

5.3.1 Mean Wind Vertical Profile

The mean wind vertical profile was measured repeatedly at the model inflow edge near to the wind tunnel centreline (at x_{FS} = -144 m and y_{FS} = 2.25 m) and far in front of the S tower. Four profiles were averaged and the resulting profiles are shown in Fig. 5.5, where the values from z_{FS} = 1.9 m to 12.5 m (red filled diamonds) have been chosen for the logarithmic profile fit determined by the least square method. This range has been chosen because of its best logarithmic fit (the upper points do not lie on the line - upper graph in Fig. 5.5) and the $5H$-thick (12.5 m in full scale) layer with a proper logarithmic vertical profile is sufficiently deep to properly model dispersion within the canopy (VDI Guideline 3783/12, 2000). The parameters obtained from the logarithmic profile are shown in the table below, where the denotation $u_{*\,\mathrm{log}}$ indicates a value obtained from the logarithmic fit of the mean wind vertical profile.

parameter	in the model scale	in the full scale
z_0	0.22 mm	0.0165 m
d_0	0 mm	0 m
$u_{*\,\mathrm{log}}$	0.33 m s^{-1}	0.33 m s^{-1}

The field data from all three levels on the south tower are also shown in Fig. 5.5 by the blue squares, however, they do not match with the wind tunnel data very well. This disagreement can not be caused by a too short averaging time in full scale, since the presented data are average values for the chosen days. However, this long averaging could mixed together different Pasquill's stability classes (see section 3.4), which are connected with different vertical profiles of the mean wind speed. This can result in an inaccurate vertical profile.

The power law exponent $\alpha = 0.16$ has been also identified from the upper part of the vertical profile in this case, which according to Counihan (1972) corresponds very well with the roughness length obtained.

5.3.2 Intensity of Turbulence

The vertical profile of the intensities of turbulence for all three wind components are shown in Fig. 5.6. They were measured at the same position as the vertical profile of the mean wind. The profiles obtained are compared with the recommended values (the red lines in Fig. 5.6 determine values which correspond with the different types of the surface roughness defined in section 2.4, ESDU, 1985) and they are also compared with the MUST field data measured on the south tower (orange triangles). The field values are missing for I_w, since the south tower provided only the 2-D flow velocity measurement in the horizontal plane. The turbulence intensities of the wind tunnel boundary layer lie between the 'slightly rough' and 'moderately rough' surface types, which is in good agreement with the parameters of the mean wind profile (z_0 and d_0) and the field topography of the site (low bushes).

The turbulent velocities scaled by the friction velocity $u_{*\,\log}$ are shown in the bottom right graph of Fig. 5.6. The $\sigma_u/u_{*\,\log}$ vertical profile shows a value 2.4 at the lowest elevations and decreases slowly with the height. Stull

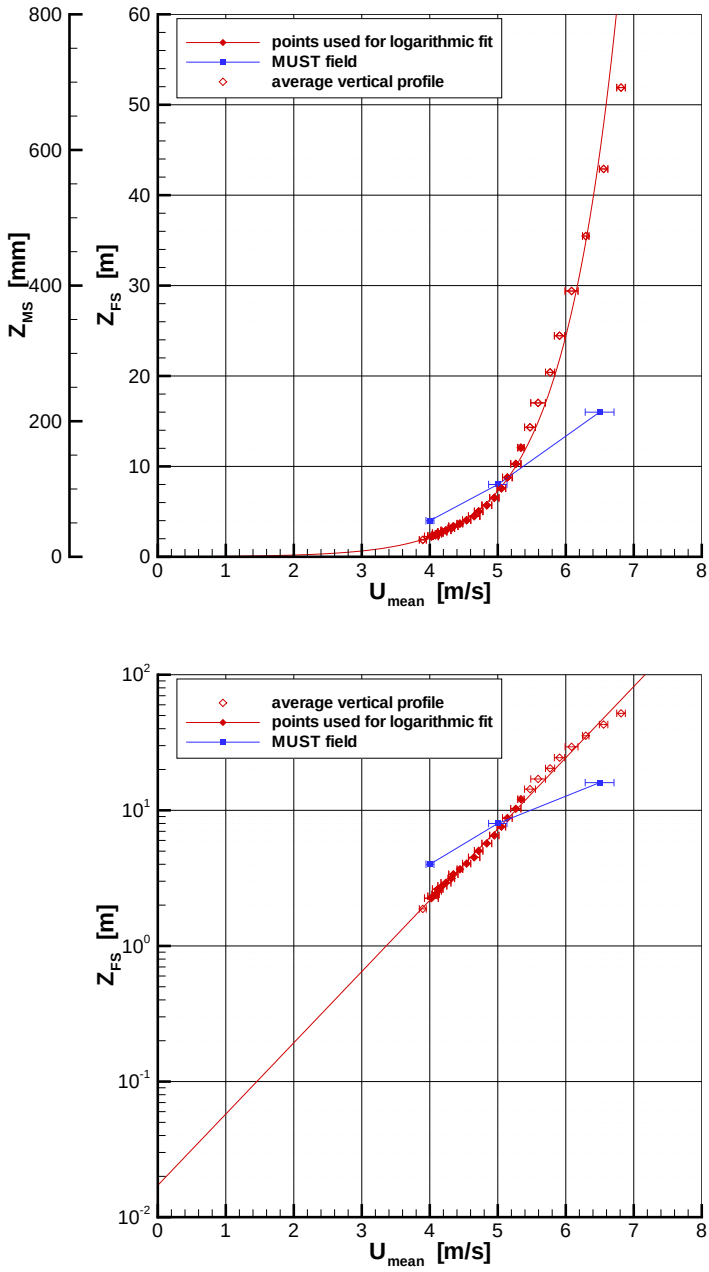

Figure 5.5: The average mean wind speed as a function of the vertical coordinates plotted on the linear scale (upper picture) and semi-logarithmic scale (bottom picture). The values used for the logarithmic fit are red filled, values measured at the field (on the S tower) are blue. All values are re-scaled to $U_{ref} = 5$ m s^{-1}.

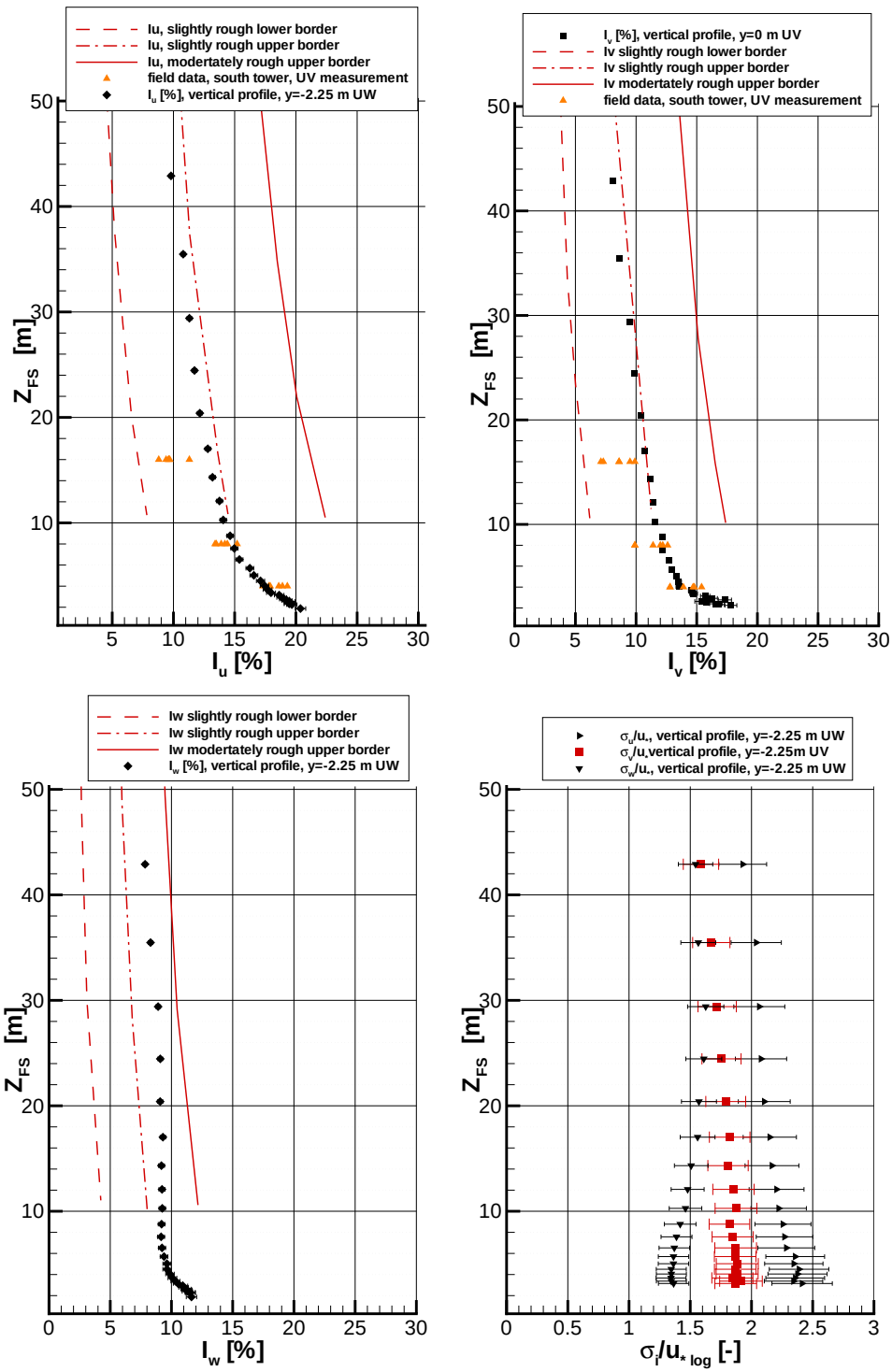

Figure 5.6: Intensities of turbulence I_u, I_v, I_w, and turbulent velocities σ_i scaled by $u_{*\,\mathrm{log}}$ as a function of vertical coordinates. The tabled regions for I_i corresponded to different surface roughness types (ESDU, 1985) are depicted by the red lines, the field data by the orange triangles.

(1988) proposed values between 2 and 3, however, in wind tunnels it is often closer to 2 perhaps because the flow is more channelled and less subject to inhomogeneities of surface friction than atmospheric flows (Briggs et al., 2001). Raupach et al. (1991) found an even smaller value 2.1 ± 0.2. For the lowest elevation the average value can be estimated as 1.9 for $\sigma_v/u_{*\,\mathrm{log}}$, which is higher than the value 1.4 ± 0.1 proposed by Raupach et al. (1991). Stull (1988) gave a range of 1 to 1.4 as a reference for the $\sigma_w/u_{*\,\mathrm{log}}$ values. The MUST wind tunnel value 1.4 is in the upper end of this proposed range. An increase of the values in the lowest elevations (up to 20 m in the full scale) was also observed by Raupach et al. (1991), even though he showed values of 1.1 ± 0.1. The higher values of turbulence (described by the turbulence intensity etc.) in w-component compared to the atmosphere are often observed in wind tunnels and can be connected with an artificial creation of the turbulence by sharp edges features like the spires used in this set-up and the roughness elements (see appendix A).

The ratio between each standard deviation $\sigma_u : \sigma_v : \sigma_w = 1 : 0.79 : 0.58$ is in good agreement (except the last one for σ_w) with the values given by ESDU (1985) in equation 2.33, which are 1 : 0.75 : 0.5. The greater uncertainty, i.e. error bars, of the $\sigma_i/u_{*\,\mathrm{log}}$ profiles is mostly caused by the uncertainty of the $u_{*\,\mathrm{log}}$ value, and will be discussed later in this section.

5.3.3 Reynolds Stress

The momentum flux $\overline{u'w'}$, which is connected with the Reynolds stress τ_{uw} via the definition 2.15, is shown in Fig. 5.7, where the black horizontal line depicts the container height. A constant Reynolds stress, i.e. the momentum flux when neglecting density changes, is characteristic for the Inertial Sublayer. This constant value can be used for the friction velocity, $u_{*\,\mathrm{flux}}$, defined by $-\overline{u'w'} = u^2_{*\,\mathrm{flux}}$. Another way to obtain u_* is from the logarithmic fit of the mean wind profile (see section 5.3.1), where $u_{*\,\mathrm{log}} = 0.33 \pm 0.02$ m s^{-1} was estimated from the logarithmic fit of the mean wind profile. It corresponds to $-\overline{u'w'} = 0.11 \pm 0.01$ m^2 s^{-2}, which is depicted in Fig. 5.7 by the red line. The momentum flux profile appears to be constant up to $10H$ and also in good agreement with $u_{*\,\mathrm{log}}$ (red line).

The friction velocity estimated from the vertical profile of the vertical momentum transport is $u_{*\,\mathrm{flux}} = 0.35 \pm 0.02$. This value agrees with $u_{*\,\mathrm{log}}$ in the range of uncertainty. However, the friction velocity is an important scaling parameter and a proper estimation of it is crucial. For example, profiles in the lower right chart in Fig. 5.6 would be shifted to the smaller values of factor 0.06 when using $u_{*\,\mathrm{flux}}$ instead of $u_{*\,\mathrm{log}}$.

5.3.4 Wind Direction Fluctuations

Another parameter to be checked is a probability distribution of the lateral deviations of the measured wind vector from the mean wind direction shown in Fig. 5.8, where the abscissa gives the lateral deviation from the mean wind direction in degrees and the ordinate measures the probability distribution of

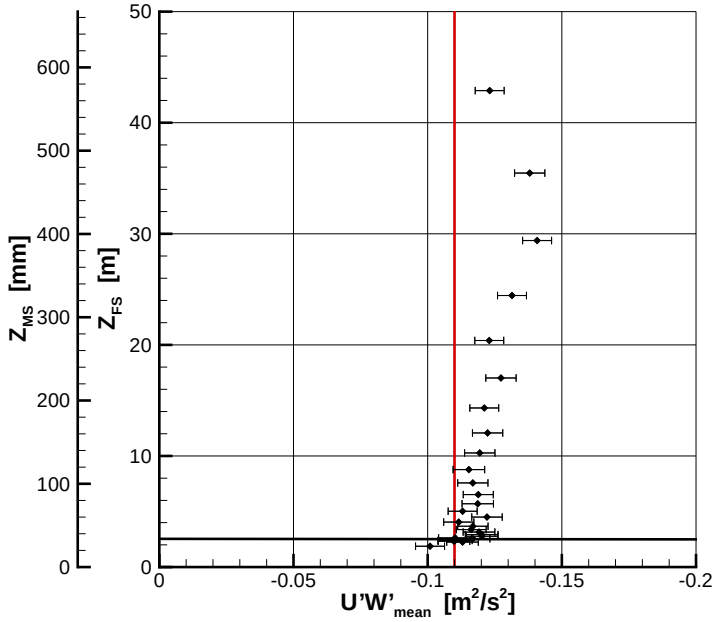

Figure 5.7: Vertical profile of the momentum flux. The black horizontal line is showing the container height. The red vertical line shows $\overline{u'w'}$ = -0.11 m^2 s^{-2}, which corresponds to u_* = 0.33 m s^{-1} obtained from the logarithmic fit of the vertical profile of the mean wind.

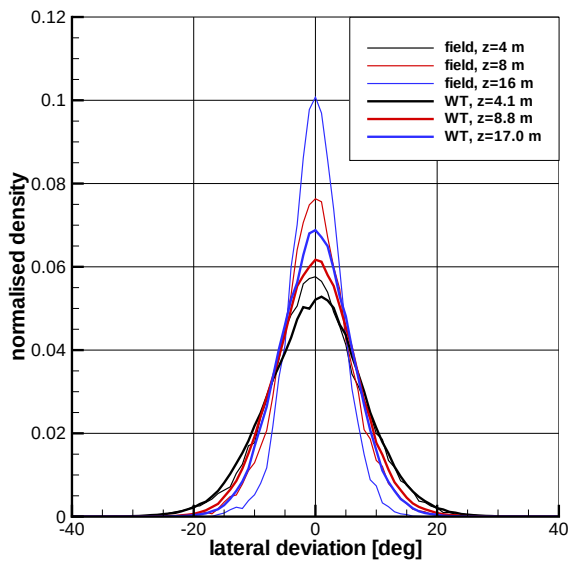

Figure 5.8: Probability distribution of the lateral deviations of measured wind vector from the mean wind direction at three different heights. Field data are shown by normal line, wind-tunnel data by bold line.

the deviations. The field data (obtained from the south tower measurement and depicted by the normal lines in Fig. 5.8) are compared with the wind tunnel results (bold lines) at three different heights (4, 8, and 16 m AGL). The wind tunnel results show more fluctuations ('wider curves') at all elevations. The time series, from which the fluctuation statistics were derived, had the same temporal length (approximately half an hour at full scale) for both the wind tunnel and field data. The lateral fluctuation is closely connected with the integral length scale and therefore smaller field lateral fluctuations are in a good agreement with the smaller field values of L_{ux} (see below, Fig. 5.9).

5.3.5 Spectral Characteristics

The integral length scales L_{ux} have been calculated from the autocorrelation functions (equations 2.34–2.36) and compared to the MUST field data (processed in the same way), and to the reference from Counihan (1972) in Fig. 5.9. The reference data labelled as 'roughness class 1 and 2' were obtained above open flat terrain - similar to the MUST surroundings and therefore these values should be primarily the reference in our case. The 'roughness class 3 and 4' corresponds to more rough cases like suburban and urban areas. The wind tunnel data shows a big scatter and smaller values than the reference, nevertheless, the field data appears to be even smaller with the same scatter magnitude. The reason for the significantly smaller values in the field measurement could be the slightly stable stratification of ABL (discussed in section 3.4) which has reduced the level of turbulence and therefore has changed the spectral characteristics. The reason for too small L_{ux} in the wind tunnel is different: the scale 1:75 used and the less rough ABL type, where larger vortexes play an important role, maybe to big for the WOTAN wind tunnel. The optimal L_{ux}, which should represent the dimension of the energy containing eddies, for an open terrain are more than 100 m (Counihan, 1972) that means about 1.5 m at the model scale. The wind tunnel cross-sectional is 4 m and could therefore not fully model vortices up to several metres. As a consequence the energy cascade ends sooner and the biggest vortices are not modelled.

Further wind speed time series characteristics are the Fourier spectra of the autocorrelation functions introduced in section 2.4.1, which represent the spectral distribution of the turbulent kinetic energy. The normalised turbulent kinetic energies S^*_{uu}, S^*_{vv}, and S^*_{ww} as a function of the normalised frequency n at two different heights are shown in Fig. 5.10. The measured spectra of S^*_{uu} and S^*_{vv} in the wind tunnel (green circles) coincide well with the theoretical functions developed by Simiu and Scanlan (1986) and Kaimal et al. (1972) (black lines), with a similar distribution being found in the field data (blue diamonds). As expected, the spectral distribution of the measured values is shifted towards higher frequencies for an increasing height above ground and a better agreement was achieved for the lower elevations.

The w velocity component bore more turbulent kinetic energy than it should according to the theoretical curves. This phenomenon is often found in wind tunnels and can be again connected with an artificial creation of the boundary layer flow by spires and roughness elements. The higher energy contain in the

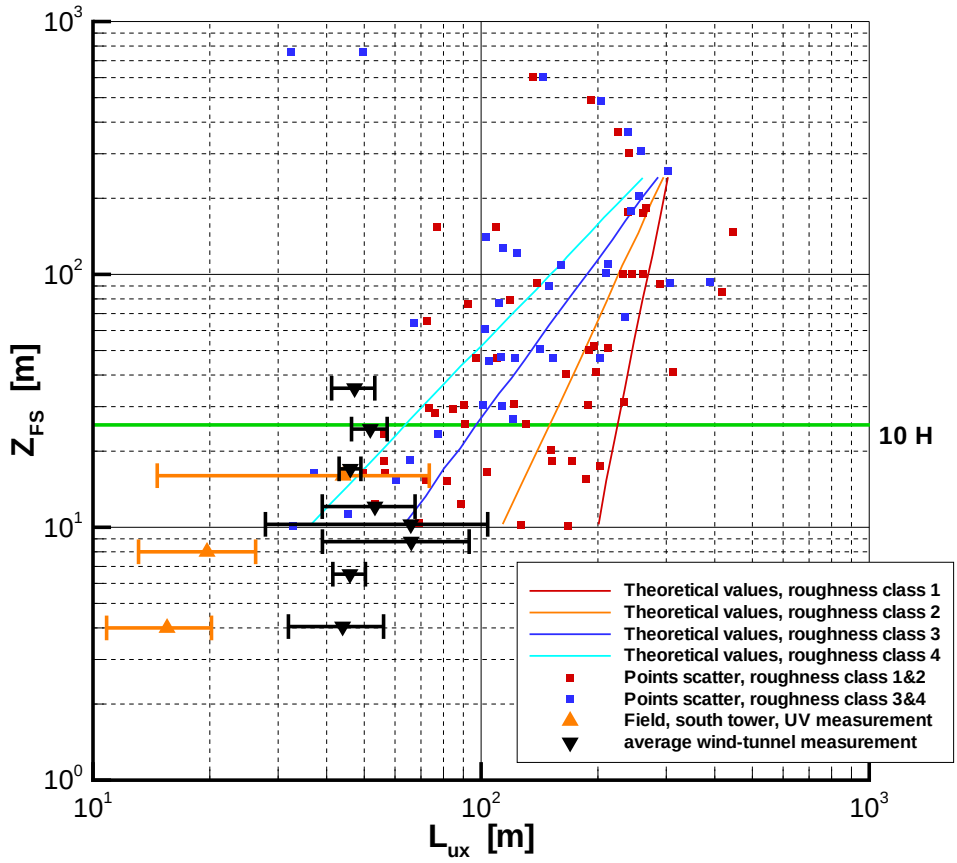

Figure 5.9: The wind tunnel integral length scale compared to the reference (blue and red points and lines, Counihan, 1972) and to the MUST field measurement (orange triangles).

w velocity component than proposed can indicate different shapes of vortices: a vortex dimension in z direction is bigger in the wind tunnel than it theoretically should be in the atmosphere.

The boundary layer above described was found after nearly 3 month of trialing different set-ups of spires and roughness elements in order to find the 'most suitable' boundary layer for our model. Unfortunately we have not found a 'perfect' boundary layer, only the one, which was described above. While a more suitable boundary layer could be found, our time in the wind tunnel was limited and therefore we had to use the set-up that was most suited to the MUST conditions. The wind tunnel boundary layer has some minor weaknesses (mainly connected with w velocity component and the increased turbulence in this component). The deviations of our boundary layer from a 'most suitable' state can effect the measurements, however, the effects are small compared to the measurement uncertainties and errors (see sections 4.5 and 5.4) and therefore this boundary layer has been accepted.

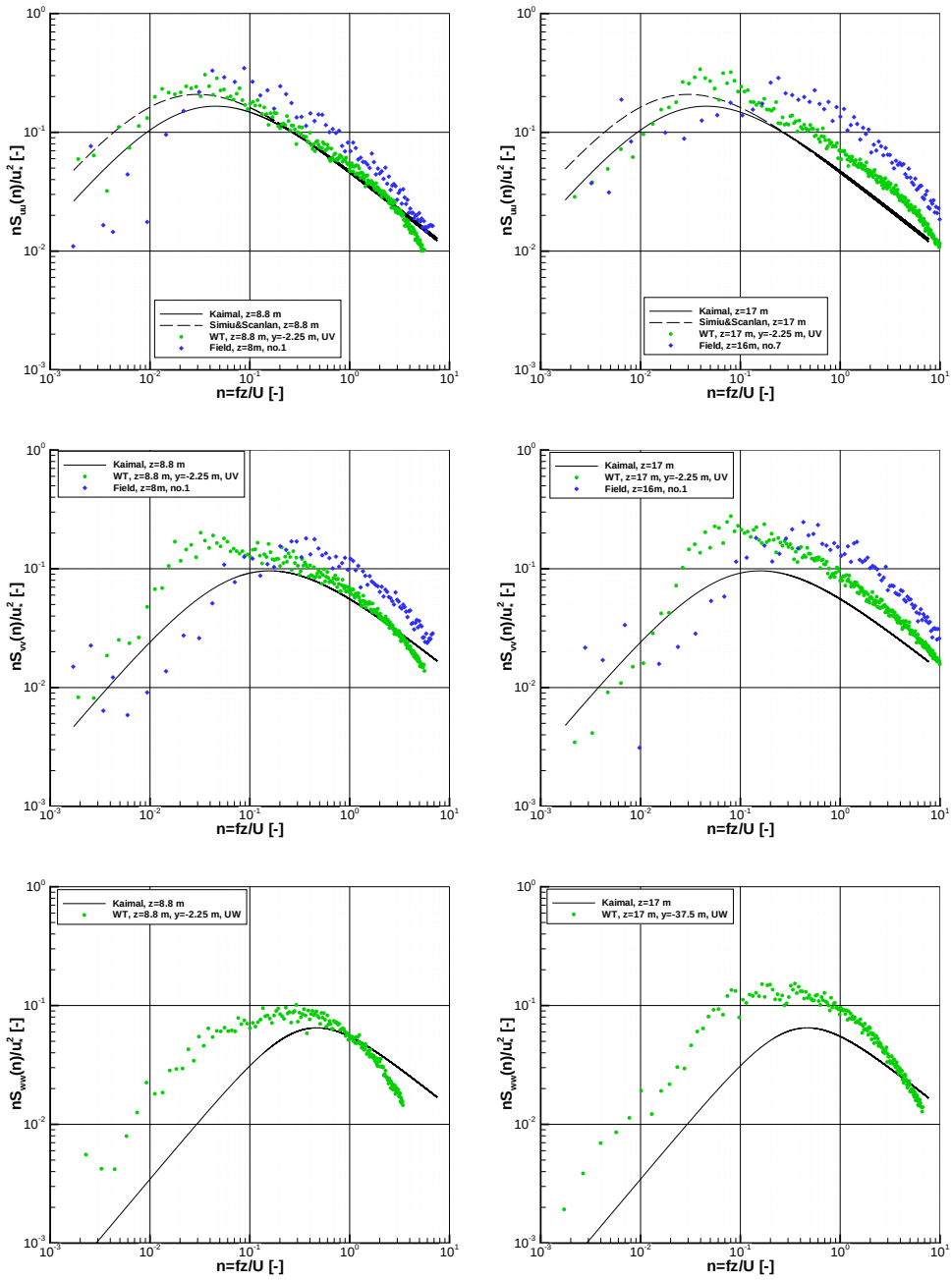

Figure 5.10: Smooth normalised spectral distribution of the turbulent kinetic energy of u- (the first row), v- (the second row), and w- (the third row) component of the wind vector at 8 (left column) and 17 (right column) m AGL.

5.4 Measurement Repeatability and Reliability

The most important advantage of wind tunnel modelling in comparison with field campaigns is the ability to closely control initial and boundary conditions (it is hard and very expensive to control weather). Since the full control of the flow were proposed in the case of the wind tunnel modelling, the same results should be obtained independently on the date of the measurements, however, some measurement uncertainties were unavoidable. The magnitude of these uncertainties will be shown below. Sources of measurement inaccuracy could be: variations of the wind tunnel operating speed during 180 s acquisition periods; built-in inaccuracies of the LDA system; and the statistical scatter.

The LDA system used was only 2-D and therefore the set-up changes during the flow measurements were unavoidable to measure all three velocity components.LDA was operated in two modes: the longitudinal wind velocity component u was measured together with the horizontal velocity component v or the vertical velocity component w in the first case (UV mode) and in the second case (UW mode), respectively. A careful adjustment of the LDA probe always is necessary when the mode is set up. The acquisition time per measured point was set to either 180 s or a statistical stop criteria provided by the BSA Flow Software (DANTEC Dynamics, 2006), which allows us to define a confidence limit for the measured characteristics like U or $\overline{u'w'}$, the measurement being stopped when this confidence is reached (1% stop criterium for $\overline{u'w'}$ was typically used). The sample size per location was almost always more than 50000 samples and the acquisition frequencies were roughly about 500 Hz with exceptional regions close to the ground where lack of the seeding particles caused a decrease in data rate to approximately 100 Hz.

Some profiles where measured repeatedly using both set-ups. The mean wind speed is compared in Fig. 5.11, where repetitive measurements, at one location, were obtained using the UW set-up (individual measurements are depicted by the black triangles, the average profile by the blue diamonds, and the error bars show the standard deviation of the ensemble) is compared with the data obtained using the UV set-up (green squares). A very good agreement was reached at the higher altitudes (approximately above 8 m at the full scale) and the measurement uncertainty can be estimated to $\pm$ 0.15 m s^{-1}. The discrepancy in the lower altitudes, where the highest velocity gradient takes place, is closely connected with the orientation of the LDA measurement volume described in the section 4.3. The shear stress, i.e. the momentum flux, (Fig. 5.12) shows larger variability and the measurement uncertainty has been estimated to $\pm$ 0.009 m^2 s^{-2} which means $\pm$ 8%.

The measurements shown in Figures 5.11 and 5.12 were obtained during several days of measurement and the overall reproducibility was been found to be very good, however, the quality tended to decrease with the increasing order of the statistical moments. This quality decrease can be caused by the length of the time series, since for the same accuracy in the higher order moments as in the mean (zero central moment) a longer time is needed, which was not assured in our case (the time was always 180 s).

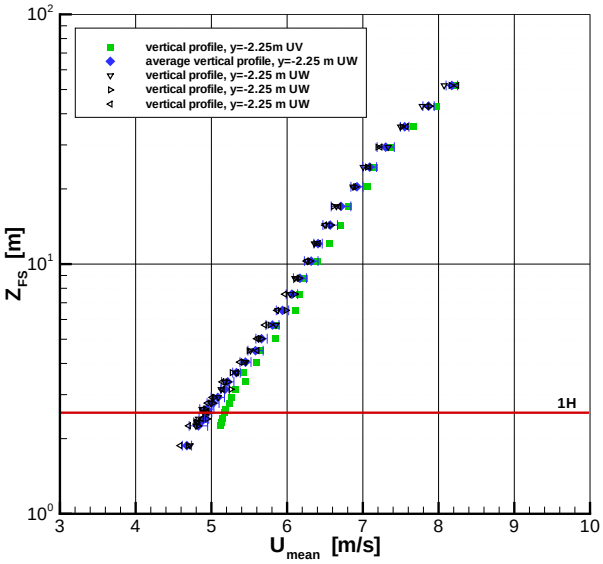

Figure 5.11: Comparison of the mean wind speed vertical profile measured at position x_{FS} = -144 m, y_{FS} = -2.25 m obtained using UW set-up and UV set-up of LDA. The error bars show the standard deviation of the ensemble. The red line depicts the container height.

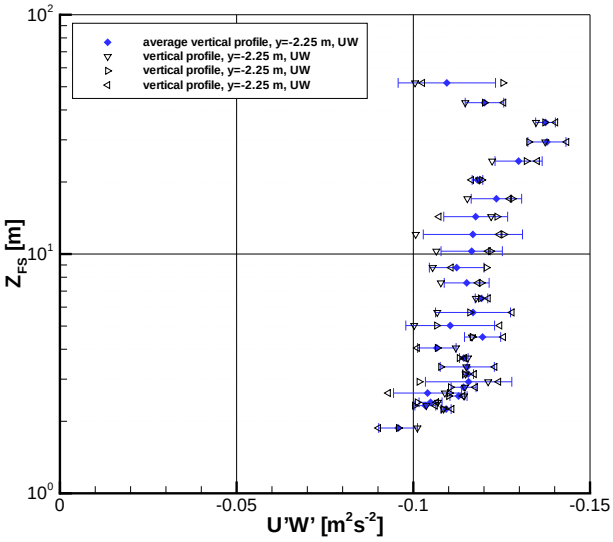

Figure 5.12: Repetitive measurement of the momentum flux vertical profile at position x_{FS} = -144 m, y_{FS} = -2.25 m. The error bars show the standard deviation of the ensemble.

Chapter 6

Flow Field

Laser Doppler Anemometry (sometimes called Laser Doppler Velocimetry), described in section 4.3, was used for the flow field measurements. The results are divided into two sections according to the measured wind components: section 6.1 describes u and v components measured in the different horizontal planes; section 6.2 describes vertical profiles of the u and w components as well as measurement taken in the horizontal plane with a high spatial resolution. Due to the validity of the Reynolds number independency theory for the reference wind speeds higher than 4.5 m s^{-1} ($Re_B \approx 10\,000$, see section 5.2), all measured values were measured with the $U_{ref} > 4.5$ m s^{-1} and scaled afterwards to the reference wind speed at $z_{\mathrm{FS}} = 8$ m at the S tower $U_{ref} = 5$ m s^{-1} to homogenise the results.

In the terms of the undisturbed approach flow the reference wind speed at 8 m $U_{ref} = 5$ m s^{-1} means that:

z_{FS} [-]	z_{FS} [m]	wind speed [m s^{-1}]	determined by
$2H$	5.08	4.8	direct measurement
H	2.54	4.2	direct measurement
$0.66H$	1.73	3.9	direct measurement
$0.5H$	1.27	3.6	derived from logarithmic profile
$0.33H$	0.9	3.3	derived from logarithmic profile

These values, which are derived from the direct measurement or the logarithmic law are given for the comparison of those, which were measured within the container array and presented below. The measurements at the two lowest elevations were not conducted, because these elevations belong to the Roughness Sublayer, where the mean velocity is influenced by the individual roughness elements. Therefore values characteristic for these points were extrapolate from the logarithmic law.

6.1 Flow in Horizontal Planes

To begin with, our focus lies with how the container array guide and channel the flow for different wind directions. Since the array set-up is symmetric, we considered only the approach wind direction from one quadrant (from 0°

to -90°) and we assume that the results potentially obtained from other wind directions would be very similar (the only reason why this might not occur is because of the slight irregularities in the array arrangement, see appendix B).

6.1.1 Flow Adaptation and Channelling

Since an adaptation of the approach flow to the container array was expected (many studies of the 'step change roughness' problem were published, e.g.: Kaimal and Finnigan, 1994; Antonia and Luxton, 1971; Cheng and Castro, 2002b), the first part of the measurements were conducted on a coarse grid, which consisted of about 300 measurement points and covered approximately one half of the container array. This set-up allowed an adaptation zone to be detected as well as a zone, where the flow adapts to the new underlying roughness. The measurement was done for the three wind directions (0°, -45°, -90°) and three heights ($2H$, H, and $0.5H$), where H is the container height.

0° Approach Flow

Figure 6.1 shows the layout of measurement points (approximately 300) in one of the three heights measured. Figures 6.2 and 6.3 show the velocity fields at the $2H$, H, and $0.5H$ levels, respectively. The influence of the array is clearly visible in all figures.

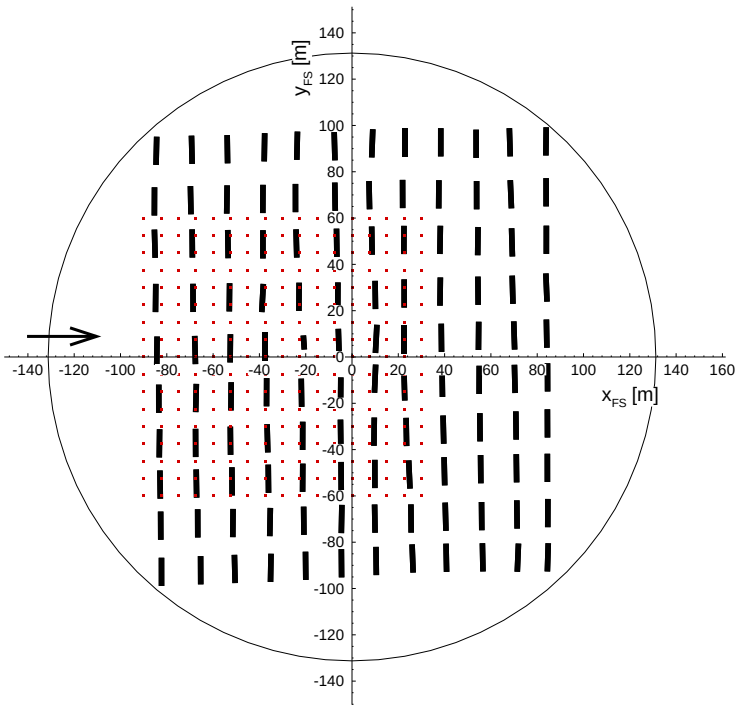

Figure 6.1: Layout of the measurement points, the arrow shows the 0° oriented approach flow.

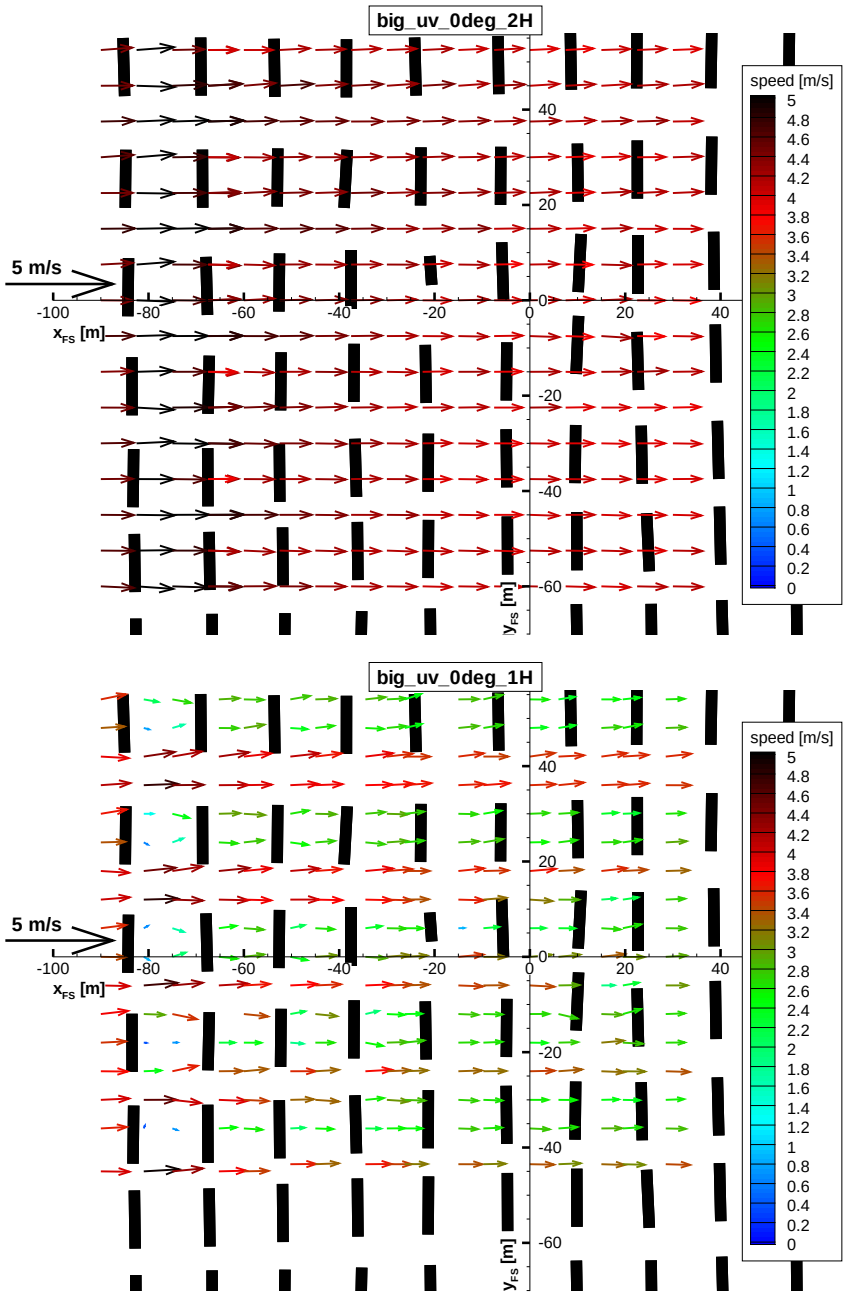

Figure 6.2: Measured wind field at the $2H$ level (upper chart) and at the H level (lower chart), 0° approach flow.

At the $2H$ level (upper chart of Fig. 6.2) the flow is accelerated (black arrows show a wind speed greater than 4.7 m s^{-1}, which was observed in the undisturbed flow) over the front of the container array because of the blockage effect of the array. The acceleration is even stronger and visible in the passages (or narrow street canyons) between containers deeper in the array (i.e. about the second container row). After approximately the third container row the

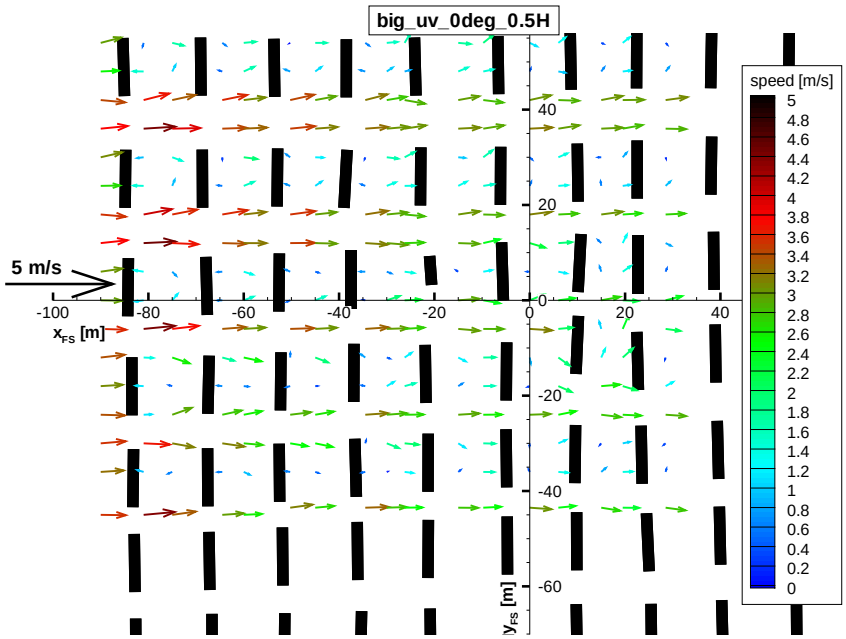

Figure 6.3: Measured wind field at the $0.5H$ level, $0°$ approach flow.

flow slows down to approximately 4 m s^{-1} as a result of increased surface roughness and related processes, i.e. enhanced downward momentum transport (see section 6.2), etc.

The acceleration zone within the first three container rows, although only in the along-wind oriented narrow street canyons, is still visible at the container height (lower chart of Fig. 6.2), as well as at the $0.5H$ (Fig. 6.3). Behind this acceleration zone the flow slows down to speeds significantly smaller than the undisturbed flow even in the along-wind oriented narrow street canyons.

The significant difference appears between the first and other cross-wind oriented wide street canyons mainly at the container height. The first container generats a vortex shading in the first street canyon in contrast with the following street canyons, where the pronounced flow direction, which corresponds with the approach flow direction, indicates the regime of an isolated or wake interference flow, see Fig. 2.5. The flow at half container height is very slow and scattered in the wide street canyons and well channelled in the narrow street canyons. The measurement grid is too coarse to show details and therefore the detailed measurement was carried out and the results are shown later in section 6.1.2.

-45° Approach Flow

Figure 6.4 shows the measurement point layout for -45° approach flow direction. Figures 6.5 and 6.6 show the velocity field at $2H$, H, and $0.5H$ levels, respectively. The channelling of the flow is increasing with decreasing height above ground.

The situation is very similar to the previous 0° wind direction case at $2H$

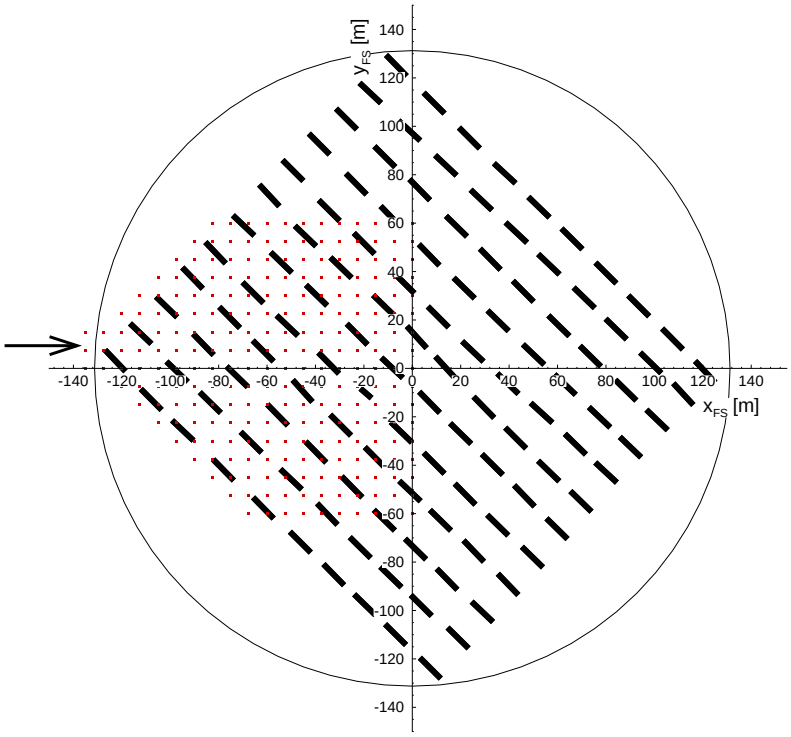

Figure 6.4: Layout of the measurement points for the -45° approach flow.

(Fig. 6.2). The flow is accelerated in the beginning and slows down deeper in the array. Almost no channelling caused by an oblique container orientation is visible at this level in contrast to the lower levels (Fig. 6.6), at which the flow has adapted to the easiest penetrable way, i.e. the wide street canyons. The flow prefers the way of least resistance, i.e. the passages open to the wind direction, which are represented by the narrow street canyons lying in one row (for example passages along lines $y_{\mathrm{FS}} = 10$ m and $y_{\mathrm{FS}} = 30$ m, Fig. 6.6). The flow at the container height is significantly slowed down except these in passages. The channelling is not fully developed, however, the lateral velocity component caused by the container orientation is evident.

The wind direction is completely changed because of the array at the $0.5H$ level (lower chart of Fig. 6.6). After a very short impact zone, the flow is fully channelled by the wide street canyons and even the passages are much less apparent than at the container level height.

-90° Approach Flow

The layout of the measurement points is given in Fig. 6.7. Figures 6.8 and 6.9 show the velocity field at levels $2H$, H, and $0.5H$, respectively. The blockage effect of the containers is very small for this wind direction and therefore no significant acceleration of the flow due to the blockage effect of frontal area has been observed.

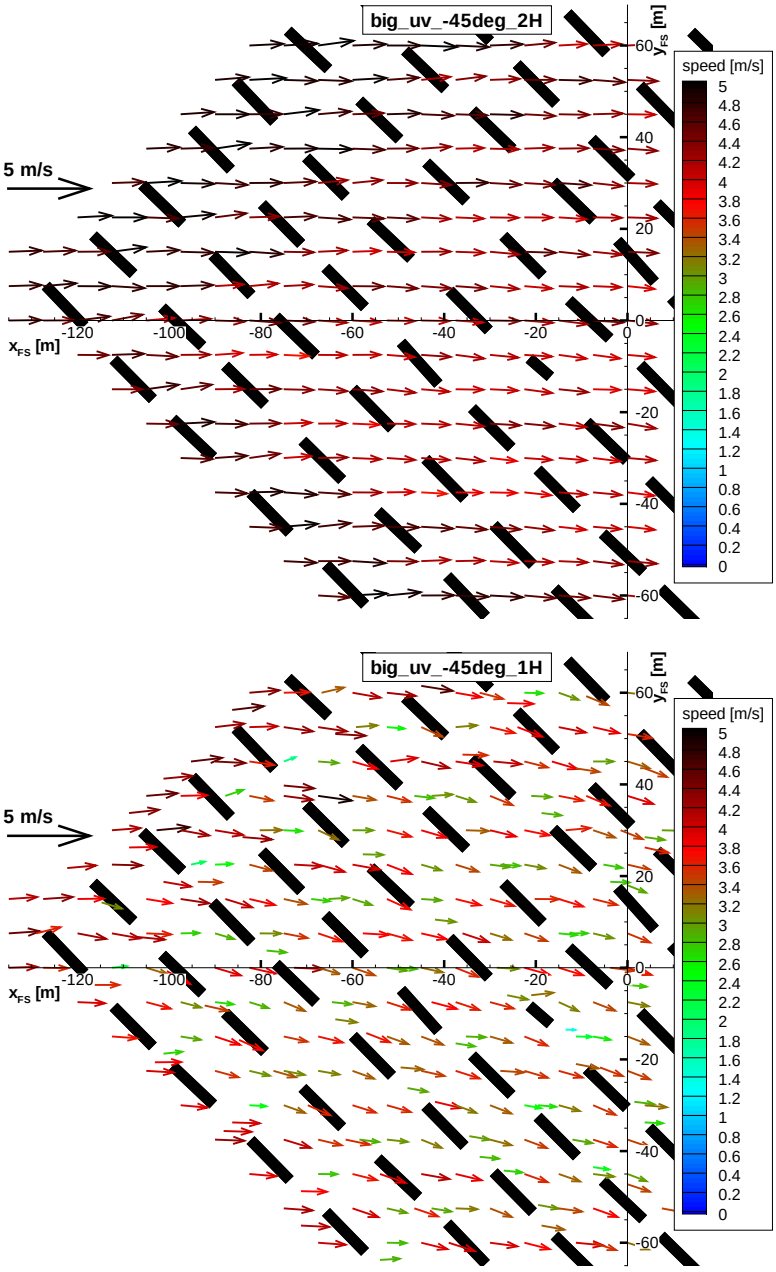

Figure 6.5: Measured wind field at the $2H$ level (upper chart) and at the $1H$ level (lower chart), -45° approach flow.

Flow parallel to the streets can cause the 'jetting effect' (Oke, 1987) characterised by wind speed magnitudes in the each level greater than in the approach flow. The wind speed of an undisturbed approach flow at $0.5H$ equals to 3.6 m s^{-1} (shown by the light red by means of the wind speed colour scale in Fig. 6.9). However, the wind speed in the centre of the wide street canyons is greater than 3.6 m s^{-1} (typically slightly over 4 m s^{-1} represented by the dark

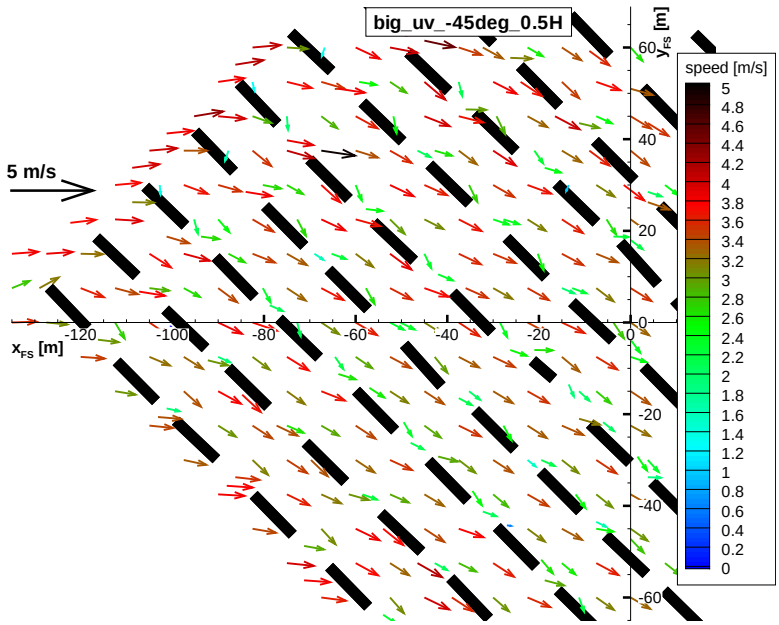

Figure 6.6: Measured wind field at the $0.5H$ level, -45° approach flow.

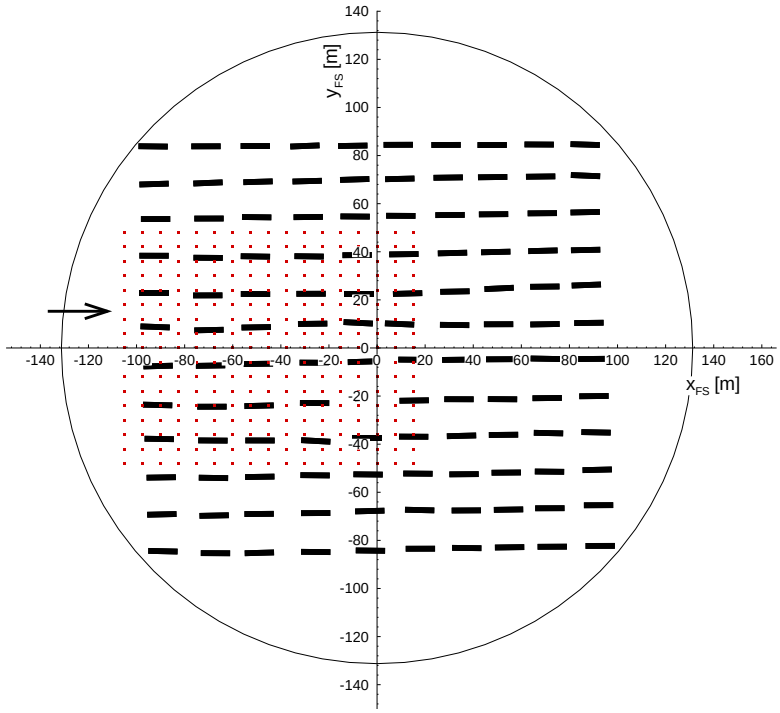

Figure 6.7: Layout of the measurement points for the -90° approach flow.

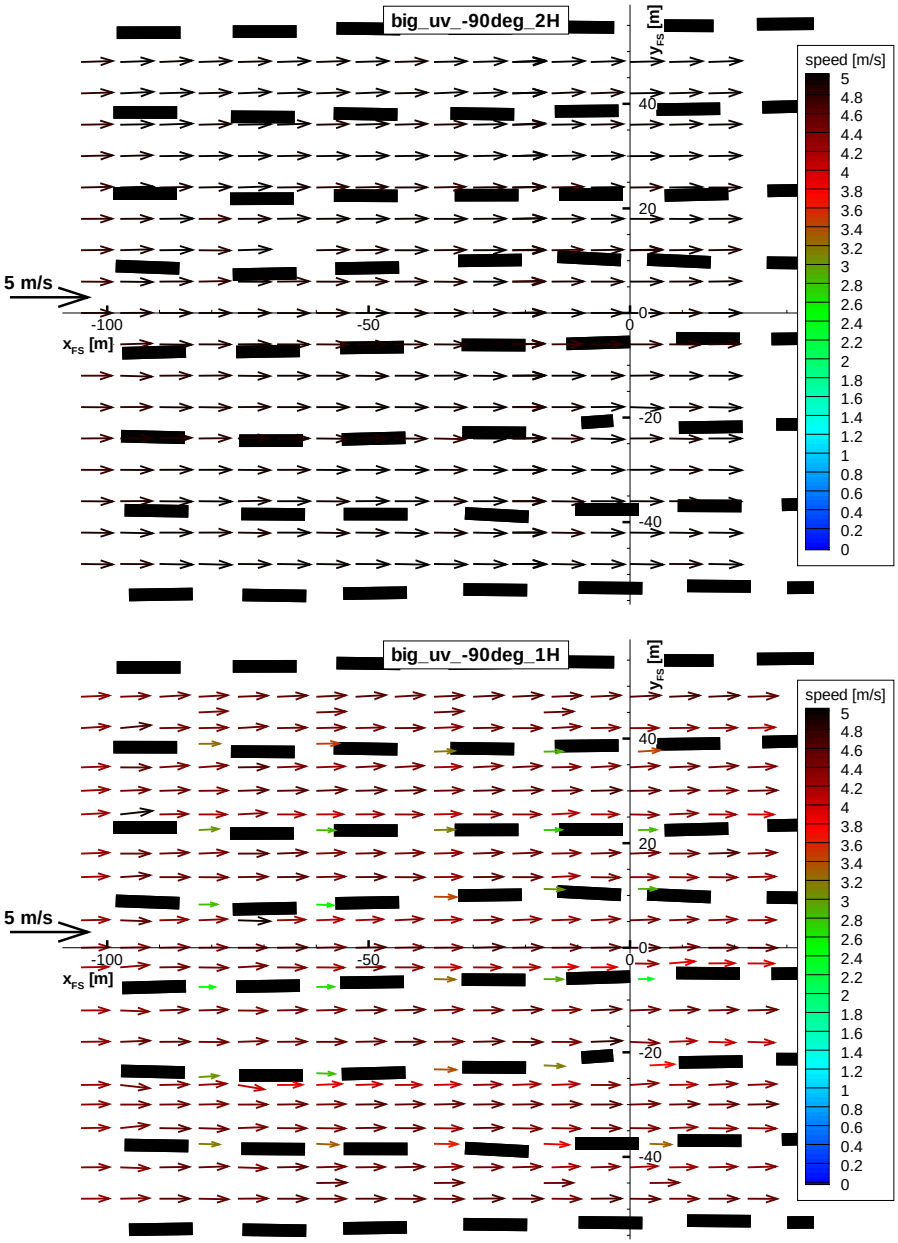

Figure 6.8: Measured wind field at the $2H$ level (upper chart) and at the H level (lower chart), -90° approach flow.

red colour). The narrow street canyons lie in the wake behind the containers, however, the area of the wake is very small due to the small dimensions of the container cross-section and strong wind speed in the neighbouring areas (for more detailed measurement see next section 6.1.2).

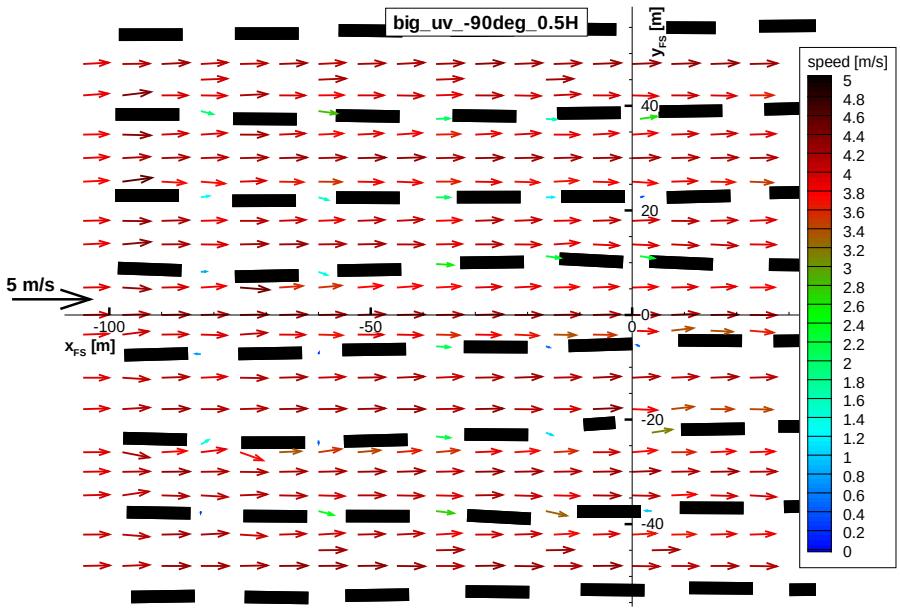

Figure 6.9: Measured wind field at the $0.5H$ level, -90° approach flow.

6.1.2 Flow Inhomogeneities within the Street Canyon

Since the results presented in the previous section showed only the overall behaviour of the flow field within the container array, a smaller area of one street canyon had been chosen for the more detailed horizontal flow field measurement (Fig. 6.10). The measurement grid consisted of 94 points with the measurements being conducted at three levels (container height, H; two thirds of the container height, $0.66H$; and one third of the container height, $0.33H$), for five wind directions (0°, -45°, and -90° like in the coarse grid measurement and additionally for -30° and -60°).

This particular one street area was chosen for two reasons: it is located approximately in the centre of the array to show the adapted flow; and there is an obvious misalignment in the container arrangement so the influence of array irregularities may be studied in detail, since they are not visible on the coarse grid measurement. The significantly smaller container close to the detailed measurement area is the VIP car, which had completely different dimensions than the rest of the containers. Unfortunately the highest T tower, with its many measurement devices, was placed behind the VIP car and in the next sections the influence of its different dimensions will be shown.

The wind speed in Figures 6.11 to 6.16 is depicted by arrow length (the reference vector of the magnitude 5 m s^{-1} is given in all figures). The coloured squares show the horizontal velocity standard deviation, $U_{\mathrm{rms}} = \sqrt{\sigma_u^2 + \sigma_v^2}$.

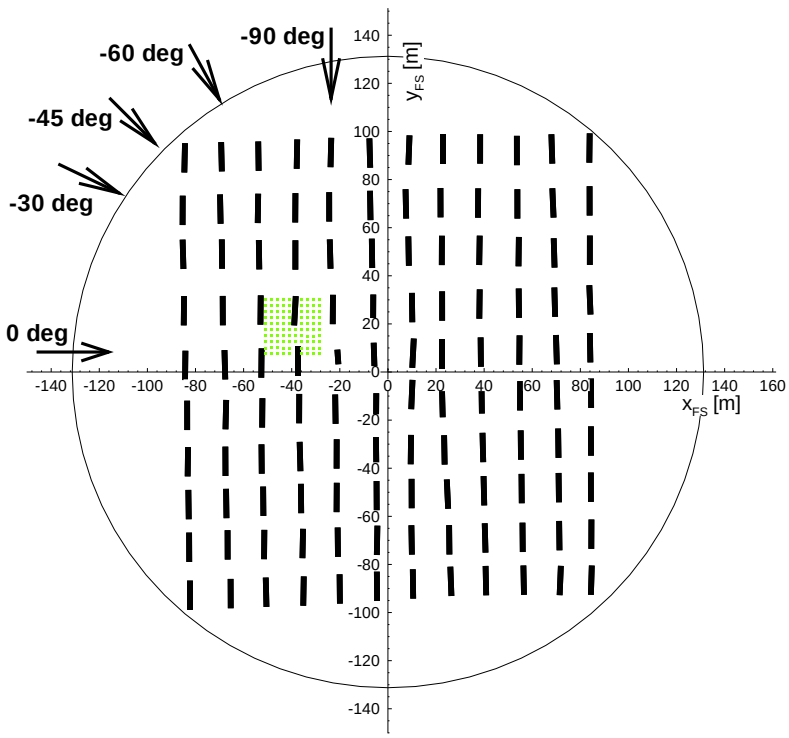

Figure 6.10: Layout of the measurement points for the detailed horizontal flow case with the depicted approach flow directions.

0° Approach Flow

The detailed flow field for 0° approach wind direction at the H, $2/3H$, and $1/3H$ is shown in Fig. 6.11. The highest mean wind speed can be found in the narrow street canyons, i.e. between the shorter container walls. The lowest turbulence intensity level, i.e. a combination of a small velocity standard deviation and a high mean wind speed also appeared there. Individual containers create a wake region characterised by a small mean wind speed, small velocity standard deviation, but high turbulence intensity, which can be detected at $2/3H$ and $1/3H$ levels. The intensity of turbulence is highest directly in front of the container, where the bi-model probability density function can be found (showing intermittency of the flow in this area), which provides the mean wind speed close to zero and a significant velocity standard deviation.

The picture of the detailed flow field provides information about the flow between individual containers and can be used for distinguishing between the isolated roughness and wake interference flow cases (Fig. 2.5). Since the flow does not indicate any presence of the interference between the wake behind a container and the corner vortex in front of the next container and that flow reattachment has been observed (i.e. the same direction of the flow as the approach orientation has been found directly in front of the next container),

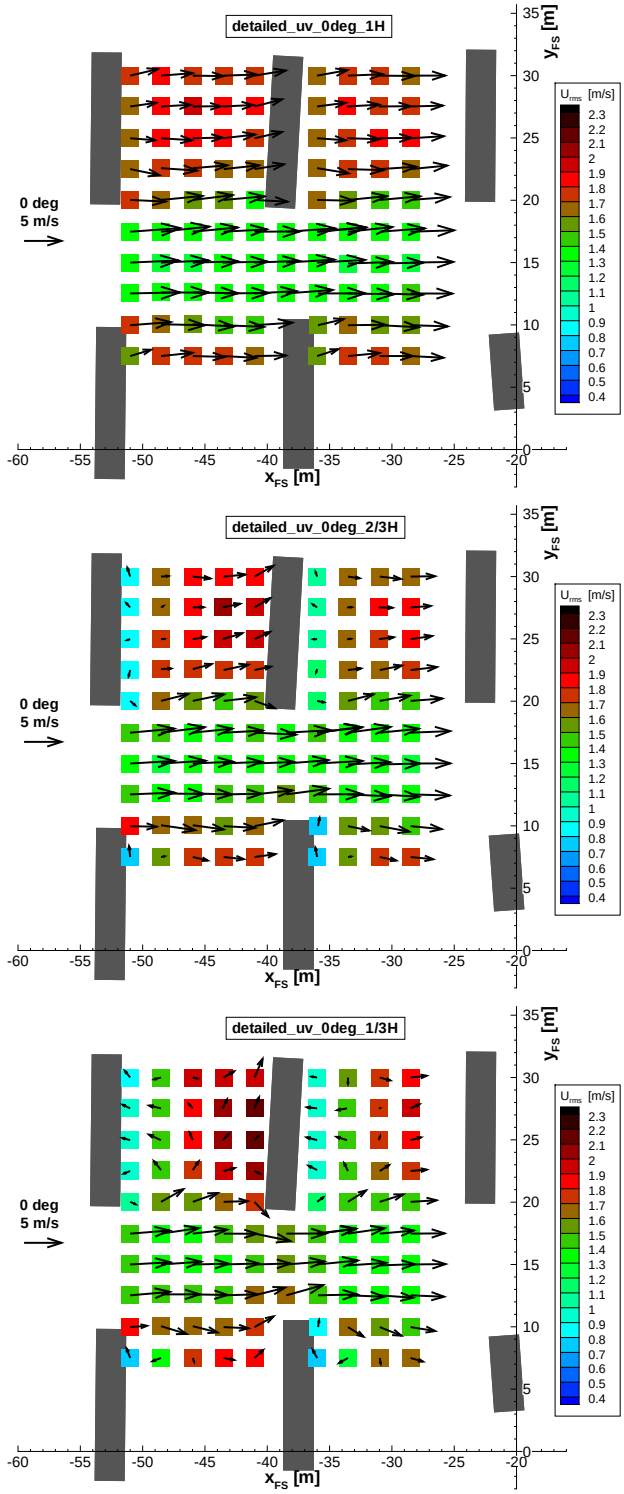

Figure 6.11: The mean velocity and standard velocity deviation depicted by the arrows with magnitudes related to the reference vector and coloured squares, respectively, for 0° approach wind direction at the H (upper chart), $2/3H$ (middle chart), and $1/3H$ (lower chart) level.

the flow regime is closer to the ideal case of the isolated roughness flow than the weak interference flow.

-30° Approach Flow

The detailed flow field for -30° approach wind direction at the H, $2/3H$, and $1/3H$ levels is shown in Fig. 6.12. This approach wind direction was added after the coarse grid measurements (section 6.1.1) to find the critical angle, under which the flow is fully channelled by the container array. The flow is much less turbulent (higher mean wind speed and smaller U_{rms}) than in the case of 0° approach wind direction (Fig. 6.11). At the lower levels ($2/3H$ and $1/3H$) the flow direction inside the container array is turned from the original orientation (about -30° and -45° at the $2/3H$ and $1/3H$ level, respectively), however, the flow is not fully channelled, i.e. the flow direction within the wide street canyon is not parallel to the longer container walls (-90°). The vortex shading is highly asymmetric and the wake area is much smaller than in the cases of 0° approach wind direction.

-45° Approach Flow

The detailed velocity field for -45° approach wind direction at the H and $2/3H$ is shown in Fig. 6.13, and at $1/2H$ and $1/3H$ in Fig. 6.14. A less turbulent flow as in the previous case (-30° approach wind direction, Fig. 6.12) has been observed at all four levels with only exceptional points situated in the container wake and very close to the container wall. The wind direction changes from the original orientation at the container height to the -90° direction (parallel with the wide street canyons) at half of the container height and lower. Even at the lowest elevations the flow has a tendency to flow parallel with the approach wind, which is clearly visible in the narrow street canyons. The maximum intermittent behaviour appears in the narrow street canyons, where wake structures interfere with the main flow.

-60° Approach Flow

The detailed flow field for -60° approach wind direction at the H, $2/3H$, and $1/3H$ level is shown in Fig. 6.15. The maximum turbulence intensity is smaller than in the previous cases. The flow channelling has the same character as in the previous case of -45° approach flow direction: nearly no channelling at container height and a fast switch to the parallel flow inside the canopy. The flow in the narrow street canyons is at the lowest level no longer driven by the original wind direction preserved in the higher levels (above the container array), but by the local irregularities in the container arrangement, which is demonstrated by the changing of the wind direction at $2/3H$ and $1/3H$ in the narrow street canyon (Fig. 6.15, x_{FS} = -38 m, y_{FS} = 15 m).

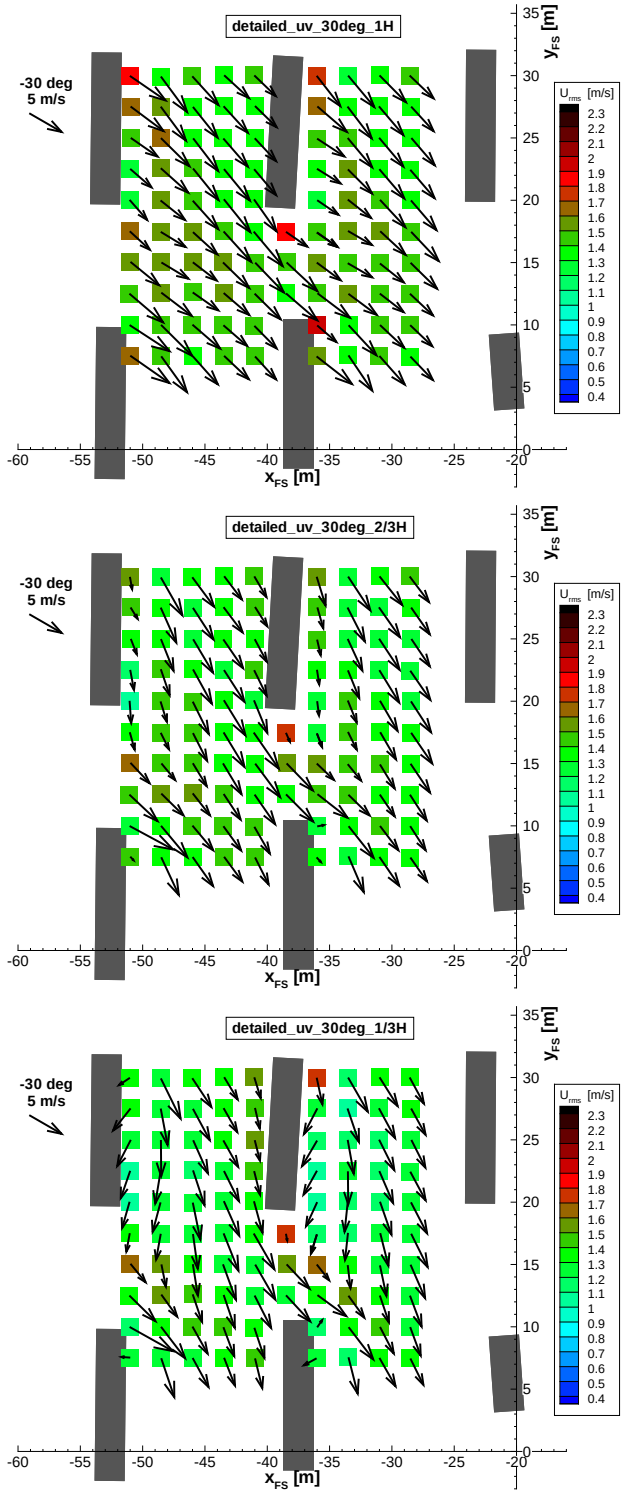

Figure 6.12: The mean velocity and standard velocity deviation depicted by the arrows with magnitudes related to the reference vector and coloured squares, respectively, for -30° approach wind direction at the H (upper chart), $2/3H$ (middle chart), and $1/3H$ (lower chart) level.

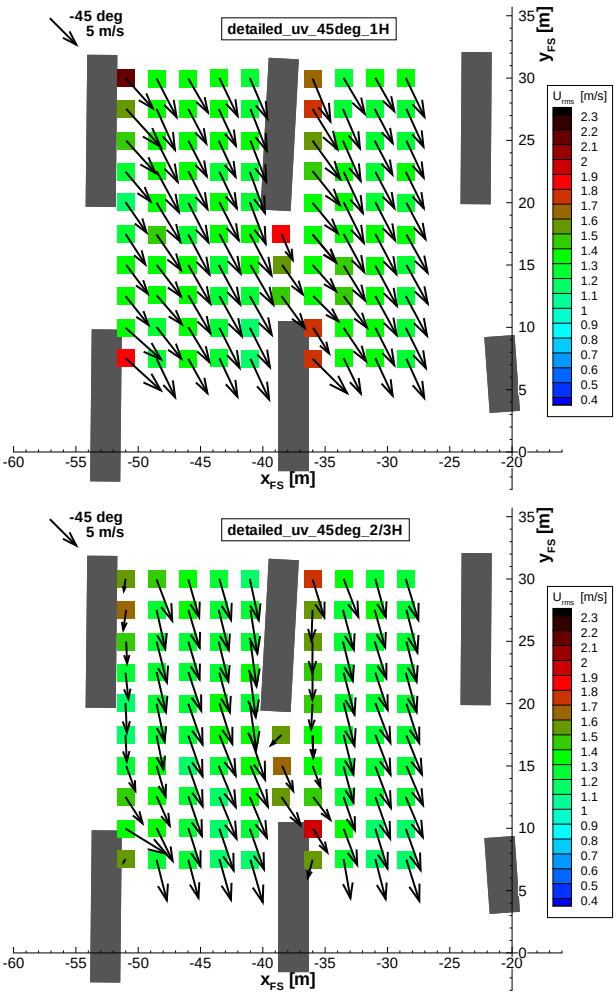

Figure 6.13: The mean velocity and standard velocity deviation depicted by the arrows with magnitudes related to the reference vector and coloured squares, respectively, for -45° approach wind direction at the H (upper chart) and $2/3H$ (lower chart) level.

-90° Approach Flow

Figure 6.16 represents the detailed flow field for the -90° approach wind direction at H, $2/3H$, and $1/3H$. This set-up has the least influence and the flow adapts to it very quickly. The only 'interesting' regions are the container wakes (very small in this case) and points close to the container walls, where the irregularities in the container set-up play an important role.

It should be note, that with the increasing approach flow direction (from 0° to -90°) the absolute maximum value of U_{rms} within the measurement grid gets smaller. This behaviour proves that -90° wind direction is the least influential set-up, which is also supported by the minimum blockage coefficient for this set-up (see section 5.1).

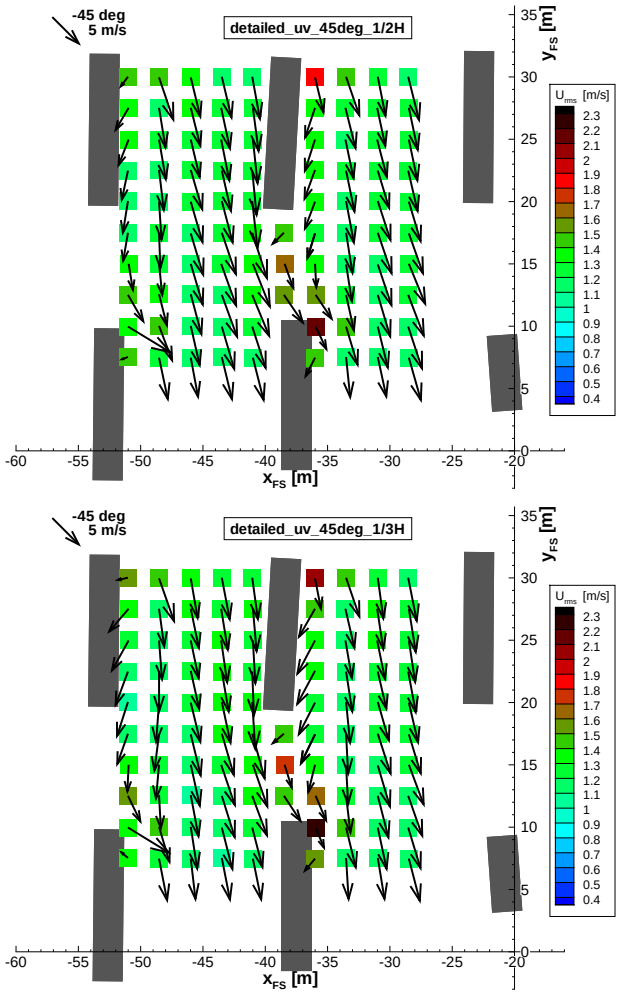

Figure 6.14: The mean velocity and standard velocity deviation depicted by the arrows with magnitudes related to the reference vector and coloured squares, respectively, for -45° approach wind direction at the $1/2H$ (upper chart) and $1/3H$ (lower chart) level.

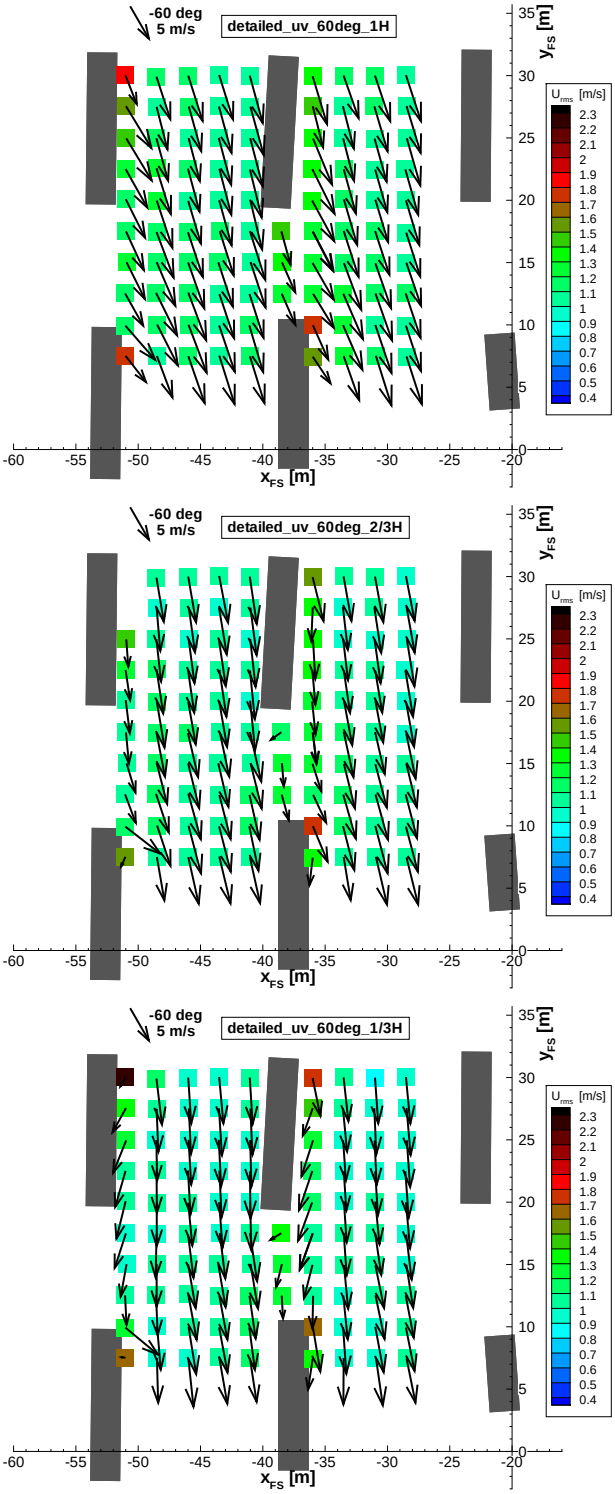

Figure 6.15: The mean velocity and standard velocity deviation depicted by the arrows with magnitudes related to the reference vector and coloured squares, respectively, for -60° approach wind direction at the H (upper chart), $2/3H$ (middle chart), and $1/3H$ (lower chart) level.

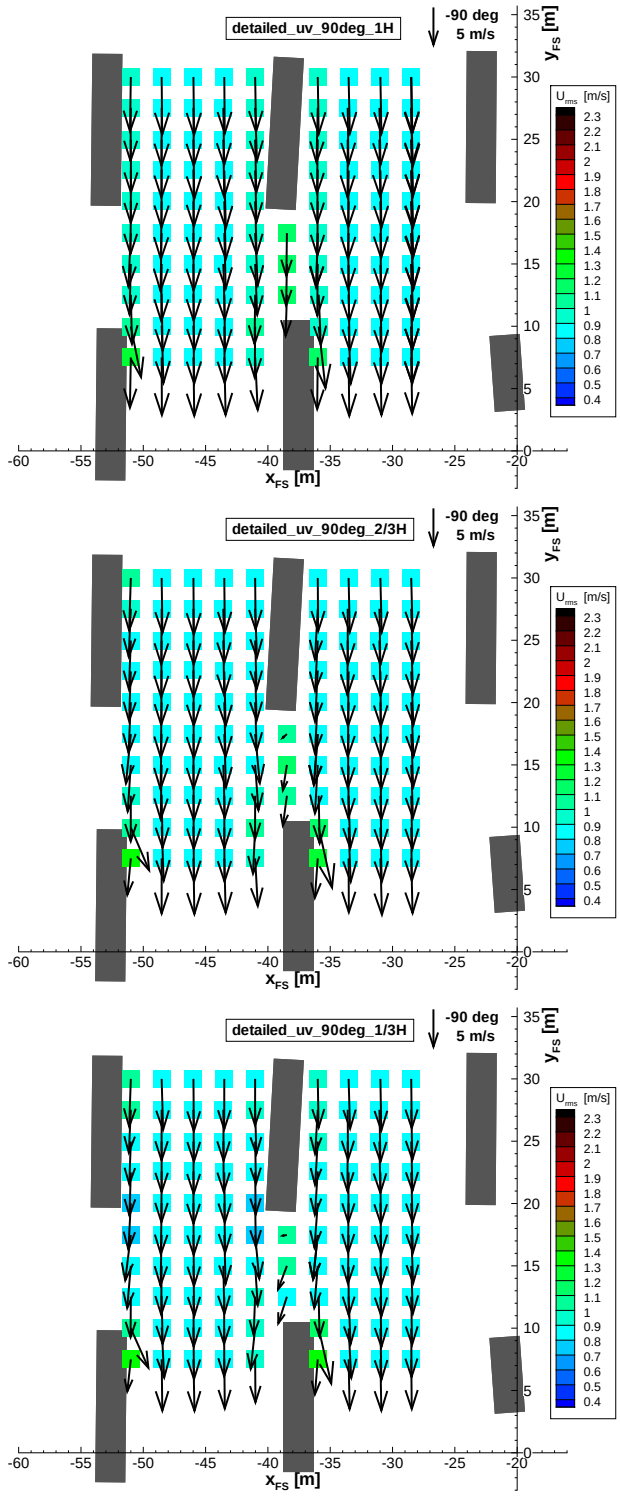

Figure 6.16: The mean velocity and standard velocity deviation depicted by the arrows with magnitudes related to the reference vector and coloured squares, respectively, for -90° approach wind direction at the H (upper chart), $2/3H$ (middle chart), and $1/3H$ (lower chart) level.

6.2 Vertical Momentum Fluxes

The vertical momentum fluxes or Reynolds shear stresses (i.e. $\overline{u'w'}$ in our case since the coordinate system is related to the mean wind direction and therefore the magnitude of the $\overline{v'w'}$ term is negligible for the overall vertical momentum flux) are very important quantities, as discussed in section 2.4.1. Therefore the systematic study of the vertical profiles and horizontal distribution of the momentum fluxes within the street canyon has been conducted.

The overall layout of the measurement area is shown in Fig. 6.17. The main part of the measurement consists of $\overline{u'w'}$ vertical profiles. The positions of the vertical profiles in the range from $z_{\mathrm{FS}} = 0$ to 16 m ($6H$) are shown by the coloured symbols in Fig. 6.17. Different colours and shapes show different wind directions and the numbers of the individual profiles are also depicted. The profiles can be divided into three major groups according to their position in the array: the profiles measured in the narrow street canyons (profiles number 1, 4, 7, .., 88, and 91); cross-sections (2, 5, 8, .., 89, and 92); and wide street canyons (3, 6, 9, .., 90, and 93). The positions were always chosen to be exactly in the middle of the street or cross-section. The cyan coloured dense grid shows

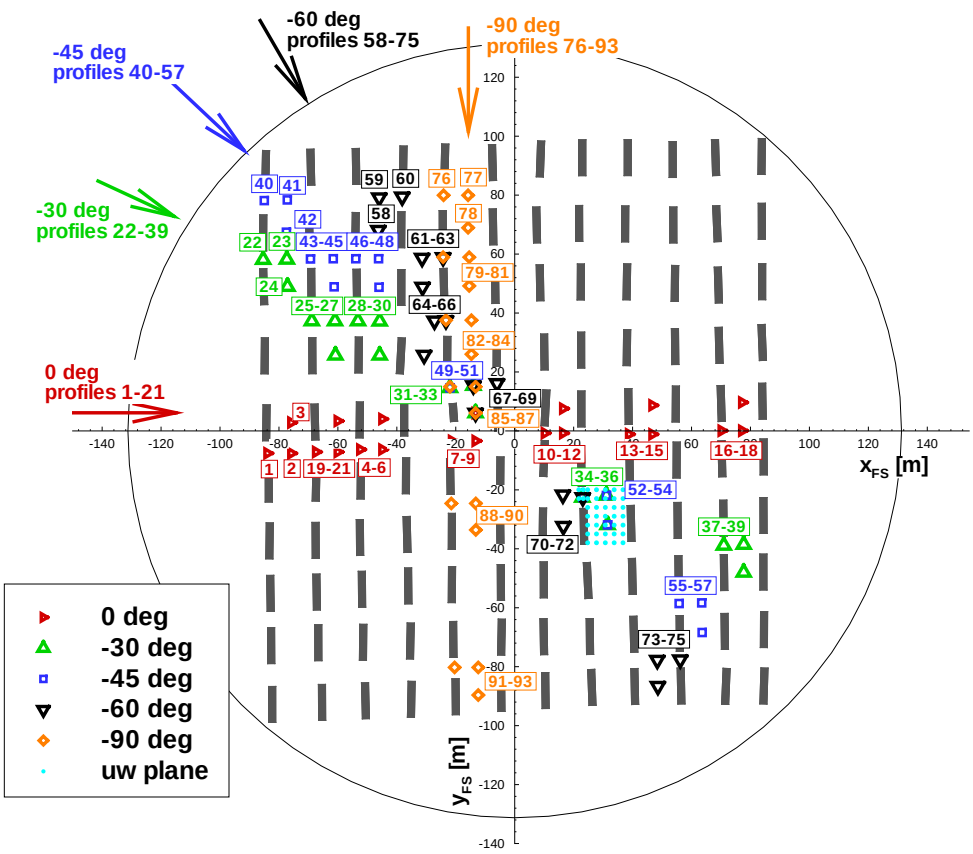

Figure 6.17: Layout of the measurement points where the vertical momentum fluxes were measured.

the area, where the vertical momentum fluxes were measured in a horizontal plane at container height.

6.2.1 Vertical Profiles of Momentum Fluxes

The vertical profiles of momentum fluxes are shown in this section. Symbols and colours are used according to the following rules. The colours distinguish the profile positions: the narrow street canyons are black, the cross-sections are red, and the wide street canyons are blue. The shapes determine the distance between the array edge and the profile position: the triangles show the first street canyon, the diamonds show the T tower location (x_{FS} = 13.26 m, y_{FS} = -6.04 m, Fig. 6.17), and the squares show the average profile of the rest profiles (for every wind direction at least 6 different distances for the each position were measured, i.e. the average over at least 4 profiles and the error bars represent scatter of these ensembles). The green line depicts the container height H, z_{FS} = 2.54 m.

0° Approach Flow

The positions of the vertical profiles measured within the container array for 0° approach flow are depicted in Fig. 6.18. The same symbols, which was used in Fig. 6.19, were used for easy reference. The narrow street canyons (black) and the cross-sections (red) create a clear alley for 0° approach wind direction. The wind speed is at all heights increased in the first street canyon (profiles 1 and 2 in the upper chart of Fig. 6.19, compare with the approach mean wind profile in Fig. 5.5). Behind the front area of the container array the flow slows down and establishes a new mean wind speed vertical profile, which does not vary significantly through the array (very small error bars of the average profiles). The vertical profiles of the vertical momentum flux are very similar to the undisturbed profile (lower chart of Fig. 6.19, a constant value in the region of the Inertial Sublayer $\overline{u'w'}$ = - 0.11 m^2 s^{-2}, see Fig. 5.7) in the first street canyon at the positions of the narrow street canyon and the cross-section. Turbulent mixing does however increase while the flow gets deeper to the container array. The turbulent vertical momentum flux is also increasing. The maximum reached was approximately 3 times greater than value of approach flow and its vertical position lies around container height.

The situation in the wide street canyon, which is perpendicular to the approach flow, is completely different. The first container causes a separation of the flow, creating a complex vortices structure. The leeward vortex behind the first container can be identified by the negative mean wind speed in the lowest part of the street canyon (blue triangles in Fig. 6.19). This leeward vortex is not so strong and large in the following street canyons (average profile, blue squares in Fig. 6.19). The sharpened turbulence mixing behind the first container row is also demonstrated by a dramatic increase of the vertical momentum transport (lower chart of Fig. 6.19). Vertical momentum flux is sharply increasing up to 1.2H, where the maximum value $\overline{u'w'}$ = - 1.35 m^2 s^{-2} is reached, and then a fast decay occurs (values at the 2.5H are not different from values taken

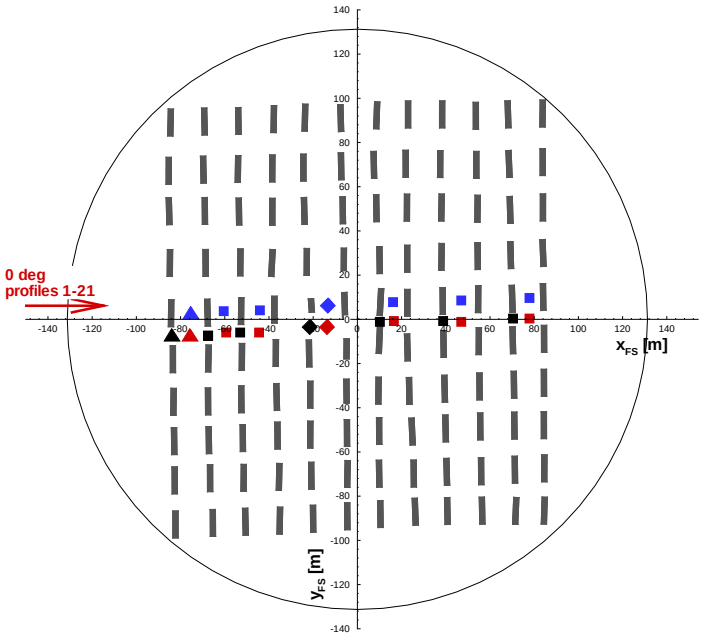

Figure 6.18: The position of the vertical profiles measured for 0° approach flow.

in the narrow street canyon positions). The $\langle\overline{u'w'}\rangle$ profile inside the container array is representative (small error bars) and reaches a maximum $\langle\overline{u'w'}\rangle$ = -0.75 m^2 s^{-2} slightly below container height at approximately $0.8H$.

The reason why the measurements at the location of the T tower were not included in the average and were plotted separately, is obvious when comparing the average profiles (squares) with the T tower measurement (diamonds) in Fig. 6.19. The vertical profiles of both U_{mean} and $\overline{u'w'}$ at the wide street canyon position are heavily influenced by the presence of the VIP car directly in front of the T tower. The VIP car is significantly higher than the containers ($H_{\text{VIP}} = 1.4H$) and narrower ($W_{\text{VIP}} = 0.5H$). The wake behind the VIP car is therefore much smaller (no negative wind speeds), but higher (slower mean wind speed increase with the height and a noticeable elevation of the vertical momentum transport maximum to the approximately $1.2H$ level).

-30° Approach Flow

The positions of the vertical profiles measured within the container array for -30° approach flow are depicted in Fig. 6.20. The same symbols, which was used in Fig. 6.21, were used for easy reference. The distinguishing of the positions in respect with the container array (street canyons versus cross-sections) loses sense with an oblique wind direction. Therefore all profiles, except the first street canyon, are close to each other. There is no step change between them, it is more a slow transformation between the extreme cases. The U_{mean} profiles are slightly varying inside the canopy and converge very quickly above. The first street canyon again shows an increase of the wind speed in the passages,

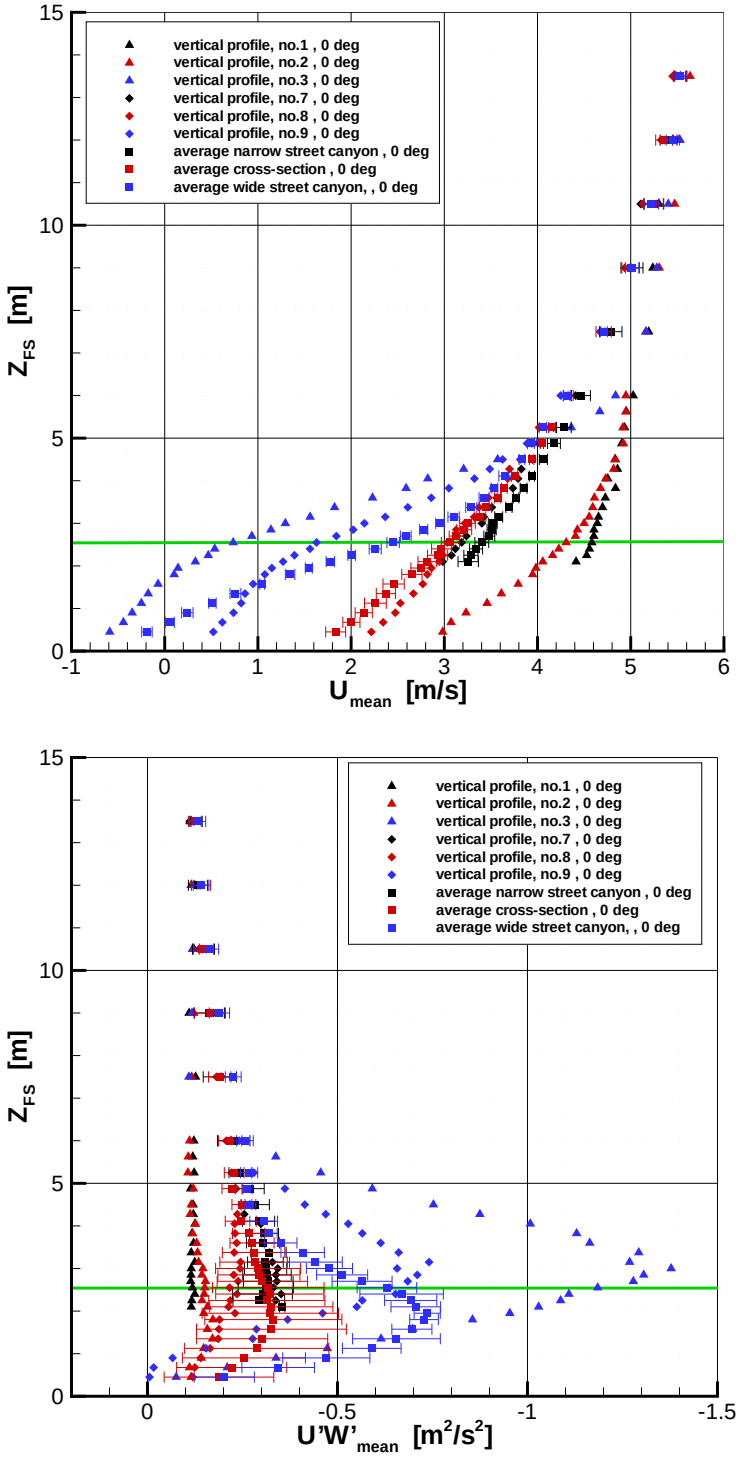

Figure 6.19: The vertical profile of the mean wind speed (upper chart) and the vertical momentum flux (lower chart) for 0° approach wind direction.

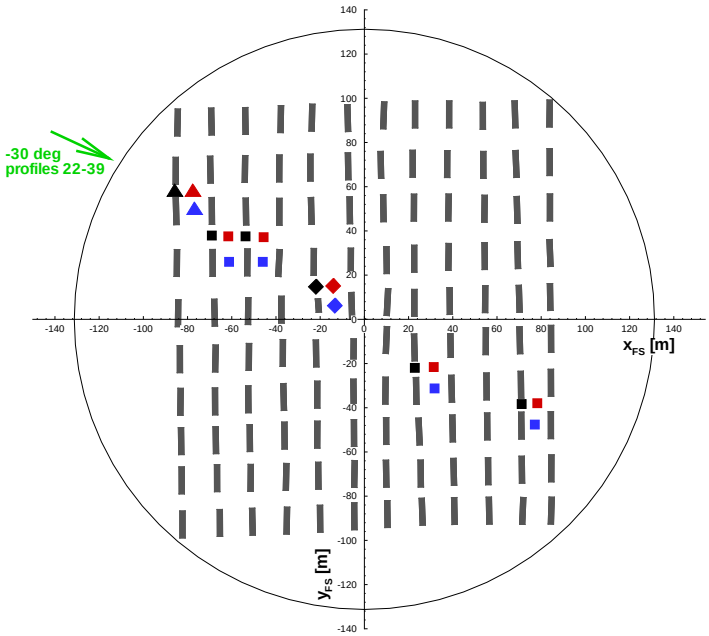

Figure 6.20: The position of the vertical profiles measured for -30° approach flow.

i.e. in the narrow street canyons in the first row, and a greater wake behind the first container (the cross-section profile number 23, Fig. 6.21) with the interesting inverse mean wind speed gradient in the lowest elevations.

The average vertical momentum flux profiles show a typical urban-type shape with a maximum around the container height level or slightly above it. The first cross-section profile has the same shape, but the maximum is two times greater and it is reached at the $1.5H$ level. The T tower was not directly behind the VIP car for this wind direction and therefore there is no big difference between the average profiles and those of the T tower.

-45° Approach Flow

The positions of the vertical profiles measured within the container array for -45° approach flow are depicted in Fig. 6.22. The same symbols, which was used in Fig. 6.23, were used for easy reference. The -45° approach wind direction is an important case because of the comparison with the MUST field experiment. On 25th September, 2001, the wind directions ranged from -40° to -51° (for more details see chapter 3 or Biltoft, 2001). The orange circles in Fig. 6.23 are showing the MUST field data.

The mean wind speed profiles measured in the wind tunnel are very similar with nearly no differences between different positions (the most extreme values were of course measured in the first street canyon). The MUST field data profile shows significantly smaller U_{mean} values below $z_{\text{FS}} = 16$ m, where the agreement has been reached (upper chart of Fig. 6.23). In contrast, the vertical momentum fluxes (lower chart of Fig. 6.23) do not differ. The $\langle\overline{u'w'}\rangle$ profiles

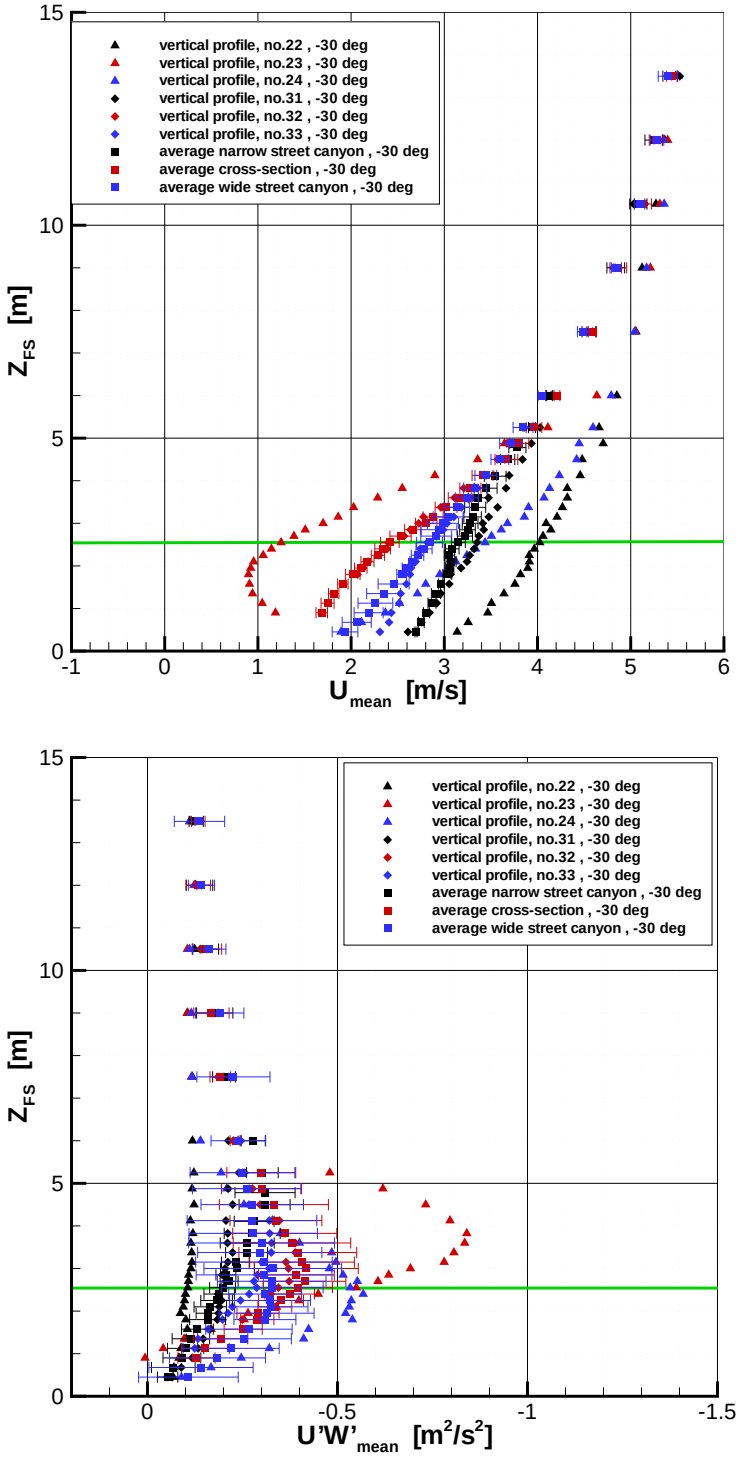

Figure 6.21: The vertical profile of the mean wind speed (upper chart) and the vertical momentum flux (lower chart) for -30° approach wind direction.

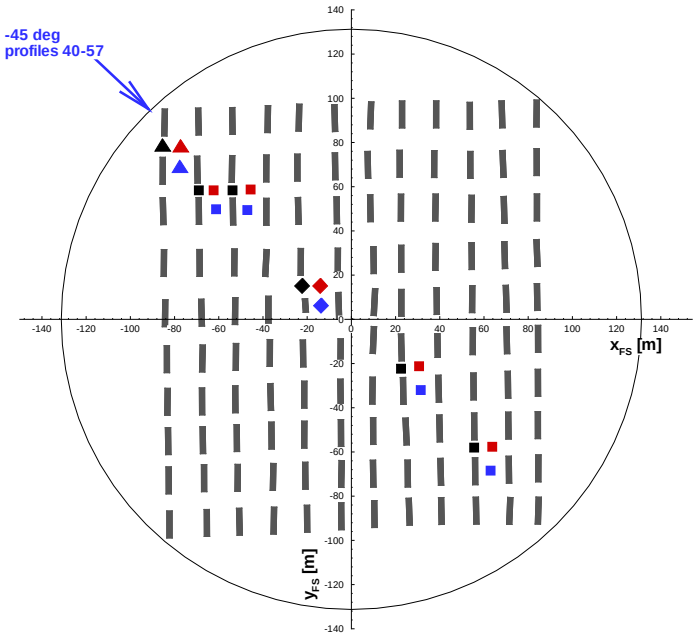

Figure 6.22: The position of the vertical profiles measured for -45° approach flow.

keep the urban-like shape, however, the maximum values are much smaller than in the previous wind directions and the level, where the maximum is reached, varies with the position. The cross-section position has very flat maximum range between $0.7H$ and $1.5H$; the wide street canyon position has the best pronounced maximum at $1.3H$ level; and the narrow street canyon position has a weak maximum at the $2H$ level. It should also be mentioned that the scatter in the values is much smaller for this wind direction than in the previous cases.

-60° Approach Flow

The positions of the vertical profiles measured within the container array for -60° approach flow are depicted in Fig. 6.24. The same symbols, which was used in Fig. 6.25, were used for easy reference. For the -60° approach wind direction the narrow street canyon position takes the 'leading position'. That means the strongest speed inhibition inside the canopy, i.e. the smallest wind speeds, and an enhanced vertical momentum transport can be observed there. It is interesting that in the first row the wide street canyon is the most influenced position (blue triangles in Fig. 6.25, in fact it is the second wide street canyon, see Fig. 6.17), but deeper in the canopy the highest turbulence level was observed in the narrow street canyon positions (black squares).

The vertical momentum flux profiles (lower chart of Fig. 6.25) are very similar to the previous ones and the only difference is the position where the absolute maximum was reached. If the first row is not taken in account (the maximum at the $1.5H$ level appeared in the wide street position), then the $\langle\overline{u'w'}\rangle$ maximum was reached in the narrow street canyon position at the con-

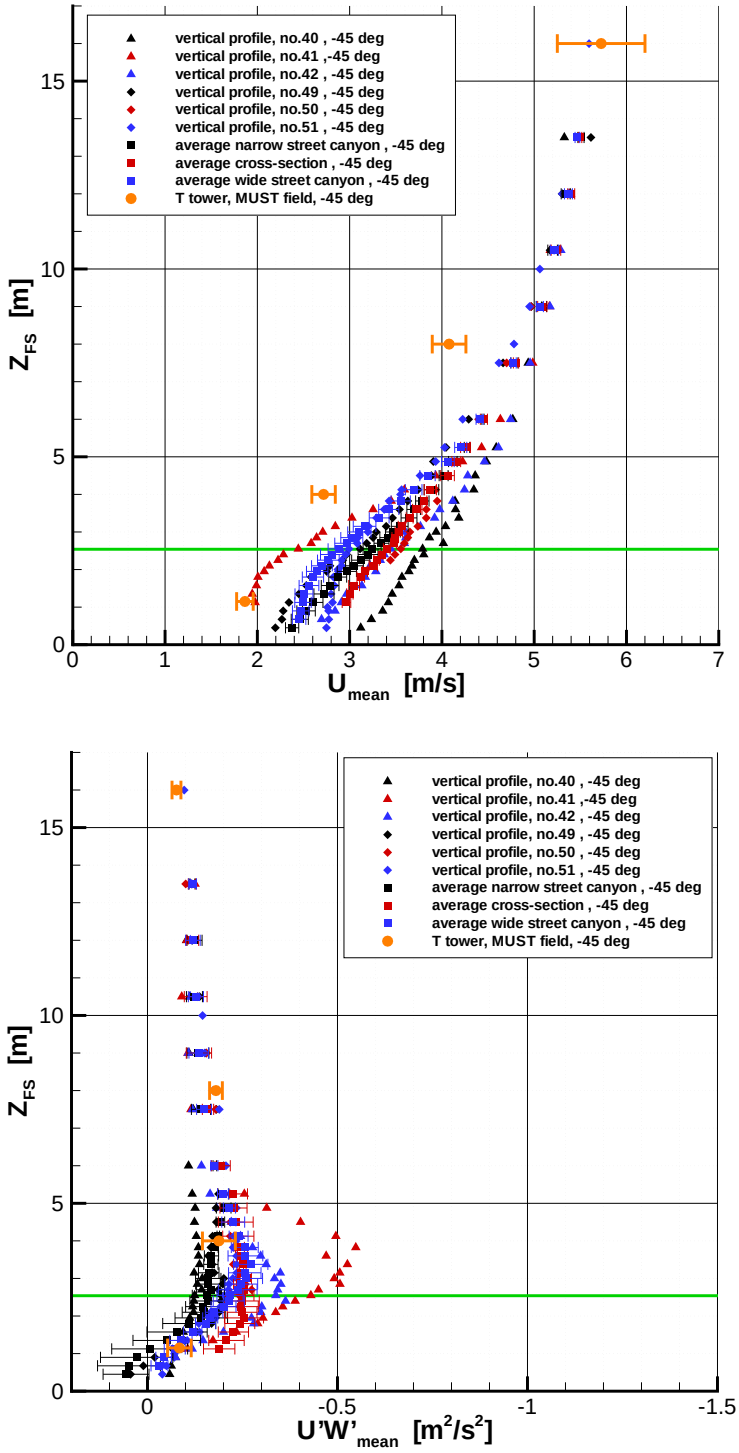

Figure 6.23: The vertical profile of the mean wind speed (upper chart) and the vertical momentum flux (lower chart) for -45° approach wind direction. Orange points are showing the T tower measurement of the MUST field experiment.

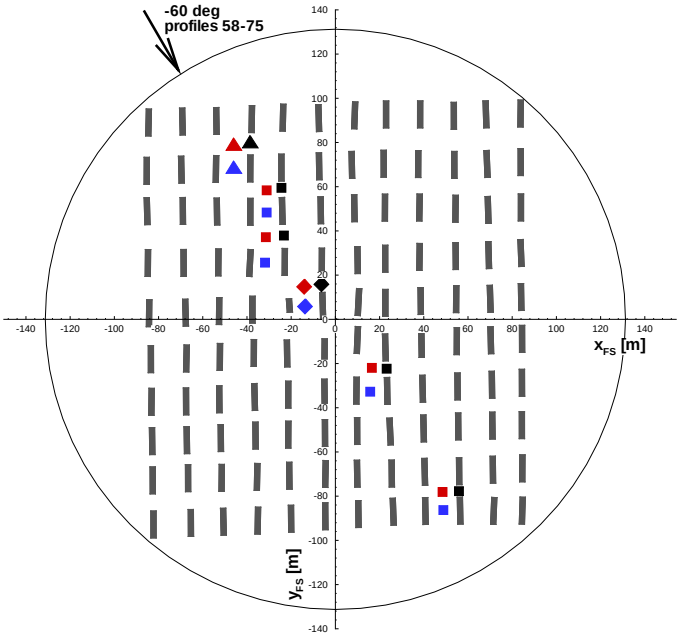

Figure 6.24: The position of the vertical profiles measured for -60° approach flow.

tainer height level. The maximum is sharply pronounced, since the lowest part of the profile shows positive values of $\langle\overline{u'w'}\rangle$ (the upward momentum transport). The values obtained at the container height in different positions are not significantly smaller, only the profiles shapes are much flatter.

-90° Approach Flow

The positions of the vertical profiles measured within the container array for -90° approach flow are depicted in Fig. 6.26. The same symbols, which was used in Fig. 6.27, were used for easy reference. The flow parallel with the wide street canyons can be compared with the 0° approach flow case. The basic principle is the same - flow is blowing along the walls and has to pass the obstacles, however, the important difference is the dimensions of the obstacles and the passages (for 0° the obstacles were dominant, therefore for -90° the dominant role was played by the passages).

The narrow street canyons are the most influenced places in the container array. The mean wind speed is significantly decreased there and the vertical momentum flux has a typical urban-like profile with a relatively large maximum value $\langle\overline{u'w'}\rangle$ = -0.45 m^2 s^{-2} being reached at approximately the $0.8H$ level (black squares in Fig. 6.27). The first street canyon profile no. 76 and the T tower profile no. 85 are very similar because of the container array arrangement irregularities. They are both not completely centred behind the front container and therefore they are not fully in the wake region, but more in the area between the wake and the free stream region. The free stream region, due to an array channelling of the flow, is characterised by an increase of the mean velocity and

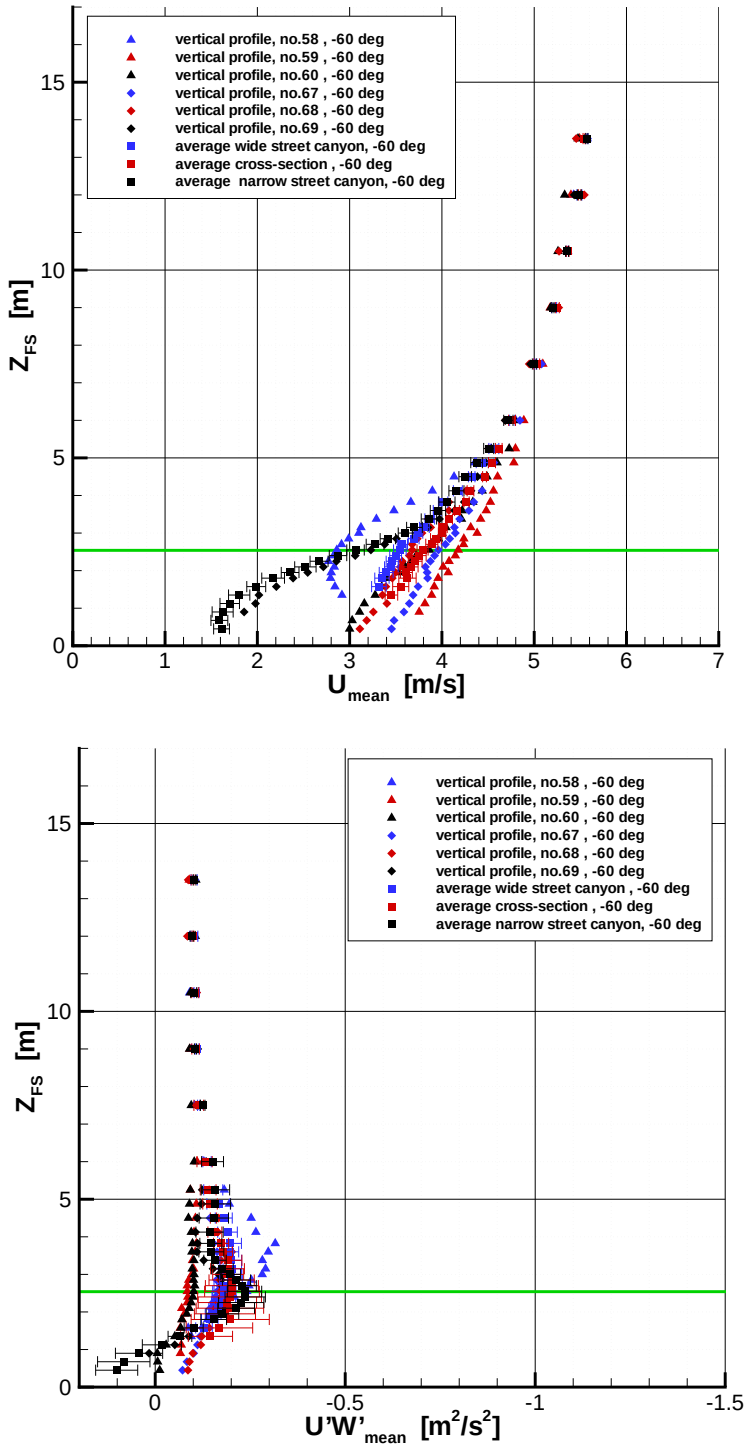

Figure 6.25: The vertical profile of the mean wind speed (upper chart) and the vertical momentum flux (lower chart) for -60° approach wind direction.

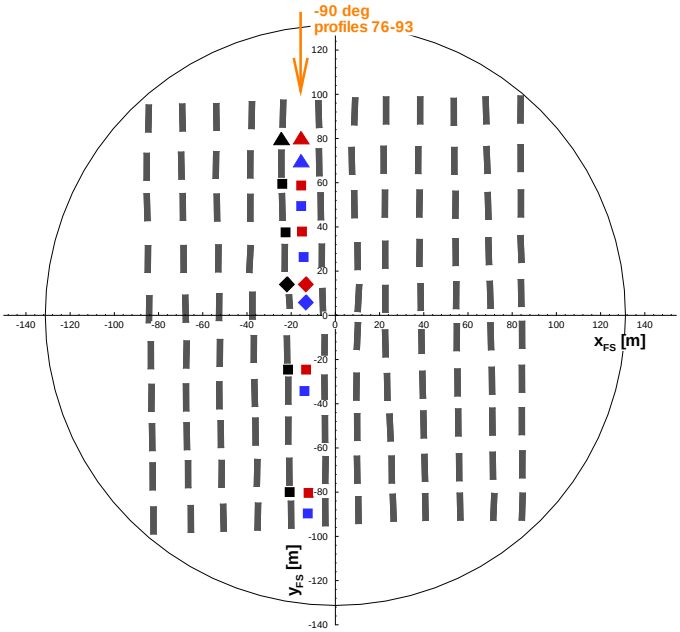

Figure 6.26: The position of the vertical profiles measured for -90° approach flow.

decrease of the vertical momentum transport in comparison with the approach profiles (Fig. 5.5 and Fig. 5.7) approximately up to the 3H level.

6.2.2 Horizontal Planes

Since in the previous section only three profiles per street canyon were measured, it was necessary to also measure the horizontal distribution of the vertical momentum flux with a fine resolution to evaluate the obtained results in a context of the whole street canyon. The maximum value of the vertical momentum flux was not obtained at the same height for different approach wind directions and various positions. Therefore the container height H had been chosen for the measurement because the maximum values were usually obtained very close to this level. It is also a well defined height, which is very often used for the friction velocity estimation in urban areas.

The measured values are shown in Fig. 6.28. All results correspond well with the vertical profiles (section 6.2.1) and also with the detailed horizontal flow measurement (section 6.1.2). The greatest values were reached for 0° approach wind direction in the middle of the wide street canyon (compare with Fig. 6.19, Fig. 6.11, and related discussion). The maximum of $\overline{u'w'}$ was found in the wake created by a container for all wind directions and with the increasing approach wind direction angle the maximum values were decreasing. Therefore the three profiles, which have been chosen in the previous section, were able to capture all important phenomena and describe the situation in the container array.

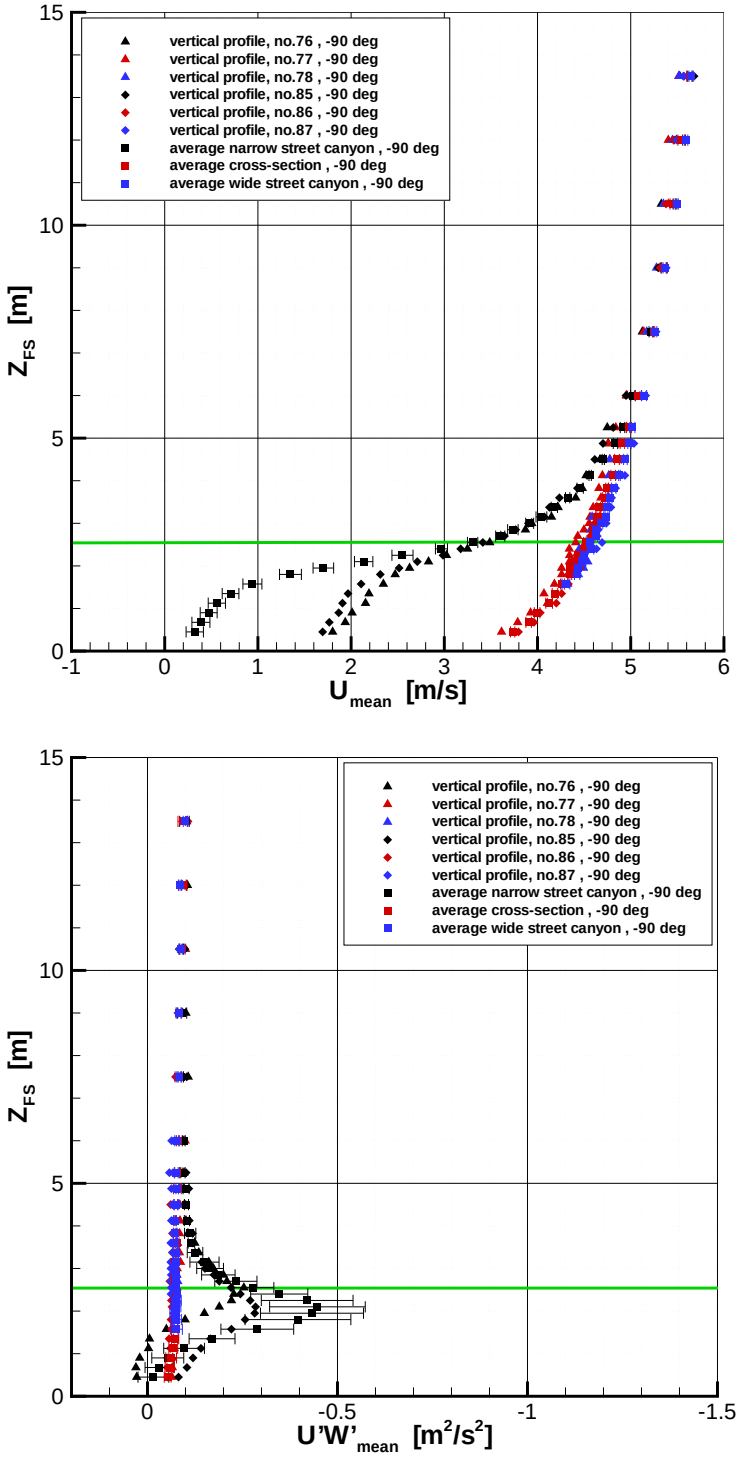

Figure 6.27: The vertical profile of the mean wind speed (upper chart) and the vertical momentum flux (lower chart) for -90° approach wind direction.

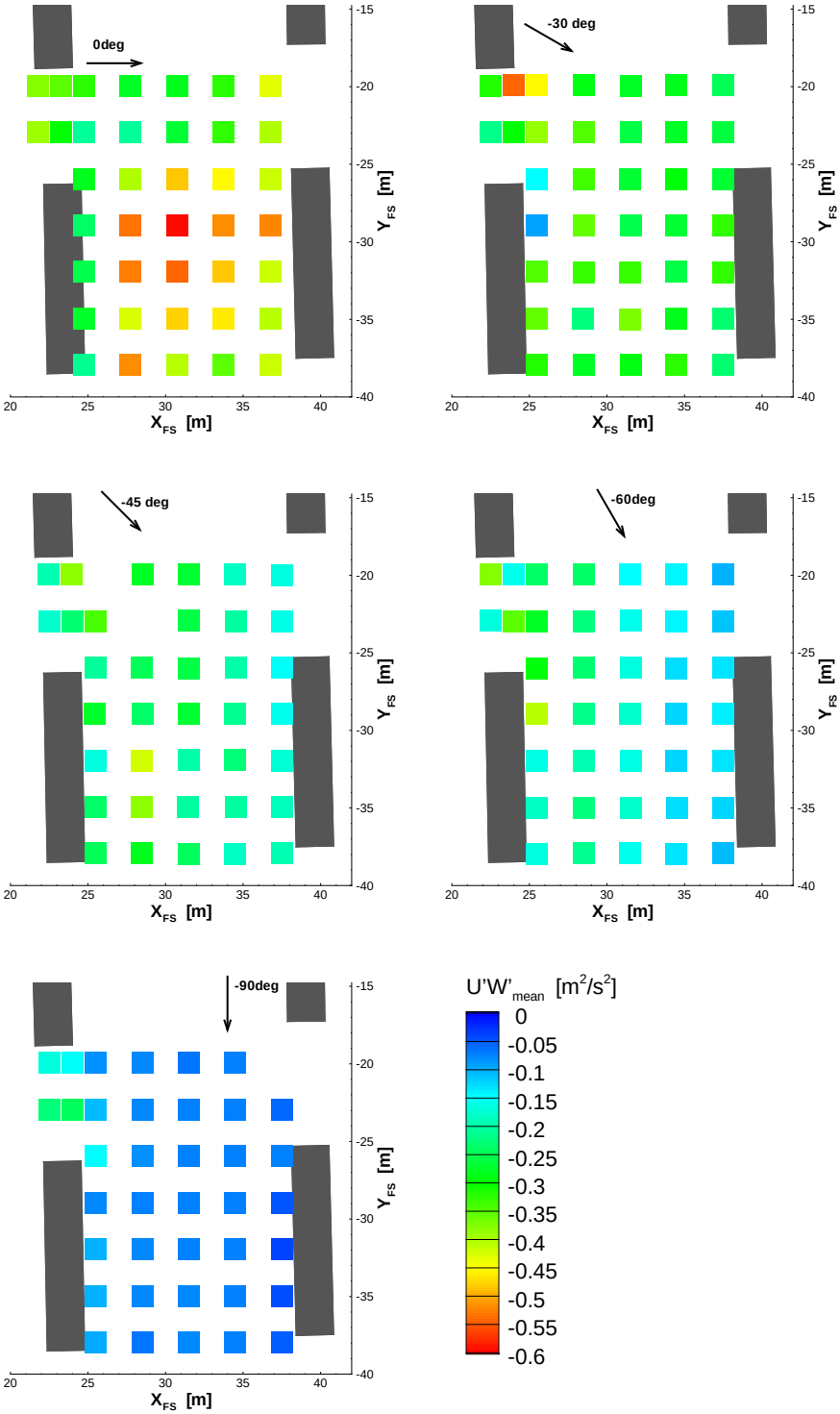

Figure 6.28: The horizontal plane distribution of the vertical momentum flux at container height for different approaching wind directions, from the upper left corner: 0°, -30°, -45°, -60°, and -90°.

6.3 Conclusions

The wind tunnel measurements of the flow field inside the container array significantly extended the MUST field measurements and highlight the influence of the irregular array arrangement on the obtained results. The comparison between the wind tunnel and MUST field data has been shown on the vertical profiles of the mean wind speed and vertical momentum flux at the position of the T tower (Fig. 6.23). The values of $\overline{u'w'}$ agree very well, whereas the U_{mean} profiles differ significantly inside and directly above the container array (the field values are about 1 m s^{-1} smaller at the 1, 4, and 8 m levels; the same values in the wind tunnel and field were measured at the 16 m level). The reason for this difference can be the MUST field atmospheric thermal stratification, which was E (slightly stable conditions) or F (moderately stable conditions) class according to the Pasquill's stability classes classification (see section 3.4). A stable stratification of ABL is characterised by a suppressed mean wind speed and turbulence level in the Surface Layer. Since we observed only a suppressed mean wind speed, the turbulence level had to be increased by the mixing effects of the containers.

The measurement at the 2H level for various wind directions showed no effects of the container array on the flow direction and only minor effect on the wind speed. The wind speed was increased approximately 5% (from 4.8 to 5.1 m s^{-1}) due to the blockage effect of the array, which force flow to slow down in the canopy and consequently to speed up above it to ensure the conservation of mass.

Inside the canopy the flow was guided by the containers. The street canyons oriented along the x-axis (Fig. 6.1) were approximately 1.5 wider than the street canyons oriented along the y-axis (12.9 and 7.9 m, respectively). They were also much longer since the container walls, which were creating these canyons, were 12.2 m long in contrast with 2.42 m of the walls in the the street canyons oriented along the y-axis. Therefore the flow preferred the street canyons oriented along the x-axis (called the wide street canyons) and if the wind approached under an oblique angle, i.e. different from 0° and -90°, it adapted to the array geometry very quickly: below the shallow transition zone around the container height the velocity vectors were oriented parallel with the wide street canyons. The original wind direction appeared only in the street canyons oriented along the y-axis (called narrow street canyons), where a changeover between two wide street canyons took place.

The velocity standard deviation, U_{rms}, which was chosen as a measure of turbulence level, was highest at the container height level for all wind directions. This was in good agreement with the observation of the vertical momentum fluxes, which showed maximum values also at this height. Hence, the roof level was an area of the maximum vertical mixing, where vortex structures created by the individual containers interacted with the free stream above the canopy. With the increasing approach wind angle (from 0° to -90°) the absolute maximum of the U_{rms} decreased, which is again connected with the overall blockage of each set-up, which gets smaller with increasing approach wind angle. Since the containers projection to the plane, which is normal to the wind direction,

is smaller the wakes behind the individual containers also get smaller and less pronounced. The turbulence level is even higher inside the canopy, below the container height level, although the U_{rms} values are smaller. This is due to also smaller mean wind speed at this area.

For the wind directions 0° and -90° the sharp border between the U_{rms} values measured in the along-wind and across-wind street canyons was pronounced. The along-wind street canyons are 'alleys' or 'passages', where the flow can go though easily and even the 'jetting effect' was seen, with low turbulent flow. The cross-wind street canyons created a sequence of cavities, where the flow had to 'jump' from one to the other. Such a blockage is of course connected with the vortex shading, very intermittent flow field pattern, and enhanced turbulence. The situation was different for oblique wind directions: there were no 'alleys' and the flow had to override scattered obstacles, which caused an increased turbulence at the whole array.

A significantly different behaviour of the flow field was seen in the first street canyons (in the direction of the approach wind) in contrast with the rest of the array (Figures 6.19–6.27). The impact of the relatively less turbulent approach flow (class 'moderately rough' according to the VDI Guideline 3783/12, 2000) to the container array created a large wake structure on the roof and behind the first container, decreased the mean wind speed, and enhanced turbulence of the flow (especially the vertical momentum transport). The flow was displaced upwards, i.e. it was slower and more turbulent inside the canopy behind the first container row. Therefore a wake adherent to the next container was smaller and weaker, and also the vertical momentum transport was smaller. The structure of wakes is unchangeable inside the array (from the second container row) except from the VIP car and misaligned containers (discussed later). The same influence of the upwind obstacle configuration was shown by Kastner-Klein and Plate (1999) and lead to the assignment of the flow structure within the container array to be the wake interference flow (according to work of Oke, 1987).

The level of the container height was chosen for the horizontal plane measurement of the vertical momentum transport since the vertical profiles of $\overline{u'w'}$ at this level often reached their maximum values. The enhanced vertical momentum transport is connected with the wake behind the container and therefore the highest values were observed in the case with the largest wake, i.e. 0° approach wind direction. Also an area of higher values was larger for this wind direction. With the increasing approach flow direction angle, the wake structure became smaller and weaker, which consequently influenced the values of the vertical momentum transport.

The VIP car, which was place instead of one container in the middle of the array near to the T tower and which had completely different dimensions to the other containers (see chapter 3) could heavily influenced measurement taken at the T tower. The profiles of the mean wind speed and vertical momentum transport (Figures 6.19–6.27) were significantly different from the spatial averaged profiles if the profiles were situated directly behind, i.e. in the wake, the VIP car. The VIP car was 1.5 times higher than containers and consequently its wake had different parameters, which have clearly demonstrated in

the measured profiles. For example, the T tower was situated in this influential position for the 0° approach wind direction (Fig. 6.19); both the U_{mean} and $\overline{u'w'}$ profiles were remarkably different from the spatial averaged ones. Without a knowledge of this phenomenon, the measurement taken at the T tower could be consider as a typical profiles for the whole array and wrong statements could be drawn as a result. Also the array irregularities played an important role, when focusing in detail on the flow within the canopy.

Chapter 7

Passive Pollutant Dispersion

The wind tunnel dispersion experiment as described here was designed to replicate the MUST field campaigns and also extend the available data sets. The first group of experiments in the MUST field campaigns consisted of continuous tracer releases with a typical time of continuous release of 15 minutes in the full scale. The extended data sets include measurements with high spatial resolution, which were not available from the MUST field campaign, the validation of the simultaneous concentration measurements at different places and derived characteristics as the spatial cross-correlation coefficients and the travelling time. The second group of the MUST field campaigns were sudden (often called puff) releases experiments. An evaluation of these puff releases with respect to the Reynolds number, duration of releases, position in the container array, etc., was also part of this work. All measurements were taken using a fast Flame Ionisation Detectors (FFID, described in section 4.4) with every measurement taking four minutes in the model scale to ensure a sufficient long time for statistical data processing (see discussion in section 7.1.2). Background concentration measured by a slow Flame Ionisation Detector (SFID) in front of the wind tunnel test section was subtracted from the FFID data.

All concentration values will be presented in dimensionless form according to equation 2.20:

$$c^* = \frac{c\,U_{ref}\,H^2}{Q_{\text{source}}} \tag{7.1}$$

where c is the measured volume concentration, U_{ref} is the reference wind speed measured at 8 m at the location of the south tower (obtained from equation 5.4, see discussion in section 5.2), H is the container height, and Q_{source} is the volume source strength controlled by a mass flow controller (for instrumentation details see chapter 4).

7.1 Validation of the Experiment

The legitimacy of using the dimensionless concentration c^* (equation 7.1) is among others based on the Reynolds number independency theory (section 2.3.2) and on an assumption of a passive behaviour of the tracer. Both theories have been proven at a few points within the container array and their position

can be found in Fig. 7.1. The tests were conducted for the approach wind direction of -41° and for the source number 29. This set-up corresponds to the MUST trial number 2681849 (see Biltoft, 2001) on 25th September, 2001. Also measurement uncertainties, repeatability, and influence of the averaging time will be discussed and evaluated.

7.1.1 Measurement Uncertainties and Repeatability

Uncertainties of the results will be described here. During one month of measurement several points were measured repeatedly with a different reference wind speed and different source strength. A summary of these points is given in table 7.1. The number of repetitions (the fifth column) ranged from 42 to 343.

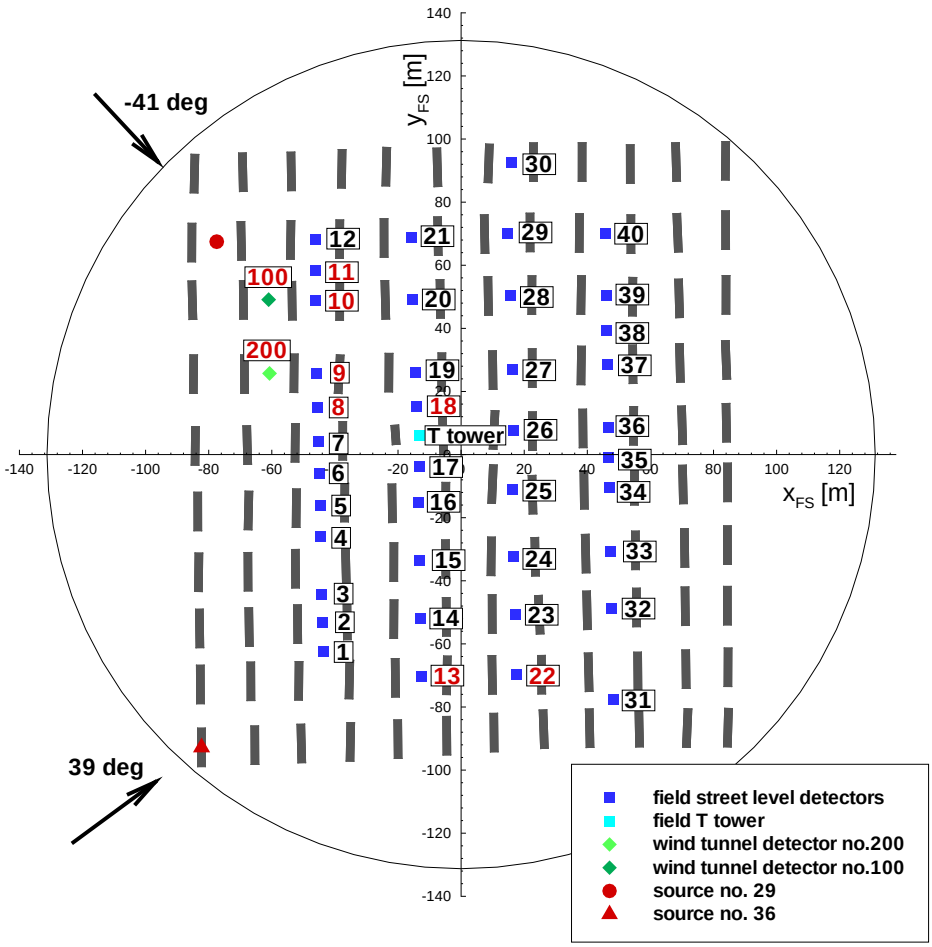

Figure 7.1: The sketch of the container array with the depicted approach wind directions and used sources (source no. 29 and no. 36 were used for the -41° and 39° wind direction, respectively). The numbering of the detectors according to the MUST field campaign (street level dPIDs no.1–40 and dPIDs no. 41–48 placed on the T tower, Biltoft, 2001) and the additional wind-tunnel ones (no. 100 and 200) is shown. Red labelled detectors were used for the experiment evaluation.

The sixth column in table 7.1 shows the dimensionless ensemble mean concentration values $\langle c^* \rangle$, the seventh and eighth columns show the ensemble standard deviation and relative ensemble standard deviation in percentage, respectively. The relative ensemble standard deviation can be assigned as a natural fluctuation caused by environmental and small instrumentation fluctuations (for example: temperature, pressure, and humidity fluctuations in the wind tunnel; stability of instruments; electricity noise; uncertainty of the position setting; etc.). Since the presented ensembles were obtained during such a long time period, all random fluctuation are assume to have normal distribution, i.e. 95% of the samples lie in the range $\langle c^* \rangle \pm 2 \cdot c^*_{\mathrm{rms}}$.

detector number	x_{FS} [m]	y_{FS} [m]	z_{FS} [m]	no. of samples	$\langle c^* \rangle$ [-] $\cdot 10^{-3}$	$\langle c^* \rangle_{\mathrm{rms}}$ $\cdot 10^{-3}$	$\langle c^* \rangle_{\mathrm{rms}}$ [%]
8	-45.50	14.85	1.60	72	35.8	0.7	1.9
8	-45.50	14.85	2.55	75	36.6	0.9	2.5
8	-45.50	14.85	5.10	42	28.0	0.4	1.6
9	-45.80	25.65	1.60	71	30.2	1.7	5.5
10	-46.02	48.72	1.60	66	2.24	0.31	14
11	-46.20	58.43	1.60	52	0.15	0.09	57
18	-14.00	15.35	1.60	62	4.87	0.41	8.5
100	-77.85	8.47	1.28	260	87.3	6.3	7.3
200	-60.72	25.72	1.28	343	68.5	2.6	3.7

Table 7.1: Repeatability test overview.

The uncertainties value does not indicate any relation to the numbers of the samples, i.e. the smallest ensemble with 42 samples is statistically treatable. It is obvious that the measurement uncertainties increases with decreasing mean concentration value. This phenomena is caused by the highly intermittent behaviour of the plume within the container array. Detector no. 11 lies at the edge of the plume (see Fig. 7.9)and the four minutes sampling time does not ensure trustworthy mean value in this case. The closer the detectors are to the centre of the plume, the smaller the uncertainties (detectors 11, 10, 9, 8 in row from the plume edge to the plume centerline - see Fig. 7.1 for the detector positions and Fig. 7.5 for the position of the plume centreline).

7.1.2 Averaging Time Independence

The above mentioned data set (table 7.1) was used for the averaging time independency test. Time series of different length were cut out from the 4-minutes time series taken in the wind tunnel. The ensemble statistic for each cut was conducted for measurements at the positions of detectors 8, 9, 10, and 18 containing 72, 71, 66, and 62 samples, respectively. The shortest cut had length $t^* = 1000$ (typically $t_{\mathrm{MS}} \doteq 8$ s, $t_{\mathrm{FS}} \doteq 10$ min), the longest $t^* = 30000$ (typically $t_{\mathrm{MS}} \doteq 4$ min, $t_{\mathrm{FS}} \doteq 4$ hours). The cuts were treated as a whole time series and the ensemble standard deviations of the statistical moments and the concentration integral length scale (for the definitions see section 7.2) are shown

in Fig. 7.2.

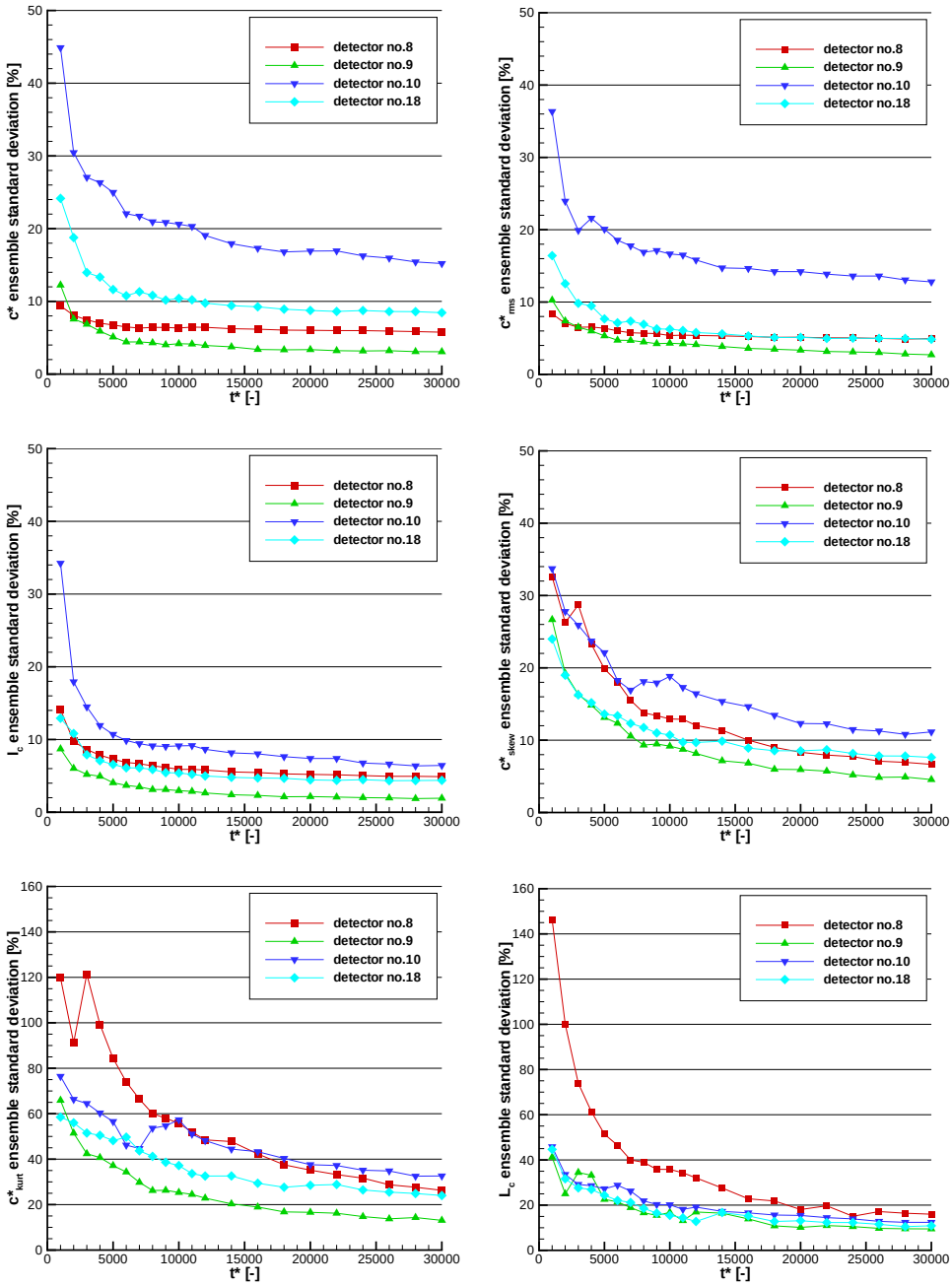

Figure 7.2: Dependency of the ensemble standard deviations of the concentration time series statistical moments (mean (upper left chart), standard deviation (upper right), concentration fluctuation (middle left), skewness (middle right), kurtosis (lower left), and integral length scale (lower right)) on the dimensionless time length of the concentration time series at the locations of detectors no. 8, 9, 10, and 18 (see Fig. 7.1).

This test was motivated by an effort to estimate measurement errors for the field measurements, where no repetition of the trials were available. The typical trial time in the field was 15 minute, which means $t^* \doteq 3100$ for the 2681849 trial and $t^* \doteq 1100$ for the 2692157 trial. In contrast the wind tunnel series were always longer than $t^* = 30000$. Therefore a different accuracy of the statistical characteristics based on both measurements was expected.

The ensemble standard deviation decreases with increasing concentration time series length, i.e. the statistical moments based on the longer time series is more precise. The shape of all curves in Fig. 7.2 can be described as an exponential decrease of the ensemble standard deviation with the time. Different moments have different minimum ensemble standard deviation (called value of convergence and given by the turbulent characteristic of the flow and instrumentation uncertainties) and speed of decay. The accuracy of the statistical moments estimation is dramatically improving for each time step ($t^* = 1000$) for the shortest averaging times. After this region of the shortest times only the very low improvement (below 0.5%) is associated with the next increase of the time series length. Therefore the value of convergence can be estimated as a extrapolation of the ensemble standard deviation curve to infinity.

The value of convergence for the ensemble standard deviation of the dimensionless concentration (upper left chart in Fig. 7.2), standard deviation of the dimensionless concentration (upper right chart in Fig. 7.2), and fluctuation intensities (middle left chart in Fig. 7.2) vary between 4% (position of the detector no. 9 at the first detector row, close to the plume centerline) and approximately 12% (position of the detector no. 10, at the plume edge area). The decay of the ensemble standard deviation for these three characteristics is faster than in the case of the higher order moments (see later). The value of convergence is reached for the averaging time $t^* \approx 15000$ with reasonable accuracy (+5% of the value of convergence).

The higher statistical moments are more sensitive to the length of the time series. Therefore the decay of the ensemble standard deviation of the skewness (middle right chart in Fig. 7.2) and kurtosis (lower left chart in Fig. 7.2) is slower than in the case of the lower statistical moments. The dimensionless time $t^* = 30000$ is not long enough to reach a value of the convergence for these characteristics. The uncertainty caused by an insufficient averaging time can not be completely removed from the results for this averaging time. The ensemble standard deviation values also vary for different locations: the highest uncertainties (11% for skewness and 35% for kurtosis) were found at the plume edge, and the smallest at the plume centerline (5% for skewness and 15% for kurtosis).

The value of convergence for the ensemble standard deviation of the concentration integral length scale (lower right chart in Fig. 7.2) was reached with the sufficient accuracy within the conducted averaging time range. In this case all locations showed very similar values (value of convergence was about 14%) independent of the location within the plume, i.e. the edge and centerline locations did not differ in accuracy of the concentration integral length scale estimation. Also the decay was fast enough to reach value of convergence with reasonable accuracy (+5% of the value of convergence) around $t^* = 20000$.

The highest ensemble standard deviations for all statistical moments were found at the position of detector no. 10, at which the lowest dimensionless concentrations were measured (see table 7.1). This point was situated at the plume edge area, at which mixing of the clear and polluted air took place. Prediction of the behaviour is very difficult at the plume edge due to the influence of the atmospheric motion of the largest turbulent scales, which appears approximately once per hour in the atmosphere and therefore a long averaging time is needed to obtain representative value (see discussion in section 2.2). In contrast the smallest ensemble standard deviations, i.e. the most accurate results, were found near the plume centerline, where smallest spatial gradient of the concentration could be found. This nearly homogeneous concentration field provides the low sensitivity of the concentration field on the largest, i.e. most seldom occurred, vortices, since the turbulence mixes parcels of air with very similar content of a passive tracer.

7.1.3 Reynolds Number Independence

The Reynolds number dependency test is closely related to the Reynolds number independency test carried out during the boundary layer documentation campaign (section 5.2). In the case of the constant averaging time (also our case) the Reynolds number test is influenced by the length of the averaging time, since the dimensionless time (equation 2.23) is a function of the reference wind speed. The accuracy of the statistical properties (e.g. mean, standard deviation, etc.) increases with the length of the time series (see previous section 7.1.2). Therefore the concentration mean values plotted in Fig. 7.3 were obtained from the concentration time series of the same length $t^* = 14133$, which means 240 to 77 s in the full scale for the reference wind speeds from 2 to 6.3 m s^{-1}.

A different critical Building Reynolds numbers was found for different orders of the velocity moments. The upper left and right charts in Fig. 7.3 show the dependency of the dimensionless concentration c^* and concentration standard deviation c^*_{rms} on the reference wind speed and consequently on the Building Reynolds number (equation 2.28). Detectors no. 10, 13, and 18 indicate the Reynolds number independency in the whole measured velocity range $U_{ref} =$ 2–6.4 m s^{-1}, i.e. $Re_B = 4500$–14500. The position of detector no. 9 shows a different behaviour: both the dimensionless concentration and concentration standard deviation decrease with increasing wind speed for $Re_B < 8500$.

The highest variances of the concentration fluctuation (middle left chart in Fig. 7.3), skewness (middle right chart in Fig. 7.3), and kurtosis of the concentration time series (lower left chart in Fig. 7.3) were found at the location of detector no. 10, where also the highest uncertainties of the values appeared. The values are constant for all measured positions in the range of the uncertainties. The concentration integral length scale (lower right chart in Fig. 7.3) is also independent on the reference velocity at all four positions.

Reynolds number independency is assumed to be valid above $U_{ref} = 4$ m s^{-1}, i.e. $Re_B = 9000$, since no dependence of the measured properties on the reference wind speed was found above these values. The result is in good

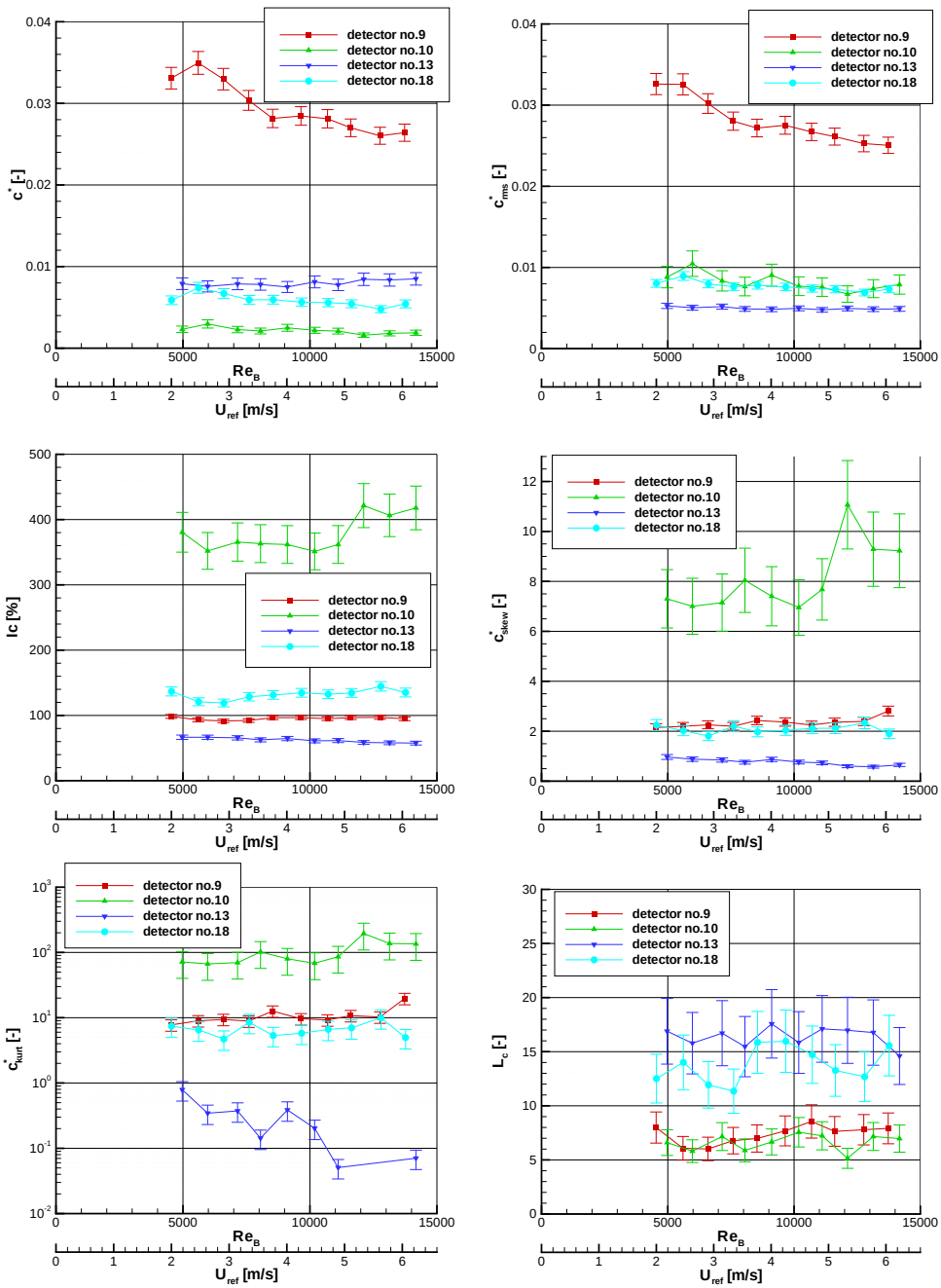

Figure 7.3: Building Reynolds number independency test at four different locations (see Fig. 7.1 and tables 7.1, B.6 for the position description). X-axis is showing the reference wind speed at 8 m on the S tower and the corresponding Building Reynolds number, y-axis is showing the dimensionless concentration (upper left chart), dimensionless concentration standard deviation (upper right), concentration fluctuation (middle left), concentration skewness (middle right), concentration kurtosis (lower left), and concentration integral length scale (lower right), respectively. The error bars are based on the measurement uncertainties specified in section 7.1.2 for the given averaging time.

agreement with the estimation of the critical Building Reynolds number based on the velocity time series examination (see section 5.2).

7.1.4 Source Strength Independence

Equation 7.1 also proposes that the dimensionless concentration is independent of the source strength. This fact is based on the assumption of a passive behaviour of the tracer, i.e. the amount of the released tracer is negligible in comparison with the amount of passed air and also that the density of the tracer is comparable with the air density and therefore no buoyancy forces appear. The density of ethane, which was used as a tracer during the wind tunnel measurements, is $\varrho_{\text{ethane}} = 1.25$ kg m^{-3} in standard atmospheric conditions ($T = 15°$C, $p = 101.3$ kPa). The variation from air density $\varrho_{\text{air}} = 1.229$ kg m^{-3} is negligible in the very turbulent flow inside and above the container array.

Propylene with standard density $\varrho_{\text{propylene}} = 1.72$ kg m^{-3} was used as a tracer during the MUST field campaign. The density difference between the tracer and air is almost 40%, which could be significant. Unfortunately no source strength test was conducted during the MUST field campaign, but on the other hand the typical measured concentration was of the order of tens of ppm (particles per million), in which case the different propylene density can hardly change the overall density of the mixture of air and tracer. The effects of the density is important near to the source (up to several source diameters), where also the source design is important. Since this area (near the source) was out of our focus the effects of both different density and source design was neglected for the values measured in the next street canyon behind the source.

Figure 7.4 illustrates the tests, for which the source strength has been systematically changed for stationary flow conditions (constant wind speed $U_{ref} \doteq 5$ m s^{-1} and wind direction, averaging time $t^* \doteq 35000$). No dependence of c^* on the source strength was found for the whole measured range $Q_{\text{source}} =$ 10–100 l hour^{-1}.

The intervals for the reference wind speed and the source strength were established based on the results of the tests. The reference wind speed was always in the range $U_{ref} \in (4.5;\ 5.5)$ m s^{-1}, i.e. $Re_B \in (10000;\ 12500)$, and the source strength varied in the range $Q_{\text{source}} \in (10;\ 70)$ l hour^{-1} depending on the reference wind speed, a distance between the measurement point and the source, and a measurement range of FFID. The measurement time was set up to be four minutes, which according to equation 2.23 corresponds with the dimensionless time in the range $t^* \in (32000;\ 39000)$ and full scale time $t_{\text{FS}} \doteq 5.5$ hours, to capture a sufficiently long concentration time series and to minimise measurement uncertainties due to averaging time phenomena.

7.2 Single Concentration Statistics

As was said in chapter 3, only two particular days (25th and 26th September, 2001) were chosen for the comparison. From these two days two trials (named 2681849 and 2692157 in Biltoft, 2001) were repeated in the wind tunnel for

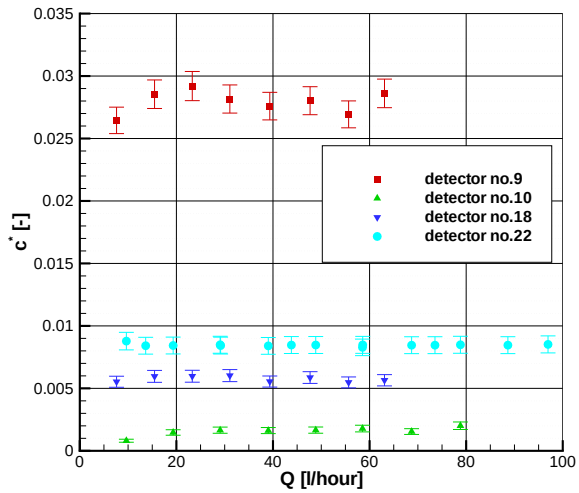

Figure 7.4: Source strength independency test at four different locations (see Fig. 7.1 and tables 7.1, B.6 for positions description). The error bars are based on the measurement uncertainties specified in section 7.1.2 for the given averaging time.

the comparison. The MUST field detectors sampled with 50 Hz frequency and the time series with continually released tracer and steady atmospheric conditions lasted 900 s, i.e. 0.25 hour. Single concentration statistics (e.g mean, standard deviation, and many others) were, in the case of the wind tunnel campaign, derived from the four-minute (in model time, which according to equation 2.23 typically corresponds with 5 hours) time series with a typical sampling frequency of 150 Hz.

Since the flow measurements were not taken for either -41° nor 39° wind direction, which are the wind directions connected with the trials 2861849 and 2692157, another measurement was conducted with the set-up, which was changed according to the wind tunnel flow measurement performed. The wind direction was set to -45° and the height of all detectors to half of the container height ($z_{\mathrm{FS}} = 1.275$ m) instead of 1.6 m in the case of the MUST field campaign. The established set-up corresponded with the case, for which the flow field has already been measured - see chapter 6. These experimental procedure were motivated by an effort to complete flow and concentration data for one particular case, which would be helpful for a deeper insight of physical phenomena.

The comparison between the wind tunnel and field data for trial 2681849 (and also for 2692157 in the case of the mean dimensionless concentration) as well as a spread of the statistical characteristics within the whole plume for the case of the changed set-up (-45°) can be found in the following section. The results presented here are based on the continuous tracer releases.

7.2.1 Mean Concentration

The mean concentration was calculated as a zero central moment (see section 5.2) of the dimensionless concentration time series calculated according to equation 7.1. The approaching wind direction, source, and detector positioning is depicted in Fig. 7.1, exact coordinates of the sources and detectors can be found in appendix B.

The comparison of the street level detected concentrations (measured at z_{FS} = 1.6 m = $0.63H$) for the 2681849 case is shown in Fig. 7.5. The upper chart shows the first and the second detector row, the lower shows the third and the fourth row. The error bars in the figures are based on the ensemble standard deviations (see section 7.1.2) for the corresponding averaging time. The reason for greater error bars on the field values is the much shorter averaging time in the field ($t^* \doteq 3100$) than in the wind tunnel ($t^* \doteq 30000$).

It should be mentioned that the detector rows did not lie in a line perpendicular to the wind direction. Therefore the shape of the mean concentration horizontal profiles created by detector lines are not symmetric and the position of the plume centerline tends towards the right hand side (in the fourth detector row the plume centerline is already out of the container array). The qualitative comparison of the MUST field data and the wind tunnel data is reasonable: the corresponding curves have the same shape - the maximum of the mean concentration was reached at the same position. The absolute wind tunnel values near the plume centreline was about two thirds of the field values, however, the plume edge values were in a very good agreement. This observation points to a wider plume in the wind tunnel. The disagreement in the plume centerline concentration magnitudes can be caused for two reasons: firstly, the stratification during the field campaign was slightly stable, secondly, the propylene, which was used as a tracer during the MUST field campaign can tend to behave like a heavy gas, i.e. stays on the ground.

The slightly stable stratification can be connected with several phenomena: (i) a weaker turbulence level, which can cause a higher ground level concentration and also a weaker horizontal spread of the tracer; (ii) the vertical mean wind speed profile can not be described by the logarithmic law as is shown in section 5.3.1. The modified mean wind vertical profile can be found e.g. in Stull (1988) where it suggests a lower wind speed at the lower elevations than for the neutrally stratified ABL. This can cause nonuniform scaling, i.e. the same reference velocity, which was measured at the 8 m level at the position of the S tower, means a different velocity at the lower levels (inside the container array) for neutral (i.e. wind tunnel) and slightly stable (i.e. field) stratification. The lower wind speed inside the canopy, which will appear during the slightly stable period in the field, would cause worse ventilation, i.e. higher concentration values; on the other hand, a higher wind speed in the neutral case in the wind tunnel would enhance higher turbulence level and consequently a wider plume with smaller centreline values.

The theory of higher ground level concentrations can be proven by measurement from the T tower (see Fig. 7.1) shown in Fig. 7.6. Since both the MUST field and wind tunnel concentration vertical profiles have again the same shape

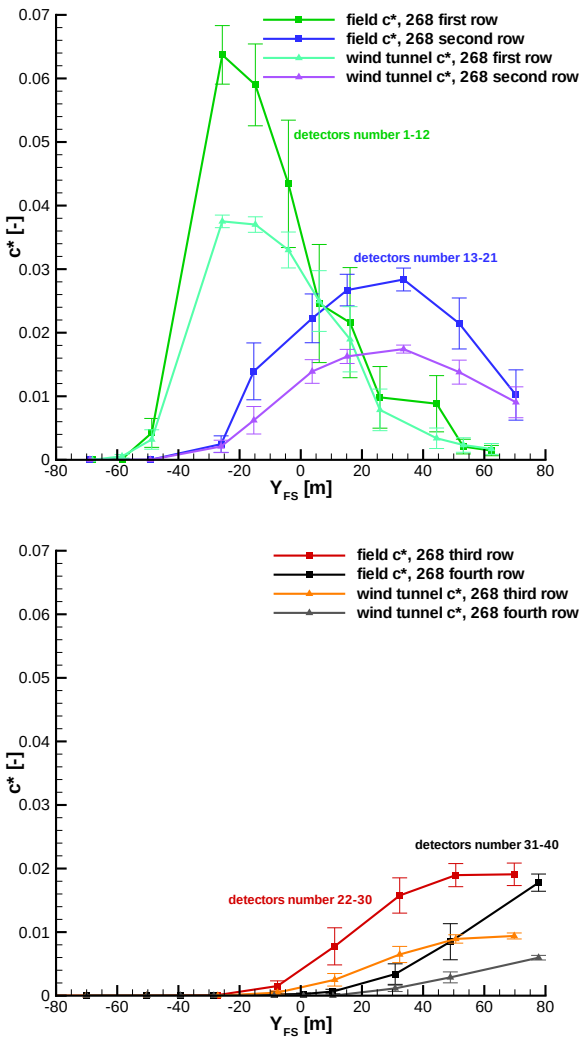

Figure 7.5: Comparison of the MUST field (depicted by the squares) and wind tunnel (depicted by the triangles) mean dimensionless concentration for the trial 2681849 (-41° wind direction and source no. 29). The first row of detectors (from dPID no. 1 on the right hand side to dPID no. 12 on the left hand side, see Fig. 7.1) is drawn by the blue coloured symbols, the second row (no. 13–21) by the green ones, the third row (no. 22–30) by the red ones, and the fourth row (no. 31–40) by the black coloured ones.

and different magnitudes (in the higher elevations the MUST field data are approximately twice that of the wind tunnel data), the different tracer density (i.e. the tendency of the heavier gas to stay near the ground) can not be the reason for the measurement disagreement.

Figure 7.7 shows the same comparison as Fig. 7.5, but for trial 2692157 (conducted on 26th September, 2001, used source no. 36, wind direction 39°, detector height $0.63H$, see Fig. 7.1). The wind came from the other direction than in the case of trial 2681849, but both directions were close to the diagonal.

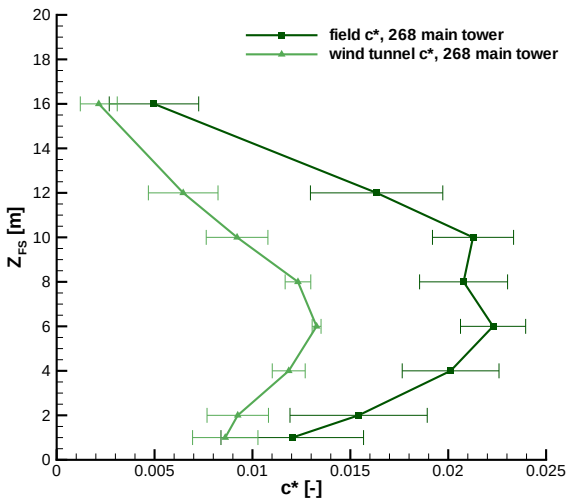

Figure 7.6: Comparison of the MUST field (depicted by the squares) and wind tunnel (depicted by the triangles) vertical profiles of the mean dimensionless concentration at the position of the T tower for the trial 2681849 (-41° wind direction and source no. 29.)

Therefore the behaviour is very similar: the plume centreline moves to left with increasing row number and the shape along the row is highly asymmetric. The greater width of the wind tunnel plume is evident in the first and second row, where the centreline values are in very good agreement with the field data (except a slight centerline position shift), however, the edge values are slightly greater for the wind tunnel measurement.

The mean concentration field is shown in Fig. 7.8 in detail. The position of the selected street canyon is depicted in the upper right picture of Fig. 7.8 and the whole set-up was the same as for the 2681849 trial: -41° wind direction and the ground level source number 29. The concentration inside this street canyon allocated by containers I4, J4, I5, and J5 was measured at three different heights: half of the container height, container height, and twice the container height. The first two cuts at $0.5H$ and $1H$ show nearly exactly the same values, which are in good agreement with the observed strong vertical mixing within the canopy. The concentration values decrease at $2H$ to approximately half of the values reached in the canopy. This observation is in contrast with Fig. 7.6, where an increase of the mean concentration was observed up to the $3H$ ($z_{\mathrm{FS}} \doteq 7.5$ m). However, the position of the T tower, at which the profile in Fig. 7.6 was taken, was found to behave differently then other positions. This position is highly influenced by the presence of the VIP car, which caused enhanced vertical mixing to higher elevations than the regular containers (for more details see section 6.2.1). Therefore the higher concentrations above the container height level are expected in the position of the T tower and the disagreement between the T tower and street canyon (in Fig. 7.8) mean concentration profiles only illustrate the VIP car influence on

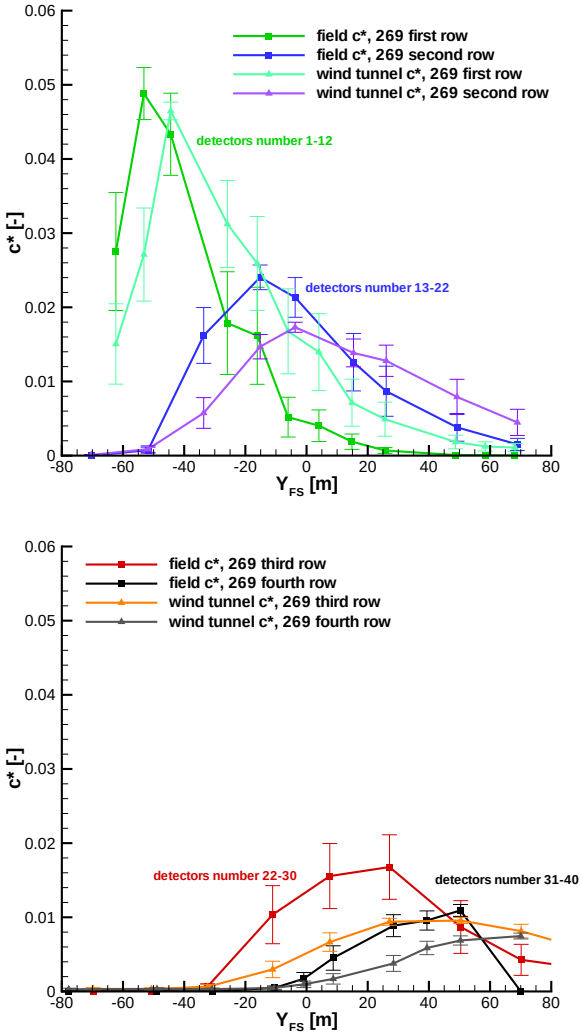

Figure 7.7: Comparison of the MUST field (depicted by the squares) and wind tunnel (depicted by the triangles) mean dimensionless concentration for the trial 2692157 (39° wind direction and source no. 36). The first row of detectors (from dPID no. 1 on the right hand side to dPID no. 12 on the left hand side, see Fig. 7.1) is drawn by the blue coloured symbols, the second row (no. 13–21) by the green ones, the third row (no. 22–30) by the red ones, and the fourth row (no. 31–40) by the black coloured ones.

the concentration field.

The detectors, which were used during the MUST field campaign (see Fig. 7.1), did not cover the whole plume with a satisfactory spatial resolution. Therefore a more detailed grid of measurement points was created for the wind tunnel campaign so as to describe the whole plume. The experiment was set as follows: the source no. 29, wind direction -45°, and all measurements were taken at half of the container height ($z_{\mathrm{FS}} = 1.275$ m). Figure 7.9 shows the results. Measurements were conducted at the points, which are indicated by black dots,

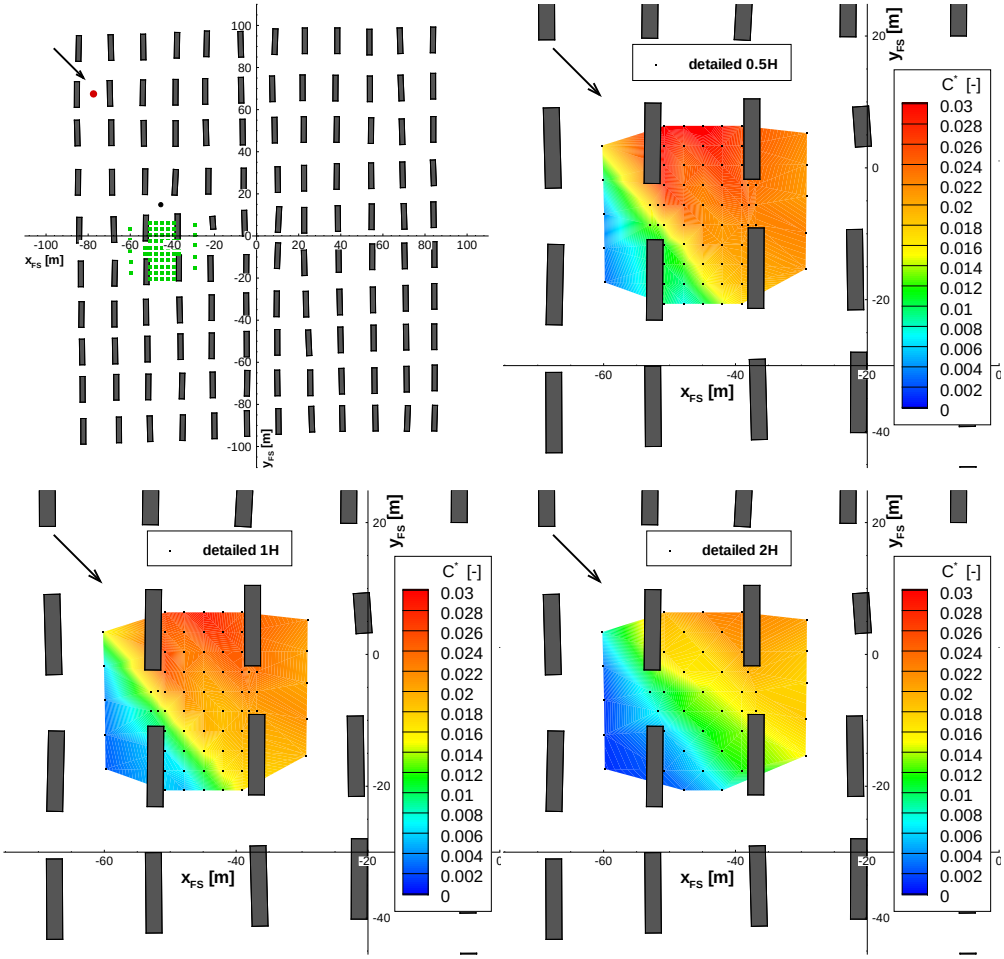

Figure 7.8: Field of the mean dimensionless concentration in one street canyon (its position is depicted in the upper left sketch) at half of the container height (upper right picture), at the container height (lower left), and at the two container heights (lower right) for -41° wind direction and the ground level source no. 29.

the rest of the concentration field was obtained by a triangulation (provided by software Tecplot®) between the measured values. The source is indicated by the red circle and the red line shows an ideal centreline of the plume, which corresponds to the approach wind direction and would be expected in open terrain. The centreline is, however, shifted to the right, which is in good agreement with observation made in chapter 6 that the flow at half of the container height is channelled by the container array and parallel to the 'wide' street canyons oriented along the y-axis. The red line can be more associated with the plume edge.

Flow visualisation conducted during the wind tunnel campaign showed that the ground level source placed in the first street canyon, where the strongest wake vortex is created (discussed in chapter 6), acts more like a volume source: firstly the tracer emitted from the source filled the wake region and than it was

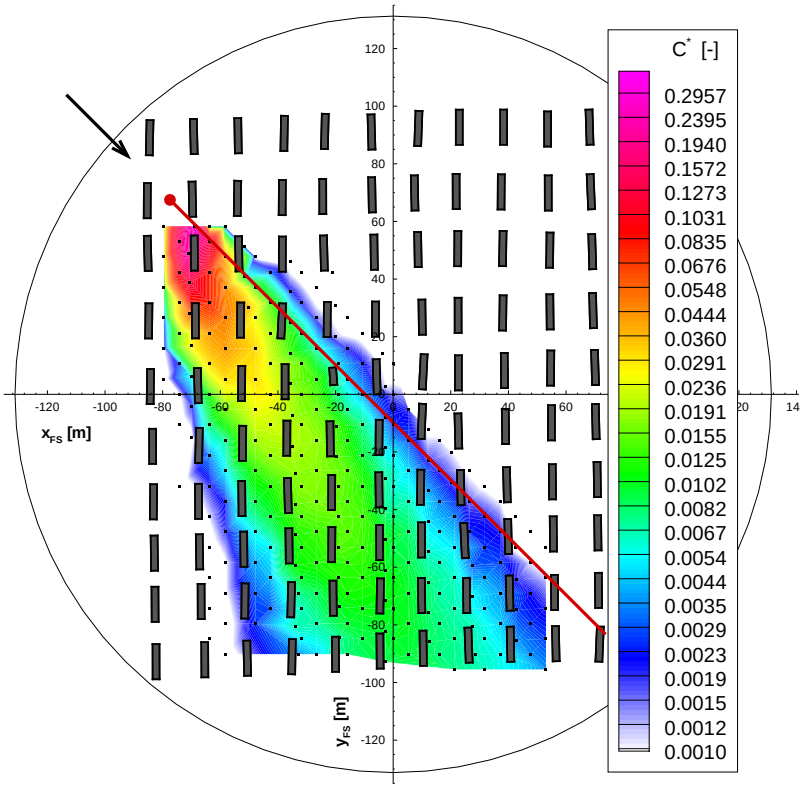

Figure 7.9: Field of the mean dimensionless concentration at half of the container height for -45° wind direction and the ground level source number 29 (red circle). The concentration scale is exponential to highlight the plume structure.

transported further into the array from the volume of the wake and dependently on the wake ventilation, i.e. very randomly in the sense of an amount and direction. Another important phenomenon, which was discovered, is the nature of the tracer transportation: the tracer is advected by the mean wind inside the canopy along the 'wide' street canyons (oriented along the y-axis) taking advantage of enhanced vertical mixing at the positions of container edges and 'narrow' street canyons (oriented along the x-axis) (see Figures 6.14 and 6.28) moving up and down and even reaching the neighbouring street canyon.

7.2.2 Concentration Fluctuations

The same time series as in the previous section were used for the calculation of the second order central moments, i.e. standard deviations labelled c^*_{rms} or σ_c. Figures 7.10 (upper chart), 7.11, and 7.13 (upper chart) show the measured values in the same scale as used in Fig. 7.5. Therefore a direct comparison of the figures is possible. It is obvious that the magnitudes of the mean and standard deviation values are comparable, which is normal in the urban canopy (e.g. Yee and Biltoft, 2004; Pavageau and Schatzmann, 1999). The upper chart in Fig. 7.10 shows the comparison of the concentration standard deviations of

the MUST field and wind tunnel data for trial 2681849. The agreement between the MUST field (depicted by the diamonds in the Fig. 7.5) and wind tunnel (triangles) data is good.

The concentration fluctuation intensity, I_c, which corresponds to the turbulence intensity, can be defined as a ratio of the concentration standard deviation

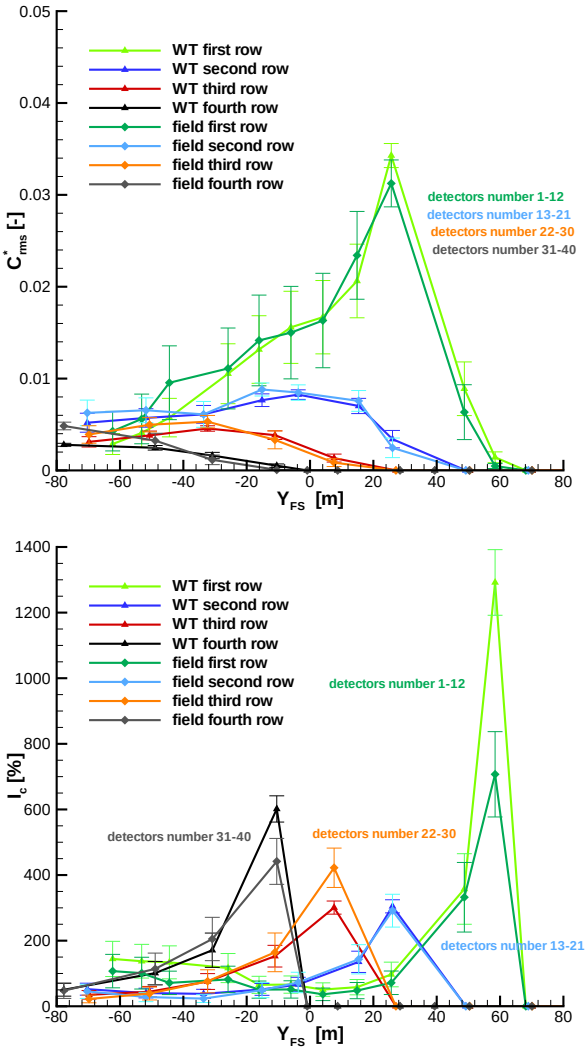

Figure 7.10: Comparison of the MUST field (depicted by the squares) and wind tunnel (depicted by the triangles) dimensionless concentration standard deviation (upper chart) and concentration fluctuation intensity (lower chart) for the trial 2681849 (-41° wind direction and source no. 29). The first row of detectors (from dPID no. 1 on the right hand side to dPID no. 12 on the left hand side, see Fig. 7.1) is drawn by the blue coloured symbols, the second row (no. 13–21) by the green ones, the third row (no. 22–30) by the red ones, and the fourth row (no. 31–40) by the black coloured ones.

c^*_{rms} and mean concentration value $\overline{c^*}$.

$$I_c = \frac{c^*_{\mathrm{rms}}}{\overline{c^*}} \tag{7.2}$$

The comparison of the fluctuation intensity (Fig. 7.10, lower chart chart) is also good, except for the points at the plume edges. However, the values at the plume edge are burdened with a much greater measurement uncertainty than the centerline points. The greatest disagreement appeared in the plume edge due to relatively large uncertainties of the estimation of the concentration mean value (see table 7.1, detector no. 11). In the following rows the coincidence of the slightly higher values of both the mean and standard deviation in the field resulted in very similar values of the concentration fluctuation intensity.

Detailed fields of the c^*_{rms} and I_c are shown in Fig. 7.11 and 7.12, respec-

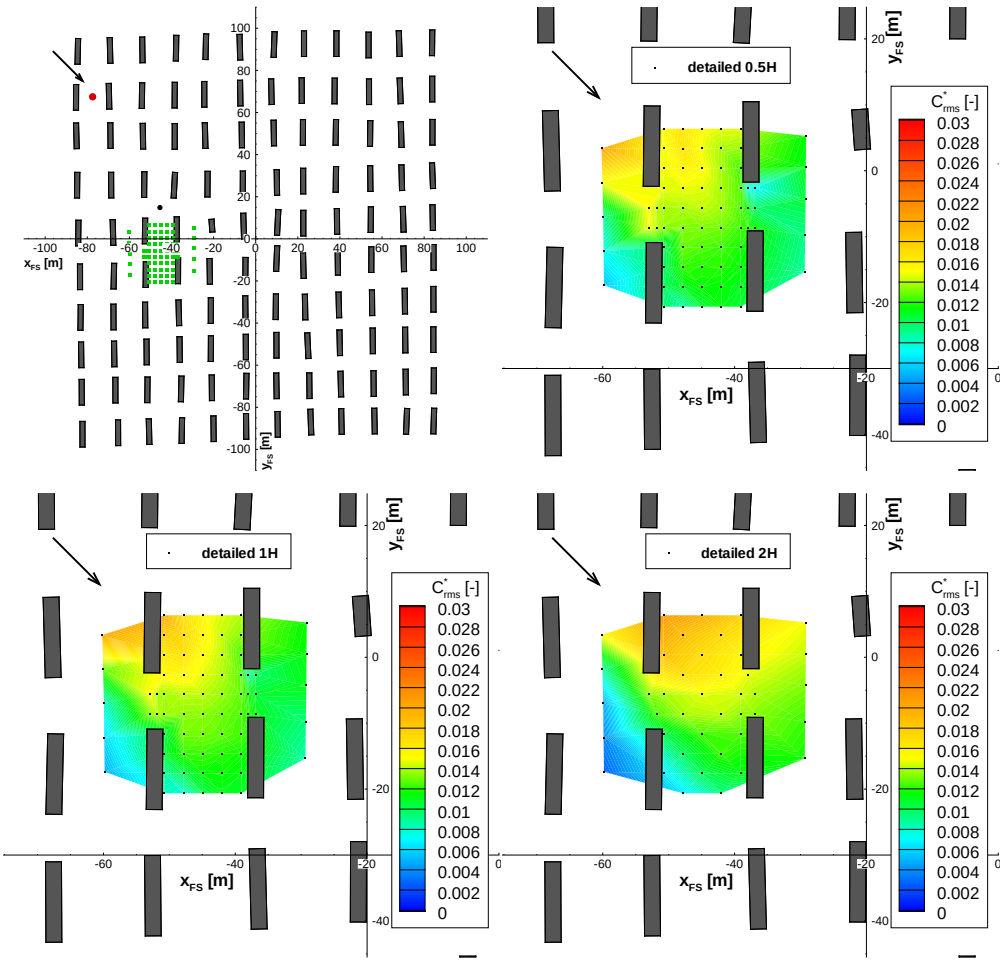

Figure 7.11: Field of the dimensionless concentration standard deviation in one street canyon (its position is depicted in the upper left sketch) at half of the container height (upper right picture), at the container height (lower left), and at the two container heights (lower right) for -41° wind direction and the ground level source no. 29.

tively. The area presented lies in the first detector row around the y-coordinate $y_{\mathrm{FS}} \doteq$ -40 m. The green lines in the Fig. 7.10 show the horizontal profiles along the street canyon, in which the measured area lies, and they indicate the same behaviour as is clearly seen from Fig. 7.11 and 7.12: a decrease of the c^*_{rms} and an increase of the I_c with increasing distance from the source (i.e. with decreasing y-coordinate). This behaviour is even stronger across a section cut perpendicular to the approach wind direction. Also the observation based on the mean concentration field (Fig. 7.8), that very similar values appear at $0.5H$ and H, is still valid. Since the highest level $2H$ is closer to the plume edge (the smaller mean concentration and standard deviation values were observed) the concentration fluctuation intensity at this level is higher than inside the canopy.

The whole plume c^*_{rms} and I_c in a finer resolution is shown in Fig. 7.13. The shape of the contour plots in the upper chart in Fig. 7.13 have the same at-

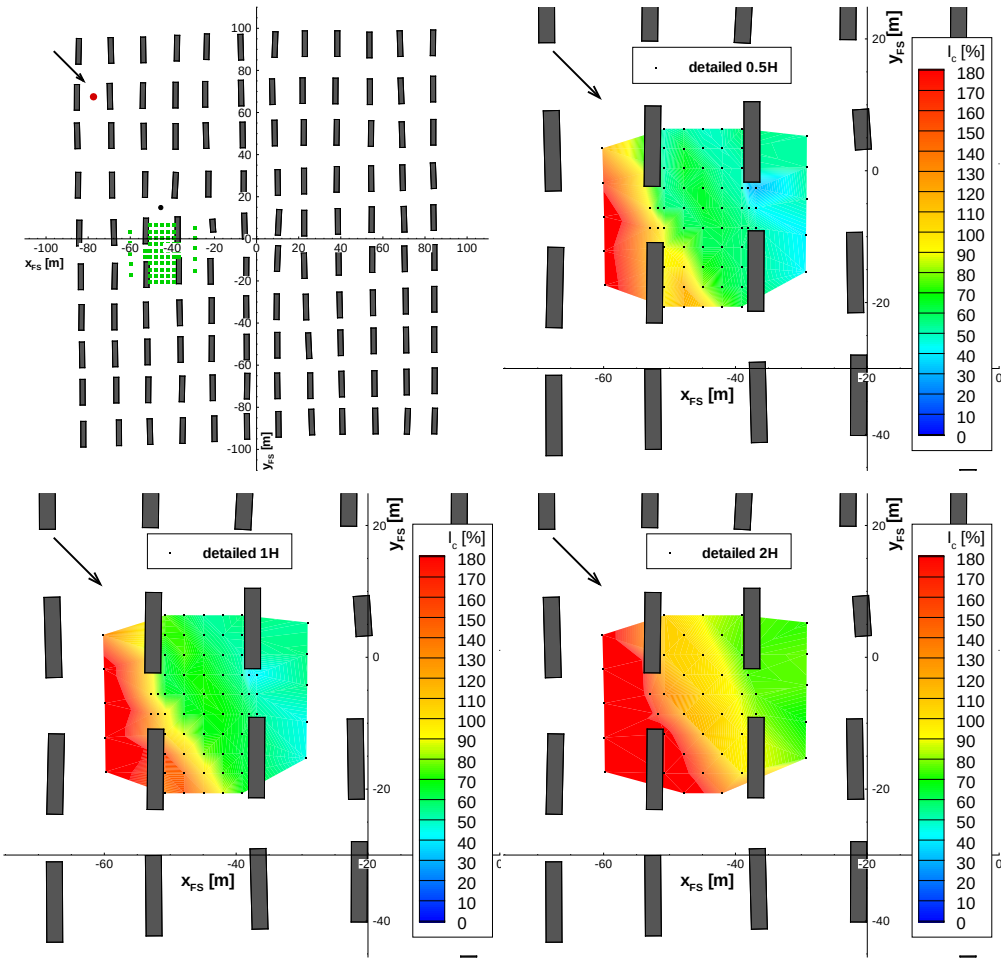

Figure 7.12: Field of the concentration fluctuation in one street canyon (its position is depicted in the upper left sketch) at half of the container height (upper right picture), at the container height (lower left), and at the two container heights (lower right) for -41° wind direction and the ground level source no. 29.

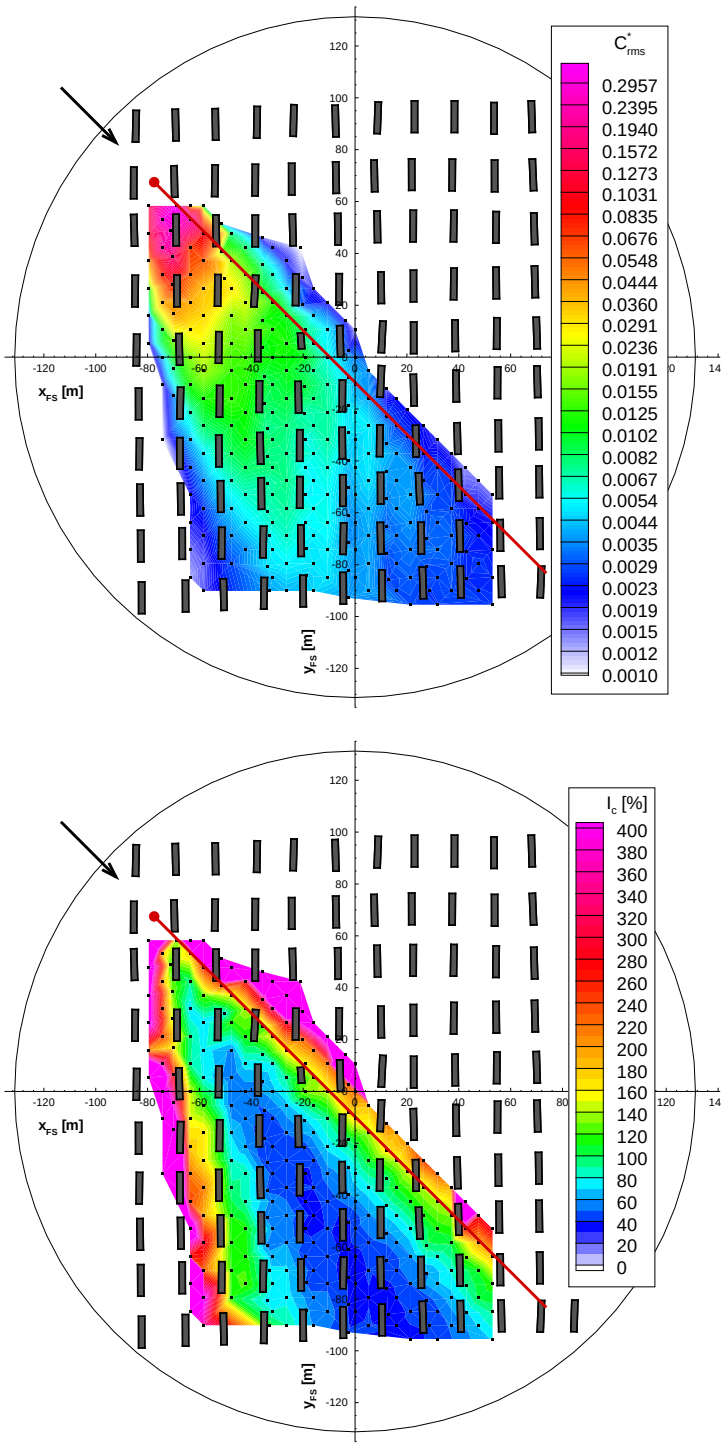

Figure 7.13: Field of the mean dimensionless concentration standard deviation (upper chart) and concentration fluctuation intensity (lower chart) at half of the container height for -45° wind direction and the ground level source no. 29 (red circle).

tributes as the concentration mean values of the plume in Fig. 7.9. The plume is shifted towards the right hand side and the centerline is not straight. This behaviour is not any more visible in the field of the concentration fluctuation intensity (lower chart in Fig. 7.13), which shows the values approximately symmetrically around an axis, which is closer to the approach wind direction than the plume $\overline{c^*}$ and c^*_{rms} centerline. The magnitude of the concentration fluctuation intensity increases at the edges of the plume, where due to measurement uncertainties of about 50% the estimation of I_c is very approximative.

7.2.3 Skewness of the Concentration Time Series

The third moment, skewness (defined in the section 5.2), is shown in Figures 7.14–7.16 (the logarithmic scale is used in Figures 7.15 and 7.16 to enhanced the plume structure). Since all obtained values were positive, the probability distribution of the concentration time series has positive skew, i.e. the higher tail is longer or the higher values are much less probable, at all positions. The magnitude of the concentration skewness c^*_{skew} varies from nearly zero (in the middle of the plume, far from the source, Fig. 7.16) to several tens (estimated with large error, at the edge of the plume). The zero value in the plume centerline far from the source shows a normal probability distribution, which is

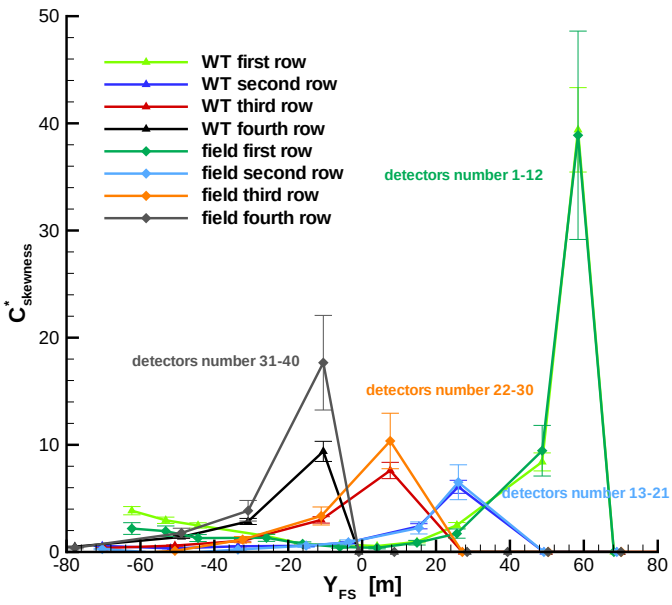

Figure 7.14: Comparison of the MUST field (depicted by the squares) and wind tunnel (depicted by the triangles) skewness of the concentration time series for the trial 2681849 (-41° wind direction and source no. 29). The first row of detectors (from dPID no. 1 on the right hand side to dPID no. 12 on the left hand side, see Fig. 7.1) is drawn by the blue coloured symbols, the second row (no. 13–21) by the green ones, the third row (no. 22–30) by the red ones, and the fourth row (no. 31–40) by the black coloured ones.

expected at locations where the tracer is well mixed with the air.

Figure 7.14 shows the comparison of the MUST field and wind tunnel data for the trial 2681849. The comparison is good and the skewness behaves exactly in the same manner as was observed in the concentration fluctuation intensity case: the minimum value at the plume centerline and the maximum value at the plume edges. The same values were observed at the $0.5H$ and $1H$ levels, and the values at $2H$ reflected the positioning closer to the plume edge by heightened values.

As was showed in sections 5.2 and 7.1.2, the higher order statistical moments are much more sensitive to the stationarity, quality, and length of the time series. Some results in the Fig. 7.16 do not compared well to the others (e.g. the red squares in the area of the blue ones). The points would be expected to lie within

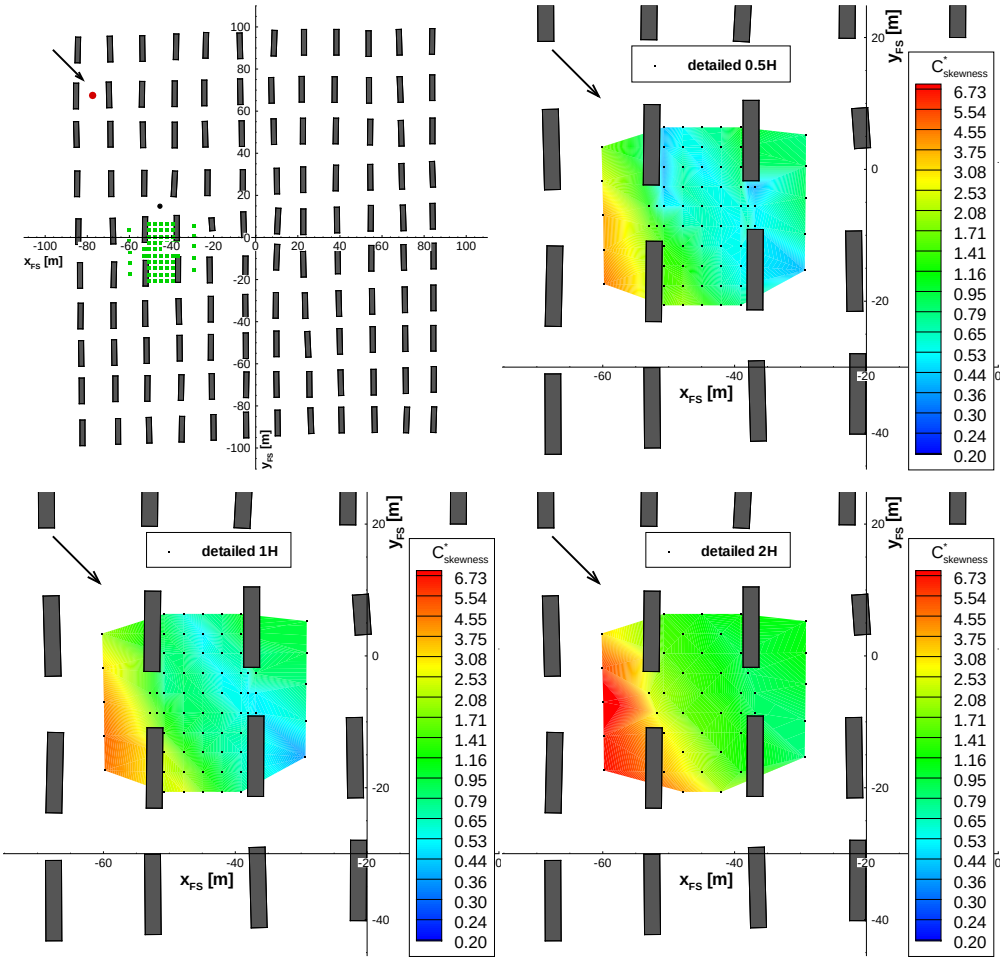

Figure 7.15: Field of the skewness of the concentration time series in one street canyon (its position is depicted in the upper left sketch) at half of the container height (upper right picture), at the container height (lower left), and at the two container heights (lower right) for -41° wind direction and the ground level source no. 29.

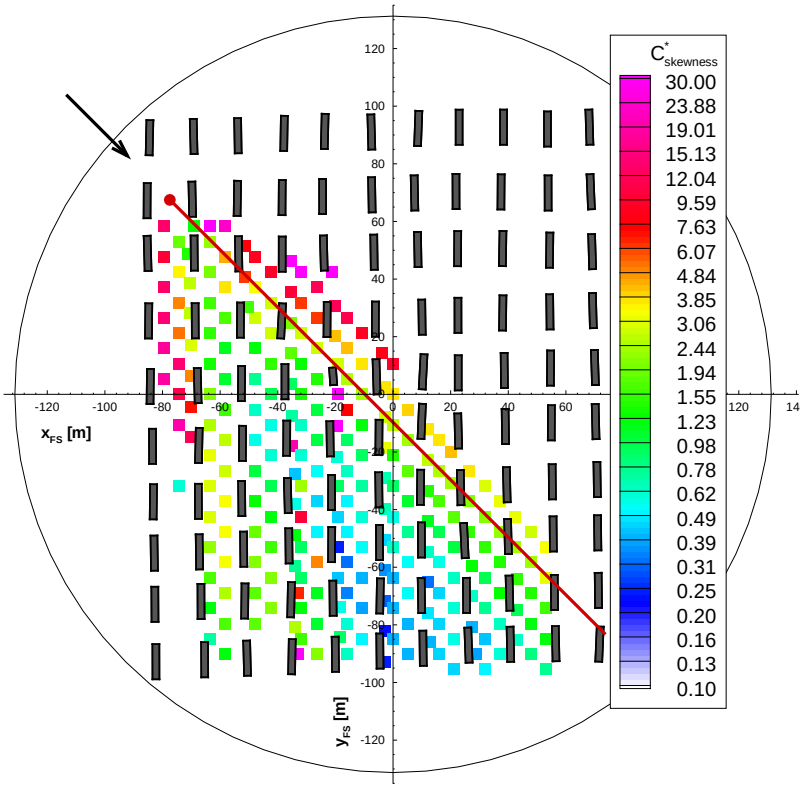

Figure 7.16: Field of the skewness of the concentration time series at half of the container height for -45° wind direction and the ground level source no. 29 (red circle).

the wake area of the container but here show markedly different values from the others. Therefore the triangulation of the result made no sense and a scatter type of the plot was chosen for the representation of these results. The high values appear repeatedly and highlighting more complicated processes, which should not be omitted.

7.2.4 Kurtosis of the Concentration Time Series

The fourth moment, kurtosis (defined in the section 5.2), is shown in Figures 7.17–7.19 (the logarithmic scale is used to enhanced the plume structure). The time series with a high kurtosis is more 'spiky' and the probability distribution has a sharper 'peak' and flatter 'tails', while the normal distribution has a kurtosis that equals to three.

The obtained kurtosis values vary from nearly zero, which means constant time series (downwind in the plume centerline) to several thousands at the plume edges. The spatial distribution within the plume is again the same as in the case of the concentration standard deviation and skewness: a very good agreement between the MUST field and wind tunnel data, with the minimum value at the plume centerline, the maximum value at the plume edge, a constant

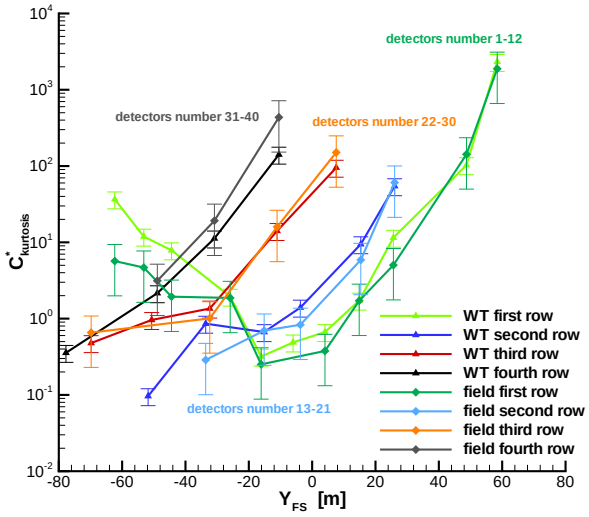

Figure 7.17: Comparison of the MUST field (depicted by the squares) and wind tunnel (depicted by the triangles) kurtosis of the concentration time series for the trial 2681849 (-41° wind direction and source no. 29). The first row of detectors (from dPID no. 1 on the right hand side to dPID no. 12 on the left hand side, see Fig. 7.1) is drawn by the blue coloured symbols, the second row (no. 13–21) by the green ones, the third row (no. 22–30) by the red ones, and the fourth row (no. 31–40) by the black coloured ones.

value inside the canopy, and increased values with the height. The same points, which showed enhanced values of the concentration skewness in the Fig. 7.19, showed also enhanced values of the concentration kurtosis. This observation confirms the theory that the skewness values are not measurement errors but show different behaviour of the wake areas.

7.2.5 Concentration Autocorrelation function

Additionally, for better understanding of connections and structures within the plume it is useful to consider the autocorrelation function of the concentration fluctuations r_c. For both the MUST field and wind tunnel concentration time series, the autocorrelation function was calculated. Some examples of the autocorrelation functions are given in Fig. 7.20. Wind tunnel measurements were extensively repeated at several positions (see table 7.1) to provide repeatability and uncertainty tests. The measurement in the detector positions no. 9 (upper left picture in Fig. 7.20) and 18 (upper right) were repeated 71 and 62 times, respectively. All autocorrelation curves obtained in the wind tunnel are depicted in Fig. 7.20 (coloured lines) and also the MUST field autocorrelation curve (black line, calculated from the time series measured in the field) are shown.

The wind tunnel results show reasonable scatter (up to 10%) in both cases: detectors no. 9 and 18 with more than 60 repetitions and detectors no. 23 and 32 with 7 repetitions. The agreement between the MUST field and wind tunnel

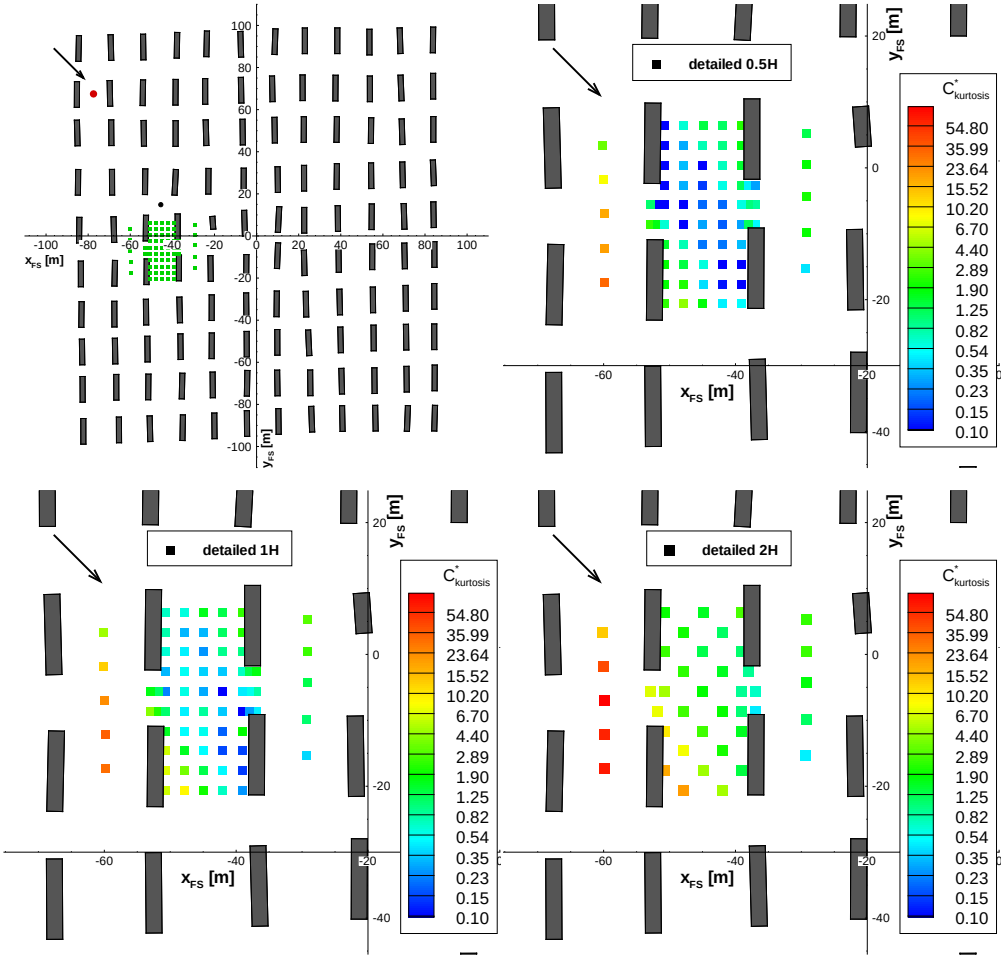

Figure 7.18: Field of the kurtosis of the concentration time series in one street canyon (its position is depicted in the upper left sketch) at half of the container height (upper right picture), at the container height (lower left), and at the two container heights (lower right) for -41° wind direction and the ground level source no. 29.

curves was achieved (within the measurement uncertainties) for detector no. 9 at the first detector row but got worse with increasing detector distance from the source. The exponential form of the autocorrelation functions obtained in the wind tunnel was in good agreement with the experimental study of Yee (1991); Pavageau and Schatzmann (1999) and the theoretical work of Degraziaa et al. (2005). The time scale in all charts is in the dimensionless time ($t^* = 50$ means $t_{\mathrm{MS}} \doteq 0.4$ s or $t_{\mathrm{FS}} \doteq 26$ s according to the t^* definition (equation 2.23)).

The concentration autocorrelation function can be utilised as well as the velocity autocorrelation function r_u (see section 2.4.1) to obtain the integral time scale T_c of the concentration fluctuation defined as

$$T_c \equiv \int_0^\infty r_c(\tau)\, d\tau. \tag{7.3}$$

Since the dimensionless time scale was used, the obtained integral time scale

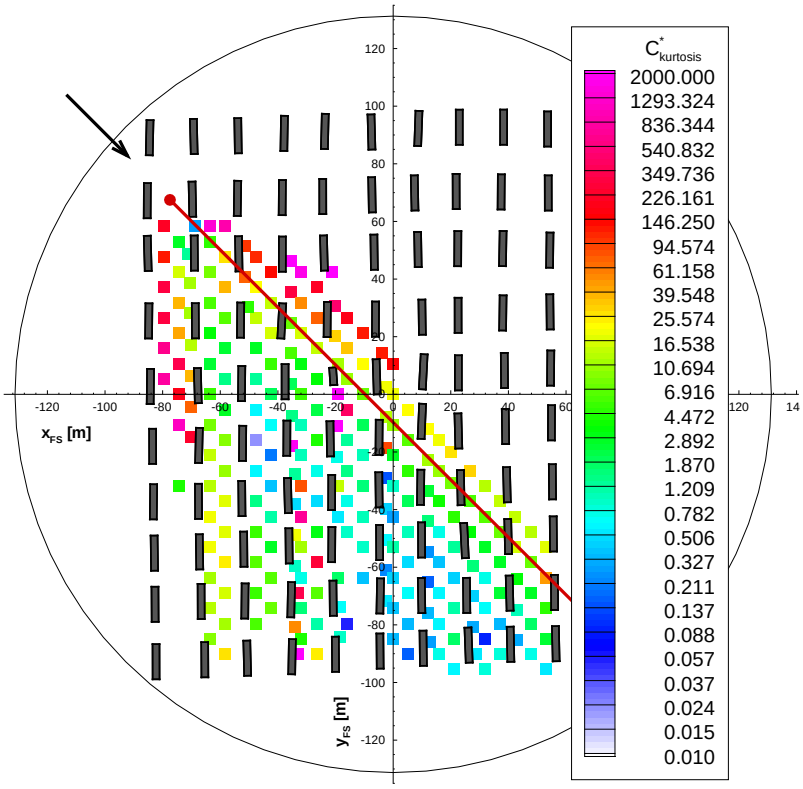

Figure 7.19: Field of the kurtosis of the concentration time series at half of the container height for -45° wind direction and the ground level source no. 29 (red circle).

will be also dimensionless, T_c^*. This is very useful, because in the dimensionless notation the length and time scales are uniquely determined by the reference wind speed U_{ref} as follows

$$L_c \equiv T_c\, U_{ref} = T_c^* \frac{H}{U_{ref}}\, U_{ref} = T_c^*\, H. \tag{7.4}$$

Due to the similarity theory all length variables can be scaled by a length reference value, the container height H in our case, and the final identity is obtained

$$L_c^* = \frac{L_c}{H} = T_c^*. \tag{7.5}$$

The magnitude of the integral time (or length) scale corresponds to the area under the autocorrelation curve and represents the time (or space) surrounding, in which the history of the plume pattern is influenced by this particular point. Consequently a high integral time (or length) scale means a longer interval (or larger region), which is 'connected' together (there is a non-zero correlation between them).

The comparison of the integral time scales obtained from the MUST field and wind tunnel concentration autocorrelation function is shown in Fig. 7.21.

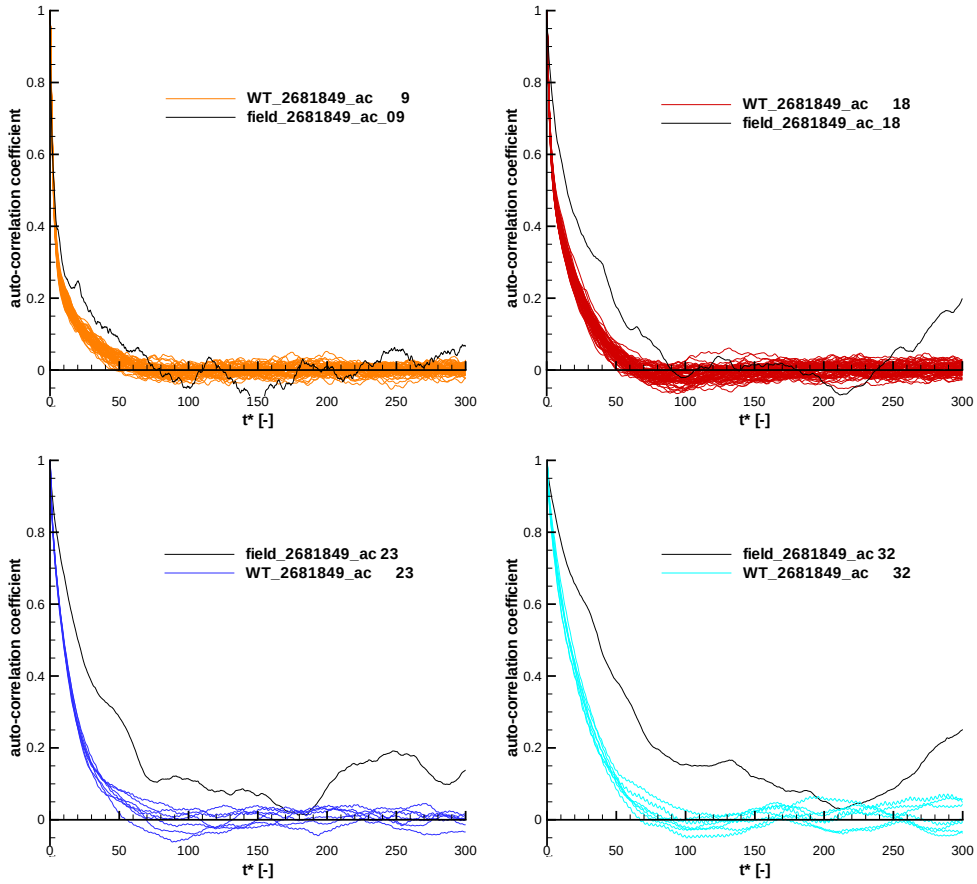

Figure 7.20: Comparison of the concentration autocorrelation functions obtained in the MUST field (black lines) and wind tunnel (colour lines) 2681849 trial for detectors no. 9 (upper left picture, 71 wind tunnel samples), 18 (upper right, 62 wind tunnel samples), 23 (lower left, 7 wind tunnel samples), and 32 (lower right, 7 wind tunnel samples).

Although the comparison is quite good in the first and the second row (upper chart), the MUST field values are much greater in the third and fourth row. The reason is clear from the Fig. 7.20: the MUST field autocorrelation functions are far from an exponential shape and in the interval showed they do not cross at zero. This behaviour is characteristic for a time series with a trend. However, the trend in the concentration time series was very probably caused by a trend in the atmospheric conditions (e.g. in the wind speed and direction) and therefore it would be impossible to remove this trend from the concentration time series. Also the uncertainty of the MUST field data is three times larger due to the ten times shorter averaging time (see section 7.1.2).

The detailed integral time scale field is shown in Fig. 7.22. The dimensionless concentration length scale shows a very similar pattern within the plume as the higher order statistics moments, i.e. skewness and kurtosis: nearly no difference between values measured at the $0.5H$ and $1H$, but with values decreasing

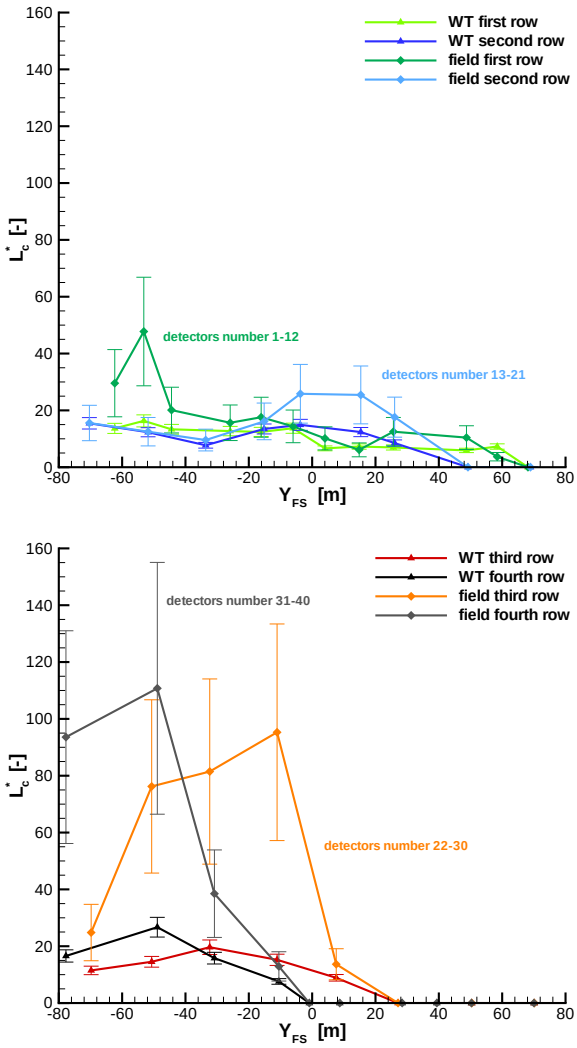

Figure 7.21: Comparison of the MUST field (depicted by the squares) and wind tunnel (depicted by the triangles) dimensionless concentration integral time (or length) scale for the trial 2681849 (-41° wind direction and source no. 29). The first row of detectors (from dPID no. 1 on the right hand side to dPID no. 12 on the left hand side, see Fig. 7.1) is drawn by the blue coloured symbols, the second row (no. 13–21) by the green ones, the third row (no. 22–30) by the red ones, and the fourth row (no. 31–40) by the black coloured ones.

with height and at the plume edges in contrast.

One of the most interest perhaps is Fig. 7.23, where the dimensionless concentration integral length scale for the whole plume is shown. Two major features are evident. Firstly, the plume is split into two parts by an area of relatively small L_c values, which corresponds with the plume centerline (see Fig. 7.9). The L_c maximum is reached at each side (it is slightly stronger on the left hand side of the plume) and then decreases to the plume edge. Secondly, significantly higher values appear near to the containers walls and in the wake

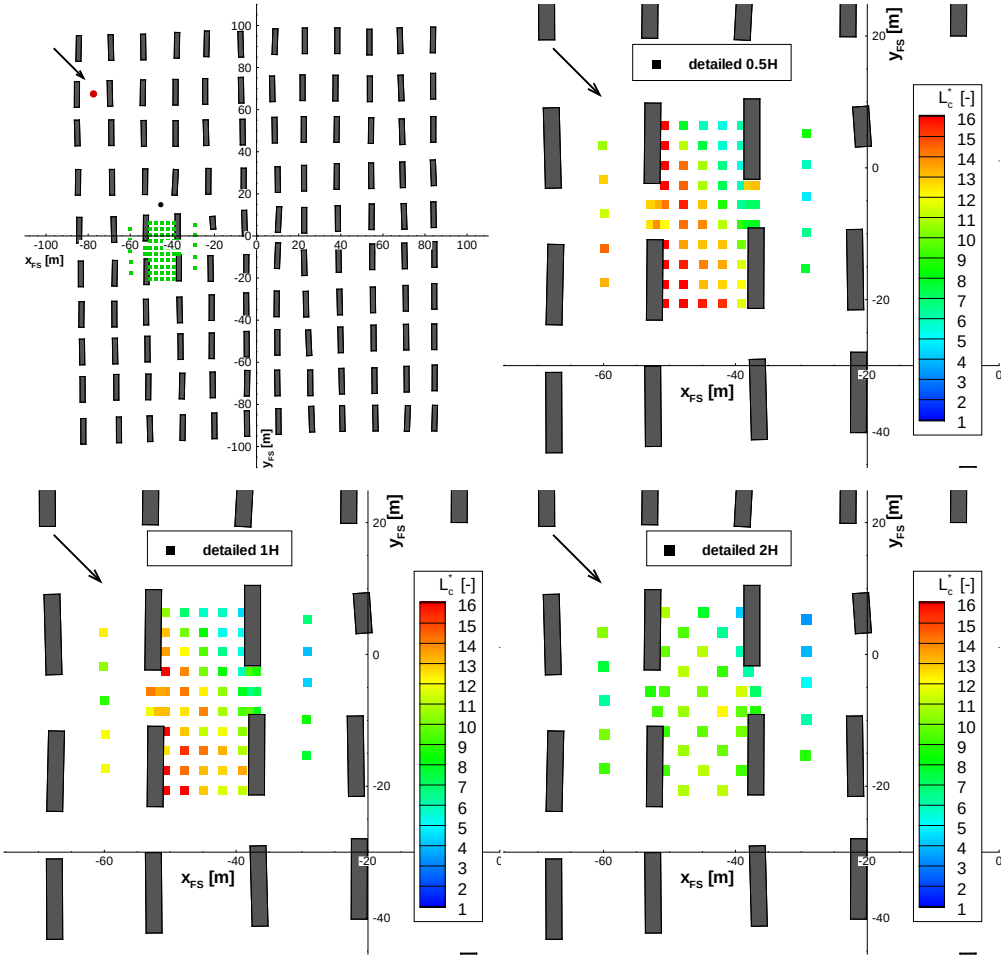

Figure 7.22: Field of the dimensionless concentration integral time (or length) scale in one street canyon (its position is depicted in the upper left sketch) at half of the container height (upper right picture), at the container height (lower left), and at the two container heights (lower right) for -41° wind direction and the ground level source no. 29.

regions.

The absolute L_c values increase with increasing distance of the measurement point from the source and their unit of magnitude corresponds to H. This is in good agreement with the founding of Yee et al. (1994a) whom found for a homogeneous flat terrain an exponential increase of L_c with the downwind distance x from the source and also related concentration integral length scale to the mean puff width L_{puff} as $L_c/L_{\text{puff}} \approx x^{2/3}$.

The integral length scale distribution validates the above mentioned theory that the strong and fast mixing, which can be linked with the smallest value of the mean concentration, appears close to the source and at the plume centerline. On the other hand, regions with the greatest mean concentration gradients and the wake regions denote the greatest L_c values. The concentration signals

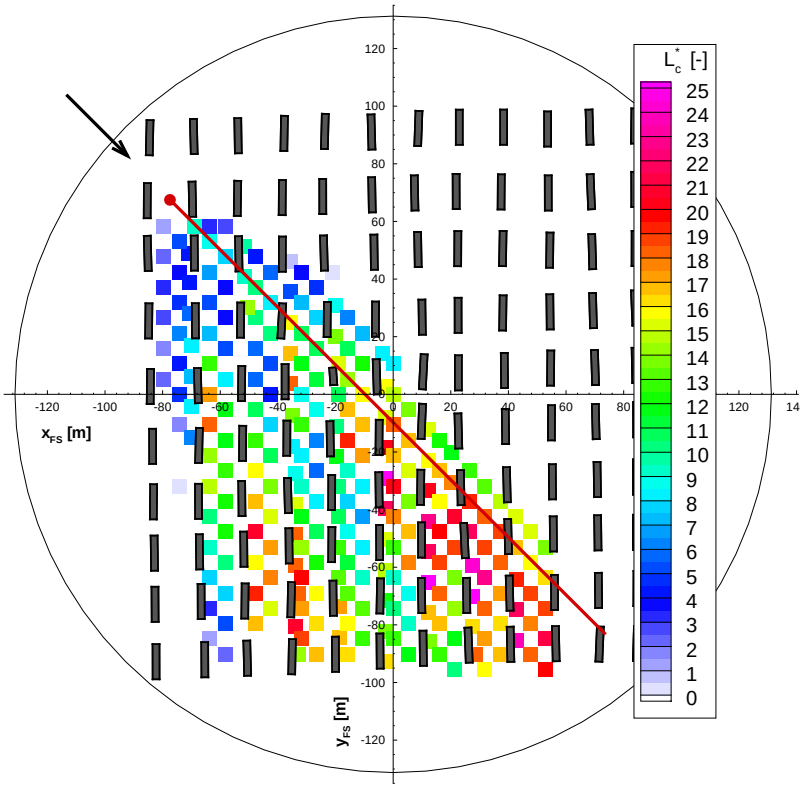

Figure 7.23: Field of the dimensionless concentration integral time (or length) scale at half of the container height for -45° wind direction and the ground level source no. 29 (red circle).

remain autocorrelated remarkably longer in this regions, which means that dispersion is much more influenced by the trapping of the pollutant in the wake region, which slows dispersion down.

7.3 Concentration Spatial Correlations

The MUST field experiment was unique due to the fact that concentrations were sampled with high frequency response simultaneously at approximately 50 positions (see chapter 3). This instrumentation set-up allowed the utilisation of advanced statistical methods like Principle Component Analysis, etc. The wind tunnel experiment could unfortunately only be run with two simultaneously sampling detectors (Fig. 4.6) due to lack of instruments and the severity of maintenance of a reliable FFID operation. Therefore only two simultaneously concentration time series were available and only two components statistical method was used. The method used for the travelling time estimation will be described first, the obtained results will be shown there after. All results shown below are based on the continuous tracer releases.

7.3.1 Spatial Correlation and Travelling Time Definition

The synchronised concentration sampling was conducted during the wind tunnel campaign at two places within the plume. Only two simultaneously measuring detectors were used in the wind tunnel in contrast with the MUST field campaign, since only two FFID chambers were available. Two examples (only a short part of the time series is shown: $t^* = 400$ means $t_{\mathrm{MS}} \doteq 3$ s or $t_{\mathrm{FS}} \doteq 200$ s, the whole time series has $t_{\mathrm{MS}} = 400$ s, which means approximately $t^* = 54000$) of simultaneously sampled concentration time series in the wind tunnel are given in Fig. 7.24. The experimental setup was the same as for 1681849 trial, i.e. -41° approach wind direction, source no. 29, and detector height $z_{\mathrm{FS}} = 1.6$ m.

The upper chart shows negatively correlated time series (with the maximum

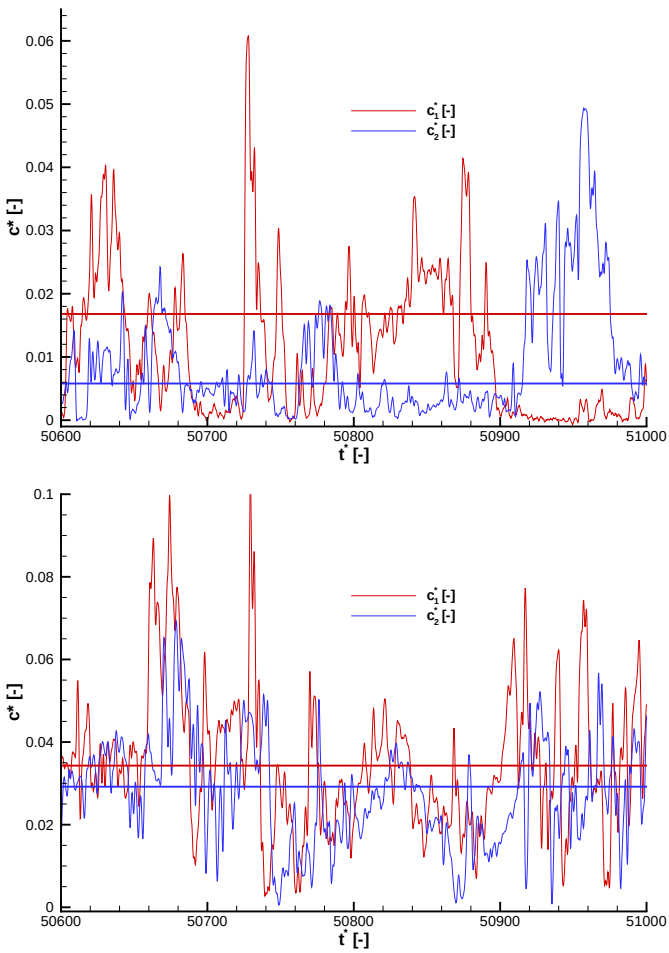

Figure 7.24: Two examples of simultaneously sampled concentration time series in the wind tunnel: strongly negatively (r_{SC} = -0.3) and positively (r_{SC} = 0.67) correlated time series in the upper chart and lower chart, respectively. The mean concentration values of the time series is depicted by the horizontal line in the corresponding colour.

r_{SC} = -0.3 reached at time τ^* = 17.9) sampled at detector positions no. 18 (labelled $c1$) and no. 5 ($c2$): when the first signal shows a positive deviation (values greater then mean value depicted by the horizontal line), the second signal very probably shows a negative deviation and vise versa. The lower chart shows positively correlated (with the maximum r_{SC} = 0.67 reached at time τ^* = 5.6) time series sampled at the detector positions no. 8 (labelled $c1$) and no. 7 ($c2$): the time series are very close to each other, when the first signal shows a positive deviation, the second signal very probably shows also a positive deviation and vise versa. A slight time shift between the two signal, which is equal to the time corresponding to the maximum of r_{SC}, is clearly seen.

The spatial correlation function defined analogically to the autocorrelation function (equation 2.34) as

$$r_{\mathrm{SC}}(\tau) = \frac{\overline{c_1'(t)\, c_2'(t+\tau)}}{\sigma_{c_1}\, \sigma_{c_2}}, \tag{7.6}$$

where c_1' and c_2' are the concentration fluctuations in each component, σ_{c_1} and σ_{c_2} are the corresponding standard deviations, and τ is the time lag. In contrast with the autocorrelation function the spatial correlation function is not symmetric in τ.

The definition of the travelling time is based on the shape of the concentration spatial correlation curve (see Fig. 7.25). If the randomness of turbulence is assumed, the correlation of two time series, which are very remote in space or time should be zero (the acceptance of Taylor hypothesis of frozen turbulence described in section 2.2.3 allows easily converting time to space coordinates and vise versa). Since, the turbulence has some structure, which can be simplified as a system of vortices with different size and energy content (see section 2.2), the dispersion processes in the locations which are close in space or time should be correlated. The spatial correlation coefficient of two concentration time series sampled at different places within the plume can be plotted as a function of the time lag between these two time series, which is shown in Fig. 7.25. The absolute maximum, or more precisely the maximum of the absolute value, of the spatial correlation coefficient is reached at a particular time lag, which can be positive or negative depending on the relative position of the first and second sampling location. Therefore the distance between two sampling locations, Δ, can be easily assigned to the time, when the absolute spatial correlation coefficient was reached.

The plume inside the urban canopy is highly intermittent and periods of high and low pollutant concentration are alternating. The basic idea is that the pollutant stays somehow in 'puffs', which are passing the container array on the Lagrangian trajectories (see section 2.2.3). Locations, which lie within one trajectory (trajectories are usually smooth lines, which do not cross the plume in the lateral direction), are hit by the same 'puffs' with a time shift, which results in a positive correlation between these two points. Locations, which lie on the completely different trajectories, are hit by different 'puffs', and assuming that at one moment only one 'puff' is creating near the source,

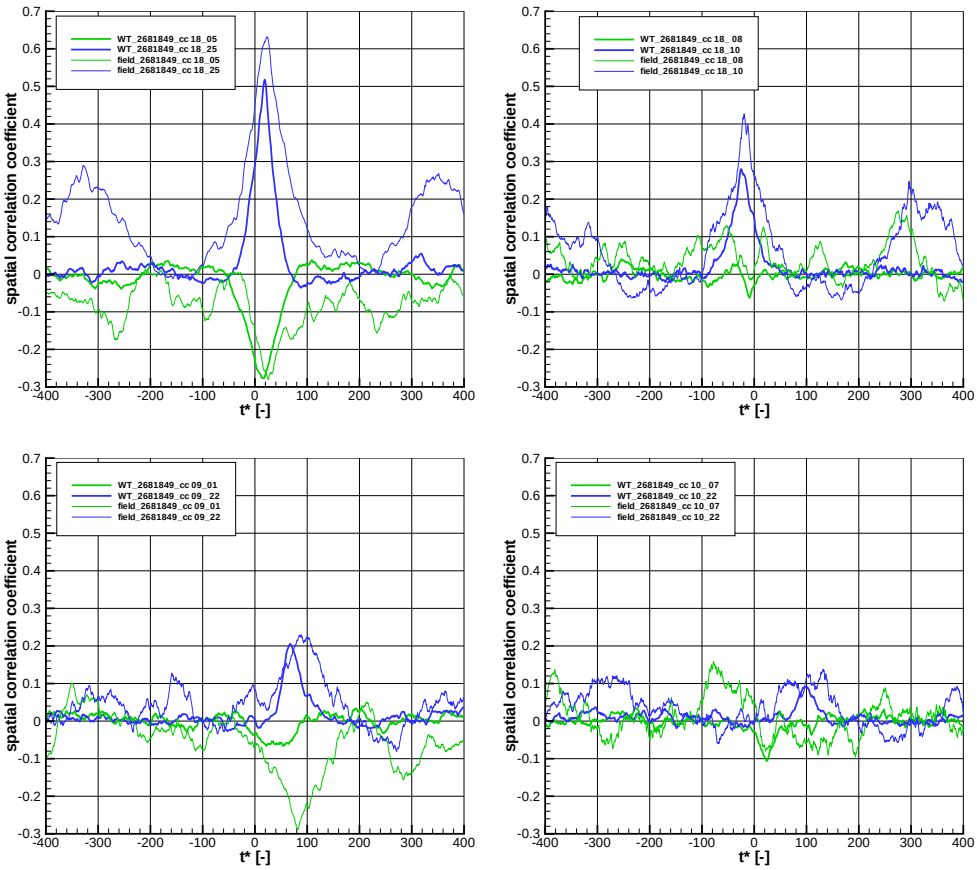

Figure 7.25: Four example comparisons of the spatial concentration correlations as a function of the time lag based on the 2681849 trial conducted in the MUST field (thin lines) and in the wind tunnel (thick lines). Detectors involved can be found in the legend (last two numbers) and their positions are depicted in Fig. 7.1.

it results to a negative correlation between these two points. The relatively small values (typically 0.2) of the spatial correlation coefficient are caused by a unsteady structure of the puffs due to the turbulent mixing and interactions between the puffs. The 'puff' theory is just a theory, since the concentration field is highly intermittent and can not be split to individual puffs. Therefore it is impossible to track the puffs and estimate their characteristics such as the life time, the time a puff stays at one side of the plume, etc. Another way to show the spatial structure of the plume is a map of the concentration spatial correlation coefficients and corresponding time lags.

Now, the definition of the **travelling time**, t^*_{SC}, based on the concentration spatial correlation function is clear: it is the time, when the absolute maximum of the concentration spatial correlation coefficient is reached (for other definitions of the travelling time see section 7.5). The advective velocity of the

pollutant, $v^*_{\text{pollutant}}$, inside the urban canopy can be defined as

$$v^*_{\text{pollutant}} = \frac{\Delta}{t^*_{\text{SC}}} \tag{7.7}$$

where Δ is the distance between two sampling locations. Other definitions of the travelling time are possible: (i) the most straightforward definition would be the time needed for a tracer to travel from the source to the sampling location (measurement based on the instantaneous releases, see section 7.4), but also (ii) the effective transport speed (equation 2.40) based on the integral of the concentration weighted wind speed.

Figure 7.25 shows an example of the spatial correlation functions obtained from simultaneous measured concentration time series in the MUST field (thin lines) and in the wind tunnel (thick lines). The upper left chart in Fig. 7.25 shows an example of the spatial correlations of the very strongly negatively (green line, measured at the position of the detectors no. 18 and 5) and positively (blue line, detectors no. 18 and 25) correlated concentration time series. The wind tunnel results are in a very good agreement with the MUST field data in both quantities; the absolute maximum of r_{SC} and the time, at which it was reached. These two spatial correlation functions are examples of the very well pronounced and high r_{SC} maxima, which were reached for positive time lags. Examples of the r_{SC} functions with the negative time lag, when the r_{SC} maximum was reached are shown in the upper right chart in Fig. 7.25 (detectors no. 18 and 8, 18 and 10). However, the comparison of the MUST field and wind tunnel data is not as good as in the first cases, as is shown in the lower charts in Fig. 7.25. The lower left chart shows a weaker maximum spatial correlation coefficient but a not so bad agreement between the MUST field and wind tunnel data. The lower right chart shows the r_{SC} function with very weak maxima (about 0.1). The comparison was very poor in these cases.

The MUST field time series seem to show much larger motion structures which are relatively strong ($t^* = 400$ means $t_{\text{FS}} \doteq 200$ s or in the space dimension $L_{\text{FS}} \doteq 1000$ m). When the absolute maximum of r_{SC} of the concentration time series gets smaller, the large motion structures are of the same order of magnitude as a plume structures (clearly showed in the wind tunnel measurement), which are of prime interest. These larger structures, which appeared in the MUST field data, could not be easily connected with the large scale motion since there was no repetition of the MUST field concentration time series. Also the autocorrelation function is highly sensitive to the drift in the time series and if any drift is present in the concentration time series it is due to a changes in the approach wind conditions, which is impossible to remove from the concentration time series without exact knowledge of dispersion phenomena. Therefore it can be difficult or even impossible (lower right chart in Fig. 7.25) to evaluate which peak belongs to a plume structure and what is 'noise'. The wind tunnel r_{SC} did not show this behaviour on any occasion, which verifies the theory of a drift of the approach wind conditions during the MUST field campaign, while the sampling conditions in the wind tunnel were stationary.

The comparison of $r_{\text{SC amax}}$ values obtained at the same place during the trial 2681849 in the MUST field and in the wind tunnel are plotted against

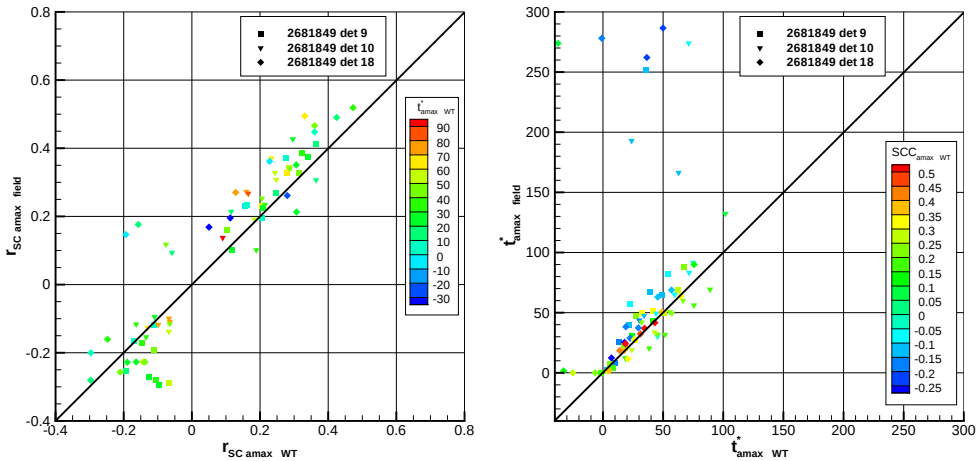

Figure 7.26: Relation of the maximal spatial correlation coefficients (left chart) and the corresponding dimensionless time (right chart) based on the 2681849 trial conducted at the same positions in the MUST field (on the ordinate) and in the wind tunnel (on the abscissa).

each other in Fig. 7.26. If the agreement were perfect, all values had to be the same for the MUST field and wind tunnel, i.e. all points would lie on the black diagonal line. The points compared are from the three different placements of the first detector: the first detector was sequentially fixed in the position of detector no. 9, 10, and 18. The second detector then measured at the positions of another detectors (no. 1–40). The placement of the first detector is depicted by the scatter shape in Fig. 7.26 (squares indicate first detector no. 9, triangles no. 10, and diamonds no. 18), the scatter colour indicates the time, when the absolute maximum of r_{SC} was reached in the left chart in Fig. 7.26, or the absolute maximum r_{SC} value in the right chart in Fig. 7.26, respectively. The comparison of the r_{SC} maxima in the left chart of Fig. 7.26 is very good, nevertheless the MUST field results show slightly higher values (approximately of about 0.1). However, the travelling time comparison (right chart of Fig. 7.26) is worse, mainly for the negatively correlated time series (blue colour), for which the comparison completely failed due to the small maximum r_{SC} values, which were 'taken over' by large scale motions in the MUST field data.

Since the MUST field trials were not repeated (the atmospheric conditions were different for each trial and therefore they could not be compared against each other), Fig. 7.27 shows only the repeatability of some wind tunnel results. The measurements were repeated several times for different reference velocity. The repeatability of the r_{SC} functions is very high even for the very small values of r_{SC} maximum values (e.g. for detectors no. 10 and 8, orange line, $r_{\mathrm{SC\ amax}} \doteq 0.05$). It should be mentioned that the r_{SC} estimation is very precise, since the spatial correlation coefficient is a dimensionless value and no calibration of the FFID was needed. The uncertainty of both the maximum of the spatial correlation coefficient and the time when it was reached was estimated to be 5%. The 'noise' signal in the wind tunnel r_{SC} function is in the range $\pm$ 0.02, i.e.

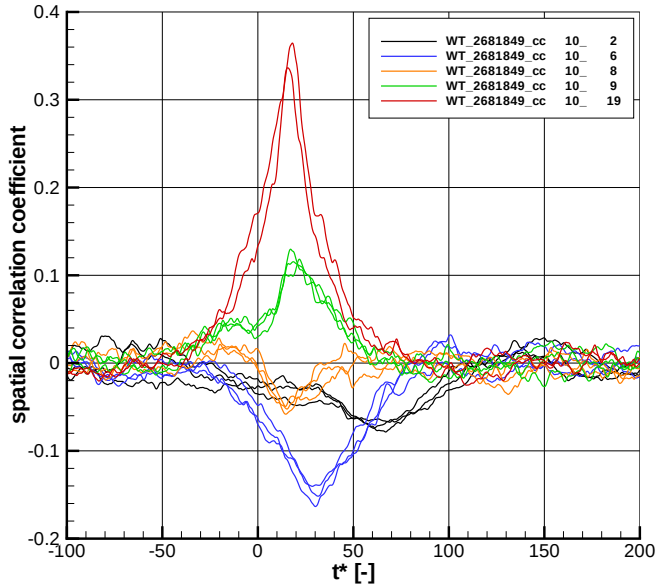

Figure 7.27: An example of repeatability of the spatial correlation functions based on wind tunnel measurement.

the threshold value of the meaningful correlation signal was set up to be 0.02 for the wind tunnel experiment. The large structures detected by the MUST field r_{SC} functions (Fig. 7.26) could not be evaluated because of the unknown experiment accuracy.

7.3.2 Plume Meandering

Detailed measurements (about 260 points) of the whole plume were conducted in the wind tunnel in contrast with the MUST field campaign, where only 40 detector positions were available. The experimental set-up corresponded with the flow measurement set-up, i.e. the source no. 29, the wind direction -45°, and all measurements were taken at half of the container height, $z_{\mathrm{FS}} = 1.275$ m). The measurement lay-out consisted of one fixed detector (the black circle in Figures 7.28 and 7.29) with the other FFID detector travelling within the whole plume (the black dots in Figures 7.28 and 7.29). Therefore the results shown in Figures 7.28 and 7.29 are always related to the fixed detector position.

The position labelled 100 (Fig. 7.28) was chosen on the left hand side of the plume. Due to its position the plume is clearly divided into two halves: the left half is strongly positively correlated with this position, the right half is strongly negatively correlated (upper chart in Fig. 7.28). The transition zone between these two halves is very sharp and it has a 'step-like' shape. The splitting of the plume is also visible on the plot of the travelling time (lower chart in Fig. 7.28). The travelling time logically increases with increased distance between the detectors, however, the structure is much more complicated as will be discussed later in section 7.5.

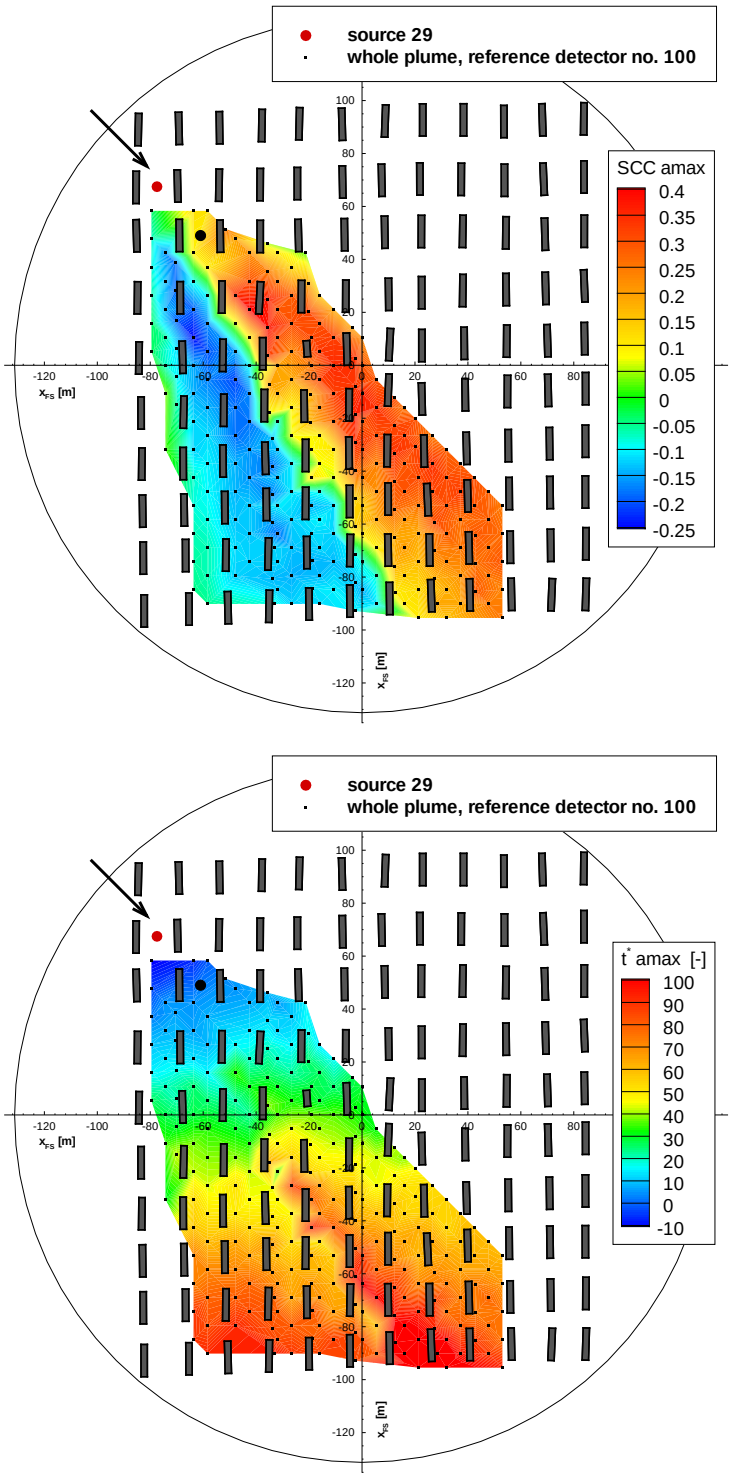

Figure 7.28: Maximum of the spatial correlation coefficient (upper chart) and the corresponding travelling time (lower chart) between the detector position number 100 (black circle) and the other positions within the field (black dots) at half of the container height for the -45° approach wind direction and the source no. 29.

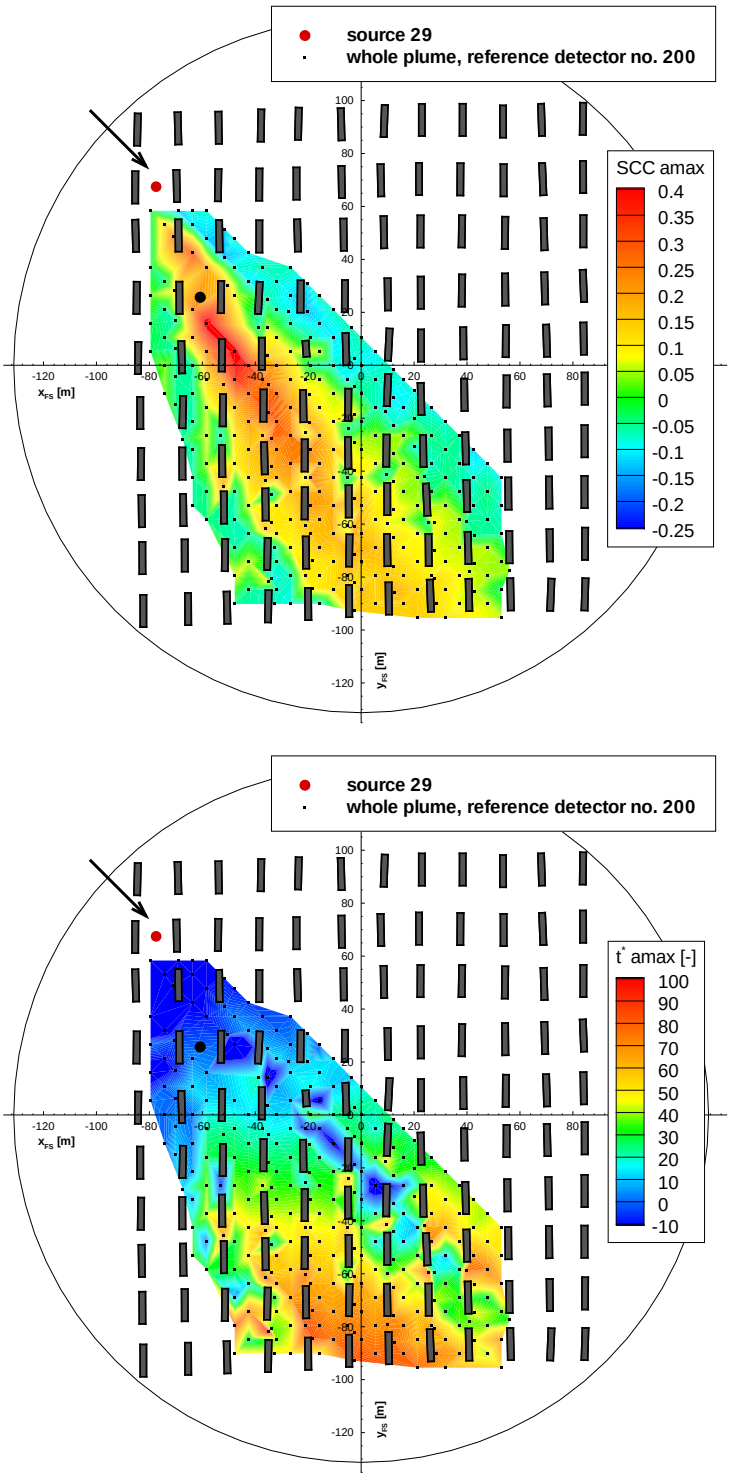

Figure 7.29: Maximum of the spatial correlation coefficient (upper chart) and the corresponding travelling time (lower chart) between the detector position number 200 (black circle) and the other positions within the field (black dots) at half of the container height for the -45° approach wind direction and the source no. 29.

The position labelled 200 (Fig. 7.29) was chosen as it lies approximately on the plume centerline (refer to Fig. 7.9). The positively correlated region appears along the plume centerline and the plume edges are negatively correlated in this case. The borders between these two regions are not so sharp as they with the previous case of detector no. 100 and the container wakes play an important role. The maximum values of the spatial correlation coefficients reached smaller values in general and the values of the r_{SC} maximum decreased with increasing distance faster than in the previous case. The travelling time map has a complex structure, which needs to be evaluated further.

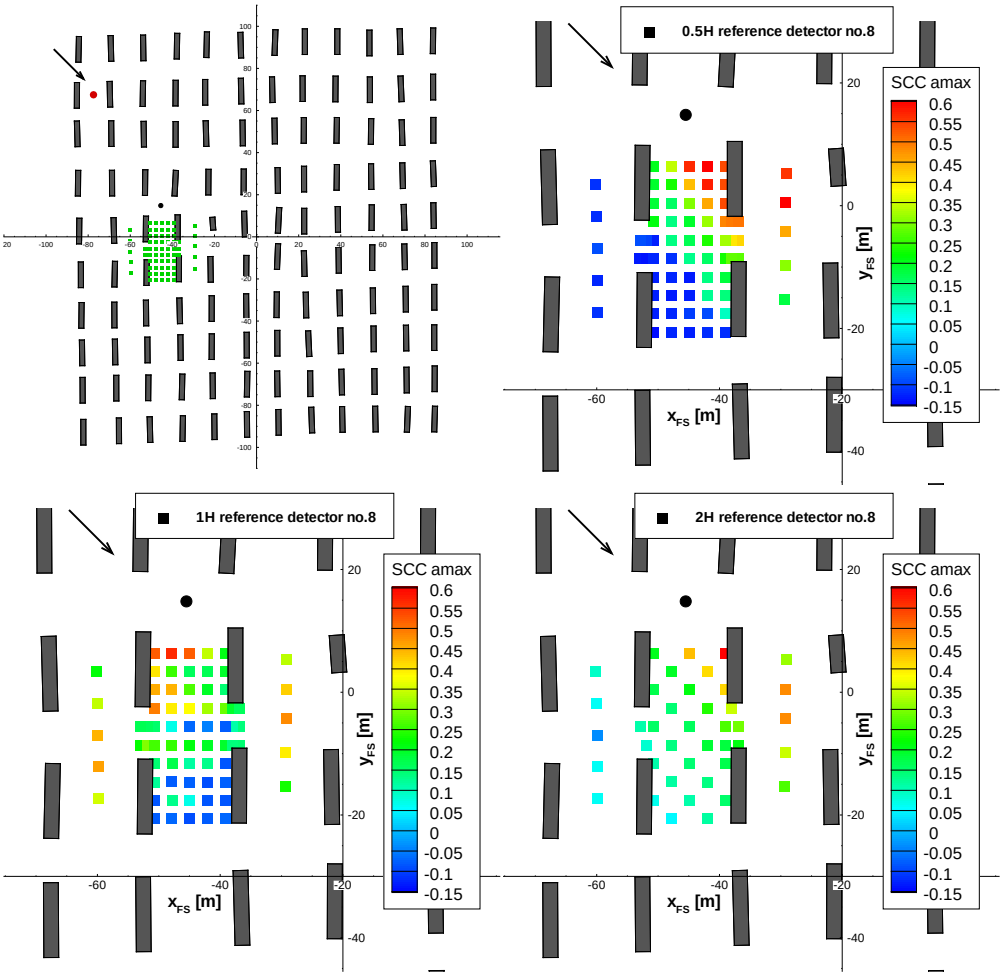

Figure 7.30: Spatial correlation coefficient maxima between the detector position number 8 (black circle) and part of the field (black dots) at half of the container height (upper right chart), container height (lower left), and twice container height (lower right) for the -41° approach wind direction and source no. 29 (red circle).

7.3.3 Detailed Spatial Correlation Measurement

The detailed measurement of the spatial correlation function, r_{SC}, and travelling time, tt, was conducted in the street canyon between detectors no. 5 and 7, where also the detailed single concentration statistics were measured. The measurement levels (both detectors were placed at $0.5H$, $1H$, and $2H$) were also the same. The maps of the maximum values of spatial correlation coefficients are shown in Fig. 7.30. The transition zone between positively and negatively correlated regions were caught at half of the container height (upper right picture). It can be said that the zone is sharp and well pronounced even with fine resolution. The situation at the container height (lower left picture) is very complex probably because of the enhanced vertical mixing (see section 6.2.1). The highest level (lower right picture) with the lowest turbulence level

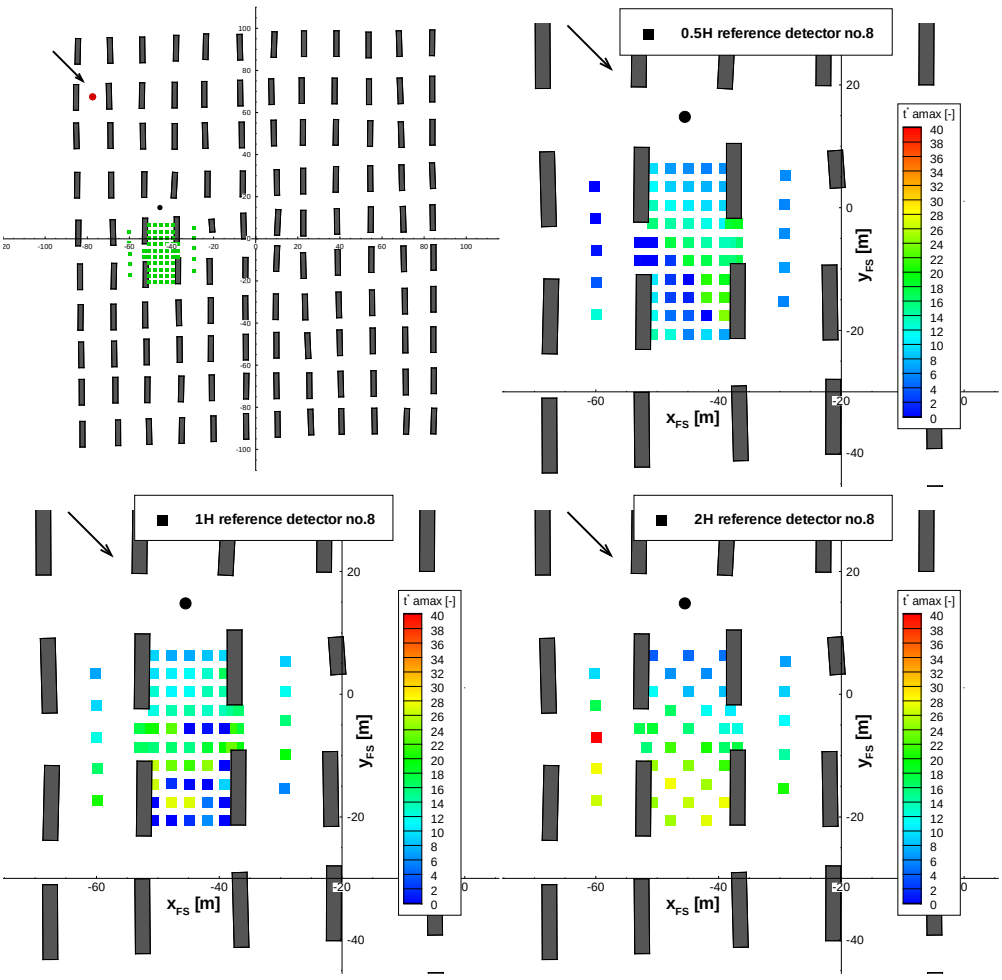

Figure 7.31: Travelling time between the detector position number 8 (black circle) and part of the field (black dots) at half of the container height (upper right chart), container height (lower left), and twice container height (lower right) for the -41° approach wind direction and source no. 29 (red circle).

shows a very smooth field of r_{SC} maxima without any sharp transition zones and extremal values.

The corresponding travelling times are shown in Fig. 7.31. The maps are complicated at $0.5H$ and $1H$ in contrast with $2H$, where the travelling time map is smooth (except one edge point). A detailed discussion of travelling time properties is given later in section 7.5.

7.4 Instantaneous Releases - Puffs

A sudden release of a quantity of a pollutant into the atmospheric boundary layer (e.g., from bombs, artillery shells, tanks), and the subsequent dispersion of the instantaneous cloud formed from the release, is an important problem in both civilian and military risk analysis. Unfortunately, there has been relatively little effort expended in the measurement and investigation of concentration fluctuations in dispersing clouds resulting from instantaneous releases of a tracer into the ABL. A major difficulty is that a pollutant cloud is a non-stationary and inhomogeneous phenomenon, requiring the measurement of a large number of realisations (replications) of the dispersing cloud under the constraint that the conditions at the release and in the atmosphere (e.g. the mean wind and turbulence characteristics) are the same in each realisation of the ensemble. In particular, achieving stationarity in the atmospheric conditions over an extended measurement period is problematic, given the fact that atmospheric flow is generally time-dependent and inhomogeneous.

Experimental investigations devoted to the study of concentration fluctuations in instantaneous clouds are very limited so far. Meroney and Lohmeyer (1984) studied concentration fluctuations resulting from the sudden release of a volume of dense gas in a neutrally stable wind tunnel boundary layer. Zimmerman and Chatwin (1995) described statistical properties of instantaneous releases of dense gas measured in a wind tunnel by Hall et al. (1996a). Yee et al. (1994b, 1998) investigated the statistical properties of the turbulent concentration field in a cloud dispersing in a near-neutral atmospheric surface layer. These tracer experiments were limited to measurements of concentration fluctuations at fixed points downwind of a quasi-instantaneous release of a tracer for ranges between about 25 and 300 m. Furthermore, a small number of detectors available for these tracer experiments did not allow the cross-puff concentration structure to be investigated. Because data from controlled field experiments will be needed for the validation of models and wind tunnel studies of concentration fluctuations in dispersing clouds, series of puff experiments were conducted with the goal of providing more extensive measurements of concentration fluctuation statistics in a sudden released dispersing cloud.

The overall experimental set-up was the same as in the previous flow and concentration experiments: the wind direction was -45°, the ethane tracer was released from the source no. 29, concentration measurements were conducted by FFID and taken at half of the container height ($z_{\mathrm{MS}} = 17$ mm, $z_{\mathrm{FS}} = 1.3$ m), and the reference velocity was measured by the Prandtl tube (for more details see chapter 4). For each experimental set-up (given wind speed and direction,

releasing source, and time of source opening) at least 70 individual puffs were realised to obtain a sufficient ensemble for a statistical processing. Six points (no. 200, 201, 300, 301, 400, and 401 depicted in Fig. 7.32) were chosen for extensive measurement campaigns, where the ensembles for different wind speed and time of source opening were collected to evaluate puff experiments. Also the measurement for one experimental set-up through the whole plume (brown dots in Fig. 7.32) was conducted.

7.4.1 Data Pre-processing

Part of a raw measured concentration time series is shown in Fig. 7.33. Each time series had 480 s and contained many individual tracer releases. The source flag (black line creating steps in. Fig. 7.33) was used to cut out the individual puffs: the puff beginning was set-up at the source opening (i.e. the source flag jumps from 0 to 1) and it ends at the next source opening. The time and concentration were recalculated to the dimensionless values according to equations 2.23 and 2.20.

Ensembles obtained for each experimental set-up always contained more

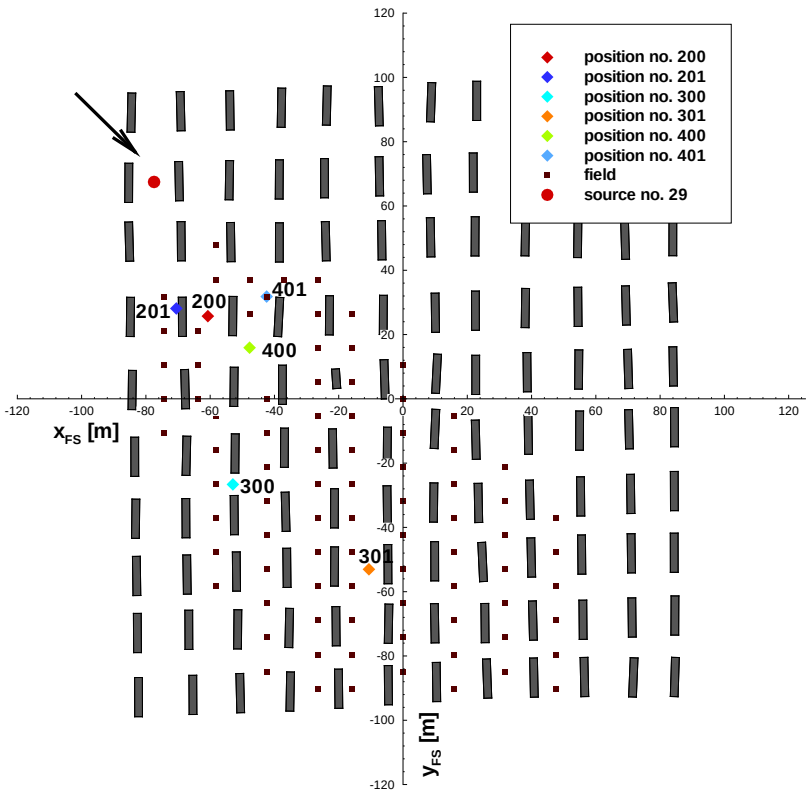

Figure 7.32: The sketch of the container array with the depicted approaching wind directions -45°, used source no. 29, six positions within the array where the experiment validation was conducted, and 90 locations for the whole plume measurement.

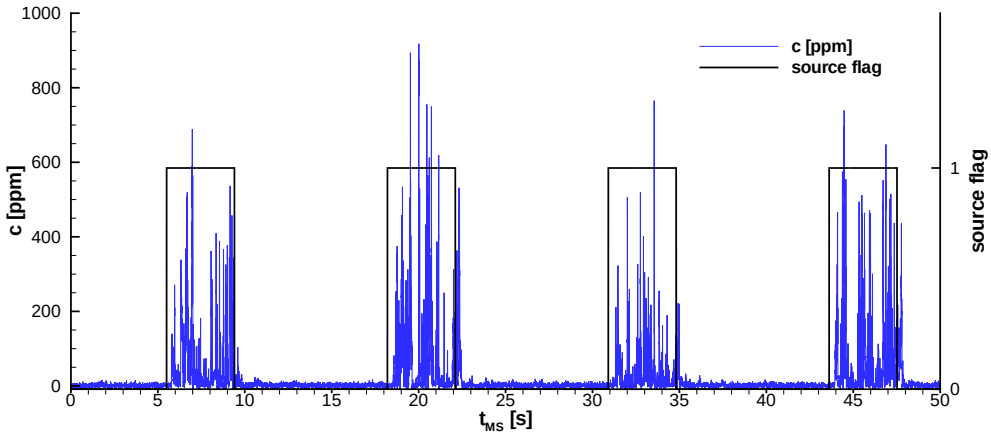

Figure 7.33: An example of a detected concentration time series: blue line shows the concentration signal, black line is a source opening pointer.

than 70 samples and was used to calculate statistical properties. The individual puffs within one ensemble showed considerable variation from realisation to realisation as is shown in Fig. 7.34, in which four examples of individual puffs are shown together with the source flag, ensemble average puff (the bold blue line), and stationary mean value obtained during 240 s of averaging during a continually released tracer (the bold violet line, data were presented in section 7.2). Some puffs show large concentration fluctuations about the average value (lower left chart in Fig. 7.34), other exhibit some fragmentation in which the puff appears to be split into two or more discrete parts (upper charts in Fig. 7.34). The average puffs were always smoothed with 11 points running average (since the scanning frequency was 500 Hz, 11 points in time series mean $t_{\mathrm{MS}} = 0.022$ s, which in most of the measurements mean $t^* \doteq 2.8$).

7.4.2 Average Puff Statistics

Since the dimensionless time is also dependent on the reference wind speed (equation 2.23), the same dimensionless time of the source opening can be achieved by many combination of different times in model scale and different reference wind speeds. An example of such combinations is given in Fig. 7.35. Two and two different combination of the reference wind speed and time of the source opening gave the same dimensionless time of the source opening. The difference between the average puffs are not significant, nevertheless some matter-of-fact criteria for average puff description had to be defined.

The average puffs were treated to obtain various characteristics: mean concentration of the puff stationary part (part, at which no trend in the concentration time series can be observed, i.e. an analog to the continually open source trials, see section 7.2), travelling time (time needed by the tracer to come from the source to a detector position), filling time (time needed by the tracer to fill detector position surroundings including wake regions; this interval is characterised by a increasing tendency in the concentration time series), and flushing

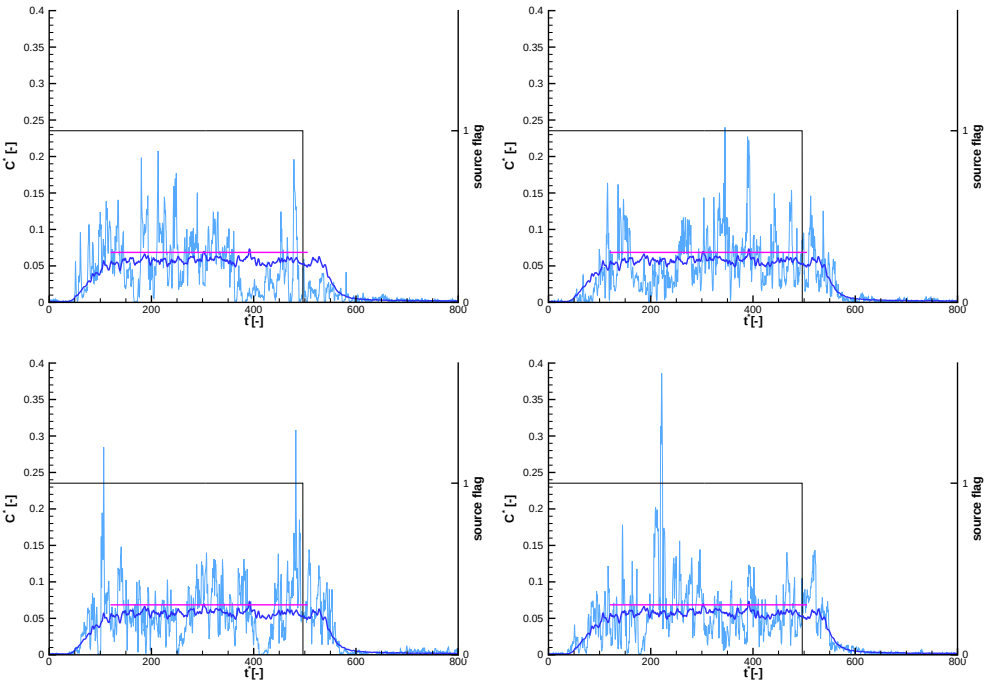

Figure 7.34: Examples of four individual puffs (light blue colour) sampled at position no. 200 at half of the container height after cutting and recalculation to the dimensionless values. The dark blue line shows an average puff out of the 79 puff's repetitions, the horizontal blue line shows the four-minutes average concentration measured at this position, and the black line is a source opening pointer. Sampling conditions were following: U_{ref} = 4.32 m s^{-1}, opening time of the source $t_{\text{source MS}}$ = 3.9 s, which means t^* = 496.

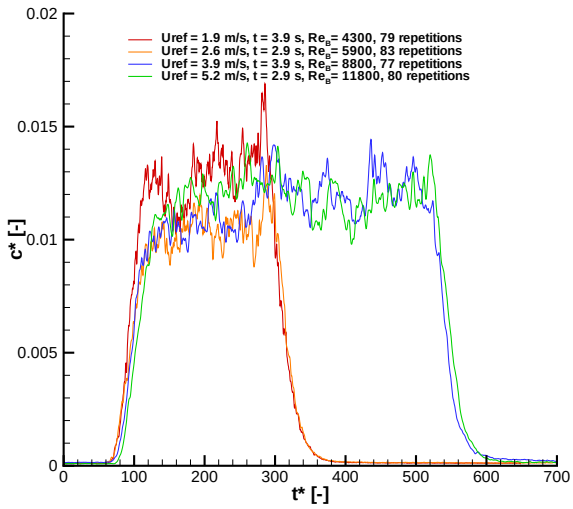

Figure 7.35: Comparison of the average puffs obtained under different conditions (mean wind speed and source opening time) at the location of detector no. 300 at half of the container height.

time (time needed to completely flush out all tracer from detector position surrounding including wake regions; this interval is characterised by a decreasing tendency in the concentration time series). The assessment of these characteristics was complicated process, which is described below and illustrated in Fig. 7.36. The starting procedure consisted of:

1. an estimation of an upper limit for the filling, ft^*, and flushing, lt^*, times ($ft^* = 70$, $lt^* = 120$),
2. set the concentration time series offset value as the average value of the first and last 0.2 s in the model scale time (200 points) of the concentration time series,
3. set a starting guess of $ft1$ and tt ($ft1 = tt$) to be the time when the concentration of the average puff reaches the offset value + 0.3 ppm for the first time,
4. set a starting guess of $lt2$ to be the time when the concentration of the average puff reaches the offset value + 1 ppm for the first time when going from the end of the time series,
5. $ft2 = ft1$ + upper limit for the filling time,
6. $lt1 = lt2$ - upper limit for the flushing time,
7. set the stationary time to be $lt1$ - $ft2$ and stationary mean concentration $c^*_{\text{puff mean}}$, which is an avearge concentration within this interval.

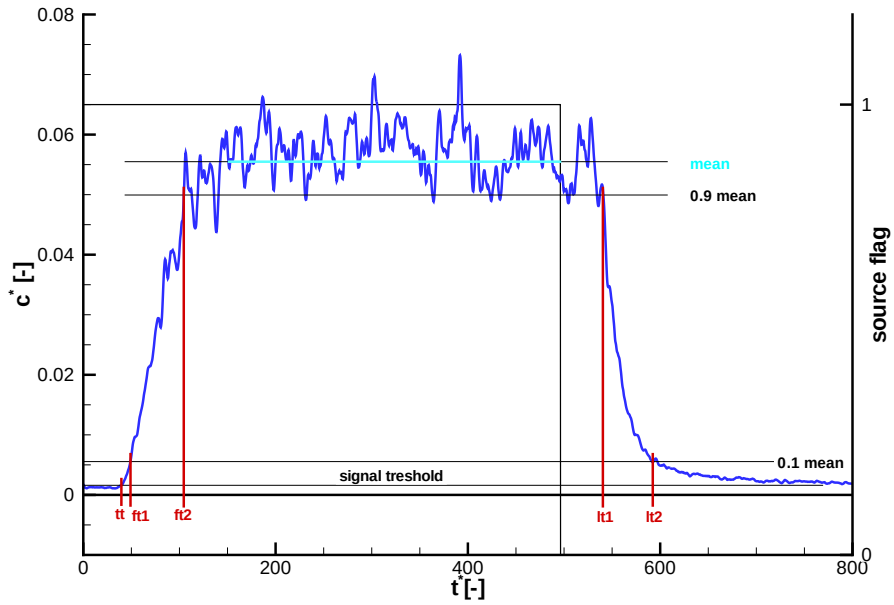

Figure 7.36: An average puff and derived properties: travelling time tt, filling time $ft2 - ft1$, stationary time $0.8(lt1 - ft2)$, and flushing time $lt2 - lt1$.

Then the iteration procedure came:

1. set $ft1$ and $lt2$ as the times when the average concentration time series reach 10% of the $c^*_{\text{puff mean}}$ value for the first time and for the first time when going from the end of the time series, respectively,

2. set $ft2$ and $lt1$ as the times when the average concentration time series reach 90% of the $c^*_{\text{puff mean}}$ value for the first time and for the first time when going from the end of the time series, respectively,

3. set the stationary part to be between $ft2$ + 0.1($lt1$-$ft2$) and $lt1$ - 0.1($lt1$-$ft2$), i.e. middle 80% of the interval between $ft2$ and $lt1$ (0.9$c^*_{\text{puff mean}}$ points),

4. get the new stationary mean concentration $c^*_{\text{puff mean}}$ within the new stationary interval,

5. start the iteration procedure with the new $c^*_{\text{puff mean}}$.

The iteration procedure run till the deviations between values obtained in two following cycles is less then 1%. The time flags tt, $ft1$, $ft2$, $lt1$, and $lt2$ was used to define characteristic times for an average puff:

travelling time $tt = tt$,

filling time $ft = ft2$ - $ft1$,

flushing time $lt = lt2$ - $lt1$,

flushing time $st = lt1$ - $ft2$.

Figure 7.37 shows a dependency of $c^*_{\text{puff mean}}$ of the average puffs on the Building Reynolds number (left chart) and on the dimensionless stationary time, st^* (right chart) at the six reference positions within the container array (for its locations see Fig. 7.32). The value scatter is more than 10% for the detector locations no. 200 and 201 (red squares and blue triangles in Fig. 7.37, respectively), which are the closest to the source. At these locations the design of the source and the magnetic valve for source opening (described in chapter 4) can be significant. Since the passive pollutant released from source filled first a wake behind the upwind container and then spread downwind as was shown by flow visualisation, the concentration at the close locations (e.g. detectors no. 200 and 201) is dependent on the state and position of the wake, which is non-stationary, at the moment of the passive pollutant release. Therefore the scatter at these position is primarily caused by short averaging time as is shown in the right chart in Fig. 7.37.

The locations no. 300, 301, 400, and 401 deeper in the container array (the second row of the street canyons behind the source or farther) proved Building Reynolds number independence of $c^*_{\text{puff mean}}$ in the whole examined range $Re_B \in$ (4000; 14000). Also the time dependency was found to be very weak even for the shortest times of the source opening $t_{\text{MS}} \doteq 1$ s, $t^* \doteq 110$.

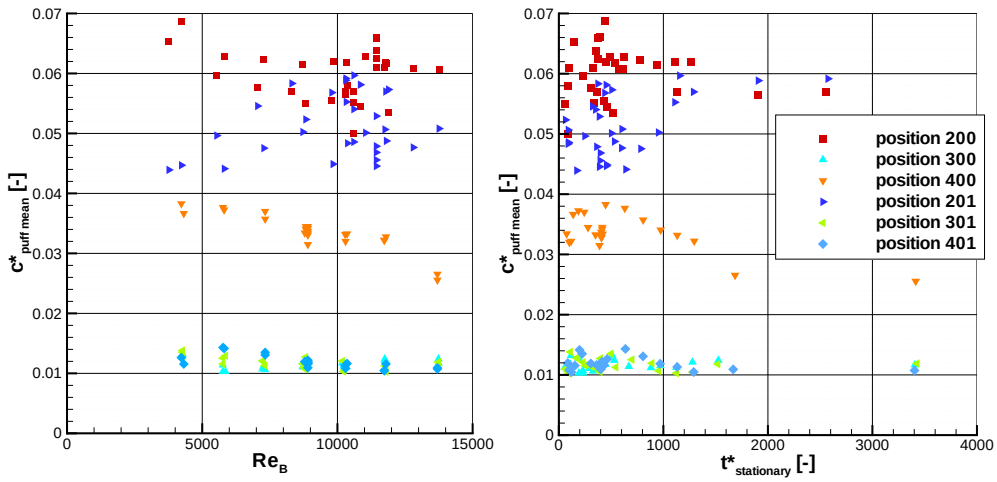

Figure 7.37: Dependency of the concentration average values obtained during the stationary phase of the puffs on the Building Reynolds number (left chart) and the stationary time (right chart) at half of the container height.

The surprising independence of the $c^*_{\text{puff mean}}$ on the stationary time lead to comparison between $c^*_{\text{puff mean}}$ and c^*_{mean} obtained form 240 s averaging with continuous tracer release. The measurement from the whole plume (brown dots in Fig. 7.32 show the locations of the measurement) was used for the comparison (Fig. 7.38). The reference wind speed was $U_{ref} = 4$ m s^{-1}, the time of the release $t_{\text{MS}} = 3.9$ s, i.e. $t^* = 460$, during the puff experiments. The continuous source data were taken from Fig. 7.9. The agreement is very good except the locations with the highest concentration, at which the $c^*_{\text{puff mean}}$ gave greater values than c^*_{mean}. However, as was mentioned before, these points are very close to the source and the data uncertainty due to a short averaging time in the case of puff data is large (approximately 20 %, see Fig. 7.38).

Usual plume characteristics are cross-plume and along-centerline concentration profiles. Since the plume inside the container array had centerline, which was not parallel to the wind direction and was not straight, a definition of the cuts for the cross and along-wind profiles would be difficult. Therefore all puff properties will be plotted as a function of the separation distance between the source and the detector position, Δ, and projection of Δ to the y-axis, $\triangle y$. Figure 7.39 shows a dependence of the puff stationary mean concentration $c^*_{\text{puff mean}}$ on the dimensionless separation distance (left chart) and its projection to the y-axis (right chart).

These results demonstrate that $c^*_{\text{puff mean}}$ is upper-bounded by the following empirical equations (the lines belong to this equations are depicted in both charts in Fig 7.39) at half of the container height level :

$$c^* = \frac{0.4}{\Delta^{1.5}}, \text{ or } c^* = \frac{0.35}{\triangle y^{1.5}}. \tag{7.8}$$

This observation is in reasonably good agreement with concentration data anal-

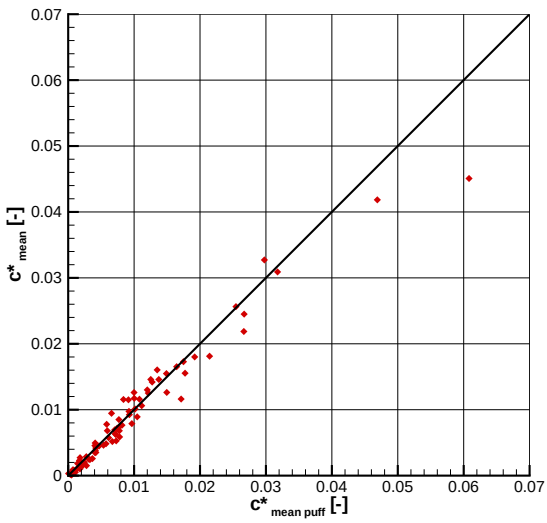

Figure 7.38: Comparison of the concentration average values obtained during the stationary phase of the puffs (on the abscissa) and four-minutes average (on the ordinate) from whole plume locations (see Fig. 7.32) at half of the container height.

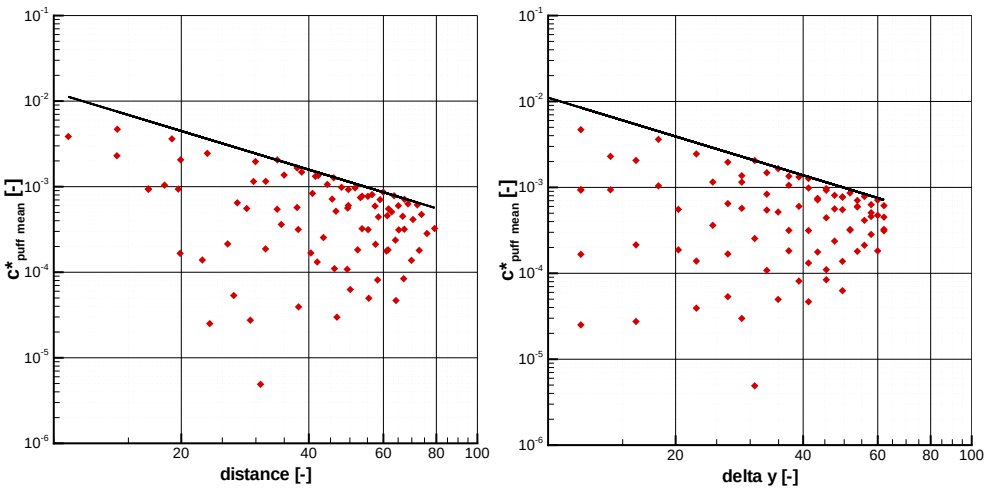

Figure 7.39: Dependency of the puff stationary mean concentration $c^*_{\text{puff mean}}$ on the separation distance between the source and the detector position (left chart) and the separation distance projection to the y-axis (right chart) at half of the container height.

ysis of the wind tunnel observation within the DAPPLE project (Robins and Cheng, 2005) and measurement conducted in the wind tunnel in the frame of BUBBLE project (Feddersen, 2005), at which the similar upper-bounded equation was found, however with different coefficients. Robins and Cheng (2005) found coefficient 50 instead of the coefficient 0.4 and exponent 2 instead of 1.5 in equation 7.8 for the ground level concentration from the ground level tracer

release. (Feddersen, 2005) found coefficient 58 and exponent 1.3, however the distance was not dimensionless (it was measured in metres), the source was at the roof top level and concentrations were at the height $1.8H$. The differences in equations could be caused by different reference velocity definition (the 8 m level in our case and free stream velocity in work of Robins and Cheng, 2005), by different site geometry (a low density regular container array of MUST and the dense built-up area of the centre part of London and Basel in the case of DAPPLE and BUBBLE experiment, respectively).

The Reynolds number independence can be studied also in the case of the characteristic times for average puffs. The travelling, filling, and flushing time as a function of Re_B is shown in the upper left, upper right and lower chart in Fig. 7.40, respectively. The travelling time, which is a time from the opening of a magnetic valve to the first arrival of the tracer to the measurement location, was steadily increasing with increasing Reynolds number. The increase is linear and the same for all six reference positions (increase of approximately 20 in the

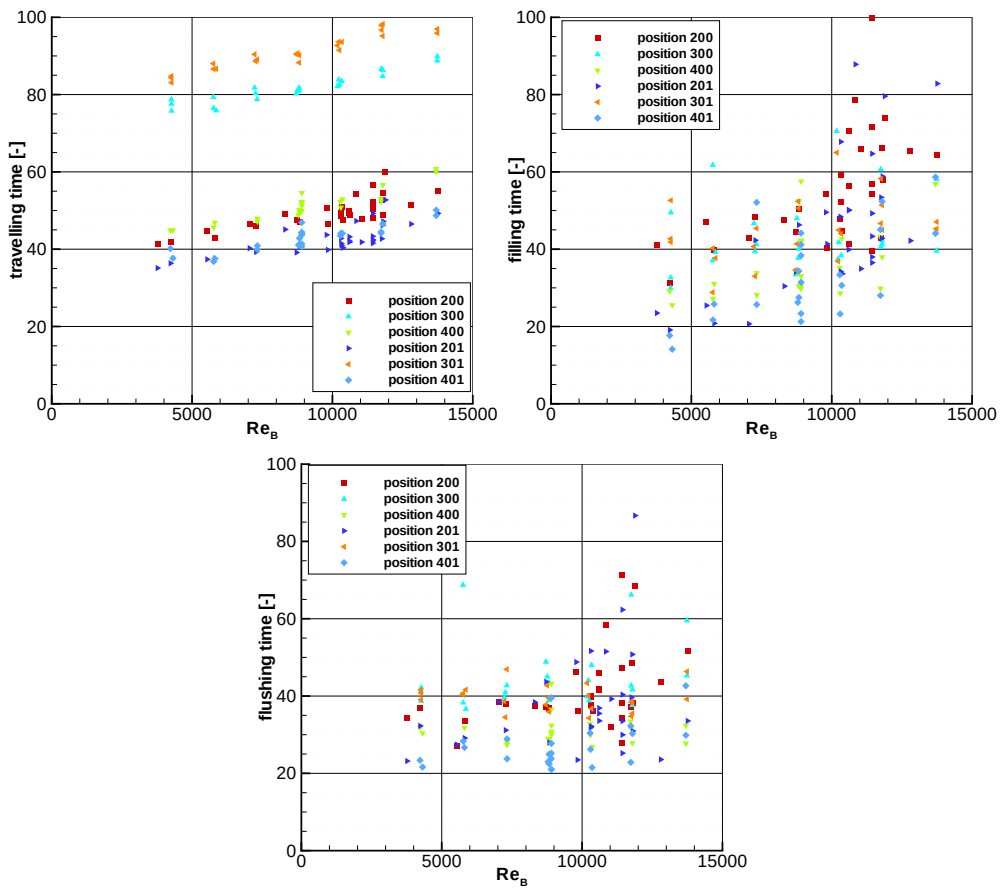

Figure 7.40: Dependency of the travelling (upper left chart), filling (upper right chart), and flushing (lower chart) time on the Building Reynolds number at six reference positions at half of the container height.

Re_B range (4000, 14000)). This behaviour could be caused by the Reynolds number dependence of the concentration field in the vicinity of the source (up to the next street canyon behind the source), which was shown in section 7.1.3 (Fig. 7.3) for the continuous release within the MUST container array and by Bezpalcová (2005) for an idealised street canyon. As was said before, the source was placed in a region of a wake area, which is driven by an overlying flow and in the range of the Reynolds number independence it is proportional to it. However, the source flow rate and consequently the outlet tracer velocity were constant (approximately Q = 20 l hour^{-1} and v_{source} = 0.1 m s^{-1}, see section 4.2) for all Reynolds numbers. Therefore the interaction of the tracer and the oncoming flow and consequently the dispersion of the suddenly released passive pollutant within the wake area, at which the source was located, could be dependent on the approach wind speed.

The filling and flushing time definitions seemed to be very sensitive to the average puff shape and therefore they exhibited large value scatter (about 50 %) even for the same Reynolds number. Due to this value scatter no matter-of-fact analysis is possible. Nevertheless, both characteristics by eye sight indicated an increase with increasing Reynolds number (stronger increase showed the filling time). A reason for this behaviour could be again the Reynolds number dependence of the concentration field in the vicinity of the source described above, which could propagate to the whole plume in the form of different characteristics times of the puff experiments.

Anyway, the lay-outs of the characteristics times within the whole plume for the Building Reynolds number equals approximately 8600 are shown in Fig. 7.41. The travelling time (upper left chart in Fig. 7.41) increased with increasing distance from the source as was expected. The filling (upper right chart in Fig. 7.41) and flushing (lower chart) time also exhibited rising trend with the distance from the source, however, the layout is more scattered than in the case of the travelling time. The dependency of these characteristics times of the average puffs on the separation distance from the source will be discussed later in section 7.5 in detail.

7.4.3 Fluctuation Statistics

Since the average puff smoothed out lots of important characteristics like the peak concentrations and fluctuation intensity, (a comparison of some individual puffs and the average puff is shown in Fig. 7.34) some fluctuation statistics were calculated to show detailed puff structure. Figure 7.42 shows examples of the instantaneous concentration histogram and cumulative sum curve for the same time series which were shown in Fig. 7.34, i.e. detector position no. 200, U_{ref} = 4.32 m s^{-1}, Re_B = 9790, opening time of the source $t_{\text{source MS}}$ = 3.9 s, or t^* = 496. Both characteristics, the histogram and cumulative sum, are shown in two versions: (i) the statistics of the whole puff (depicted by light blue colour), i.e. from the source opening to the next source opening, in which case an interval with zero concentration between two individual puffs is included; (ii) the statistics of the stationary part of the puff, which is defined in the previous section 7.4.2 (depicted by dark blue colour). The shape of the histogram can

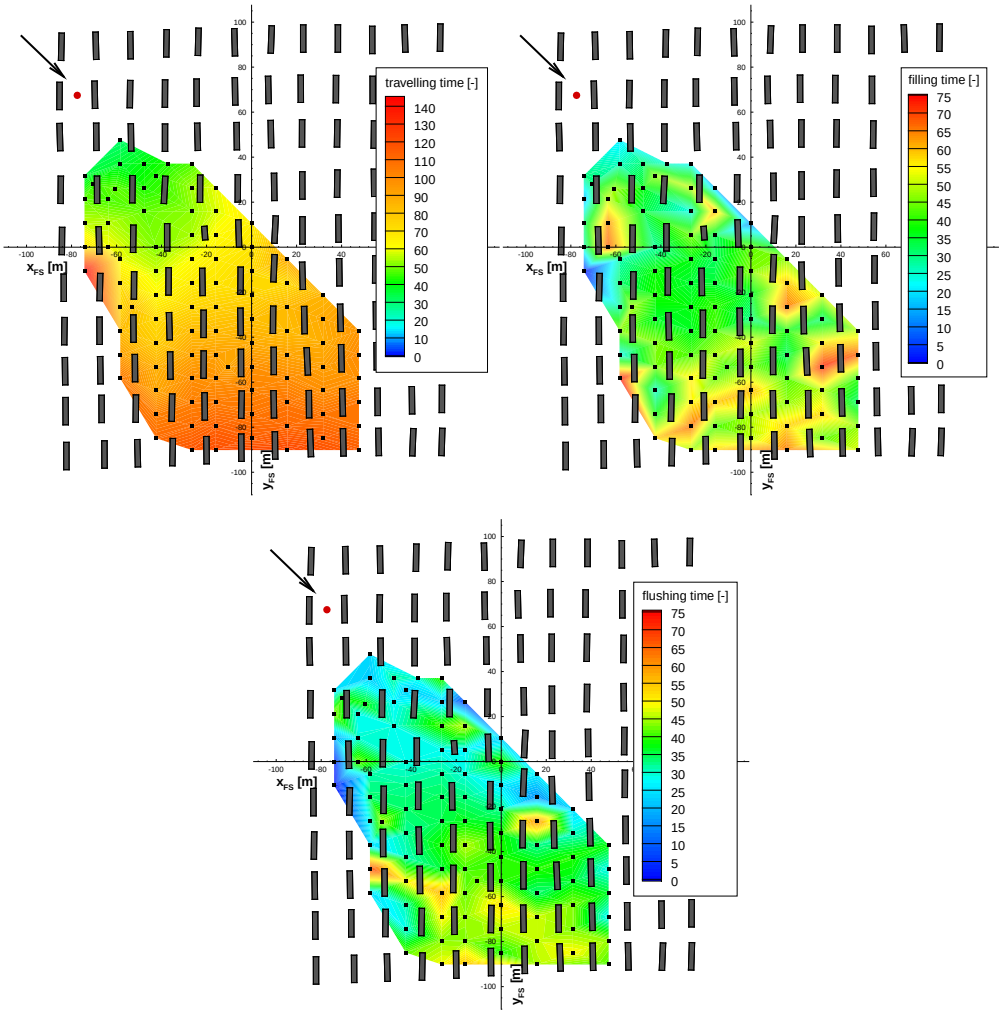

Figure 7.41: Lay-out of the travelling (upper left chart), filling (upper right chart), and flushing (lower chart) time within the whole plume. Source no. 29 is depicted by the red circle, $Re_B \doteq 8600$, $st^* \doteq 430$, at half of the container height.

vary a lot from one individual puff to another as is shown in Fig. 7.34.

Peak Concentration

The difference between the histograms based on the different selection of the intervals is greatest for the zero concentration, where the stationary part of the puff showed just a 'natural' intermittency (i.e. occurrence of the zero concentration, see intermittency definition below) of the dispersion, while the whole puff statistics showed also an interval with the zero concentration due to the closed source. The amount of the zero concentration counts was obviously dependent on the time lag between two source opening, which was set by the experimentalist. Therefore the statistics based on the whole puff time series had no use value. The 0.99 percentile value of the histogram based on the

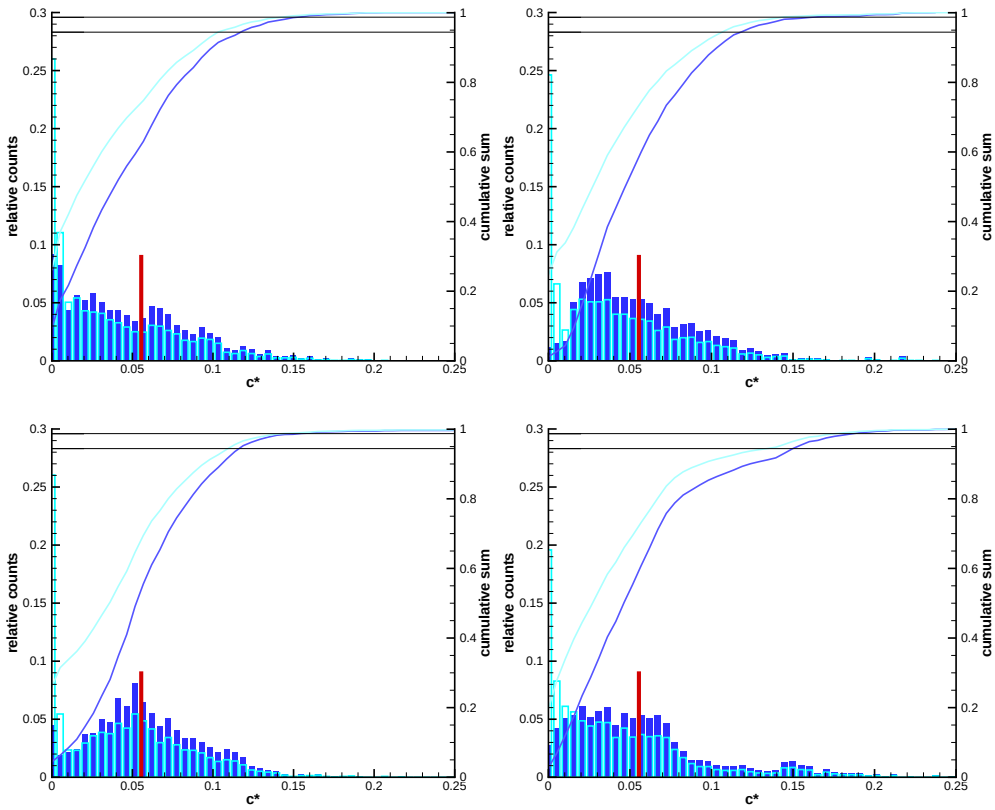

Figure 7.42: Examples of the concentration histograms and corresponding cumulative sum curves at half of the container height for the whole puff duration (light blue) and the stationary part (dark blue). The horizontal black lines show 0.95 and 0.99 percentiles, the red vertical line shows the ensemble mean concentration of the stationary part of the puff, $c^*_{\text{puff mean}} = 0.056$.

stationary part of the puff was chosen as a peak concentration indicator. This value was calculated for every individual puff and the values shown in Figures 7.43 and 7.44 are the ensemble mean values (error bars indicate the ensemble standard deviation).

The ensemble standard deviation of the 0.99 concentration percentile (i.e. error bars shown in Fig. 7.43) is highly dependent on the stationary time of the puff. It is less than 5% of the ensemble mean value for the longest stationary times (more than $t^* = 1000$), while it reached more than 50% of the ensemble mean value for the shortest time (t^* about 200). The mean values of the 0.99 concentration percentile did not show dependence neither on the Building Reynolds number (left chart Fig. 7.43) nor on the duration of the puff stationary part (right chart Fig. 7.43).

Figure 7.44 shows the lay-out of the 0.99 concentration percentile within the whole plume. The shape of the 0.99 concentration percentile plume is very similar to the shape of the mean concentration plume (shown in Fig. 7.9 for the case of continuous release and the comparison between the continuous and puff

mean values is shown in Fig. 7.38), only the values are greater. The relation between the mean concentration and the peak concentration, which is in our case represented by the 0.99 concentration percentile, is shown in Fig. 7.45.

Both scales in Fig. 7.45 is logarithmic and the black lines indicate the minimum of the 0.99 concentration percentile observed. These observations

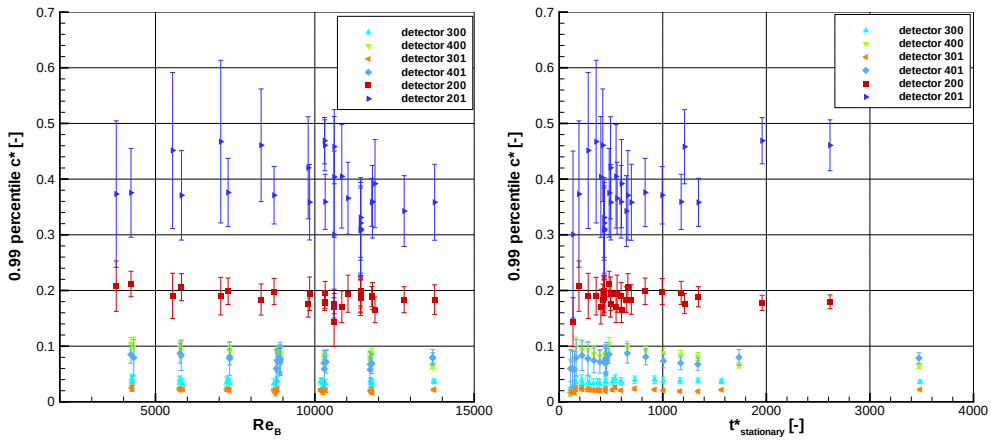

Figure 7.43: Dependency of the 0.99 concentration percentile on the Building Reynolds number (left chart) and on the stationary time (right chart) at six reference positions at half of the container height and based on the puff experiments.

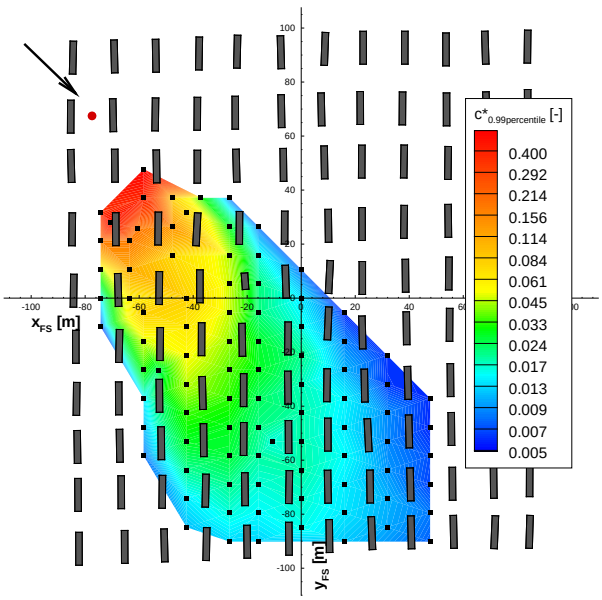

Figure 7.44: Lay-out of the 0.99 concentration percentile within the whole plume in the exponential concentration scale. Source no. 29 is depicted by the red circle, $Re_B \doteq 8600$, $t^*_{\text{stationary}} \doteq 430$, at half of the container height, and based on the puff experiments.

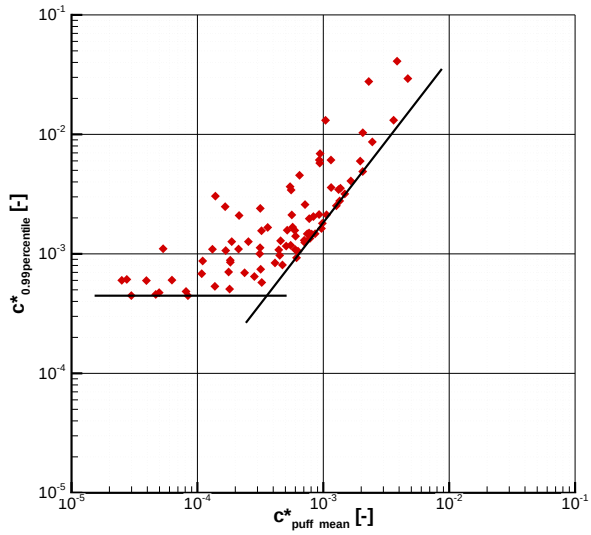

Figure 7.45: The peak concentration $c^*_{99\ \mathrm{percentile}}$ as a function of $c^*_{\mathrm{puff\ mean}}$ at half of the container height based on the puff experiments.

demonstrate that the peak concentration (represented by the 0.99 concentration percentile) is lower-bounded by the two black lines, i.e. by the following empirical equation:

$$c^*_{99\ \mathrm{percentile}} \geq \max(3.1 \cdot c^*_{\mathrm{puff\ mean}} - 0.0008; 0.00045) \tag{7.9}$$

The data that rise above the straight lines are concentration values at locations away from the plume centreline, and the larger the distance from the plume centreline, the lower is the mean concentration. However, the peak concentration can stay very high even in the case of low mean value. This behaviour is also connected with an enhanced fluctuation intensity on the edge of the plume (see section 7.2.2). The peak-to-mean value of 3 (slope of the slanted line in Fig. 7.45) was also observed by Rodean and Cederwall (1982) in the case of heavy gas dispersion.

Dependency of the peak concentration (represented by the 0.99 concentration percentile) on the separation distance is shown in Fig. 7.46. The peak concentration exhibited the same behaviour as the mean concentration in Fig. 7.39, only the values are greater. The bounding lines can be described by the following equations:

$$c^*_{99\ \mathrm{percentile}} = \frac{6}{\Delta^2}, \text{ or } c^*_{99\ \mathrm{percentile}} = \frac{5}{\triangle y^2}. \tag{7.10}$$

In general terms, these result are roughly in agreement with those given by Yee et al. (1994b) and Nickola (1971) who found that the peak concentration decrease with downwind distance approximately as $\Delta^{-2.2}$ for the field tests conducted under near-neutral conditions.

The equations 7.8, 7.9, and 7.10 are not consistent, e.i. $c^*_{99\ \mathrm{percentile}} \approx 3.1 \cdot c^*_{\mathrm{puff\ mean}}$, $c^*_{99\ \mathrm{percentile}} \approx 6 \cdot \Delta^{-2}$, and $c^*_{\mathrm{puff\ mean}} \approx 0.4 \cdot \Delta^{-1.5}$. This inconsistency

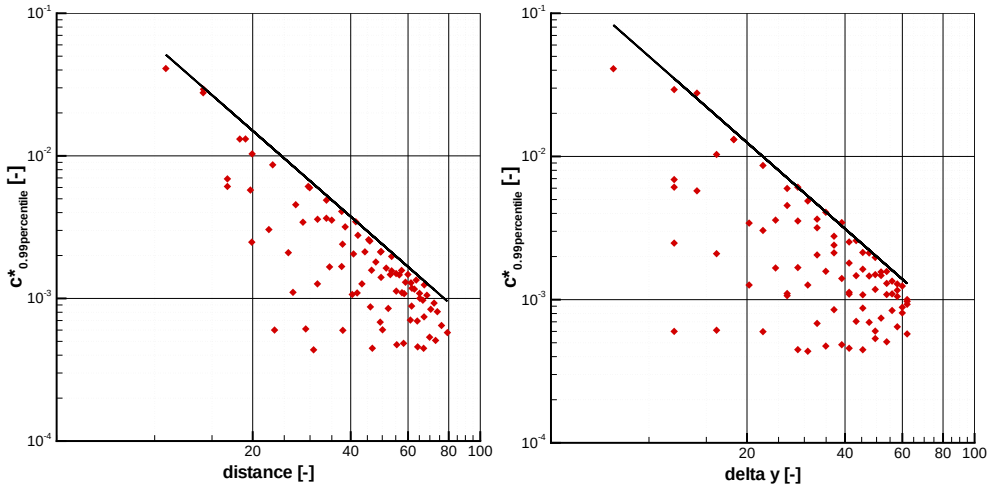

Figure 7.46: Dependency of the peak concentration $c^*_{99\ \mathrm{percentile}}$ on the distance between the detector and the source (left chart) and distance's projection to the y-axis (right chart) at half of the container height based on the puff experiments.

pointed out, that the points lying on the above mentioned lines are not always the same, e.g. the centerline values, but also some different ones.

Intermittency

It can be easily seen that the concentration appears at the detector site as a pulses of high concentration separated by intervals of zero or nearly zero concentration (see individual puff examples in Fig. 7.34). The zero intermittency, γ_0, is defined as the fraction of the time of non-zero concentration at a given point (Dinar et al., 1988). Analogically, the twice mean intermittency, γ_{tm}, is defined as the fraction of the time when instantaneous concentration was less than the twice stationary mean concentration $c^*_{\mathrm{puff\ mean}}$ at a given point. To illustrate just defined characteristics: the zero (twice mean) intermittency would be 0.8, if during 20% of the puff stationary part the instantaneous concentration would be zero (greater than the twice mean value).

The averaging time and Reynolds number tests of the intermittency factors are shown in Fig. 7.47. The accuracy (i.e. ensemble standard deviation depicted by the error bars) of both intermittency factors γ_0 and γ_{tm} are improving dramatically with increasing stationary time of the puffs: from inaccuracy ± 0.2 of the most intermittent and the shortest puff realisations (e.g. detectors no. 201 and 401 located at the plume edge) to the ± 0.03 at the same positions but for the longest times (upper row in Fig. 7.47). The locations near the plume centreline and far in the container array (i.e. the detector position no. 200, 300, 400, and 301) exhibited as less intermittent in both intermittency characteristics, γ_0 and γ_{tm}. Also the inaccuracy is much smaller (about $\pm$ 0.01) than in the case of the detectors no. 201 and 401 and independent on the averaging time. It is worth to mention that the ensemble average value is for both intermittency

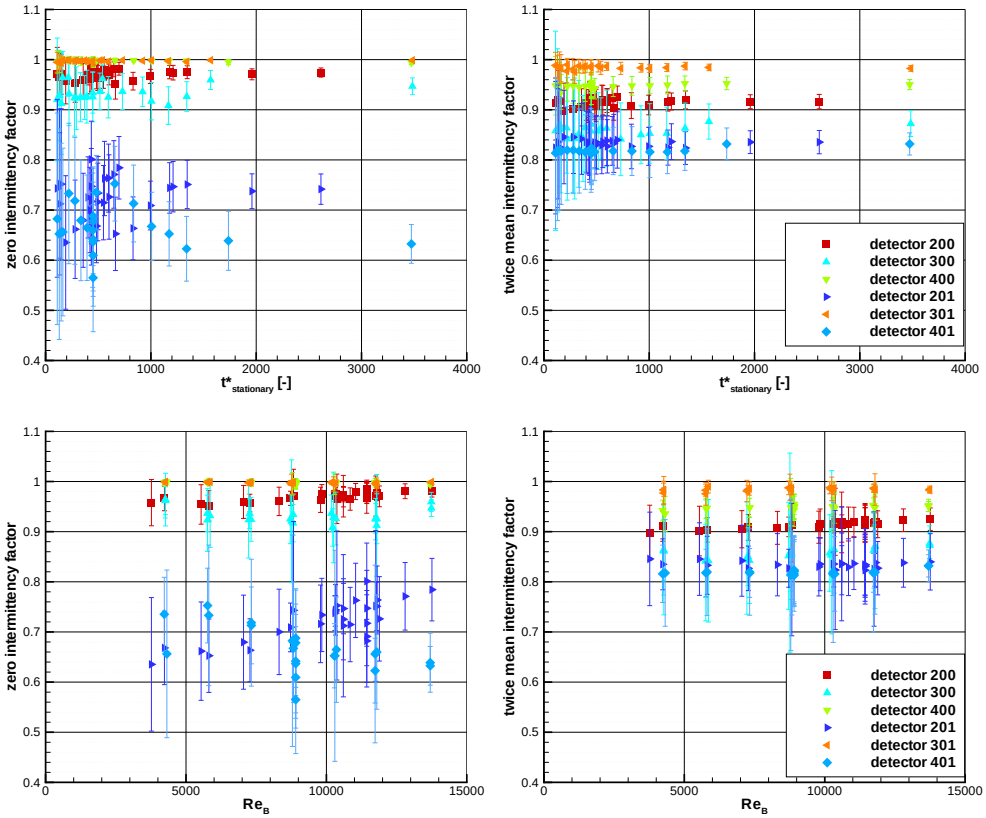

Figure 7.47: Dependency of the zero (left column) and twice mean (right column) intermittency factor on the duration of the puff stationary part (upper row) and the Building Reynolds number (lower row) at six reference positions at half of the container height.

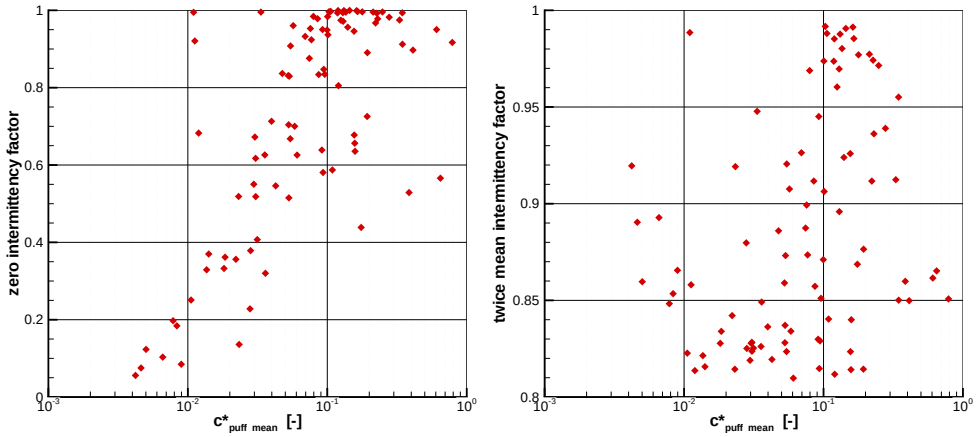

Figure 7.48: Dependency of the zero (left chart) and twice mean (right chart) intermittency factor on the stationary mean concentration at the whole plume positions at half of the container height based on the puff experiments.

factors (especially γ_{tm}) very well stationary time independent, even thought the ensemble standard deviation is very large for the shortest stationary times.

The Reynolds number dependence (lower row in Fig. 7.47) was not observed for both intermittency factors at any position. Exception is the dependency of the zero intermittency factor on Re_B at the locations no. 201 (dark blue triangles) and 401 (light blue diamonds), which showed a trend. However, this trend is negligible within the range of uncertainty, which was essessed to be ensemble standard deviation.

Figure 7.48 shows the zero (left chart) and twice mean (right chart) intermittency factors as a function of the puff stationary concentration $c^*_{\mathrm{puff\ mean}}$. It can be said in general that the zero intermittency factor (left chart in Fig. 7.48) is increasing with increasing $c^*_{\mathrm{puff\ mean}}$, i.e. the higher mean concentration, the less occurrence of zero instantaneous concentrations. The twice mean intermittency factor (right chart in Fig. 7.48) had no significant dependence on the puff stationary concentration.

Lay-out of the zero and twice mean intermittency factors within the whole plume is shown in left and right chart in Fig. 7.49, respectively. Both characteristics had pronounced a much greater cross-plume than along-plume variation. The zero mean intermittency factor, γ_0, is very close to 1 near the plume centreline and decrease to the plume edges to the values about 0.5 and less, except the first two street canyons behind the source, at which significantly intermittent ($\gamma_0 \approx 0.7$) concentration time series were found even at the positions close to the plume centreline. The twice mean intermittency factor lay-out is very similar to the lay-out of γ_0, only the the minimum values on the plume edges have magnitude about 0.8 and they increase in the direction to the plume centreline, where they reached values very close to 1. Very similar behaviour of

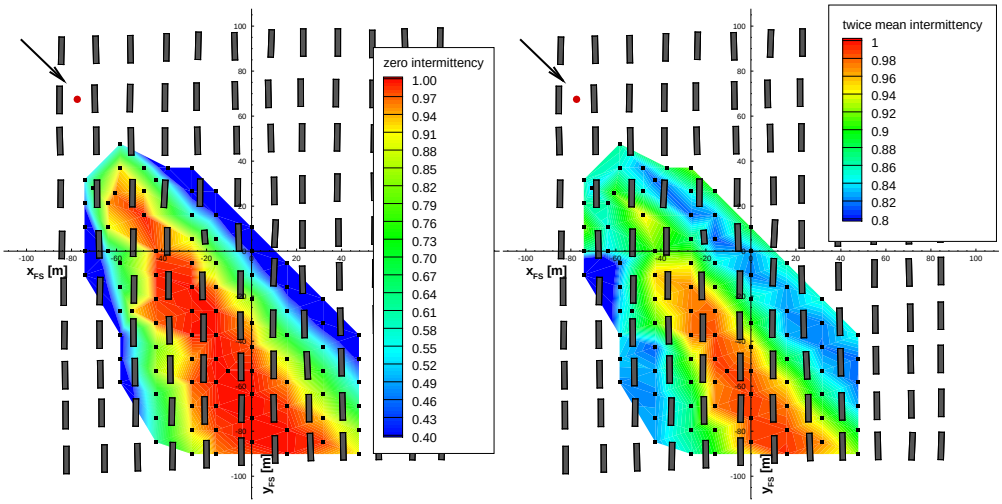

Figure 7.49: Lay-out of the zero (left chart) and twice mean intermittency (right chart) within the whole plume at half of the container height based on the puff experiments.

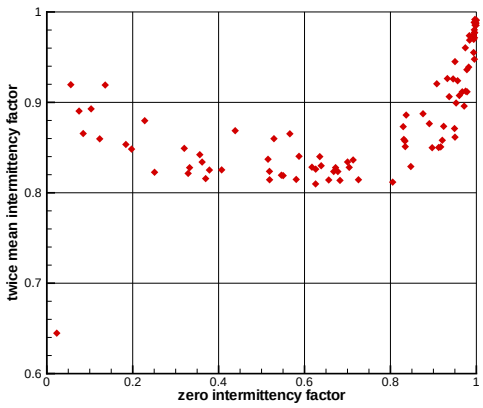

Figure 7.50: Relation between zero (on the abscissa) and twice mean (on the ordinate) intermittency factors at half of the container height based on puff experiments.

both characteristics γ_0 and γ_{tm} within the whole plume gave birth to Fig. 7.50, in which both characteristics are related to each other at given points.

The relation between γ_0 and γ_{tm} can be described as follows: for highly intermittent concentration time series ($\gamma_0 < 0.8$) the twice mean intermittency factor stays approximately constant within the range (0.8; 0.9); for the less intermittent concentration time series ($\gamma_0 > 0.8$) the relation $\gamma_0 \approx \gamma_{\mathrm{tm}}$ is valid. It should be mentioned that while zero non-intermittent concentration time series ($\gamma_0 = 1$), which have been found in the plume centerline, are not exceptional, time series with $\gamma_{\mathrm{tm}} = 1$ were not detected at any location within the whole plume (maximum $\gamma_{\mathrm{tm}} = 0.99$).

7.5 Travelling Time

The time needed by a passive pollutant to travel between two points is the meaning of the travelling time quantity (labelled tt) in this work. There are many methods how to obtain the travelling time and a comparison of different definitions of the travelling times is the aim of this section. In general, the methods can be divided into two groups: methods based on theoretical models of pollution dispersion and methods based on experimental results.

Methods based on theoretical models trade on a knowledge (or assumptions) of flow and dispersion phenomena within the atmospheric boundary layer. These models usually contain experimentally proven coefficients. As an example a Gaussian dispersion model (discussed in section 2.4.2) can be named.

The most straightforward way from the experimental method is to release a passive tracer at one point and measure the time, at which the tracer can be detected in the second point. This method was used in section 7.4 for the travelling time estimation. Another ways are more sophisticated and they are based on the knowledge of the flow and concentration field. An example of integral definition of the travelling time is equation 2.40 in section 2.4.2 proposed by (Hanna and Britter, 2002), where knowledge of whole flow and

concentration field is required. New method was developed in the frame of the presented work and it is based on the concentration spatial correlations (see section 7.3).

The experimental results showed below were obtained under these conditions: the MUST container array, the approach wind direction -45°, ground level source no. 29, and measurements were carried out at half of the container height (for experimental detail see chapter 4 and appendixes A and B).

Firstly, the results of different times defined in section 7.4.2 and based on the puff measurements will be discussed. Figure 7.51 shows a dependency of the dimensionless travelling, tt^*, (upper row), filling, ft^*, (middle row), and flushing, lt^*, (lower row) time on the dimensionless distance between the detector and the source (left column) and the distance's projection to the y-axis (right column). The significantly less scattered dependency was obtained for the cases, where the characteristics times are treated as a function of the dimensionless distance's projection to the y-axis, $\triangle y^*$ and therefore the following discussion will be focused on these results.

The travelling time (upper right chart in Fig. 7.51) exhibits well pronounced linear dependency on $\triangle y^*$. This dependency will be parameterised later in this section. The filling time (middle right chart in Fig. 7.51), i.e. the time from the first arrival of the tracer to the saturation of the sampling point surrounding with the tracer, which displays itself as a continual ensemble mean concentration increase, shows a linear increase with the distance in general. The filling time can be parameterised as $ft^* \approx \triangle y^*$, however, the scatter of the values is large (approximately 50%). The flushing time dependency on the $\triangle y^*$ (lower right chart in Fig. 7.51) is also scattered, however majority of the points lying along the line $lt^* \approx 0.5 \cdot \triangle y^* + 16$. An increase of all three characteristic times with increasing distance or with distance's projection to the y-axis is expected since the urban canopy acts like a reservoir of the pollutant with a certain capacity, which of course linearly depend on the area of the urban canopy. The more separated is the detector location from the source, the larger area has to be filled before the tracer reaches the detector. This phenomena causes: (i) a delay of the first detection of the tracer (i.e. travelling time); (ii) a longer filling time since the area which is filled in one moment is getting larger with increasing distance as the lateral spread of the plume is increasing; (iii) a longer flushing time since after the source closing all the tracer captured by an up-lying urban canopy has to pass the detector position and the longer fetch, the more tracer has to be flush out. The reservoir effect is mainly cased by wake regions connected with the sharp edges structures inside the urban canopy and their poor ventilation.

The magnitudes of the filling and flushing times are very similar (between 20 and 60 within the whole plume, see middle and lower right charts in Fig. 7.51), however, the average puffs (a representative example is shown in Fig. 7.36) by eye-sight observation exhibit much longer end tail (i.e. flushing time) than start tail (i.e. filling time). The magnitudes of both characteristic times is very dependent on the definition of the border points $ft1$, $ft2$, $lt1$, and $lt2$ (see Fig. 7.36), which were set as 10% and 90% of the stationary mean concentration

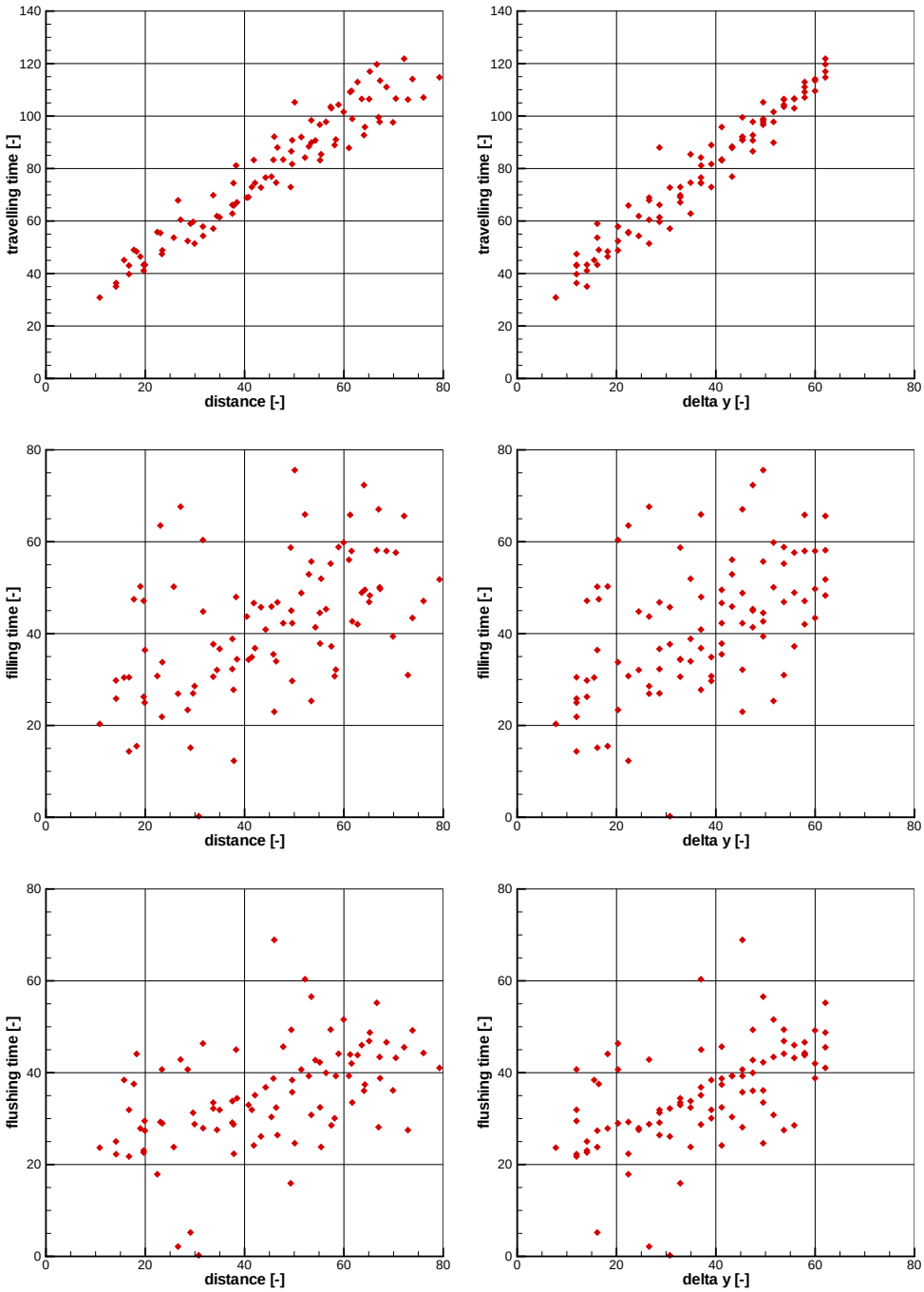

Figure 7.51: Dependency of the travelling (upper row), filling (middle row), and flushing (lower row) time on the distance between the detector and the source (left column) and distance's projection to the y-axis (right column) based on puff experiments and measured at half of the container height.

value. The longer end tail (i.e. flushing time) of the average puffs is pronounced by a very slow increase of the concentration long after the source closing. Since the increase is so slow, an estimation of the time when the concentration reach a threshold value is can be estimated only with a large uncertainty. Therefore a 'safe' (i.e. large enough to concentration time series fall reasonably fast at this concentration) threshold of $0.1c^*_{\text{puff mean}}$ has been chosen at this work to ensure reasonable uncertainty of the characteristic times estimation.

The same charts as was shown in the upper row in Fig. 7.51 are presented in Fig. 7.52, however, these are based on the spatial concentration correlations (the results with reference sampling locations no. 100 and 200 are plotted in the upper and lower row, respectively, see section 7.3 for details). The left and right chart shows the time lags when the spatial concentration correlation coefficients, r_{SC} were maximal against the distance between two detectors and distance's projection to the y-axis, respectively. The points are coloured according to the absolute maximal spatial concentration correlation coefficient reached.

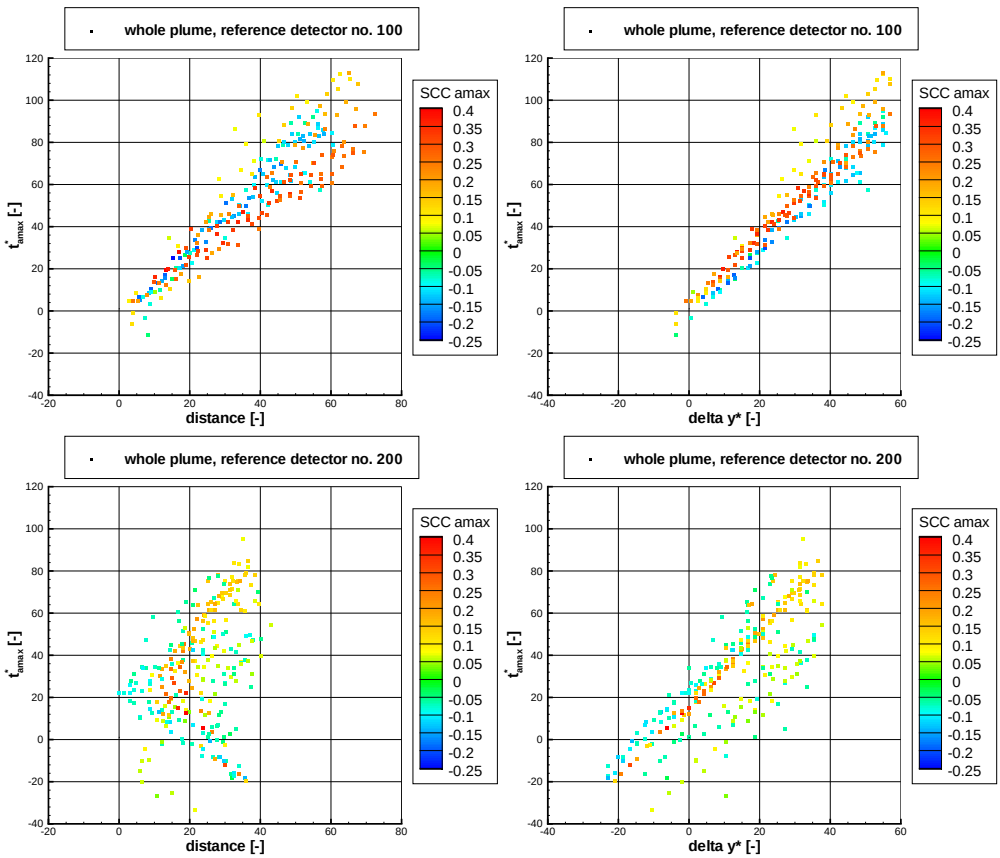

Figure 7.52: Dependency of the travelling on the distance between two detectors (left column) and distance's projection to the y-axis (right column) based on the time lags when the spatial concentration correlation coefficients were maximal (the absolute maximum value is depicted by the colour of the points) for two different reference detector positions.

Let us focus firstly on the left charts. The values indicate a linear dependence of the travelling time between two locations based on the spatial concentration correlation measurement on the distance between these two locations, however, the scatter of values is large, especially in the case of detector no. 200 (± 30). The distance between to sampling position was calculated independently on the relative position of these points in respect to the flow and container array, i.e. only positive values of distance were obtained. In contrast, the time lag, at which the absolute maximum of r_{SC} was reached, could be also negative since the first detector could be placed behind the second detector in respect to the flow. This is a reason why there is a group of points at the negative time region, which do not fit with the positive time region (the dependence is turn about 90°). Another aspect of these charts is that the locations with negative r_{SC} (blue colour), positive r_{SC} (red colour), and small values of both signs ($r_{SC} \in$ (-0.1; 0.15), depicted by green and yellow colour) were somehow agglomerated together.

Surprisingly much less scattered data are shown in right charts in Fig. 7.52, in which the distance between the detectors were replaced by the dimensionless distance's projection to the y-axis. Also another aspects are clear now: the $\triangle y^*$ quantity took into account an order of the detector, i.e. if the first detector was placed behind the second one, the $\triangle y^*$ was negative; and an agglomeration of the points, at which similar magnitudes of the maximal r_{SC} were obtained, is much evidently pronounced.

Finally, it can be conclude that a stronger (or more evidently pronounced) dependence of the travelling time was found for the distance's projection to the y-axis than for the separation distance itself. The compilation of the results based on both of the above described methods is shown in Fig. 7.53. The results based on the puff experiments (blue colour) are identical to those shown in the upper right chart in Fig. 7.51. The results based on the spatial concentration correlation, which are shown in right chart in Fig. 7.52, were divided according to the sign of the maximal r_{SC} to the positive r_{SC} (green colour) and negative r_{SC} (red colour), while the points with small absolute maximal value of the spatial concentration correlation coefficient, $r_{SC} \in$ (-0.1; 0.15), were excluded.

The following trend lines can be fitted to the data:

$$\begin{aligned} tt^*_{\text{puff}} &= 1.54\triangle y^* + 21 \\ tt^*_{\text{SC positive}} &= 1.78\triangle y^* + 1.6 \\ tt^*_{\text{SC negative}} &= 1.64\triangle y^* - 3.8 \end{aligned}$$

The slopes of the dependency fitted curves in Fig. 7.53 are very similar, which has been proven by the trend lines fitting. The most remarkable difference is a large offset in the case of the puff experiments. This offset was caused by the releasing conditions of the ground level source. The tracer first had to fill the cavity of the street canyon, at which the source was placed, and after then it dispersed into the container array. This phenomenon was not included in the case of the spatial concentration correlation measurement. The travelling time based on the negative r_{SC} data is not the pure time needed by the tracer to travel from one to another point. If the idea of the travelling tracer puffs from

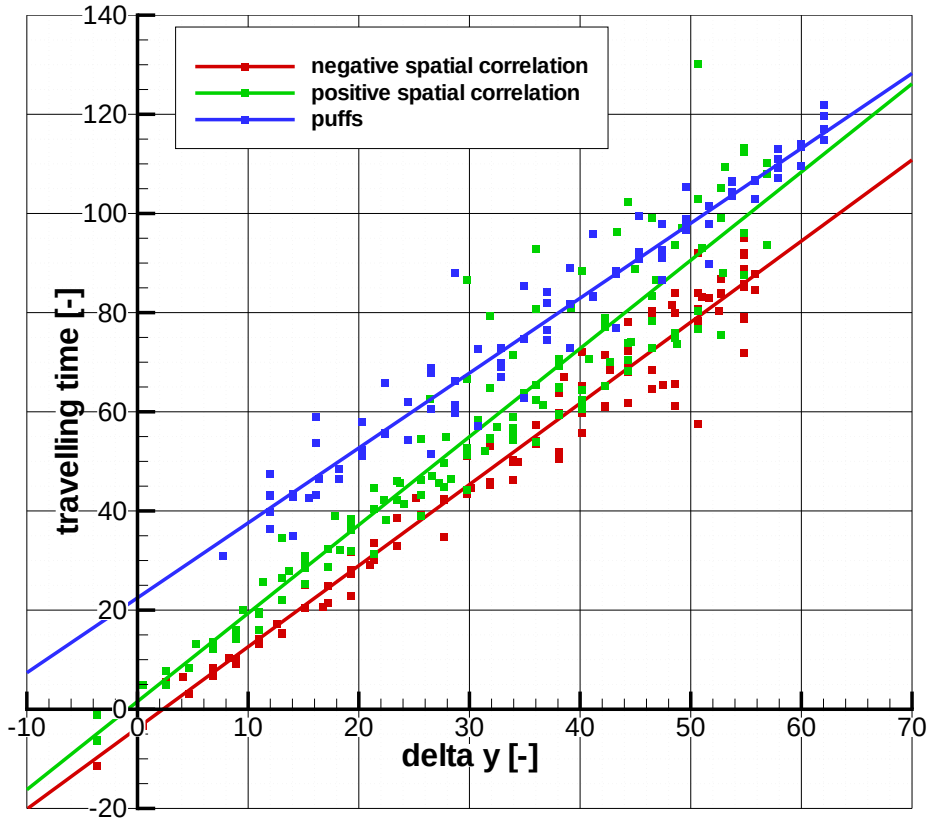

Figure 7.53: Travelling time as a function of the dimensionless y^*-distance between two places. Comparison of the results based on the maximal spatial concentration correlation coefficients (divided according to the sign of the spatial correlation coefficient) and the puff experiments.

section 7.3.1 is recalled (let us assume, for simplicity, that the puffs have two preferred trajectories. Our two detectors are located at different trajectories and the source releasing the tracer continually. Therefore if the first detector at the first trajectory very close to the source is measuring nothing, there is an already released puff, which is following the second trajectory and will hit the second detector after some time lag), the same slope of the dependency of tt^* on $\triangle y^*$ can be interpreted as the same travelling time of the tracer on both trajectories. The negative offset is caused because of the two time series, from which the r_{SC} was calculated, are created by completely different tracer particles or puffs and the process near the source played a role.

The travelling speed of the tracer can be obtained using the definition of the advective pollutant speed (equation 7.7):

$$v^*_{\text{pollutant}} = \frac{\triangle y^*}{tt^*} \Rightarrow \begin{array}{l} v^*_{\text{puff}} = 0.65 \pm 0.05 \\ v^*_{\text{SC positive}} = 0.56 \pm 0.06 \\ v^*_{\text{SC negative}} = 0.61 \pm 0.02 \end{array} \Rightarrow v^*_{\text{pollutant}} = 0.61 \pm 0.04$$

The wind speed measured inside the container array (shown in chapter 6) can be compared with the pollutant speed, $v^*_{\text{pollutant}}$. The flow measurement showed in Fig. 6.6 was conducted under the same conditions as the concentration measurement showed in Fig. 7.53. Since the reference wind speed of the approach flow was $U_{ref} = 5$ m s^{-1}, the integral value of the wind speed measured at half of the container height $U_{0.5H\,-45^\circ} = 3.2$ m s^{-1} means

$$v^*_{\text{advective}} = 0.64 \pm 0.02,$$

while undisturbed approach flow reached at half of the container height speed 3.6 m s^{-1}, i.e. 0.72 in the dimensionless notation.

It can be concluded that the passive tracer travelling speed, $v^*_{\text{pollutant}}$, based on both methods is in good agreement with the measured advective speed estimated on the basin of the LDA measurement within the range of uncertainty. The pollutant speed within the container array is about 90% of the approach wind speed at the same height.

7.6 Conclusions

Foremost the validation of the concentration measurement conducted in the wind tunnel on the scaled model was performed. The uncertainties of the measured concentration characteristics, i.e. the mean, standard deviation, skewness, kurtosis, and integral length scale of the concentration time series, as a function of the averaging time at 4 locations within the container array were determined. The value uncertainties decreased with increasing averaging time for all examined characteristics to a convergence value, which was given by the turbulent character of the flow and instrumentation uncertainties. The uncertainty convergence value for one characteristic varied a lot dependently on the position within the plume (the smallest values were found near the plume centerline, the highest at the plume edge). The decrease was faster for the lower order statistical moments (i.e. the mean, standard deviation, and integral length scale) and slower for the higher order statistical moments (i.e. skewness and kurtosis). Also the independency of all concentration characteristics on the Building Reynolds number and source strength was checked to ensure the validity of the dimensionless concentration definition (equation 7.1).

The wind tunnel measurements of the concentration characteristics inside the container array significantly extended the MUST field measurements, which were conducted only at several fixed positions and for given wind direction. The comparison of various concentration characteristics obtained during the wind tunnel and MUST field measurement (the field trial 2681849, see section 7.2 and Biltoft, 2001, for experimental details) has been shown on the horizontal profiles along the street canyons and vertical profiles at the position of the T tower. The shapes of the profiles agree very well (except the values the concentration mean value (Fig. 7.5 and 7.6) and concentration integral length scale (Fig. 7.21) were significantly greater than value obtained in the wind tunnel), however, the measurement from the T tower showed stable thermal stratification during the

field campaign (see section 3.4). The wind tunnel used allows to model only the neutral stratification therefore even greater disagreement was expected.

Except the comparison exercises, the experimental set-up corresponded with the case, for which the flow field has already been measured (i.e. wind direction -45° and the detector height at half of the container height) to get deeper insight into physical phenomena in context. The measurement of the concentration characteristics within the whole plume (about 300 points) shows that the plume centreline (i.e. position with the maximal concentration in the cut perpendicular to the wind direction, see Fig. 7.9) at half the container height was not parallel to the approach wind direction, but was influenced by the orientation of the containers and therefore it is curved to the right hand side. The higher order statistical moments (skewness and kurtosis) and intensity of fluctuation (ratio of the concentration standard deviation and mean value) exhibited remarkable cross plume variation, i.e. they significantly increase towards the plume edges, which corresponds with a highly intermittent character of the concentration time series and highly asymmetric concentration probability density function at the plume edges.

The detailed measurement of one street canyon at three heights ($0.5H$, $1H$, and $2H$; about 70 points per level) were conducted to uncover how variable and smooth the concentration characteristics are (i.e. how big could the difference be between the two sides of the street canyon and is the character of this transition). The results proved an expectation of a smooth transition of the concentration characteristics between positions, at which the whole plume measurement was conducted, in the case of the lower order moments. The higher order moments and concentration integral length scale are characteristics much more sensitive to the character of the flow and therefore very changeable values of these characteristics were found in the wake regions and at the container height, at which the vertical mixing was enhanced.

A completely new method of passive tracer travelling time estimation was shown in section 7.3. The travelling time estimation was based on simultaneous measurements of the concentration time series at two different positions within the pollutant plume. The spatial concentration correlation coefficient, r_{SC}, between these two time series were plotted as a function of time lag (see Fig. 7.25). Then the maximum of the spatial correlation coefficients and the corresponding time lag were found. However, the maximal absolute values of r_{SC} are relatively small (typically about 0.2, but also less than 0.1), they are statistically significant due to the large number of the samples in the time series ($2 \cdot 10^5$ samples per time series). Two lay-outs of the maximal r_{SC} values within the plume, when the position of the first concentration time series detector was fixed at different locations, are shown in Fig. 7.28 and 7.29. The evident division of the plume into two parts (one positively and other negatively correlated with the fixed location) proved the theory of plume meandering.

The plume meandering is just part of the idea that the pollutant stays somehow in 'puffs', which pass the container array on Lagrangian trajectories. Locations, which lie within one trajectory (trajectories are usually smooth lines, which do not cross the plume in the lateral direction), are hit by the same 'puffs' with a time shift, that results in a positive correlation between these two points.

Locations, which lie on the completely different trajectories, are hit by different 'puffs', and assuming that at one moment only one 'puff' is created near the source, results in a negative correlation between these two points. The definition of the travelling time is therefore the time when the maximum of r_{SC} is reached.

The last part of the concentration measurement focused on the sudden and time limited releases of a quantity of a pollutant, so called 'puff' experiments. A large number of realisations of the dispersing cloud was required for a statistically relevant description of the dispersion phenomena since individual puff release realisations are non-stationary, inhomogeneous, and highly variable. Therefore at least 70 realisation of the individual puff releases were carried out and the average puff releases were calculated as an ensemble mean value. The dependency tests of the puff average characteristics (e.g. the mean concentration and the travelling, filling, and flushing times) on the source opening time, and on the Building Reynolds number were performed. Surprisingly reasonably good results were obtained even for the shortest source opening times (approximately 1 s in model scale, or 2 min in full scale), even for which a step-like concentration time series (i.e. with well pronounced part of stationary mean concentration) was measured and this stationary mean value was the same as for the longer source opening times, only the value scatter was larger.

The fluctuation statistics were based on the concentration probability density functions of the stationary parts of the individual puffs. The peak concentration, defined as 99 concentration percentile, was found to be independent on Re_B and the source opening time and at least three time higher than the mean concentration. The zero and twice mean intermittency factor, defined as the fraction of time of non-zero and less than twice mean value concentration at a given point, respectively, were calculated. The well pronounced cross-plume structure (values close to 1 at the plume centreline and a decrease towards the plume edges) as well as dependency of both intermittency factor on each other were found.

The last part dealt with the characteristic times (i.e. travelling, filling, and flushing times) and their dependency on the position within the array. The most evident dependency was found on the projection of the separation distances to the y-axis, i.e. the axis parallel to the long container faces (also other dependency on the separation distance itself, or on two parameters - $\triangle x$ and $\triangle y$, were examined, however, always with worse results). Since the filling and flushing times are very dependent on the definition (especially on the set-up of the zero concentration threshold at the long flushing tail of the average concentration time series), the interest was on the travelling time. The travelling times as a function of the separation distances to the y-axis based on two different methods (the spatial concentration correlation and the puff experiments) and the advective wind speed measured by the LDA system were compared with a reasonable good agreement. It is however worth mentioning that the spatial correlation method was the most effective and reliable. The time needed for the experiment was approximately five times shorter and the precision of the results obtained two times higher.

Chapter 8

Summary

The study of dispersion through large idealised arrays of obstacles was conducted to obtain a better understanding of dispersion through a real urban environment. The MUST field and laboratory study of idealised obstacle arrays were necessarily simplifications of the real, complex, urban environment. This type of geometry, however, displayed some of the characteristic behaviour of more complex, real-world configurations, and showed some generally valid rules.

The MUST outdoor dispersion field trials were made unique by numerous precise and high time resolving measurement instruments. However, the merits of the field measurements do not allow for the systematical study of the flow and dispersion phenomena, since the atmospheric conditions are extremely variable and often difficult to measure and characterise. There was limited time for the MUST field campaign and certain interesting configurations were just not realised or could not be repeated to estimate the measurement uncertainties. Laboratory (i.e. wind tunnel) experiments , on the other hand, allowed the experimentalist to strictly control experimental environments, where particular configurations of interest were investigated in detail, thus the wind tunnel measurement were able to fill in data gaps unavoidably encountered in the MUST field experiment and to validate experimental errors and uncertainties. Because of the ability to tightly control parameters in the wind tunnel more stationary conditions were simulated, giving measurements and results based on more certain input conditions, which lead to better convergence of the statistics of the time series obtained on the model.

This type of wind tunnel experiment also provides better defined boundary conditions when running computational models for validation or other purposes. The presented experimental data set - MUST wind tunnel and field measurement - is to become a validation set for atmospheric boundary layer numerical models, especially for models dealing with flow and dispersion phenomena in the micro scale with a high spatial and temporal resolution. An excellent opportunity has been opened for a direct comparison of the field, wind tunnel, and numerical modelling results. The presented results will be one part of the validation data base being prepared within the frame of the European Concerted Research Action COST 732 'Quality Assurance and Improvement of Microscale

Meteorological Models'.

The simulation in the wind tunnel gave a very detailed and complete physical picture of flow and plume dispersion within the container array. Therefore the reproducibility and uncertainty of not only the wind tunnel, but also of the MUST field results were estimated and the dependency of results uncertainty on the averaging time was shown.

Detailed flow and dispersion measurements were carried out for one particular experimental set-up (with an oblique wind direction -45° and ground level source) inside the MUST container array. For this experimental set-up the mean flow and turbulence characteristics (i.e. the intensity of turbulence and Reynolds shear stress) as well as a range of concentration characteristics (i.e. the mean, intensity of concentration fluctuation, skewness, kurtosis, and integral length scale based on the concentration time series) were measured at several horizontal planes and vertical profiles within the whole plume.

The dispersion study was conducted not only with a continually open source, but also the sudden release of a quantity of the tracer (known as puff experiments) was studied. This part of the work primarily focused on the validation of these experiments, i.e. the dependency of the results on the experimental conditions such a approach wind speed (or Reynolds number), a source opening time, etc.

The goal of the work presented was the estimation of the travelling time of a pollutant inside an idealised urban canopy (i.e. the MUST container array) using two different methods of the travelling time estimation. The first was an entirely new method developed here based on the simultaneous concentration sampling at two different locations with the plume with high temporal resolution. Two synchronised time series obtained were used for the calculation of the spatial concentration correlation function and the time lag, at which the maximum of this function was obtained, was assigned as a travelling time between the measurement locations. The second method was based on the measurement of the time between the source opening and the first arrival of the tracer at the detector position. This experiment needed to be repeated many times (approximately 70 repetitions) to obtained reasonably accurate results, however, the accuracy could never be as good as in the case of the first method. The strongest dependence of the travelling time was found on the separation distance's projection to the y-axis, i.e. to the axis parallel to the long container faces. This result is in very good qualitative and even quantitative agreement with the flow field measured, which is strongly channelled along the long container faces inside the container array.

The amount of both the MUST field and wind tunnel data is enormous. This study therefore could not 'mine' all information contained in these data sets and only some selected quantities were objectives of this work. Following works on this data sets are highly expected.

The presented work, next to some new method of the concentration time series processing, should be useful for the numerical modelers as a testing and validation example for their numerical models of the lowest part of the atmospheric boundary layer with high temporal and spatial resolution.

Appendix A

Spires and Roughness Elements

The sketch of the spires section used in the wind tunnel is shown in Fig. A.1. The spires were intentionally irregularly placed to compensate hall dimensions irregularities, which could cause the lateral flow inhomogeneities.

The sketch of the roughness elements used and their placement on the wind tunnel floor is shown in Fig. A.2. The roughness elements filled the entire space between the wind tunnel entrance with the spires and the model.

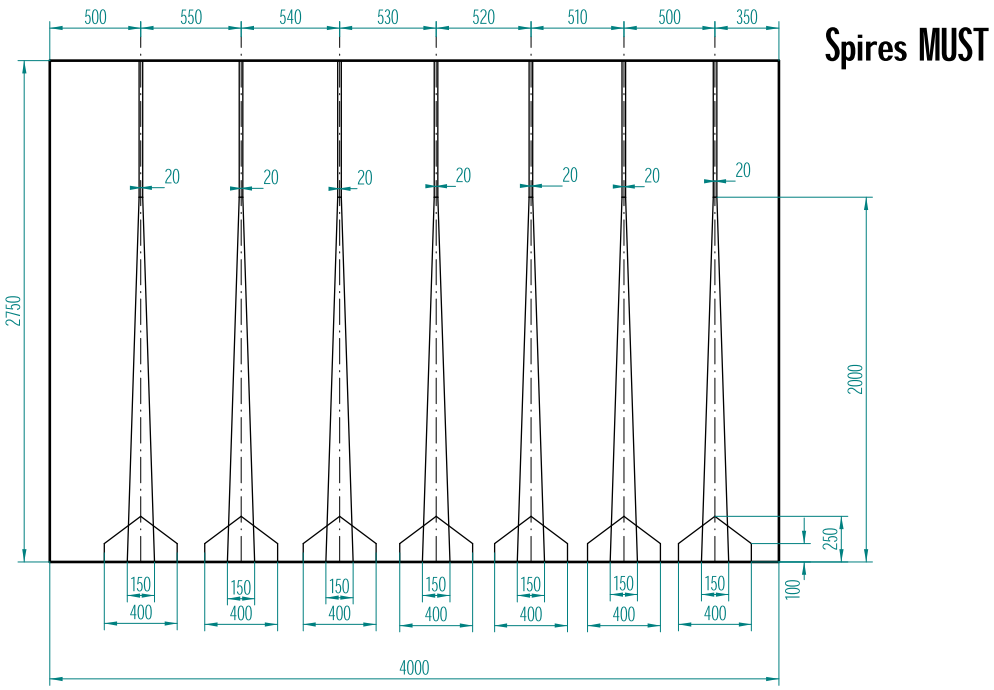

Figure A.1: Spires dimensions and positioning in the wind tunnel entrance. All measures are in millimetres.

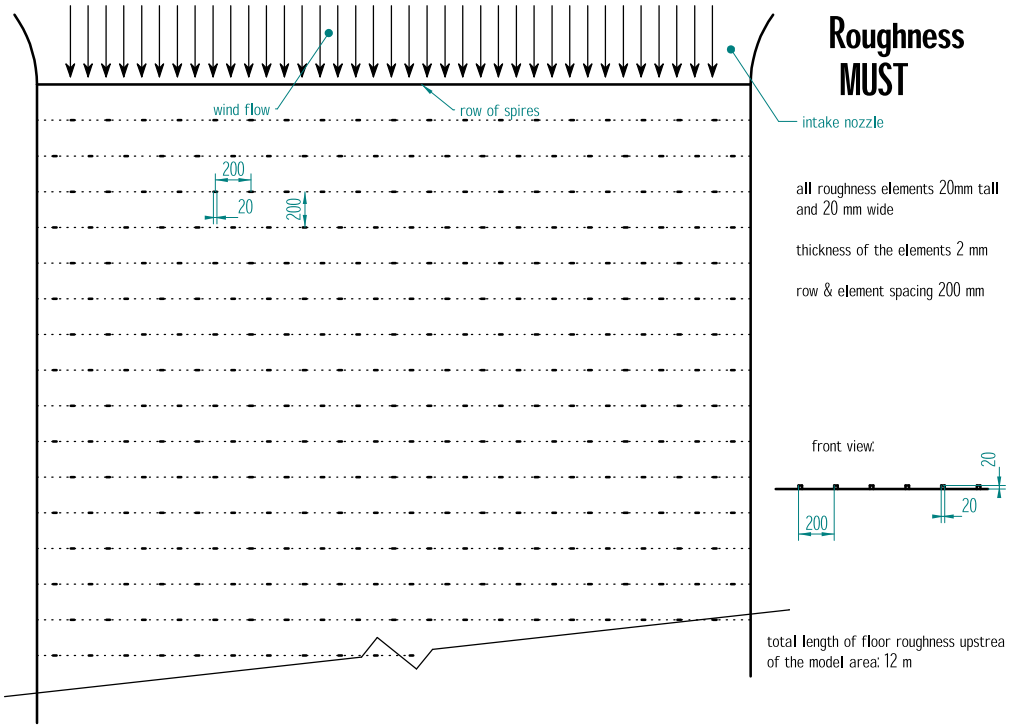

Figure A.2: Roughness elements dimensions and positioning on the wind tunnel floor. All measures are in millimetres.

Appendix B

Model Coordinates

Each standard shipping container has a width $W_{c\,\mathrm{FS}} = 12.2$ m, length $L_{c\,\mathrm{FS}} = 2.42$ m, and height $H_{\mathrm{FS}} = 2.54$ m. The position H5 were instead of a container occupied by the VIP car with dimensions: width $W_{\mathrm{VIP\,FS}} = 6.1$ m, length $L_{\mathrm{VIP\,FS}} = 2.44$ m, and height $H_{\mathrm{VIP\,FS}} = 3.51$ m. The following Tables B.1 - B.4 are giving the coordinates of the two corners of each container based on the MUST field set-up (Biltoft, 2001). The letter and first number indicate the container, the second number indicates the corner position: 1 (first column in the tables) means the north-east corner, 4 (second column in the the tables) means north-west corner, see Fig. 3.3.

north-east corners			north-west corners		
corner label	x_{FS} [m]	y_{FS} [m]	corner label	x_{FS} [m]	y_{FS} [m]
A91	84.94	87.00	A94	78.97	105.20
A81	85.07	65.04	A84	79.07	83.24
A71	85.16	44.52	A74	79.16	62.72
A61	85.44	23.95	A64	79.34	42.14
A51	85.38	4.01	A54	79.34	22.21
A41	85.70	-14.91	A44	79.69	3.29
A31	85.65	-34.79	A34	79.64	-16.59
A21	85.61	-53.98	A24	79.61	-35.78
A11	85.77	-73.52	A14	79.78	-55.32
A01	85.59	-92.68	A04	79.67	-74.49
B91	69.55	86.67	B94	63.47	104.86
B81	70.08	64.25	B84	63.98	82.44
B71	70.49	43.44	B74	64.42	61.63
B61	70.73	22.98	B64	64.67	41.18
B51	71.46	3.24	B54	65.38	21.43
B41	71.67	-15.54	B44	65.61	2.66
B31	72.14	-35.67	B34	66.11	-17.47
B21	72.32	-54.15	B24	66.29	-35.95

Table B.1: The container corners exact coordinates. Part 1.

north-east corners			north-west corners		
corner label	x_{FS} [m]	y_{FS} [m]	corner label	x_{FS} [m]	y_{FS} [m]
B11	72.55	-74.11	B14	66.52	-55.91
B01	72.61	-92.82	B04	66.71	-74.63
C91	54.83	85.98	C94	48.83	104.18
C81	55.04	63.78	C84	49.04	81.98
C71	55.50	43.93	C74	49.53	62.13
C61	55.71	22.53	C64	49.68	40.73
C51	55.82	3.01	C54	49.84	21.21
C41	56.12	-15.99	C44	50.13	2.21
C31	56.54	-36.45	C34	50.52	-18.25
C21	56.86	-54.54	C24	50.84	-36.34
C11	57.27	-74.82	C14	51.25	-56.62
C01	57.78	-92.62	C04	51.73	-74.42
D91	39.55	86.62	D94	33.55	104.82
D81	38.65	64.13	D84	32.67	82.33
D71	39.16	44.46	D74	33.20	62.66
D61	39.20	22.13	D64	33.23	40.33
D51	39.89	2.20	D54	33.86	20.40
D41	40.28	-17.24	D44	34.25	0.96
D31	40.84	-37.45	D34	34.78	-19.25
D21	41.26	-55.43	D24	35.21	-37.23
D11	41.79	-75.05	D14	35.73	-56.85
D01	42.07	-92.80	D04	36.02	-74.60
E91	24.15	86.60	E94	18.15	104.80
E81	23.09	64.30	E84	17.08	82.50
E71	23.61	44.44	E74	17.62	62.64
E61	23.76	21.33	E64	17.76	39.53
E51	23.83	1.35	E54	17.83	19.55
E41	24.00	-18.78	E44	17.94	-0.58
E31	24.79	-38.46	E34	18.74	-20.26
E21	26.26	-56.79	E24	20.15	-38.60
E11	26.78	-75.85	E14	20.75	-57.65
E01	27.61	-93.08	E04	21.52	-74.89
F91	9.73	86.14	F94	3.82	104.33
F81	8.79	63.81	F84	2.74	82.01
F71	9.91	44.18	F74	3.87	62.38
F61	11.35	20.70	F64	5.32	38.90
F51	11.33	1.66	F54	5.46	19.84
F41	10.90	-15.51	F44	5.01	2.68
F31	10.68	-38.37	F34	4.71	-20.17
F21	11.09	-56.63	F24	5.08	-38.43
F11	11.18	-75.90	F14	5.14	-57.70
F01	11.71	-94.19	F04	5.68	-75.99

Table B.2: The container corners exact coordinates. Part 2.

north-east corners			north-west corners		
corner label	x_{FS} [m]	y_{FS} [m]	corner label	x_{FS} [m]	y_{FS} [m]
G91	-6.15	84.97	G94	-12.22	103.17
G81	-6.03	63.15	G84	-12.07	81.35
G71	-5.31	43.25	G74	-11.34	61.45
G61	-4.95	20.00	G64	-10.94	38.20
G51	-4.32	0.02	G54	-10.40	18.21
G41	-3.73	-21.03	G44	-9.71	-2.83
G31	-3.62	-39.23	G34	-9.65	-21.03
G21	-3.45	-57.53	G24	-9.46	-39.33
G11	-3.40	-76.09	G14	-9.35	-57.89
G01	-3.29	-95.18	G04	-9.31	-76.98
H91	-22.65	85.12	H94	-28.59	103.32
H81	-23.20	62.55	H84	-29.20	80.75
H71	-22.65	42.97	H74	-28.71	61.17
H61	-21.72	19.87	H64	-27.70	38.07
H51	-19.37	3.30	H54	-25.54	15.39
H41	-20.54	-21.52	H44	-26.58	-3.32
H31	-20.13	-40.17	H34	-26.12	-21.97
H21	-20.14	-58.27	H24	-26.12	-40.07
H11	-19.56	-76.83	H14	-25.59	-58.63
H01	-18.75	-96.28	H04	-24.78	-78.08
I91	-36.72	84.45	I94	-42.68	102.65
I81	-37.32	62.15	I84	-43.30	80.35
I71	-37.27	42.56	I74	-43.27	60.76
I61	-37.77	19.32	I64	-43.64	37.50
I51	-36.30	-1.73	I54	-42.30	16.47
I41	-35.71	-21.32	I44	-41.70	-3.12
I31	-35.16	-41.20	I34	-41.22	-23.00
I21	-34.85	-58.67	I24	-40.88	-40.47
I11	-34.32	-77.41	I14	-40.27	-59.21
I01	-34.00	-97.19	I04	-39.95	-78.99
J91	-52.53	83.66	J94	-58.57	101.86
J81	-52.91	61.90	J84	-58.87	80.10
J71	-52.27	42.68	J74	-58.31	60.88
J61	-51.80	19.65	J64	-57.77	37.85
J51	-51.44	-2.38	J54	-57.41	15.82
J41	-51.09	-23.11	J44	-57.07	-4.91
J31	-51.24	-42.26	J34	-57.26	-24.06
J21	-50.56	-59.82	J24	-56.58	-41.62
J11	-50.29	-77.83	J14	-56.26	-59.63
J01	-49.29	-97.63	J04	-55.35	-79.43
K91	-67.83	83.42	K94	-73.89	101.62
K81	-68.34	61.65	K84	-74.39	79.85

Table B.3: The container corners exact coordinates. Part 3.

north-east corners			north-west corners		
corner label	x_{FS} [m]	y_{FS} [m]	corner label	x_{FS} [m]	y_{FS} [m]
K71	-67.74	42.94	K74	-73.76	61.14
K61	-67.42	19.42	K64	-73.43	37.62
K51	-66.42	-3.05	K54	-72.48	15.15
K41	-66.32	-23.84	K44	-72.27	-5.64
K31	-66.31	-43.22	K34	-72.32	-25.02
K21	-65.90	-60.75	K24	-71.94	-42.55
K11	-65.41	-77.96	K14	-71.42	-59.76
K01	-64.13	-98.21	K04	-70.14	-80.01
L91	-83.44	82.92	L94	-89.39	101.12
L81	-84.16	61.09	L84	-90.15	79.29
L71	-83.80	42.86	L74	-89.87	61.06
L61	-83.67	19.37	L64	-89.64	37.57
L51	-83.13	-3.37	L54	-89.10	14.83
L41	-82.24	-24.13	L44	-88.24	-5.93
L31	-82.05	-43.42	L34	-88.02	-25.22
L21	-81.59	-61.19	L24	-87.62	-42.99
L11	-81.40	-78.95	L14	-87.41	-60.75
L01	-81.07	-98.90	L04	-87.07	-80.70

Table B.4: The container corners exact coordinates. Part 4.

Tables B.5 and B.6 are giving the coordinates of the measurement equipment employed in the MUST field campaign. Table B.5 shows labelling, position, height and equipment of the masts within the container array. Table B.6 shows the labelling and position of the street level dPIDs.

	x_{FS} [m]	y_{FS} [m]	height [m]	position centred between	equipment
T tower	-13.26	6.04	32	G5 and H5	3-D sonics dPIDs
A tower	47.98	-58.87	6	C2, C1, D2 and D1	UVIC
B tower	45.97	60.18	6	C8, C7, D8 and D7	UVIC
C tower	-45.79	37.18	6	I7, I6, J6 and J7	UVIC
D tower	-44.22	-44.41	6	I2, I3, J2 and J3	UVIC
N tower	115.79	10.15	16	downwind of the array	2-D sonics
S tower	-115.99	2.76	16	upwind of the array	2-D sonics

Table B.5: The masts exact coordinates and equipment.

dPID number	x_{FS} [m]	y_{FS} [m]	z_{FS} [m]	position centred between
1	-43.62	-62.33	1.6	J1, J2, I1 and I2
2	-43.97	-53.16	1.6	J2 and I2
3	-44.22	-44.41	1.6	J2, J3, I2 and I3
4	-44.62	-25.89	1.6	J3, J4, I3 and I4
5	-44.57	-16.11	1.6	J4 and I4
6	-44.80	-6.03	1.6	J4, J5, I4 and I5
7	-45.05	4.04	1.6	J5 and I5
8	-45.50	14.85	1.6	J5, J6, I5 and I6
9	-45.80	25.65	1.6	J6 and I6
10	-46.02	48.72	1.6	J7 and I7
11	-46.20	58.43	1.6	J7, J8, I7 and I8
12	-46.26	68.13	1.6	J8 and I8
13	-12.66	-70.34	1.6	H1 and G1
14	-13.00	-51.81	1.6	H2 and G2
15	-13.11	-33.62	1.6	H3 and G3
16	-13.37	-15.16	1.6	H4 and G4
17	-13.22	-3.72	1.6	H4, H5, G4 and G5
18	-14.00	15.35	1.6	H5, H6, G5 and G6
19	-14.51	26.04	1.6	H6 and G6
20	-15.31	49.19	1.6	H7 and G7
21	-15.88	68.93	1.6	H8 and G8
22	17.68	-69.79	1.6	F1 and E1
23	17.31	-50.67	1.6	F2 and E2
24	16.50	-32.34	1.6	F3 and E3
25	16.29	-11.08	1.6	F4 and E4
26	16.53	7.60	1.6	F5 and E5
27	16.30	27.11	1.6	F6 and E6
28	15.51	50.42	1.6	F7 and E7
29	14.66	70.15	1.6	F8 and E8
30	15.84	92.47	1.6	F9 and E9
31	48.39	-77.74	1.6	D0, D1, C0 and C1
32	47.75	-48.90	1.6	D2 and C2
33	47.38	-30.86	1.6	D3 and C3
34	46.96	-10.51	1.6	D4 and C4
35	46.79	-0.90	1.6	D4, D5, C4 and C5
36	46.64	8.72	1.6	D6 and C6
38	46.19	39.36	1.6	D6, D7, C6 and C7
39	46.21	50.31	1.6	D7 and C7
40	45.65	70.05	1.6	D8 and C8

Table B.6: The street level dPIDs exact coordinates.

Table B.7 is giving the coordinates of the sources, which were used during the MUST field campaign on the 25th and the 26th September 2001 (Biltoft, 2001). Last column is giving the description of the source position in term of the container array.

source number	x_{FS} [m]	y_{FS} [m]	z_{FS} [m]	position
26	-53.75	89.76	2.7	roof of J9
29	-77.46	67.47	1.8	between K8 and L8
30	-61.40	89.64	1.8	between J9 and K9
31	-71.78	67.73	1.8	upwind of K8
32	-55.96	89.75	0.15	upwind of J9
33	-53.49	48.78	2.7	roof of J7
34	-80.41	-72.86	1.3	upwind of L1
35	-80.06	-92.81	1.3	upwind of L0
36	-82.27	-92.80	2.7	roof of L0
37	-104.59	-142.85	1.3	24 m south of L1

Table B.7: The sources exact coordinates and position descriptions.

Bibliography

Allwine, K. J., Overview of joint urban 2003 - an atmospheric dispersion study in oklahoma city, in *Proceedings of the AMS Symposium on Planning, Nowcasting, and Forecasting in the Urban Zone, Seattle, Washington, January 11–15*, 2004.

Allwine, K. J., Shinn, J. H., Streit, G. E., Clawson, K. L., and Brown, M., Overview of urban 2000: A multiscale field study of dispersion through an urban environment., *Bull. Amer. Meteor. Soc.*, *83*, 521–536, 2002.

Antonia, R. A. and Luxton, R. E., The response of a turbulent boundary layer to a step change in surface roughness, part 1. smooth to rough, *J. Fluid Mech.*, *48*, 721–762, 1971.

Arnold, S., ApSimon, H., Barlow, J., Belcher, S., Bell, M., Boddy, D., Britter, R., Cheng, H., Clark, R., Colvile, R., Dimitroulopoulou, S., Dobre, A., Greally, B., Kaur, S., Knights, A., Lawton, T., Makepeace, A., Martin, D., Neophytou, M., Neville, S., Nieuwenhuijsen, M., Nickless, G., Price, C., Robins, A., Shallcross, D., Simmonds, P., Smalley, R., Tate, J., Tomlin, A., Wang, H., and Walsh, P., Introduction to the DAPPLE Air Pollution Project, *Science of The Total Environment*, *332*, 139–153, 2004.

ASCE, Manual of practice for wind tunnel studies of buildings and structures, American Society of Civil Engineers, Aerospace Division, 1995.

Barad, M. L., *Project Prairie Grass, a Field Program in Diffusion*, vol. 1, Air Force Cambridge Research Center, 1959.

Barlow, J. F. and Belcher, S. E., A wind tunnel model for quantifying fluxes in the urban boundary layer, *Boundary-Layer Meteorol.*, *104*, 131–150, 2002.

Batchvarova, E. and Gryning, S.-E., Progress in urban dispersion studies, *Theor. Appl. Climatol.*, *84*, 2006.

Berkowicz, R., Modelling street canyon pollution: model requirements and expectations, *International Journal of Environment and Pollution*, *8*, 609–619, 1997.

Bezpalcová, K., Flow and dispersion in a simplified street canyon - wind tunnel study, *EURASAP Newsletter*, *56*, 1–16, 2005.

Biltoft, C. A., Customer report for mock urban setting test, Tech. rep., WDTC-FR-01-121, U.S. Army Dugway Proving Ground, Dugway, Utah, 2001.

Briggs, G. A., Britterb, R. E., Hanna, S. R., Havensd, J. A., Robinse, A. G., and Snyder, W. H., Dense gas vertical diffusion over rough surfaces: results of wind-tunnel studies, *Atmospheric Environment*, *35*, 2265–2284, 2001.

Britter, R. E. and Hanna, S. R., Flow and dispersion in urban areas, *Ann. Rev. Fluid Mech.*, *35*, 469–496, 2003.

Bubník, J., Keder, J., Macoun, J., and Maňák, J., SYMOS97, Modelling system of stacionary sources, Tech. rep., Czech Hydrometeorological Institute, in Czech, 1998.

Cambustion, Principles of the Flame Ionisation Detector, URL `http://www.cambustion.co.uk/instruments/hfr500/fidprinciple.html`, 2006.

Camelli, F. E., Hanna, S. R., and Löhner, R., Simulation of the MUST field experiment using the Feflo-Urban CFD model, in *Proceedings of 5th AMS Urban Env. Symp., Vancouver, B.C., Canada*, 2004.

Cermak, J. E., Laboratory simulation of the atmospheric boundary layer, *AIAA Journal*, *9*, 1746–1754, 1971.

Cermak, J. E., Physical modeling of flow and dispersion over complex terrain, *Boundary-Layer Meteorol.*, *30*, 261–292, 1984.

Changnon, S. A., ed., *METROMEX: A review and summary*, Meteorological Monographs, American Meteorological Society, Boston, 1981.

Cheng, H. and Castro, I. P., Near wall flow over urban-like roughness, *Boundary-Layer Meteorol.*, *104*, 229–259, 2002a.

Cheng, H. and Castro, I. P., Near-wall flow development after a step change in surface roughness, *Boundary-Layer Meteorol.*, *105*, 411–432, 2002b.

Counihan, J., Adiabatic atmospheric boundary layers: A review and analysis of data from the period 1880–1972, *Atmospheric Environment*, *9*, 871–905, 1972.

DANTEC Dynamics, Principles of the Laser Doppler Anemometery, URL `http://www.dantecdynamics.com/LDA/Princip/Index.html`, 2006.

Davidson, M. J., Mylne, K. R., Jones, C. D., Phillips, J. C., Perkins, R. J., Fung, J. C. H., and Hunt, J. C. R., Plume dispersion through large groups of obstacles a field investigation, *Atmospheric Environment*, *29*, 3245–3256, 1995.

Davidson, M. J., Snyder, W. H., Lawson, R. E. J., and Hunt, J. C. R., Wind tunnel simulations of plume dispersion through groups of obstacles, *Atmospheric Environment*, *30*, 3715–3731, 1996.

Degraziaa, G. A., Acevedoa, O. C., Carvalhob, J. C., Goularta, A. G., Moraesa, O. L. L., Campos Velhoc, H. F., and Moreirab, D. M., On the universality of the dissipation rate functional form and of the autocorrelation functionnext term exponential form, *Atmospheric Environment*, *39*, 1917–1924, 2005.

Di Sabatino, S., Kastner-Klein, P., Berkowicz, R., Britter, R. E., and Fedorovich, E., The modelling of turbulence from traffic in urban dispersion models - part i: Theoretical consideration, *Environmental Fluid Dynamics*, *3*, 129–143, 2003.

Dinar, N., Kaplan, H., and Kleiman, M., Characterization of concentration fluctuation of a surface plume in a neutral boundary layer, *Boundary-Layer Meteorol.*, *45*, 157–175, 1988.

ESDU, Characteristics of atmospheric turbulence near the ground. Part II: single point data for strong winds (neutral atmosphere), Engineering Sciences Data Unit, Item No.85020, London, 1985.

European Commision, EU directive 85/337/EEC, URL `http://europa.eu.int/comm/environment/eia/full-legal-text/85337.htm`, 1985.

Feddersen, B., *Wind tunnel modelling of turbulence and dispersion above tall and highly dense urban roughness*, Ph.D. thesis, ETH Zürich, 2005.

Fingerson, L. M. and Menon, R. K., *The Handbook of Fluid Dynamics*, chap. Laser Doppler Velocimetry, pp. 35–1–35–15, CRC Press LLC, 1999.

Finnigan, J., Turbulence in plant canopies, *Ann. Rev. Fluid Mech.*, *32*, 519–571, 2000.

Gailis, R. M. and Hill, A., A wind-tunnel simulation of plume dispersion within a large array of obstacles, *Boundary-Layer Meteorol.*, *119*, 289–338, 2006.

Gifford, F. A., J., Use of routine meteorological observations for estimating atmospheric dispersion, *Nuc. Saf.*, *2(40)*, 47–57, 1961.

Gifford, F. A., J., An outline of theories diffusion in the lower layers of the atmosphere, Tech. rep., Meteorology and Atomic Energy, USAEC Report TID-24190, U.S. Atomic Energy Commission, NTIS, 1968.

Golder, D., Relations among stability parameters in the surface layer, *Boundary Layer Meteorol.*, *3*, 47–58, 1972.

Grimmond, C. and Oke, T., Aerodynamic properties of urban areas derived from analysis of surface form, *Journal of Applied Meteorology*, *38*, 1262–1292, 1999.

Grimmond, C. S. B., Progress in measuring and observing the urban atmosphere, *Theoretical and Applied Climatology*, *84*, 2006.

Hall, D. J., Kukadia, V., Walker, S., Tily, P., and W., M. G., The effects of release time on the dispersion of a fixed inventory of havier than air gas - a wind tunnel model study, BRE Client Report CR 149/96, Building Research Establishment, 1996a.

Hall, D. J., Macdonald, R., Walker, S., and Spanton, A. M., Measurements of dispersion within simulated urban arrays a small scale wind tunnel study, BRE Client Report CR 178/96, Building Research Establishment Ltd., Garston, Watford, UK, 1996b.

Hall, D. J., Spanton, A. M., Macdonald, R., and Walker, S., A simple model for estimating dispersion in urban areas, BRE Client Report CR 169/97, Building Research Establishment Ltd., Garston, Watford, UK, 1997.

Hanna, S. R. and Britter, R. E., *Wind Flow and Vapor Cloud Dispersion at Industrial and Urban Sites*, American Institute of Chemical Engineers, New York, 2002.

Hanna, S. R., Briggs, G. A., and Hosker, R. P., *Handbook on Atmospheric Diffusion*, NTIS/USDOC, Springfield, 1982.

Hanna, S. R., Tehranian, S., Carissimo, B., Macdonald, R. W., and Lohner, R., Comparison of model simulation with observations of mean flow and turbulence within simple obstacle arrays, *Atmospheric Environment*, *36*, 5067–5079, 2002.

Hanna, S. R., Hansen, O. R., and Dharmavaram, S., FLACS CFD air quality model performance evaluation with Kit Fox, MUST, Prairie Grass, and EMU observations, *Atmospheric Environment*, *38*, 4675–4687, 2004.

Kaimal, J. C. and Finnigan, J. J., *Atmosperic Boundary Layer Flows, Their Structures and Measurement*, Oxford University Press, New York, 1994.

Kaimal, J. C., Wyngaard, J. C., Izumi, Y., and Coté, O. R., Spectral characteristics of surface layer turbulence, *Quarterly Journal of the Royal Meteorological Society*, *98*, 563–589, 1972.

Kanda, M., Progress in the scale modeling of urban climate: Review, *Theor. Appl. Climatol.*, *84*, 2006.

Kanda, M., Moriwaki, R., and Kasamatsu, F., Large-eddy simulation of turbulent organized structures within and above explicitly resolved cube arrays, *Boundary-Layer Meteorol.*, *112*, 343–368, 2004.

Kastner-Klein, P. and Plate, E. J., Wind-tunnel study of concentration fields in street canyons, *Atmospheric Environment*, *33*, 3973–3979, 1999.

Kastner-Klein, P. and Rotach, M. W., Mean flow and turbulence characteristics in an urban roughness sublayer, *Boundary-Layer Meteorol.*, *111*, 55–84, 2004.

Kastner-Klein, P., Fedorovich, E., and Rotach, M. W., A wind tunnel study of organised and turbulent air motions in urban street canyons, *J. Wind Eng. Ind. Aerodyn.*, *89*, 849–861, 2001.

Kastner-Klein, P., Fedorovich, E., Ketzel, M., Berkowicz, R., and Britter, R. E., The modelling of turbulence from traffic in urban dispersion models - part ii: Evaluation against laboratory and full-scale concentration measurements in street canyons, *Environmental Fluid Dynamics*, *3*, 145–172, 2003.

Ketzel, M., TRAPOS, URL `http://www2.dmu.dk/AtmosphericEnvironment/Trapos/cfd-wg.htm`, 2002.

Kim, J.-J. and Baik, J.-J., A numerical study of thermal effects on flow and pollutant dispersion in urban street canyons, *Journal Of Applied Meteorology*, *38*, 1249–1261, 1999.

Leitl, B., Schatzmann, M., and Kastner-Klein, P., Flow and dispersion in complex urban areas wind tunnel modelling in support of Joint Urban 2003, in *Proceedings of PHYSMOD 2005, International Workshop on Physical Modelling of Flow and Dispersion Phenomena, London, Ontario, Canada, August 24–26*, 2005.

Lohmeyer, A., Mueller, W. J., and Baechlin, W., A comparison of street canyon concentration predictions by different modellers: final results now available from the podbi-exercice, *Atmospheric Environment*, *36*, 157–158, 2002.

Macdonald, R., Griffiths, R. F., and Cheah, S. C., Field experiments of dispersion through reguler arrays of cubic structures, *Atmospheric Environment*, *31*, 783–795, 1997.

Macdonald, R., Griffiths, R. F., and Hall, D. J., A comparison of results from scaled field and wind tunnel modelling of dispersion in arrays of obstacles, *Atmospheric Environment*, *32*, 3845–3862, 1998.

McElroy, J. L., A comparative study of urban and rural dispersion, *Journal of Applied Meteorology*, *8*, 19–31, 1969.

McQuaid, J., ed., *Heavy Gas Dispersion Trials At Thorney Island, Proceedings of a Symposium held at the University of Sheffield, UK, 3-5 April 1984*, Chemical Engineering Monographs, 22, Elsevier, 1985.

Meroney, R. N. and Lohmeyer, A., Statistical characteristics of instantaneous dense gas clouds released in an atmospheric boundary-layer wind tunnel, *Boundary-Layer Meteorol.*, *28*, 1–22, 1984.

Mestayer, P., Durand, P., Augustin, P., Bastin, S., Bonnefond, J.-M., Béenech, B., Campistron, B., Coppalle, A., Delbarre, H., Dousset, B., Drobinski, P., Druilhet, A., Fréjafon, E., Grimmond, S., Groleau, D., Irvine, M., Kergomard, C., Kermadi, S., Lagouarde, J.-P., Lemonsu, A., Lohou, F., Long, N., Masson, V., Moppert, C., Noilhan, J., Offerle, B., Oke, T., Pigeon, G.,

Puygrenier, V., Roberts, S., Rosant, J.-M., Sanïd, F., Salmond, J., Talbaut, M., and Voogt, J., The Urban Boundary Layer Field Experiment over Marseille UBL/CLU - ESCOMPTE: Experimental Set-up and First Results, *Boundary-Layer Meteorol.*, *114*, 315–365, 2005.

Milliez, M., Musson-Genon, L., and Carissimo, B., Validation of a radiative scheme for cfd modeling of heat transfer between buildings and flow in urban canopies, in *Proceedings of 6th International Coference on Urban Climate, Göteborg, Sweden, June 12–16, 2006*, pp. 266–269, 2006.

Monin, A. S. and Yaglom, A. M., *Statistical Fluid Mechanics: Mechanics of Turbulence*, vol. 1, The MIT Press, 1971.

Nelson, M. A., Brown, M. J., Klewicki, J. C., and Pardyjak, E., Turbulence within and above real and artificial urban canopies, in *Proceedings of 5th AMS Urban Env. Symp., Vancouver, B.C., Canada*, 2004.

Nickola, P. W., Measurement of the movement, concentration and dimension of clouds resulting from instantaneous point source, *J. Appl. Meteorol.*, *10*, 962–973, 1971.

Oikawa, S. and Meng, Y., Turbulence characteristic and organized motion an a suburban roughness sublayer, *Boundary-Layer Meteorol.*, *74*, 289–312, 1995.

Oke, T. R., *Boundary Layer Climates*, Routledge, London, 1987.

Palmgren, F., Berkowicz, R., Hertel, O., and Vignati, E., Effects of reduction in nox on the no2 levels in urban streets, *Science of the Total Environment*, *189/190*, 409–415, 1996.

Panofsky, H. A. and Dutton, J. A., *Atmospheric turbulence*, John Wiley & Sons, 1984.

Pasquill, F., The estimation of the dispersion of windborne material, *Meteorol. Mag.*, *90*, 33–49, 1961.

Pasquill, F., *Atmospheric Diffusion*, John Wiley & Sons, New York, 1974.

Pavageau, M. and Schatzmann, M., Wind tunnel measurements of concentration fluctuations in an urban street canyon., *Atmospheric Environment*, *33*, 3961–3971, 1999.

Plate, E. J., *Engineering Meteorology*, Elsevie, 1981.

Rafailidis, S., Influence of building areal density and roof shape on the wind characteristics above a town, *Boundary-Layer Meteorol.*, *85*, 255–271, 1997.

Raupach, M. R., Thom, A. S., and Edwards, I., A wind-tunnel study of turbulent flow close to regularly arrayed rough surfaces, *Boundary-Layer Meteorol.*, *18*, 373–397, 1980.

Raupach, M. R., Antonia, R. A., and Rajagopalan, S., Rough-wall turbulent boundary layers, *App. Mech. Rev.*, *44*, 1–25, 1991.

Robins, A. and Cheng, H., Wind tunnel investigation of pollutant dispersion in urban area, in *Proceedings of PHYSMOD 2005, International Workshop on Physical Modelling of Flow and Dispersion Phenomena, London, Ontario, Canada, August 24–26*, 2005.

Rodean, H. C. and Cederwall, R. T., Analysis of turbulent wind-velocity and gas-concentration fluctuations during the Burro Series 40-m^3 LNG Spill Experiments, UCRL-53353, Lawrence Livermore Laboratory, University of California, 1982.

Rotach, M. W., Turbulence close to a rough urban surface, part i: Reynolds stress, *Boundary-Layer Meteorol.*, *65*, 1–28, 1993a.

Rotach, M. W., Turbulence close to a rough urban surface, part ii: Variances and gradients, *Boundary-Layer Meteorol.*, *66*, 75–92, 1993b.

Rotach, M. W., Vogt, R., Bernhofer, C., Batchvarova, E., Christen, A., Clappier, A., Feddersen, B., Gryning, S.-E. Martucci, G., Mayer, H., Mitev, V., Oke, T. R., Parlow, E., Richner, H., Roth, M., Roulet, Y. A., Ruffieux, D., Salmond, J., Schatzmann, M., and Voogt, J., BUBBLE - a Major Effort in Urban Boundary Layer Meteorology, *Theor. Appl. Climatol.*, *81*, 231–261, 2004.

Roth, M., Review of atmospheric turbulence over cities, *Quarterly Journal of the Royal Meteorological Society*, *126*, 941–990, 2000.

Schatzmann, M. and Britter, R., eds., *Proceedings of International Workshop on Quality assurance of microscale meteorological models, Hamburg, Germany, July 28–29*, European Science Foundation, 2005.

Schatzmann, M. and Leitl, B., Validation and application of obstacle resolving urban dispersion models, *Atmospheric Environment*, *36*, 4811–4821, 2002.

Schultz, M., Schatzmann, M., and Leitl, B., Effect of roughness inhomogeneities on the development of the urban boundary layer, *International Journal of Environment and Pollution*, *25*, 105–117, 2005.

Simiu, E. and Scanlan, R. H., *Wind effects on structures*, John Wiley & Sons, 1986.

Snyder, W. H., Guideline for fluid modeling of atmospheric diffusion, , report no. 600/8-81-009, Enviromental Sciences Research Laboratory, Office of Research and Development, U.S. Environmental Protection Agency, Research Triangle Park, NC 27711, 1981.

Snyder, W. H., Wind-tunnel study of entrainment in two-dimensional dense-gas plumes at the epa's fluid modeling facility, *Atmospheric Environment*, *35*, 2285–2304, 2001.

Snyder, W. H. and Castro, I. P., Yaw-response of hot-wire probes at ultra-low wind speeds, *Measurement Science and Technology*, *9*, 1531–1536, 1998.

Stull, R. B., *An Introduction to Boundary Layer Meteorology*, Kluwer Academic Publishers, 1988.

Sutton, O. G., A theory of eddy diffusion in the atmosphere, *Pro. R. Soc. (London), Ser. A*, 1932.

Sutton, O. G., *Atmospheric Turbulence*, Methuen, London, 1949.

Tennekes, H. and Lumley, J. L., *A first course in turbulence*, MIT Press, 1972.

Theurer, W., Plate, E. J., and Hoeschele, K., Semi-empirical models as a combination of wind tunnel and numerical dispersion modelling, *Atmospheric Environment*, *30*, 3583–3597, 1996.

Townsend, A. A., *The Structure of Turbulent Shear Flow*, Cambridge University Press, 1976.

Tritton, D. J., *Physical Fluid Dynamics*, Oxford University Press, 1988.

Uehara, K., Murakami, S., Oikawa, S., and Wakamatsu, S., Wind tunnel experiments on how thermal stratification affects flow in and above urban street canyons, *Atmospheric Environment*, *34*, 1553–1562, 2000.

Vardoulakis, S., Fisher, B. E. A., Pericleous, K., and Gonzalez-Flesca, N., Modelling air quality in street canyons: a review, *Atmospheric Environment*, *37*, 155–182, 2003.

VDI Guideline 3783/12, Physical modelling of flow and dispersion processes in the atmospheric boundary layer - aplication of wind tunnels, Beuth Verlag, Berlin, 2000.

Yee, E., Application of nonlinear dynamical systems analysis to conditionally sampled concentration fluctuations of a passive scalar in the atmospheric boundary layer, *Boundary-Layer Meteorol.*, *57*, 49–78, 1991.

Yee, E. and Biltoft, C. A., Concentration fluctuation measurements in a plume dispersing through a regular array of obstacles, *Boundary-Layer Meteorol.*, *111*, 363–415, 2004.

Yee, E., Chan, R., Kosteniuk, P. R., Chandler, G. M., Biltoft, C. A., and Bowers, J. F., Concentration fluctuations measurement in clouds released from a quasi-instantaneous point source in the atmospheric surface layer, *Boundary-Layer Meteorol.*, *71*, 341–373, 1994a.

Yee, E., Chan, R., Kosteniuk, P. R., Chandler, G. M., Biltoft, C. A., and Bowers, J. F., Experimental measurements of concentration fluctuations and scales in a dispersing plume in the atmospheric surface layer obtained using a very fast response concentration detector, *J. Appl. Meteorol.*, *33*, 996–1016, 1994b.

Yee, E., Kosteniuk, P. R., Biltoft, C. A., and Bowers, J. F., A study of concentration fluctuations in instantaneous clouds dispersing in the atmospheric surface layer for relative turbulent diffusion: Basic descriptive statistics, *Boundary-Layer Meteorol.*, *87*, 409–457, 1998.

Zimmerman, W. B. and Chatwin, P. C., Fluctuations in dense gas concentrations measured in a wind-tunnel, *Boundary-Layer Meterol.*, *75*, 321–352, 1995.